Technische Universität München
Fakultät für Maschinenwesen
Lehrstuhl für Aerodynamik und
Strömungsmechanik

Gravity-Wave Breaking and Turbulence in the Atmosphere

Sebastian Remmler

Vollständiger Abdruck der von der Fakultät für Maschinenwesen der Technischen Universität München zur Erlangung des akademischen Grades eines

Doktor-Ingenieurs

genehmigten Dissertation.

Vorsitzender:		Univ.-Prof. Dr.-Ing. Hans-Jakob Kaltenbach
Prüfer der Dissertation:	1.	Prof. Dr.-Ing. Stefan Hickel
		Delft University of Technology / Niederlande
	2.	Univ.-Prof. Dr.-Ing. Nikolaus A. Adams

Sebastian Remmler
remmler@tum.de

private address: Hitzhofener Straße 13
                    85080 Gaimersheim
                    Germany

current affiliation: AUDI AG
                    I/EK-44, Aerodynamics / Aeroacoustics
                    85045 Ingolstadt
                    Germany

Typesetting: LATEX and KOMA-Script
Fonts: Bitstream Charter (text body), Helvetica (headlines)
Print: DIEKOPIE24.de - George-Bähr-Straße 8 - 01069 Dresden, Germany

The breaking of a wave cannot explain the whole sea.

Vladimir Vladimirovich Nabokov

Abstract

In order to improve the reliability and accuracy of weather and climate models, it is necessary to deepen the understanding of buoyancy-driven turbulent flows and to find efficient numerical simulation methods for this kind of flows. The present work contributes to these objectives by providing a number of benchmark simulations of homogeneous stratified turbulence, which are investigated in detail with respect to the spectral energy fluxes and the two-dimensional spectral eddy viscosity and diffusivity. Based on these results we validate several efficient large-eddy simulation (LES) methods for stratified turbulence. Furthermore, we present high resolution reference simulations of three different cases of breaking monochromatic gravity waves in the terrestrial mesosphere. We analyse these results elaborately, compare them to previous studies and use them for the validation of different LES methods which have produced promising results for stratified turbulence. We show that it is possible to simulate the fully non-linear process of gravity-wave breaking with a comparatively low number of grid cells, as long as the computational parameters are chosen carefully.

Zusammenfassung

Um die Zuverlässigkeit und Genauigkeit von Wetter- und Klimamodellen zu verbessern, ist einerseits ein vertieftes Verständnis der Physik auftriebgetriebener turbulenter Strömungen notwendig, andererseits werden effiziente numerische Simulationsmethoden für diese Art von Strömungen benötigt. Diese beiden Fragestellungen werden durch die vorliegende Arbeit vorangetrieben. Dazu wurden mehrere Referenzsimulationen von homogener geschichteter Turbulenz angefertigt, die detailliert analysiert werden, insbesondere auch in Hinblick auf die spektralen Energieflüsse und die spektrale Wirbelviskosität und -diffusivität. Darauf aufbauend werden verschiedene Methoden der Large-Eddy-Simulation (LES) für homogene geschichtete Turbulenz validiert. Weiterhin wurden hochaufgelöste Referenzsimulationen von drei verschiedenen Fällen brechender monochromatischer Schwerewellen in der mittleren Erdatmosphäre durchgeführt. Die Ergebnisse dieser Simulationen werden ausführlich analysiert, mit älteren Ergebnissen verglichen und ebenfalls zur Validierung verschiedener LES-Methoden verwendet, die zuvor zu guten Ergebnissen bei geschichteter Turbulenz geführt haben. Es wird gezeigt, dass es möglich ist mit einer vergleichsweise kleinen Anzahl an Gitterzellen den kompletten nichtlinearen Prozess des Brechens atmosphärischer Schwerewellen zu simulieren, wenn die entsprechenden numerischen Parameter sorgfältig gewählt werden.

Contents

Danksagung – Acknowledgements

Diese Dissertation und die ihr zugrunde liegenden Publikationen entstanden in meiner Zeit als wissenschaftlicher Mitarbeiter am Lehrstuhl für Aerodynamik und Strömungsmechanik der Technischen Universität München in den Jahren 2009 bis 2014 im Rahmen des DFG-Schwerpunktprogramms 1276 "MetStröm".

Dass die Arbeit in dieser Form entstehen konnte, ist im Wesentlichen Stefan Hickel und Ulrich Achatz zu verdanken. Für die hervorragende fachliche Betreuung, Führung, geduldige Unterstützung, jederzeit verfügbare Hilfe und die gewinnbringenden Diskussionen möchte ich mich bei ihnen ebenso herzlich bedanken wie für die Ermutigung und Unterstützung bei jeder einzelnen Veröffentlichung und Konferenzteilnahme. Desweiteren danke ich Nikolaus A. Adams, dass er mir die Arbeit an seinem Lehrstuhl ermöglicht hat und für die Übernahme des Zweitgutachtens für die Dissertation und Hans-Jakob Kaltenbach für den Vorsitz der Prüfungskommission.

Sincere thanks are given to Mark Fruman, with whom I had an excellent collaboration and many interesting discussions on all gravity-wave related topics of my work.

Weiterhin möchte ich mich bei allen Kollegen am Lehrstuhl bedanken, die dazu beigetragen haben, dass mir die Zeit dort sehr angenehm in Erinnerung geblieben ist und die es nicht an fachlicher, algorithmischer und moralischer Unterstützung haben mangeln lassen.

There is a number of people who contributed to this work (without even knowing about it) by personal discussions and their own publications. The list includes, but is not limited to Geert Brethouwer, Andrzej Domaradzki, Andreas Dörnbrack, David C. Fritts, Erik Lindborg, Piotr Smolarkiewicz and Chantal Staquet. The list should be extended by the names of the anonymous reviewers of the journal articles who raised interesting questions and helped improving the articles.

Die Arbeit wurde durch das SPP "MetStröm" gefördert. Ich danke Rupert Klein und Thomas von Larcher für die Organisation dieses Schwerpunktprogramms insbesondere auch, weil der fachübergreifende Austausch und der umfassende Einblick in die Welt der Meteorologie und Klimatologie mir persönlich große Freude bereitet und meinen Horizont deutlich erweitert haben.

Abschließend möchte ich mich bei Imke und Tine für die akribische Revision und den versierten sprachlichen Feinschliff der Dissertationsschrift bedanken.

Preface

The present work is a summary of six peer-reviewed journal articles published by the author during the years 2012–2015. The included articles are:

IJHFF12: Remmler, S. and Hickel, S. (2012). Direct and large eddy simulation of stratified turbulence. *Int. J. Heat Fluid Flow*, 35:13–24.

TCFD13: Remmler, S. and Hickel, S. (2013). Spectral structure of stratified turbulence: Direct numerical simulations and predictions by large eddy simulation. *Theor. Comput. Fluid Dyn.*, 27:319–336.

JFM13: Remmler, S., Fruman, M. D., and Hickel, S. (2013). Direct numerical simulation of a breaking inertia-gravity wave. *J. Fluid Mech.*, 722:424–436.

JFM14: Remmler, S., Hickel, S. (2014). Spectral eddy viscosity of stratified turbulence. *J. Fluid Mech.*, 755, R 6:.

JGR14: Fruman, M. D., Remmler, S., Hickel, S., and Achatz, U. (2014) On the construction of a direct numerical simulation of a breaking inertia-gravity wave in the upper-mesosphere. *J. Geophys. Res.* 119:11 613–11 640.

JAS15: Remmler, S., Hickel, S., Fruman, M. D., and Achatz, U. (2015) Validation of large-eddy simulation methods for gravity-wave breaking. *J. Atmos. Sci.*, doi:10.1175/JAS-D-14-0321.1, in press.

In the following text we will use the abbreviations (IJHFF12 etc.) for these internal references and the usual "author (year)" citation style for external references.

IJHFF12, TCFD13 and JFM14 deal with direct numerical simulation (DNS) of stratified turbulence and proper turbulence subgrid-scale models for the large-eddy simulation (LES) of this kind of flow. The latter are required for the simulation of breaking gravity waves. In JFM13 we focus purely on fully resolved simulations of a first breaking wave case without a turbulence subgrid-scale model in order to create reference data for the validation of LES. In JGR14 we extend this topic by adding two new test cases and summarising the whole process of

designing, setting up and conducting the DNS. Eventually, in JAS15 we present LES of the breaking wave cases introduced before.

The following introduction (chapter 1) provides an overview of the available literature, open questions and our contribution to the field of numerical simulation of turbulence in stably stratified fluids in general and, specifically, breaking gravity waves. This chapter summarises the introductions of the respective journal articles without skipping too much information.

Chapter 2 summarises the numerical methods used without covering all details. The chapter mainly gives an overview of the methods, explains differences in the nomenclature in the articles and clarifies how the different sets of equations are related. For many details the reader is referred to the respective articles.

Instead of a "results" section, chapter 3 provides one-page summaries of each journal article included in this work. The articles, including all results, figures, tables and discussions are fully reprinted in the appendix.

The work is concluded by a summary and discussion of the results in chapter 4.

Complementary to this book there is a data DVD including initial conditions as well as time resolved integral results, energy spectra and 1-D result data from different simulations of the three investigated cases of breaking monochromatic gravity waves (JFM13, JGR14 and JAS15). These data may be used as reference for similar investigations. For details concerning the data format and accessibility, please refer to the enclosed file "readme.pdf".

1. Introduction

1.1. Gravity waves in the atmosphere

Gravity wave (fluid mechanics): A wave in a fluid medium in which restoring forces are provided primarily by buoyancy (that is, gravity) rather than by compression.

(Dictionary of scientific and technical terms: Parker, 2003)

Any vertical displacement of a fluid parcel in a stably stratified fluid induces a restoring force on that parcel. The restoring force causes the parcel to move back into its neutral position, to overshoot due to its inertia and, if viscous forces are sufficiently weak, to oscillate around its neutral position. The local displacement of fluid causes this oscillation to spread within the whole domain as a transverse wave, generally referred to as an (internal) gravity wave. Gravity waves are an important feature of the circulation within the terrestrial atmosphere and oceans. They transport energy and momentum from the source region to the region where they are dissipated, e.g. by breaking. These two regions can be located hundreds or even thousands of kilometres apart from each other. The breaking of gravity waves can locally lead to enhanced turbulence, mixing of passive tracers and induction of large scale flows. In fact, gravity wave breaking is a sine qua non for understanding the global oceanic circulation and some important phenomena in the middle atmosphere.

Atmospheric gravity waves are mostly forced by flow over orography (e.g. Smith, 1979; Lilly et al., 1982; McFarlane, 1987), by convection (e.g. Chun et al., 2001; Grimsdell et al., 2010) or by spontaneous imbalance of the mean flow in the troposphere (O'Sullivan and Dunkerton, 1995; Plougonven and Snyder, 2007). Flow over mountains, ridges or whole mountainous areas is probably the best understood source of gravity waves today. The orographic obstacle exerts a drag on the flow; this drag acts in the region where the emitted gravity waves are dissipated, i.e. possibly far away from the source. Sawyer (1959) was one of the first to note the necessity of taking gravity wave drag into account in numerical weather forecast models. Several authors (Bretherton, 1969; Lilly, 1972; Blumen and McGregor, 1976) attempted to quantify the gravity wave drag exerted

by orographic gravity waves on the mean flow, finding values of the order of 1 Pa, which can be sufficient to accelerate the mean flow by several m/s per day (Nappo, 2002). Chun and Baik (1998) found even larger values of acceleration and deceleration due to gravity waves generated by thermal forcing in cumulus convection. The direct effects of gravity waves on the general circulation in the troposphere and lower stratosphere are only minor, although gravity wave breaking can lead to clear-air turbulence and locally enhanced turbulent diffusion in that region. On the other hand, gravity waves strongly influence the circulation in the atmospheric layers above the troposphere. In the stratosphere (the altitude range between approximately 15 and 50 km) they lead, together with other equatorial waves, to the quasi-biennial oscillation in equatorial winds (Dunkerton, 1997a; Baldwin et al., 2001). In the mesosphere (approximately 50 and 90 km altitude) gravity waves are, for example, responsible for the cold summer pole mesopause (Hines, 1965; Houghton, 1978). Gravity waves generated in the troposphere (the altitude range below approximately 15 km) are subject to wave dispersion while propagating into the middle atmosphere. Prusa et al. (1996) showed in a series of numerical experiments that gravity waves generated in the troposphere at a broad wavelength spectrum reach the upper mesosphere as an almost monochromatic wave packet with a horizontal wavelength between a few kilometres and more than 100 km depending on the horizontal scale of the forcing and the background conditions. For a detailed overview of gravity waves in the middle atmosphere see Fritts and Alexander (2003).

Since most gravity waves have a wavelength that cannot be resolved in general circulation models, the effect of gravity waves on the global circulation is usually accounted for by some parametrisation[1] based on combinations of linear wave theory, empirical observations of time-mean energy spectra and simplified treatments of the breaking process. Various parametrisations have been proposed, e.g. by Lindzen (1981), Holton (1982), Palmer et al. (1986), Scinocca and Mc-Farlane (2000) and others. Reviews of gravity wave parametrisation schemes are provided by McLandress (1998), Kim et al. (2003) and Fritts and Alexander

---

[1] Geophysicists prefer the term "parametrisation" over the engineering term "model". Both terms refer to the same concept, i.e. a more or less complex mathematical description of the effect of some unresolved small scale process on the numerically resolved large scale phenomenon. To remain close to the accepted terminology of both fields, we use "gravity wave parametrisation" but "turbulence subgrid-scale model".

Furthermore, a flow solver is generally referred to as a "code" by engineers and as a "model" by geophysicists, which shall not be confused with the engineering "model" described above. We generally use "flow solver" or "code" to refer to a pure CFD computer programme, while we use "weather or climate model" for the software used in geophysics.

(2003). Generally, the upward propagation of linear waves through the atmosphere is computed using the Wentzel–Kramers–Brillouin–Jeffreys (WKBJ) approximation (Bretherton, 1966; Einaudi and Hines, 1970; Laprise, 1993), which is based on the assumption of a slowly varying background flow field. During the upward propagation of the wave, the amplitude typically grows as the ambient density decreases. Effects of non-linearity within the wave become more important until the wave reaches the threshold of static stability (i.e. when the vertical gradient of total potential temperature becomes locally negative) and breaks. Most parametrisation schemes account for this effect by rather pragmatically reducing the wave amplitude and transferring the corresponding fraction of the wave momentum to the mean flow.

The study of gravity wave breaking has been a subject of research for many decades. Theoretical analyses of inviscid (Mied, 1976; Drazin, 1977) and weakly viscous (Klostermeyer, 1982) breaking gravity waves show that monochromatic high frequency gravity waves (HGWs), i.e. waves unaffected by rotation, are linearly unstable regardless of their amplitude. As opposed to HGWs, low frequency inertia-gravity waves (IGWs) are influenced by the Coriolis force and thus have a non-zero third velocity component perpendicular to the plane of the wave. Dunkerton (1997b) and Achatz and Schmitz (2006b) showed that this influences the orientation of the most unstable perturbations. Therefore, the breaking mechanism in IGWs differs fundamentally from HGWs and has to be investigated separately.

The onset of gravity wave breaking, i.e. the initial growth of some instability modes, can be treated as a two-dimensional problem with three velocity components. However, the breaking process itself is inherently three-dimensional, and the breaking dynamics in two- and three-dimensional simulations strongly differ from each other, as pointed out first by Andreassen et al. (1994) and by Fritts et al. (1994). This was later confirmed by Fritts et al. (2009a,b, 2013) and by Fritts and Wang (2013) using simulations with much higher, and thus, more realistic Reynolds numbers. For a more comprehensive review of the most recent DNS studies on gravity wave breaking see JGR14.

The breaking of gravity waves can be studied best by means of numerical simulations, since these allow for a separation of the wave-breaking effects from all other atmospheric phenomena and offer a variety of analysis and post-processing tools. An important aspect in setting up a simulation of a gravity wave breaking event is the proper choice of the domain size and initial conditions. Since the gravity wave itself is one-dimensional, while the breaking process and the resulting turbulence is three-dimensional, proper choices have to be made for the two

directions perpendicular to the wave vector. In order to make the DNS of breaking gravity-waves feasible, Achatz (2005) and Achatz and Schmitz (2006a) analysed the optimal perturbations for a given monochromatic gravity wave. Fruman and Achatz (2012) extended this analysis for IGWs by computing optimal secondary perturbations based on the time dependent perturbed wave. They found that the wavelength of the optimal secondary perturbation can be much smaller than the original wave. Thus a three-dimensional domain does not need to have the size of the base wavelength in all three directions. They proposed the following multi-step approach to set up the domain and the initial conditions for a given monochromatic gravity wave:

1. solution (in the form of normal modes or singular vectors) of the Boussinesq equations linearised about the basic state wave determining the primary instability structures;
2. non-linear two-dimensional numerical solution of the full Boussinesq equations using the result of stage 1 as initial condition;
3. solution in the form of singular vectors (varying in the remaining spatial direction) of the Boussinesq equations linearised about the time-dependent result of stage 2;
4. three-dimensional DNS of the Boussinesq equations using the linear solutions from stages 1 and 3 as the initial condition and their wavelengths for the size of the computational domain.

In the present work, we applied this methodology to three different cases of monochromatic gravity waves breaking in the upper mesosphere. In all cases the wavelength is chosen to be $3\,\mathrm{km}$, the Coriolis parameter f is chosen such that it resembles a position at 70°N in the earth atmosphere and the kinematic viscosity is $1\,\mathrm{m}^2/\mathrm{s}$ corresponding to an altitude of $81\,\mathrm{km}$. The cases differ with respect to their non-dimensional amplitude[2] a and propagation angle Θ, and thus, oscillation period. We selected

1. an unstable IGW ($a = 1.2$, $\Theta = 89.5°$),
2. a stable IGW ($a = 0.86$, $\Theta = 89.5°$) and
3. an unstable HGW ($a = 1.2$, $\Theta = 70°$).

---

[2] The non-dimensional wave amplitude a is defined such that a gravity wave with $a = 1$ is neutrally stable at its least stable point, i.e. the minimum vertical buoyancy gradient is zero. Waves with $a < 1$ are statically stable and waves with $a > 1$ we refer to as statically unstable, although the unstable region might extend only a small portion of the wave phase depending on the actual value of a.

We conducted DNS of case 1 (JFM13) and DNS of all three cases, including spectral analysis (JGR14). Detailed lists of parameters for all cases can be found in our respective publications.

1.2. Turbulence modelling in stably stratified fluids

Simulations of gravity wave breaking events are computationally very expensive if the smallest turbulence scales have to be resolved (DNS). The necessity of a very high resolution can be avoided by applying the concept of large-eddy simulation (LES), i.e. resolving only the largest turbulence structures and modelling[3] the effect of the subgrid-scale (SGS) part of the energy spectrum on the resolved scales. Since gravity waves only occur in stably stratified fluids, studying gravity wave breaking by LES requires a model for SGS turbulence that correctly models the SGS stresses in the presence of stable stratification. In this section we will review the special characteristics of turbulence in stably stratified fluids (i.e. stratified turbulence) and the available SGS models.

Stable stratification suppresses vertical motions and thus makes the velocity field strongly anisotropic. The coherent structures in the stratified turbulent flow have much larger horizontal length scales compared to the vertical scales. Also the energy spectrum is not isotropic. The earth atmosphere is stably stratified almost everywhere at almost every time and is thus one of the most important sources of information about stratified turbulence. Nastrom and Gage (1985) analysed the horizontal velocity spectrum in the atmosphere using aircraft observations . They found a power-law behaviour in the mesoscale range with an exponent of $-5/3$, which is the same value as in isotropic turbulence (see Batchelor, 1953; based on the theory of Kolmogorov, 1941). In the vertical spectrum, Cot (2001) observed an exponent of -3 for the inertial range.

There has been a long and intensive discussion whether the observed spectra are due to a backward cascade of energy (Gage, 1979; Lilly, 1983; Herring and Métais, 1989) as in two-dimensional turbulence (Kraichnan, 1967), or due to intermittent breaking of internal waves, which means that a forward cascade is the dominant process (Dewan, 1979; van Zandt, 1982; Dewan, 1997). In different numerical and theoretical studies, ambiguous or even conflicting results were obtained (Lilly et al., 1998). Despite this discussion about its origin, the inertial range itself with an exponent of $-5/3$ in the horizontal spectrum was confirmed by most authors.

---

[3] For the terminology see footnote 1 on page 2

1. Introduction

Over the last years, a number of new simulations and experiments have addressed the issue. Smith and Waleffe (2002) observed a concentration of energy in the lowest modes in their simulations. Other studies (Laval et al., 2003; Waite and Bartello, 2004) suggested that the character of the flow depends on the Reynolds number

$$\mathrm{Re} = \frac{\mathscr{U}\mathscr{L}}{\nu}, \qquad (1.1)$$

where $\mathscr{U}$ and $\mathscr{L}$ are characteristic velocity and length scales of the flow and ν is the kinematic viscosity. High Reynolds numbers are associated with stronger three-dimensionality and a forward cascade of energy. Riley and de Bruyn Kops (2003) suggested that the flow can be strongly stratified but still turbulent if $\mathrm{Fr}^2\mathrm{Re} > 1$, where the Froude number is

$$\mathrm{Fr} = \frac{\mathscr{U}}{N\mathscr{L}} \qquad (1.2)$$

and N is the Brunt–Väisälä frequency. Lindborg (2006) presented a scaling analysis of the Boussinesq equations for low Froude and high Reynolds number. His theory of strongly anisotropic, but still three-dimensional, turbulence explains the horizontal spectrum with an exponent of -5/3 as well as the vertical spectrum with an exponent of -3. On the basis of these findings, Brethouwer et al. (2007) showed that the relevant non-dimensional parameter controlling stratified turbulence must indeed be the buoyancy Reynolds number $\mathscr{R} = \mathrm{Fr}^2\mathrm{Re}$. For $\mathscr{R} \gg 1$, they predict stratified turbulence including local overturning and a forward energy cascade. In the opposite limit, for $\mathscr{R} \ll 1$, the flow is controlled by viscosity and does not contain small-scale turbulent motions. The present work complements the previous numerical studies of stratified turbulence by a set of new DNS extending the investigated range of parameters to higher buoyancy Reynolds numbers (IJHFF12) and by an analysis of the spectral structure and spectral energy budget of homogeneous stratified turbulence (TCFD13).

Fully resolved DNS are computationally extremely expensive and are still restricted to comparably low Reynolds numbers (by orders of magnitudes smaller than Reynolds numbers realistic for tropospheric flows). Simulations that resolve only the largest turbulence eddies are typically referred to as LES. Since the small scale features in a flow are responsible for the majority of the flow energy dissipation, this natural sink of energy is missing in LES. The forward energy cascade leads to a transport of flow energy from the largest scales (where typically the flow is forced) to the smallest resolved scales. Without any countermeasures taken, the energy is not dissipated on these scales (at least not quickly

enough) and piles up on the grid scale until it spoils the whole simulation and may even cause it to break down. Providing exactly the right amount of dissipation on the coarse grid without knowing the SGS motions is the main modelling task for LES.

The first turbulence SGS model was proposed by Smagorinsky (1963). He intended to stabilise under-resolved simulations of turbulent atmospheric flows and achieved this by adding an extra term to the equations of motion to dissipate energy. What we now refer to as the "standard Smagorinsky model" (SSM) has become a robust workhorse for LES in geophysical and engineering applications. The model is based on the assumption of an eddy viscosity that adds to the molecular viscosity of the fluid. The eddy viscosity is proportional to the resolved strain rate and to a free model parameter, for which a universal value was sought for a long time. It turned out that the actual value of this Smagorinsky "constant" depends not only on the flow investigated and the underlying numerical scheme, but also on the personal preferences of the investigator. Germano et al. (1991) proposed a dynamic procedure for computing the Smagorinsky parameter based on the instantaneous flow solution. This method is based on the assumption of scale similarity, i.e. a similarity between the spectral flux to the grid scale from a (slightly larger) test grid scale and the spectral flux from the grid scale to the subgrid-scale. Lilly (1992) improved the dynamic procedure by including a robust least squares technique to minimise the difference between the closure assumption and the resolved stresses. We refer to the resulting method as the "dynamic Smagorinsky model" (DSM).

Turbulence SGS models such as the SSM and the DSM are referred to as "explicit" models since they involve additional terms in the equations of motion. On the other hand, "implicit" models rely on the ability of numerical discretisation schemes to dissipate energy. If the numerical scheme provides the right amount of dissipation, an explicit scheme is not necessary. This approach circumvents the typical problem of explicit SGS models, i.e. that the computed SGS stresses are of the same order as the grid truncation error, which can lead to numerical instability, lack of grid convergence or even wrong results on the large scales. Implicit LES (ILES) methods are particularly appealing for the simulation of stratified flows, where the fundamental assumptions of conventional eddy viscosity-based turbulence models may not hold. Several approaches to ILES have been developed in the past, for a comprehensive overview see Grinstein et al. (2007). First indications that the truncation error of linear upwind schemes in some cases may function as an implicit SGS model so that no explicit SGS model has to be added to the discretised flow equations were reported by

1. Introduction

Kawamura et al. (1986). The use of non-linearly stable higher-order schemes (i.e. monotonic, monotonicity preserving, or total variation diminishing methods) for so called Monotonically Integrated LES (MILES) has been proposed by Boris et al. (1992). Particularly noteworthy is the Multidimensional Positive Definite Advection Transport Algorithm (MPDATA) of Smolarkiewicz and Margolin (1998), which has been applied widely to geophysical flows. However, when using non-linearly stable schemes for ILES, one must be aware that most previously proposed methods only guarantee numerical stability, which is necessary, but not sufficient for the physically correct dynamics of the resolved scales. Employing ILES for predictive science requires that not only mathematical, but also physical constraints have to be incorporated into the design of an implicit SGS model. The first ILES method which is not only based on numerical considerations but also involves physical constraints is the Adaptive Local Deconvolution Method (ALDM) for incompressible neutrally stratified turbulent flows (Hickel et al., 2006) with an extension to passive scalar transport (Hickel et al., 2007).

Within the present work we conducted LES of stratified turbulence governed by the Boussinesq equations, i.e. with an active scalar, by using ALDM, SSM and DSM (IJHFF12, TCFD13) obtaining encouraging results with ALDM and DSM. The integral flow data and the energy spectra from the LES agree quite well with the various reference DNS. Beyond the present work we also applied ALDM to the problem of a differentially heated rotating annulus (Borchert et al., 2015; Vincze et al., 2015). The results obtained for this complex flow involving waves induced by buoyancy and solid body rotation as well as turbulence in boundary layers and breaking waves compare well to other numerical and experimental data.

The effect of unresolved small scales on the resolved large scale motion can be described by the spectral eddy viscosity (SEV). Heisenberg (1948) introduced the concept of modelling non-linear interactions in turbulence by a scale-dependent SEV. The underlying theory has later been refined by Kraichnan (1976) and others. Although impractical in real-space-based numerical simulations, the SEV as a function of wavenumber can be used to verify the correct behaviour of SGS models in a set-up of homogeneous (but not necessarily isotropic) turbulence.

Algebraic expressions for the SEV have been derived based on the Eddy-Damped Quasi-Normal Markovian (EDQNM) theory (Orszag, 1970) for isotropic turbulence. Furthermore, Domaradzki et al. (1987) computed the SEV from direct numerical simulations (DNS) with fully resolved turbulence by truncating the results in spectral space. They found some agreement with the theoretical

results of Kraichnan (1976) but also differences due to the finite inertial range in their simulations. Despite these discrepancies, the behaviour of isotropic turbulence is quite well understood. On the other hand, a corresponding study for anisotropic turbulence had not yet been carried out.

Semi-analytical expressions for the eddy-viscosity and eddy-diffusivity spectrum for stratified turbulence are given by Godeferd and Cambon (1994), Staquet and Godeferd (1998), and Godeferd and Staquet (2003) in the framework of the EDQNM approximation. Another form was obtained by Sukoriansky et al. (2005) through quasi-normal scale elimination (QNSE). These theoretical results show that turbulence anisotropy can significantly affect SGS energy dissipation in flows dominated by stable stratification, solid body rotation, or shear.

The present work extends the knowledge about the SEV in stratified turbulence based on DNS of homogeneous turbulence (JFM14) using the set-up of the previous articles (IJHFF12, TCFD13). We filtered the DNS results to coarser resolutions in several steps and computed the SGS stress necessary to obtain the same large-scale result on the coarse grid as on the full DNS grid. We compared this exact SEV from the DNS to the SEV of our different LES methods finding that for the horizontal kinetic energy and potential energy ALDM and the DSM yield good agreement with the DNS, whereas for the vertical kinetic energy the best results are obtained with the pure central discretisation without any SGS model.

1.3. Large-eddy simulations of gravity-wave breaking

For practical simulations of breaking gravity waves it is often impossible to resolve the smallest turbulence scales. This includes, e.g., investigations of the dependence of the gravity wave breaking on several parameters (propagation angle, wavelength, amplitude, viscosity, stratification) at the same time; problems in which many wavelengths need to be resolved, such as propagation of a wave packet or wave train through a variable background (Lund and Fritts, 2012) or simulating realistic cases of waves generated by topography or convection; validating quasilinear wave-propagation theory (Muraschko et al., 2014); or validating gravity-wave drag parametrisation schemes.

The problem of high computational costs for fully resolved DNS is especially relevant for IGWs that have large spatial scales and long oscillation periods[4] aug-

---

[4] The IGW simulated in JFM13, JGR14 and JAS15 has a horizontal wavelength of 340 km and an oscillation period of approximately 8 km.

menting both the required computational domain and the number of time steps to be computed. Various approaches have been used to avoid the high numerical resolution for DNS of breaking IGWs. Fritts et al. (2009a,b, 2013) and Fritts and Wang (2013) restricted their simulations to breaking HGWs ignoring the third velocity component induced by the Coriolis force. Lelong and Dunkerton (1998) simulated breaking IGWs at a greatly reduced ratio of the Brunt-Väisälä frequency to the Coriolis parameter compared to atmospheric values. There and in many other studies (e.g. Winters and D'Asaro, 1994; Andreassen et al., 1998; Dörnbrack, 1998; Afanasyev and Peltier, 2001) no attempt was made to resolve all turbulence scales at realistic Reynolds numbers. Instead, SGS turbulence models and/or hyperviscosity formulations were used. In none of these studies, the used SGS models have been validated using turbulence resolving reference simulations.

However, it is not clear a priori which effects a certain SGS model will have on a simulation of a complex transient stably stratified turbulent flow such as the breaking of a gravity wave. Having available the reference DNS for three different cases (JFM13, JGR14), we were able to directly validate LES methods for the breaking of gravity waves. Within the present work we conducted LES of our three reference cases with different SGS models (ALDM, SSM, DSM and no model) and on different grids with the objective of finding the most efficient set-up at an acceptable accuracy of results for each of the cases (JAS15). This involves reducing the resolution as much as possible in all directions, analysing the sensitivity of the results concerning the exact initial condition and assessing the performance of two-dimensional simulations with three velocity components.

2. Numerical methods

2.1. Boussinesq equations

Flows in the atmosphere[5] are characterised by a variable density ϱ and can thus be treated, in principle, using the full compressible set of equations. For simplicity, we omit viscosity for a moment and start with the Euler equations for an ideal gas with constant heat capacities under the influence of gravity

$$\partial_t \varrho + \nabla \cdot (\varrho \boldsymbol{u}) = 0, \qquad (2.1a)$$

$$\partial_t (\varrho \boldsymbol{u}) + \nabla \cdot (\varrho \boldsymbol{u} \boldsymbol{u}) = -\nabla p - \varrho g \boldsymbol{e}_z, \qquad (2.1b)$$

$$\partial_t (\varrho e) + \nabla \cdot (\boldsymbol{u} [\varrho e + p]) = 0, \qquad (2.1c)$$

where

$$\varrho e = \frac{p}{\gamma - 1} + \frac{\varrho \boldsymbol{u}^2}{2} + \varrho g \boldsymbol{x} \cdot \boldsymbol{e}_z \quad \text{and} \quad p = \varrho R T. \qquad (2.2)$$

Here $\boldsymbol{u}$ is the velocity vector[6], p is pressure, ϱ is density and e is the internal energy. Further, $\boldsymbol{x}$ is the spatial coordinate, $\boldsymbol{e}_z$ is the unit vector pointing in vertical direction, g is the gravitational acceleration, γ is the isentropic exponent, R is the specific gas constant and T is the absolute temperature. Equations (2.1) support sound waves, i.e. density variations due to changes in pressure. For meteorological applications this is not only unnecessary but indeed a nuisance since it strongly limits the time step for typical numerical time integration schemes (involving an explicit time integration). "Sound-proof" sets of equations that do not support sound waves but still allow density variations can be obtained by making some assumptions concerning the character of the flow. For a review of such approaches see Klein (2009).

We split the pressure, density and temperature fields into a background distribution (only dependent on the vertical direction z) as well as space and time-

---

[5] Similar considerations are, of course, valid in the oceans, in the earth mantle and other geophysical flows. For simplicity, we limit ourselves to the atmosphere, where the buoyancy is primarily a function of temperature.

[6] We use $\boldsymbol{u}$ and $\boldsymbol{v}$ for the velocity vector in the respective journal articles. Both notations are equivalent.

dependent fluctuations. For the example of density this reads

$$\varrho(\boldsymbol{x}, t) = \varrho_0(z) + \varrho'(\boldsymbol{x}, t) = \varrho_0 \left(1 + \varrho'/\varrho_0\right). \qquad (2.3)$$

If we assume the background state to be in hydrostatic equilibrium

$$\nabla p_0 = -\varrho_0 g \boldsymbol{e}_z \qquad (2.4)$$

and make the assumption that $\varrho'/\varrho_0 \ll 1$, we find the Boussinesq approximation of the Euler equations:

$$\nabla \cdot \boldsymbol{u} = 0, \qquad (2.5a)$$

$$\partial_t \boldsymbol{u} + (\boldsymbol{u} \cdot \nabla) \boldsymbol{u} = -\frac{\nabla p}{\varrho_0} - \frac{\varrho'}{\varrho_0} g \boldsymbol{e}_z, \qquad (2.5b)$$

$$\partial_t \varrho' + (\boldsymbol{u} \cdot \nabla) \varrho' = \frac{\mathrm{d}\varrho_0}{\mathrm{d}z} \boldsymbol{e}_z \cdot \boldsymbol{u}. \qquad (2.5c)$$

This system is incompressible, i.e. it does not support pressure induced density variations, but density variations are transported as an active scalar quantity providing a source of vertical momentum. The vertical velocity, in turn, is a source of density variations in case of a finite background stratification $\mathrm{d}\varrho_0/\mathrm{d}z$. This coupled system supports gravity waves if $\mathrm{d}\varrho_0/\mathrm{d}z < 0$.

We extend the system of equations (2.5) by transforming it to a frame of reference rotating at a constant angular velocity about the vertical axis $\boldsymbol{e}_z$ (ignoring centrifugal forces) and by adding diffusive terms for an incompressible Newtonian fluid. Furthermore, we replace the density fluctuations ϱ' by a buoyancy field variable $b = -g\varrho'/\varrho_0$ and introduce the Brunt–Väisälä frequency $N = \sqrt{-g/\varrho_0 \, \mathrm{d}\varrho_0/\mathrm{d}z}$ to find

$$\nabla \cdot \boldsymbol{u} = 0, \qquad (2.6a)$$

$$\partial_t \boldsymbol{u} + (\boldsymbol{u} \cdot \nabla) \boldsymbol{u} = -\frac{\nabla p}{\varrho_0} + b \boldsymbol{e}_z - f \boldsymbol{e}_z \times \boldsymbol{u} + \nu \nabla^2 \boldsymbol{u}, \qquad (2.6b)$$

$$\partial_t b + (\boldsymbol{u} \cdot \nabla) b = -N^2 \boldsymbol{e}_z \cdot \boldsymbol{u} + \alpha \nabla^2 b, \qquad (2.6c)$$

where $f = 2\Omega_E \sin \phi$ is the Coriolis parameter, ϕ is the latitude angle of the domain centre, Ω_E is the angular velocity of the earth and ν and α are the kinematic

viscosity and thermal diffusivity[7], respectively. The Boussinesq equations in the form (2.6) are equivalent to equations (2) in JGR14 and JAS15, respectively.

For many applications it is convenient to use the Boussinesq equations (2.6) in a non-dimensional form. Typically, characteristic length and velocity scales $\mathscr{L}$ and $\mathscr{U}$ are chosen and all velocities in the equations are non-dimensionalised by $\mathscr{U}$, all lengths by $\mathscr{L}$, pressure by $\mathscr{U}^2/\varrho_0$ and time by $\mathscr{L}/\mathscr{U}$. In the literature on stratified turbulence the buoyancy b is usually replaced by the non-dimensional density fluctuation $\tilde{\varrho} = -b/(N^2\mathscr{L})$. The resulting set of equations reads

$$\nabla \cdot \tilde{\boldsymbol{u}} = 0, \tag{2.7a}$$

$$\partial_t \tilde{\boldsymbol{u}} + (\tilde{\boldsymbol{u}} \cdot \nabla)\tilde{\boldsymbol{u}} = -\nabla \tilde{p} - \frac{\tilde{\varrho}\boldsymbol{e}_z}{\mathrm{Fr}_{\mathrm{met}}^2} - \frac{\boldsymbol{e}_z \times \tilde{\boldsymbol{u}}}{\mathrm{Ro}} + \frac{\nabla^2 \tilde{\boldsymbol{u}}}{\mathrm{Re}}, \tag{2.7b}$$

$$\partial_t \tilde{\varrho} + (\tilde{\boldsymbol{u}} \cdot \nabla)\tilde{\varrho} = \tilde{\boldsymbol{u}}\boldsymbol{e}_z + \frac{\nabla^2 \tilde{\varrho}}{\mathrm{Pr}\,\mathrm{Re}}, \tag{2.7c}$$

where the tilde $\tilde{\ }$ indicates non-dimensional quantities and the governing non-dimensional parameters are the Froude, Prandtl, Reynolds and Rossby numbers:

$$\mathrm{Fr}_{\mathrm{met}} = \frac{\mathscr{U}}{N\mathscr{L}}, \quad \mathrm{Pr} = \frac{\nu}{\alpha}, \quad \mathrm{Re} = \frac{\mathscr{U}\mathscr{L}}{\nu}, \quad \mathrm{Ro} = \frac{\mathscr{U}}{f\mathscr{L}}. \tag{2.8}$$

This variant of the Froude number $\mathrm{Fr}_{\mathrm{met}}$ is popular within the atmospheric and oceanographic literature. It has the advantage that only one parameter is required to control the intensity of the stratification. However, neutrally stratified flows ($\mathrm{d}\varrho_0/\mathrm{d}z = 0$) cannot be treated with this set of equations. We used equivalent formulations of the Boussinesq equations (omitting the Coriolis term) in IJHFF12 and TCFD13; see the respective equations (1).

An alternative form of non-dimensional Boussinesq equations can be obtained by using the non-dimensional buoyancy $\tilde{b} = b/g$. The equations then read

$$\nabla \cdot \tilde{\boldsymbol{u}} = 0, \tag{2.9a}$$

$$\partial_t \tilde{\boldsymbol{u}} + (\tilde{\boldsymbol{u}} \cdot \nabla)\tilde{\boldsymbol{u}} = -\nabla \tilde{p} + \frac{\tilde{b}\boldsymbol{e}_z}{\mathrm{Fr}_{\mathrm{eng}}^2} - \frac{\boldsymbol{e}_z \times \tilde{\boldsymbol{u}}}{\mathrm{Ro}} + \frac{\nabla^2 \tilde{\boldsymbol{u}}}{\mathrm{Re}}, \tag{2.9b}$$

$$\partial_t \tilde{b} + (\tilde{\boldsymbol{u}} \cdot \nabla)\tilde{b} = -\tilde{N}^2 \tilde{\boldsymbol{u}}\boldsymbol{e}_z + \frac{\nabla^2 \tilde{b}}{\mathrm{Pr}\,\mathrm{Re}}, \tag{2.9c}$$

---

[7] We use D, μ and α for the thermal diffusivity in the respective journal articles. These notations are equivalent. Note that μ is also frequently used for the dynamic viscosity.

where the alternative Froude number $\mathrm{Fr}_{\mathrm{eng}}$ and the non-dimensional Brunt–Väisälä frequency are

$$\mathrm{Fr}_{\mathrm{eng}} = \frac{\mathscr{U}}{\sqrt{g\mathscr{L}}}, \quad \tilde{N} = \sqrt{\frac{\mathrm{d}\tilde{b}_0}{\mathrm{d}z}} = N\sqrt{\frac{\mathscr{L}}{g}}. \tag{2.10}$$

$\tilde{N}$ depends on the background stratification expressed as the vertical gradient of the non-dimensional buoyancy $\mathrm{d}\overline{\tilde{b}}/\mathrm{d}z$. The Boussinesq equations in the form (2.9) are implemented in our flow solver INCA. This form was used in JFM13. It allows to control the buoyancy and the stratification independently of each other. The relation between both types of non-dimensionalisation is given by

$$\mathrm{Fr}_{\mathrm{met}} = \frac{\mathrm{Fr}_{\mathrm{eng}}}{\tilde{N}}, \quad \tilde{\varrho} = -\frac{\tilde{b}}{\tilde{N}^2}. \tag{2.11}$$

Assuming zero mean flow, the local kinetic energy and the available[8] potential energy in the flow are

$$E_{\mathrm{k}} = \frac{\boldsymbol{u} \cdot \boldsymbol{u}}{2} = \frac{\tilde{\boldsymbol{u}} \cdot \tilde{\boldsymbol{u}}}{2}\mathscr{U}^2, \tag{2.12a}$$

$$E_{\mathrm{p}} = \frac{b^2}{2N^2} = \frac{\tilde{\varrho}^2}{2\mathrm{Fr}_{\mathrm{met}}^2}\mathscr{U}^2 = \frac{\tilde{b}^2}{2\tilde{N}^2\mathrm{Fr}_{\mathrm{eng}}^2}\mathscr{U}^2. \tag{2.12b}$$

The kinetic energy E_{k} can be decomposed into a fraction E_{v} that includes only the vertical velocity component and another fraction E_{h} that includes the horizontal velocity components:

$$E_{\mathrm{v}} = \frac{(\boldsymbol{u} \cdot \boldsymbol{e}_z)^2}{2}, \tag{2.13a}$$

$$E_{\mathrm{h}} = E_{\mathrm{k}} - E_{\mathrm{v}} \tag{2.13b}$$

The dissipation rates of kinetic and potential energy are non-dimensionalised accordingly. For detailed discussions of the energy budget and the different types of energy dissipation, see TCFD13 and JAS15.

---

[8] In the following text and in the journal articles, we generally skip the term "available" which can be necessary to avoid confusion with the "total" potential energy $\int_0^H \varrho g\,\mathrm{d}z$ based on the density ϱ and absolute altitude H of a fluid parcel. In the present context, the total potential energy is never needed.

2.2. Turbulence subgrid-scale modelling

2.2.1. General concept of LES

The basic idea of LES is the separation of resolved and unresolved flow scales by a filter operation. A spatially compact filter kernel G is applied to the equations of motion yielding a set of equations for the filtered flow variables that is very similar to the original one, but has an additional term representing the effect of the unresolved subgrid scales[9] on the filtered quantities. For the momentum equation (2.6b) we obtain

$$\partial_t \overline{\boldsymbol{u}} + (\overline{\boldsymbol{u}} \cdot \nabla)\overline{\boldsymbol{u}} = -\frac{\nabla \overline{p}}{\varrho_0} + \overline{b}\boldsymbol{e}_z - f\boldsymbol{e}_z \times \overline{\boldsymbol{u}} - 2\nabla \cdot \left(\nu \overline{\boldsymbol{S}}\right) - \nabla \cdot \boldsymbol{\tau} \tag{2.14}$$

where $\overline{S}_{ij} = 0.5\left(\partial_{x_i}\overline{u}_j + \partial_{x_j}\overline{u}_i\right)$ is the filtered strain rate tensor and $\tau_{ij} = \overline{u_i u_j} - \overline{u}_i \overline{u}_j$ is the unknown SGS stress tensor, which has to be modelled. Many explicit SGS models define an eddy viscosity ν_t to model the SGS stress tensor based on the resolved strain rate

$$\boldsymbol{\tau}^{\mathrm{mod}} = 2\nu_t \overline{\boldsymbol{S}} \tag{2.15}$$

in anology to the molecular viscosity.

2.2.2. The Smagorinsky model

Smagorinsky (1963) estimated the unknown eddy viscosity ν_t from

$$\nu_t = \left(C_S \overline{\Delta}\right)^2 |\overline{\boldsymbol{S}}|, \quad |\overline{\boldsymbol{S}}| = \sqrt{2\overline{S}_{ij}\overline{S}_{ij}}, \tag{2.16}$$

where $\overline{\Delta} = \left(\Delta_x \Delta_y \Delta_z\right)^{1/3}$ is the grid or filter size, respectively. In this formulation, the unknown SGS fluxes can be computed directly from the resolved velocity field. There is no universal value for the model parameter C_S; for different flow configurations different values of the parameter have been found to be optimal. In our simulations with the standard Smagorinsky model (SSM) we use a value of $C_S = 0.18$, which follows from the theory of isotropic turbulence (Lilly, 1967) and has been found to yield good results in practice (Clark et al., 1979). The buoyancy transport equation (2.6c) is closed analogously by an eddy diffusivity model with $\alpha_t = \nu_t/\mathrm{Pr}_t$, where $\mathrm{Pr}_t = 0.4$ (see, e.g., Eidson, 1985).

---

[9] Strictly speaking, these are "subfilter"-scale features. But since the filter width is typically equal to the grid size, the term "subgrid"-scales is commonly accepted in this context.

The dynamic procedure of Germano et al. (1991) can be applied to the Smagorinsky model. For this purpose, the filtered velocities $\overline{u}_i$ are explicitly filtered by a test filter with a larger filter width $\widehat{\Delta}$. As a test filter, we use a top-hat filter with $\widehat{\Delta} = 2\overline{\Delta}$. The subfilter-scale stress tensor is $T_{ij} = \widehat{\overline{u_i u_j}} - \widehat{\overline{u}_i}\,\widehat{\overline{u}_j}$. It cannot be computed directly from the filtered velocity field, but the Leonard stress tensor $L_{ij} = \widehat{\overline{u}_i\,\overline{u}_j} - \widehat{\overline{u}_i}\,\widehat{\overline{u}_j}$ can be calculated. Using the Germano identity

$$T_{ij} = L_{ij} + \widehat{\tau_{ij}} \tag{2.17}$$

and the standard Smagorinsky model for τ_{ij} and T_{ji}, we can minimize the difference between L_{ij} and

$$
\begin{aligned}
L_{ij}^{\mathrm{mod}} &= T_{ij}^{\mathrm{mod}}(C,\widehat{\Delta},\widehat{\overline{\boldsymbol{u}}}) - \widehat{\tau_{ij}^{\mathrm{mod}}(C,\overline{\Delta},\overline{\boldsymbol{u}})} \\
&= -2C\widehat{\Delta}^2|\widehat{\overline{\boldsymbol{S}}}|\widehat{\overline{S}}_{ij} + 2C\left(\widehat{\overline{\Delta}^2|\overline{\boldsymbol{S}}|\overline{S}_{ij}}\right) \\
&= 2CM_{ij}
\end{aligned}
\tag{2.18}
$$

by a least-squares procedure (Lilly, 1992)

$$C = \frac{1}{2}\frac{\left\langle L_{ij} M_{ij}\right\rangle}{\left\langle M_{ij} M_{ij}\right\rangle}. \tag{2.19}$$

A spatial or temporal average $\langle\cdot\rangle$ can be applied to enumerator and denominator of the equation in order to prevent numerical instability. In IJHFF12 we apply this average in all spatial directions which results in a spatially constant but temporarily varying model parameter and in JAS15 we apply the average in only one spatial direction. The dynamic procedure must be applied in every time step to obtain the model parameter $C_S^2 = C$ for the flow. This involves filter operations on the whole flow field and thus increases the computational costs compared to the SSM. This dynamic procedure can also be applied to the turbulent Prandtl number. However, we use a constant value of $\mathrm{Pr}_t = 0.4$, since it has shown itself to be of minor importance for the flow results.

2.2.3. The Adaptive Local Deconvolution Method

Filtering the non-linear equations of motion leads to an unknown SGS stress term, as we have seen before. Numerical solution of the equations further requires a discretisation which leads also to an unknown discretisation error, which is similar in structure and magnitude to the SGS stress. The idea of implicit LES

(ILES) is to merge these two terms and tune the discretisation error of the numerical scheme in such a way that it acts as an SGS model. The Adaptive Local Deconvolution Method (ALDM) is a realisation of this idea, originally presented by Hickel et al. (2006).

Here we will only outline the general idea behind ALDM. For details the reader is referred to Hickel et al. (2006) and to IJHFF12 and TCFD13. Given the one-dimensional generic transport equation for the quantity v

$$\partial_t v + \partial_x F(v) = 0, \tag{2.20}$$

the numerical approximation of the flux $\tilde{F}$ is computed based on the available filtered numerical solution $\overline{v}$ by approximately reconstructing the unfiltered solution $\tilde{v}$ (deconvolution) and a numerical regularisation through a suitable numerical flux function.

The reconstruction is based on an approximate deconvolution of the unfiltered solution on the represented scales by combining deconvolution polynomials. The different polynomials are dynamically weighted based on the smoothness of the filtered solution. The regularisation is obtained through a tailored numerical flux function operating on the reconstructed solution. Both, the solution-adaptive polynomial weighting and the numerical flux function involve free model parameters that were calibrated in such a way that the truncation error of the discretised equations correctly represents the SGS stresses of isotropic turbulence. This set of parameters was not changed for any subsequent applications of ALDM. For the presented computations, we used an implementation of ALDM with improved computational efficiency (Hickel and Adams, 2007).

The extension of ALDM to passive scalar transport was developed by Hickel et al. (2007). In IJHFF12 and TCFD13 we show that the method also performs well for the active scalar in stably stratified turbulent flows governed by the Boussinesq equations. However, in simulations of breaking gravity waves sometimes strong oscillations emerged in the flow variables spoiling the whole simulation. In order to avoid this problem, we slightly modified the numerical flux function for the buoyancy transport. The original buoyancy flux function for an equidistant staggered grid reads

$$\tilde{F}^s_{j\pm1/2} = \overline{u}_{j-1/2\pm1/2}\frac{\tilde{b}^-_{j\pm1/2} + \tilde{b}^+_{j\pm1/2}}{2} - \sigma_{j\pm1/2}\left[\tilde{b}^+_{j\pm1/2} - \tilde{b}^-_{j\pm1/2}\right], \tag{2.21}$$

where the numerical viscosity is chosen to be

$$\sigma_{j\pm1/2} = \sigma_b \left| \tilde{u}^-_{j\pm1/2} - \tilde{u}^+_{j-1\pm1/2} \right| \tag{2.22}$$

with $\sigma_b = 0.615$ (Hickel et al., 2007) for $\Pr \lesssim 1$. In these equations the index $j \pm 1/2$ indicates the right/left cell face (the velocity $\overline{u}_j$ is stored on the cell faces, the buoyancy $\overline{b}_j$ is stored in the cell centers), $\tilde{b}^+$ and $\tilde{b}^-$ are reconstructed solution values primarily based on values of $\overline{b}$ on the right/left of the reconstruction position.

The formulation (2.22) was chosen in analogy to ALDM for the momentum equations and is dimensionally consistent. It proved to work very well in fully turbulent flows, but if the flow is temporarily laminar, $\left| \tilde{u}^-_{j\pm1/2} - \tilde{u}^+_{j-1\pm1/2} \right|$ approaches zero and the numerical damping is effectively turned off. Any numerical oscillations in the scalar field can then grow without bound. In order to regularise the scalar transport in case of advection by a smooth velocity field, we propose a blending of ALDM with an upwind biased flux function (JAS15). A pure upwind flux function could be obtained within the given framework through

$$\sigma_{j\pm1/2}\big|_{\text{upwind}} = \frac{1}{2} \left| \overline{u}_{j-1/2\pm1/2} \right|. \tag{2.23}$$

A pure upwind scheme like this is numerically very stable, i.e. it tends towards very strong damping of all oscillations through a huge numerical diffusivity. Despite its stability it is thus not suitable for LES, since it excessively damps all turbulent motion on the resolved scales.

The convex combination of standard ALDM flux and upwind flux leads to the following expression for the numerical viscosity:

$$\sigma_{j\pm1/2} = \alpha\sigma_b \underbrace{\left| \tilde{u}^-_{j\pm1/2} - \tilde{u}^+_{j-1\pm1/2} \right|}_{\mathscr{M}} + (1-\alpha)\sigma_b \underbrace{\left| \frac{\tilde{u}^-_{j\pm1/2} + \tilde{u}^+_{j-1\pm1/2}}{2} \right|}_{\mathscr{P}}, \tag{2.24}$$

where we approximated the advection velocity by

$$\overline{u}_{j-1/2\pm1/2} \approx \frac{\tilde{u}^-_{j\pm1/2} + \tilde{u}^+_{j-1\pm1/2}}{2}. \tag{2.25}$$

The blending parameter α is dynamically evaluated based on the instantaneous velocity values by

$$\alpha = \frac{\mathcal{M}}{\beta \mathcal{P} + \mathcal{M}},\tag{2.26}$$

where $\mathcal{M}$ denotes the velocity difference and $\mathcal{P}$ the advection velocity as defined in equation (2.24) and β is a free model parameter that controls the ratio $\mathcal{M}/\mathcal{P}$ at which the modification becomes effective. In turbulent flows, where velocity fluctuations are typically large compared to the mean advection velocity, we find $\mathcal{M}/\mathcal{P} \gg \beta$, which means that $\alpha \to 1$ and we recover the original formulation (2.22). On the other hand, if the flow is laminar or governed by a large mean advection velocity, then $\alpha \to 0$ and we have an upwinding scheme.

2.3. The flow solver INCA

INCA is a multi-purpose flow solver for compressible and incompressible problems on Cartesian grids. INCA has successfully been applied to a wide range of different flow problems, ranging from incompressible boundary layer flows (Hickel et al., 2008) to supersonic flows (Grilli et al., 2012). Among the large number of different methods implemented in INCA, we will briefly mention here only those that were actually used for the simulations within the present work.

The incompressible Navier–Stokes equations and the transport equations for scalar quantities are discretised by a fractional step method (Chorin, 1968) on staggered Cartesian mesh blocks. We used a uniform cell size and periodic boundary conditions throughout the present work. The buoyancy and Coriolis terms as well as the explicit SGS models are implemented as source terms completing the right-hand side of the equations. For time advancement the explicit third-order Runge–Kutta scheme of Shu (1988) is used. The time-step is dynamically adapted to satisfy a Courant–Friedrichs–Lewy condition (including the limits for advective, diffusive and buoyancy terms).

Two different solvers for the pressure Poisson equation were used depending on the size of the problem, the utilised computer and the grid layout. The first solver employs a Fast Fourier Transform (FFT) of the velocity field in the vertical direction and a Stabilized Bi-Conjugate Gradient (BiCGSTAB) solver (van der Vorst, 1992) in the horizontal plane. The FFT converts the three-dimensional problem into a set of independent two-dimensional problems, which are solved in parallel through shared memory parallelisation. We used this pressure solver for single-block simulations. For large simulations (DNS) we used distributed

memory computer clusters, which required a domain decomposition. For these simulations we used a Krylov subspace solver with algebraic-multigrid preconditioning to solve the pressure Poisson equation.

INCA simulations with relevance for the present work include isotropic turbulence (Hickel et al., 2006), passive scalar mixing (Hickel et al., 2007), stably stratified turbulence (IJHFF12, TCFD13, JFM14), the transition of the three-dimensional Taylor–Green vortex in the neutrally (Hickel et al., 2006) and stably stratified set-up (IJHFF12), gravity-wave breaking in the atmosphere (JFM13, JGR14, JAS15), as well as, the differentially heated rotating annulus (Borchert et al., 2015; Vincze et al., 2015).

3. Summaries of journal articles

3.1. IJHFF12: Direct and large eddy simulation of stratified turbulence (Remmler and Hickel, 2012)

In order to validate our LES methods for stably stratified turbulent flows governed by the Boussinesq equations, we performed DNS of the three-dimensional Taylor–Green vortex (TGV) and of forced homogeneous turbulence, both with a stable background stratification. For both cases we considered different Reynolds numbers and different Froude numbers. We chose the parameters such that the flow was turbulent and stably stratified at the same time, the limit of the Reynolds number being set by the maximum resolution allowed by the available computational resources. The simulated flows span the whole range from neutrally to strongly stratified turbulence.

The initial flow field of the TGV has only horizontal kinetic energy. During the evolution of the neutrally stratified flow, part of this energy is converted into vertical kinetic energy, transferred to smaller scales and dissipated. We found that this process is modified by the presence of a stable stratification to the extend that vertical kinetic energy is quickly converted into available potential energy. This leads to a periodic exchange between horizontal kinetic energy and potential energy. The associated damping of vertical motions partly inhibits the energy transfer to small scales and thus delays and reduces the energy dissipation peak. Hence the stable stratification tends to stabilise the flow.

In our simulations, neutrally stratified homogeneous turbulence, although forced only at large horizontal scales, was isotropic at medium and small scales. The large scale forcing had no effect on the inertial and dissipation range. Given a stable stratification, we found that turbulence becomes strongly anisotropic with much larger horizontal than vertical length scales. The flow was organised in thin horizontal layers that were separated by sheets of horizontally oriented small scale vortices.

We used our reference DNS for validation of LES with ALDM, SSM and DSM. For the TGV we obtained good agreement of the dissipation rates with all three SGS models, independent of the strength of the stratification. The results with ALDM were in general a little bit superior to the standard and dynamic

Smagorinsky models. In weakly stratified homogeneous turbulence, the results with all three SGS models were very similar and close to the reference DNS. In strongly stratified turbulence, however, the SSM damped small scale motions too much and the DSM did not produce the correct spectral slope in the horizontal energy spectra. With ALDM the energy spectra were predicted most accurately.

The work share of the applicant in the presented study included the implementation of the Boussinesq equations and the dynamic Smagorinsky model into the existing incompressible version of INCA; the design, set-up, conduction and post-processing of all presented simulations, including new INCA routines for separated analysis of horizontal and vertical spectra; as well as writing most of the journal article.

3.2. TCFD13: Spectral structure of stratified turbulence: Direct numerical simulations and predictions by large eddy simulation (Remmler and Hickel, 2013)

We studied stably stratified homogeneous turbulence that is maintained at an approximately constant energy level by forcing large horizontal modes of horizontal velocity. The investigated parameter range extends to higher buoyancy Reynolds numbers than in previous numerical studies and covers the whole range from the neutral to the strongly stratified turbulent regime. We put special emphasis on the analysis of the energy spectra in the two-dimensional spectral space.

We found that the horizontal kinetic energy accumulates in modes with high vertical and low horizontal wavenumber, while the vertical kinetic energy is distributed much more isotropically in spectral space. The available potential energy distribution combines elements of both kinetic energy types. Our analysis of the energy transfer spectra allows for tracking the complete path of energy being injected as large horizontal modes of horizontal kinetic energy, transformed into vertical kinetic energy and potential energy, transported to small scales and eventually dissipated. While in isotropic turbulence the turbulent diffusion is responsible for an isotropic net transport of energy from large to small scales, the picture is different for all three types of energy in stratified turbulence. E_h is primarily transported to medium vertical modes, E_v is shifted from medium vertical modes to horizontal modes and E_p is transported from medium horizontal and vertical modes to small vertical modes.

According to our findings, the relevant parameter for controlling the distribution of energy in the wavenumber space is the Froude number rather than the buoyancy Reynolds number. We observed similar spectra within simulations with comparable Froude number and strongly varying spectra if the buoyancy Reynolds number was fixed and the Froude number was varied.

We performed the same simulations on much coarser grids using ALDM and the SSM. With ALDM the integral flow data agreed well with the DNS as far as the fully turbulent parameter range is considered, while the SSM failed to correctly predict the ratios of the different energy types in strongly stratified turbulence. We also analysed the energy and energy transfer spectra for selected cases (with neutral, medium and strong stratification) with ALDM and found good agreement with the DNS in all cases. This was achieved without re-calibrating the ALDM model parameters once optimised for decaying isotropic turbulence.

The work share of the applicant in the presented study included the design, set-up, conduction and post-processing of all presented simulations, including new INCA routines for extracting two-dimensional spectra of energy and energy transfer; as well as writing most of the journal article.

Erratum Equations (5a,b) in the article contain an error. The corrected set of equations reads

$$
\partial_t E_{\mathrm{k}} + \nabla \cdot (\boldsymbol{u} E_{\mathrm{k}}) = \underbrace{-\boldsymbol{u} \cdot \nabla p}_{\mathscr{P}} \underbrace{- \frac{\varrho}{\mathrm{Fr}_0^2} \boldsymbol{u} \cdot \boldsymbol{e}_z}_{\mathscr{B}} + \underbrace{\frac{1}{\mathrm{Re}_0} \left[\nabla^2 E_{\mathrm{k}} - (\nabla \boldsymbol{u})^2 \right]}_{\mathscr{D}} + \underbrace{\boldsymbol{F}}_{\mathscr{F}}
$$

where the $-\mathscr{T}$ brace lies under $\nabla \cdot (\boldsymbol{u} E_{\mathrm{k}})$.

$$
\partial_t E_{\mathrm{p}} + \nabla \cdot (\boldsymbol{u} E_{\mathrm{p}}) = \underbrace{\frac{\varrho}{\mathrm{Fr}_0^2} \boldsymbol{u} \cdot \boldsymbol{e}_z}_{\mathscr{B}} + \underbrace{\frac{1}{\mathrm{Pr}\,\mathrm{Re}_0} \left[\nabla^2 E_{\mathrm{p}} - \frac{(\nabla \varrho)^2}{\mathrm{Fr}_0^2} \right]}_{\mathscr{D}}.
$$

where the $-\mathscr{T}$ brace lies under $\nabla \cdot (\boldsymbol{u} E_{\mathrm{p}})$.

3.3. JFM13: Direct numerical simulation of a breaking inertia-gravity wave (Remmler, Fruman and Hickel, 2013)

We present direct numerical simulations of a breaking inertia-gravity wave with a wavelength of three kilometres. The chosen parameters represent a gravity wave with almost vertical direction of propagation and a wavelength of 3 km breaking in the middle atmosphere at 81 km altitude. We initialised the simulation with a statically unstable gravity wave perturbed by its leading transverse normal mode and the leading instability modes of the time-dependent wave breaking in a two-

dimensional domain. The wave breaking was simulated for approximately 16 hours, which is about twice the wave period. The required cell size for resolving the smallest turbulent eddies was $\Delta \approx 3\,\mathrm{m}$, which corresponds to approximately 172 million cells.

Our simulations show that the primary breaking event triggered by the optimal perturbations generates turbulence in the whole domain, including the most stable part of the wave. Additionally, we observed two weaker breaking events following the first one. The second breaking is very weak and is triggered by an instability in the almost completely re-laminarised wave that is still close to the threshold of static instability. The third breaking occurs when the unstable part of the wave has travelled far enough to reach the place where strong turbulence was generated during the primary breaking in the stable part of the wave.

We compared the 3-D simulations to simulations with two spatial dimensions and three velocity components ("2.5-D" simulations). Details such as the secondary breaking events observed in the 3-D DNS were not reproduced by the 2.5-D simulation and the breaking lasted longer in the 3-D simulations. However, the overall results in terms of total amplitude reduction and breaking duration were similar between the 3-D and 2.5-D simulations. Furthermore, we varied the domain size in the direction of the secondary perturbation and replaced the secondary perturbation by white noise. We found indications that the chosen domain size is indeed optimal for triggering a fully three-dimensional breaking at the smallest possible domain size.

The work share of the applicant in the presented study included the implementation of the Coriolis term into the existing incompressible version of INCA; the set-up, conduction and post-processing of all presented three-dimensional simulations, including new INCA routines for extracting the gravity wave amplitude, horizontally and spanwise averaged data over time, coarsened three-dimensional snapshots and further diagnostics such as the Richardson number; as well as writing most of the journal article.

Erratum   Equation (2.5) in the article contains an error. The corrected equation reads

$$\varepsilon_{\mathrm{k}} = \frac{1}{2\mathrm{Re}} \left(\partial_{x_j} u_i + \partial_{x_i} u_j \right) \left(\partial_{x_j} u_i + \partial_{x_i} u_j \right).$$

The kinetic energy dissipation shown in the various figures has been computed using the correct equation.

3.4. JFM14: Spectral eddy viscosity of stratified turbulence (Remmler and Hickel, 2014)

The spectral eddy viscosity and diffusivity (SEV, SED) is a tool to derive LES turbulence models and to evaluate their performance in predicting the spectral energy transfer. It provides a descriptive representation of the SGS stresses, i.e. the unresolved part of the non-linear advection term that has to be modelled by the SGS model in an underresolved simulation. We have computed the spectral eddy viscosity and diffusivity of homogeneous turbulence with and without stable stratification. We achieved this by filtering fully resolved DNS results and by computing the additional spectral energy flux that is necessary to obtain the same total flux in the coarse-grained flow field as in the fully resolved case.

For neutrally stratified turbulence we found eddy viscosity spectra that are, in general, similar to theoretical predictions (Kraichnan, 1976) showing a plateau-cusp behaviour. However, the amplitude of the cusp at the cut-off wavenumber depended on the test filter size and at low wavenumbers we found a pronounced linear decrease of the SEV instead of a flat plateau.

If stable stratification was increased, the SEV and SED spectra became more and more anisotropic. For the most stable case investigated, the plateau-cusp topology almost completely vanished. This illustrates that the characteristics of the flow change significantly, as soon as the buoyancy Reynolds number approaches unity. The treatment of SGS stresses in such cases must generally be different than in fully turbulent flows with higher buoyancy Reynolds numbers.

We used the results from the filtered DNS to test the implicit SGS model ALDM and a central discretisation scheme with and without Smagorinsky model, either in the standard or in the dynamic form. We found that ALDM yields acceptable results for all three forms of flow energy, despite being developed based on the SEV for neutrally stratified forced homogeneous turbulence. The dynamic Smagorinsky model did a good job except for the vertical kinetic energy, which was best matched by the central discretisation without any SGS model. These results suggest that a potentially better model could be obtained by applying the dynamic Smagorinsky model only to the horizontal velocity components and leaving the vertical momentum equation unmodified.

The work share of the applicant in the presented study included the implementation of routines for the computation of two-dimensional SEV and SED spectra in DNS and LES simulations; the definition, set-up, conduction and post-

processing of all presented simulations (DNS on supercomputers, LES on a local workstation); as well as writing most of the journal article.

3.5. JGR14: On the construction of a direct numerical simulation of a breaking inertia-gravity wave in the upper-mesosphere (Fruman, Remmler, Achatz and Hickel, 2014)

We present a systematic approach to the DNS of breaking upper-mesospheric inertia-gravity waves of amplitude close to or above the threshold for static instability. First, we used normal mode or singular vector analysis (applied in a frame of reference moving with the phase velocity of the wave) to determine the most likely scale and structure of the primary instability and to initialise non-linear 2.5-D simulations. We then applied singular vector analysis to the time-dependent 2.5-D solution to predict the transition of the breaking event to three-dimensional turbulence and to initialise three-dimensional DNS. The careful choice of the computational domain and the relatively low Reynolds numbers, in the order of 25000, relevant to breaking waves in the upper mesosphere, make the three-dimensional DNS tractable with present day computing clusters.

We analyse three test cases: a statically unstable low-frequency inertia-gravity wave, a statically and dynamically stable inertia-gravity wave, and a statically unstable high-frequency gravity wave. The three-dimensional DNS are compared to ensembles of 2.5-D simulations.

In general, the results of the 2.5-D simulations are similar to those of the 3-D DNS in terms of the projection and resolved-energy dissipation diagnostics. The initial phase of wave breaking tends to be more rapid and more intense in the 3-D simulations – understandable since it provides more degrees of freedom and avenues to exchange energy between spatial scales. The spatial and temporal distributions of the energy dissipation are similar. This suggests that results of 2.5-D simulations are meaningful if the domain and initial condition are chosen properly.

The most interesting case was the unstable inertia-gravity wave (which was already investigated in JFM13), where the turbulence and wave decay was intermittent and persisted for approximately one wave period. After the first approximately 30 minutes, most of the energy dissipation in the 3-D simulation occurred near the level of static instability in the original wave, while in 2.5-D there is some strong energy dissipation also in the stable part of the wave, which significantly affects the slope of the energy spectra in a certain range of time. It

was the only case with substantial differences between the 2.5-D and 3-D DNS and with considerable variation between members of the ensemble in 2.5-D.

The stable inertia-gravity wave case showed a weak single breaking event lasting for a short time compared to the wave period and associated with a reduction of the wave amplitude of only 5%. The unstable high-frequency gravity wave showed much stronger breaking and turbulence for a time longer than the wave period. In this case the breaking was relatively isotropic and uncorrelated to the initial wave structure. For both latter cases the 2.5-D DNS are in very good agreement with the full 3-D DNS.

The work share of the applicant in the presented study included the extension of all gravity-wave related INCA routines to distributed memory systems allowing domain decomposition in all three spatial directions; the set-up, conduction and post-processing of all presented three-dimensional simulations including new INCA routines for extracting gravity wave spectra; as well as writing most of those parts of the journal article that are related to 3-D simulations and spectral analysis.

3.6. JAS15: Validation of Large-Eddy Simulation Methods for Gravity-Wave Breaking (Remmler, Hickel, Fruman and Achatz, 2015)

The DNS results presented in JGR14 provide a good insight into the physics of these specific wave breaking cases, but DNS is far too expensive to be used for systematic studies of waves breaking under different conditions or for cases that require simulating larger domains. The last article consequently has the objective of reducing the computational costs of wave breaking simulations as much as possible while still ensuring an acceptable quality of the results. In order to reduce the number of grid cells massively, it is necessary to use an LES method involving a turbulence subgrid-scale model.

We validated three different LES methods – ALDM, DSM and a central discretisation without turbulence model (CDS4) – for those cases of the breaking of monochromatic gravity waves for which we presented DNS results in JGR14. For ALDM we developed a modification of the numerical flux function for the buoyancy that significantly improved the simulation results in case of a temporarily very smooth velocity field. It consists of blending the ALDM flux function for passive scalars with an upwind flux function with a weighting factor that depends on the local smoothness of the velocity field. All simulations were carried

out both in 3-D and 2.5-D domains and for all simulations a small ensemble of simulations starting from slightly different initial conditions was performed in order to assess the sensitivity and robustness of the results.

We found that results obtained with ALDM and DSM are generally in good agreement with the reference DNS results as long as the resolution in the direction of the wave vector is sufficiently high. The resolution in the other directions had a weaker influence on the results. The simulations without turbulence model were only successful if the resolution was high and the level of turbulence comparatively low. In cases with low turbulence intensity and a smooth velocity field for long time periods (unstable and stable IGW) ALDM generated spurious oscillations in the buoyancy field, which we could avoid by using the modified numerical flux function. However, this was not necessary in the case with a high turbulence level (unstable HGW) and in all 2.5-D simulations.

We showed that with ALDM and DSM reliable results can be obtained in 2.5-D simulations with less than 2000 grid cells or in 3-D simulations with less than one hundred thousand grid cells. Such inexpensive simulations would allow running large numbers of simulations in order to study the influence of various parameters on gravity-wave breaking, such as stratification, wavelength, amplitude, propagation angle and viscosity.

The work share of the applicant in the presented study included the implementation and testing of the modified ALDM flux function; the set-up, conduction and post-processing of all presented 3-D and 2.5-D LES ensembles; as well as writing most of the journal article.

4. Summary and conclusion

The general objective of the present work was to gain a better insight into the flow physics of buoyancy-driven flows such as stratified turbulence and breaking gravity waves and finding efficient numerical simulation methods for this kind of flows. The breaking of atmospheric gravity-waves involves a large range of spatial and temporal scales and leads to enormous computational costs if all scales from the large scale flow down to the smallest turbulent eddies shall be resolved. It is thus desirable to use large-eddy simulation (LES), i.e. modelling the effect of the small-scale motion on the larger scales while resolving only the large-scale eddies.

Turbulent buoyant flows pose a special challenge to LES methods since the small-scale turbulence is not isotropic as it is assumed in many approaches. We thus had to assess the suitability of different LES methods for the simulation of gravity-affected turbulent flows. A validation of LES methods can most conveniently be done on the basis of direct numerical simulations (DNS) of idealised flows, since observations in the atmosphere usually do not allow separating different phenomena from each other and experiments in the parameter range relevant for atmospheric phenomena are not possible. Our starting point was thus the direct numerical simulation of idealised flows such as the three-dimensional Taylor–Green vortex under the influence of stable stratification (IJHFF12) and homogeneous stratified turbulence (IJHFF12, TCFD13) at different Reynolds numbers (characterising how turbulent the flow is) and Froude numbers (indicating the importance of buoyancy forces). We simulated the same cases on much coarser grids using the Adaptive Local Deconvolution Method (ALDM), an implicit turbulence model and the traditional Smagorinsky model in the static and dynamic version (SSM, DSM). We compared these results to the reference DNS in terms of different diagnostics, such as energy dissipation over time, energy distribution in the spectral space, the ratio of kinetic and potential energy in the flow and the energy conversion and transport within the spectral space (TCFD13). For all diagnostics we found a very good agreement of the ALDM results with the reference DNS for moderately stratified cases and still a good agreement for strongly stratified cases. Also, good results were obtained using

4. Summary and conclusion

the dynamic Smagorinsky model. The standard Smagorinsky model with a fixed model coefficient, however, produced in general less reliable results.

Comparing just LES flow results to a reference DNS can be misleading in some cases, since a seemingly correct result can also be produced by an unsuitable numerical method just due to coincidence. It is thus advantageous to directly analyse the way how the numerical model modifies the flow and its energy budget. Thus, we computed the spectral eddy viscosity and diffusivity (SEV, SED) from LES of homogeneous stratified turbulence and compared it to corresponding DNS results (JFM14). The best overall agreement with the reference DNS was again produced with ALDM. The dynamic Smagorinsky model did a better job in predicting the SEV for the horizontal kinetic energy and the SED; however, it failed in predicting the SEV of vertical kinetic energy.

Having analysed the behaviour of different LES methods in stably stratified turbulent flows, we turned to cases of breaking monochromatic gravity waves in the middle atmosphere. These cases are more complex than the homogeneous stratified turbulence studied before since they involve spatially and temporally varying intensities of stratification and turbulence. We thus started this chapter by running fully resolved DNS of three different cases (JFM13, JGR14). These simulations are not only a very good reference for the validation of computationally less expensive simulation methods (for our own work and potentially other groups interested in this field) but also provide a very detailed insight into the physics of gravity wave breaking under different conditions.

The last article (JAS15) finally combines the two main chapters of this work by focusing on LES of breaking gravity waves. We simulated the breaking wave cases presented in JFM13 and JGR14 using ALDM, DSM and CDS4 (a fourth order accurate central discretisation without turbulence model) and compared the results to the reference DNS in terms of wave amplitude and energy dissipation over time, variability among ensemble members (simulations with *almost* identical initial conditions) and spatial energy spectra at certain instances of time. We found that the central discretisation without turbulence model can in some cases (low levels of turbulence) yield good results, but fails completely if the turbulence intensity is too high. Therefore it cannot be recommended. ALDM in its original formulation works well in cases with high levels of turbulence but tends to generate spurious oscillations in the buoyancy field if the velocity field is very smooth. This can be avoided by adding an upwind term to the ALDM buoyancy flux function, at the cost of an increased overall energy dissipation. The DSM results were in all cases in good agreement with the reference DNS without any

modifications. The DSM was thus the most robust and reliable turbulence model for the different gravity wave breaking cases.

To sum up, among the investigated LES methods only ALDM and DSM can be regarded as reliable turbulence models for stably stratified turbulent flows and (especially) gravity wave breaking. ALDM did a better job in the simulations of homogeneous stratified turbulence and also provides a better approximation of the spectral eddy viscosity and diffusivity compared to DSM. However, ALDM tends to produce spurious oscillations of the buoyancy field in simulations of breaking waves that involve a temporally very smooth velocity field. ALDM thus requires a modification for these cases while DSM works well for all tested cases of gravity wave breaking. The computational costs of ALDM and DSM are similar, ALDM performs better in homogeneous stratified turbulence and DSM is more reliable for gravity wave breaking. So the overall score in LES for buoyancy-affected flows is even.

In conclusion, the major contributions of the present work extending the knowledge about buoyancy-affected turbulent flows include

1. a number of new DNS reference simulations of homogeneous stratified turbulence which confirm results of previous studies and extend the range of parameters investigated to higher buoyancy Reynolds numbers,

2. a detailed investigation of the spectral energy fluxes within homogeneous stratified turbulence based on DNS results,

3. the analysis of two-dimensional spectral eddy viscosity and diffusivity in homogeneous stratified turbulence,

4. the validation of different LES methods for homogeneous stratified turbulence using the results from points 1, 2 and 3, showing that ALDM performs best and DSM yields also good results without any modifications to the models,

5. reference DNS simulations of three different cases of breaking monochromatic gravity waves in the terrestrial mesosphere,

6. a modification of the ALDM scalar flux function in order to reduce scalar fluctuations in (almost) laminar flow fields and

7. the validation of different LES methods for the gravity wave breaking cases showing that DSM yields good results if the resolution in the direction of the wave vector is sufficient and ALDM also works well if the modification mentioned in point 6 is applied.

The possibility of using ALDM and DSM for simulations of breaking gravity waves will allow for the variation of basic parameters in the wave breaking set-up in order to study their effect on the results by running a large amount of sim-

ulations, and for the simulation of large domains including many wavelengths to study spatially developing gravity waves within a non-uniform background flow. A first example for this kind of application is the work of Muraschko et al. (2014), who used LES with ALDM to validate two new WKB theory based methods for the accurate and efficient simulation of gravity-wave packets travelling in a non-uniform background flow. Considering these applications, the present work will also contribute to a further deepening of the understanding of atmospheric phenomena and thus improving reliability and accuracy of weather and climate models in the future.

Bibliography

Achatz, U. (2005). On the role of optimal perturbations in the instability of monochromatic gravity waves. *Phys. Fluids*, 17(9):094107.

Achatz, U. and Schmitz, G. (2006a). Optimal growth in inertia-gravity wave packets: Energetics, long-term development, and three-dimensional structure. *J. Atmos. Sci.*, 63:414–434.

Achatz, U. and Schmitz, G. (2006b). Shear and static instability of inertia-gravity wave packets: Short-term modal and nonmodal growth. *J. Atmos. Sci.*, 63:397–413.

Afanasyev, Y. D. and Peltier, W. R. (2001). Numerical simulations of internal gravity wave breaking in the middle atmosphere: The influence of dispersion and three-dimensionalization. *J. Atmos. Sci.*, 58:132–153.

Andreassen, Ø., Øyvind Hvidsten, P., Fritts, D. C., and Arendt, S. (1998). Vorticity dynamics in a breaking internal gravity wave. Part 1. Initial instability evolution. *J. Fluid Mech.*, 367:27–46.

Andreassen, Ø., Wasberg, C. E., Fritts, D. C., and Isler, J. R. (1994). Gravity wave breaking in two and three dimensions 1. Model description and comparison of two-dimensional evolutions. *J. Geophys. Res.*, 99:8095–8108.

Baldwin, M. P., Gray, L. J., Dunkerton, T. J., Hamilton, K., Haynes, P. H., Randel, W. J., Holton, J. R., Alexander, M. J., Hirota, I., Horinouchi, T., Jones, D. B. A., Kinnersley, J. S., Marquardt, C., Sato, K., and Takahashi, M. (2001). The quasi-biennial oscillation. *Rev. Geophys.*, 39:179–229.

Batchelor, G. (1953). *Homogeneous turbulence*. Cambridge University Press.

Blumen, W. and McGregor, C. D. (1976). Wave drag by three-dimensional mountain lee-waves in nonplanar shear flow. *Tellus*, 28(4):287–298.

Borchert, S., Achatz, U., Remmler, S., Hickel, S., Harlander, U., Vincze, M., Alexandrov, K. D., Rieper, F., Heppelmann, T., and Dolaptchiev, S. I. (2015). Finite-volume models with implicit subgrid-scale parameterization for the differentially heated rotating annulus. *Meteorol. Z.*, 23(6):561–580.

Bibliography

Boris, J. P., Grinstein, F. F., Oran, E. S., and Kolbe, R. L. (1992). New insights into large eddy simulation. *Fluid Dynam. Res.*, 10(4-6):199–228.

Bretherton, F. P. (1966). The propagation of groups of internal gravity waves in a shear flow. *Quart. J. Roy. Meteor. Soc.*, 92(394):466–480.

Bretherton, F. P. (1969). Waves and turbulence in stably stratified fluids. *Radio Sci.*, 4(12):1279–1287.

Brethouwer, G., Billant, P., Lindborg, E., and Chomaz, J.-M. (2007). Scaling analysis and simulation of strongly stratified turbulent flows. *J. Fluid Mech.*, 585:343–368.

Chorin, A. J. (1968). Numerical solution of the Navier–Stokes equations. *Math. Comp.*, 22:745–762.

Chun, H.-Y. and Baik, J.-J. (1998). Momentum flux by thermally induced internal gravity waves and its approximation for large-scale models. *J. Atmos. Sci.*, 55:3299–3310.

Chun, H.-Y., Song, M.-D., Kim, J.-W., and Baik, J.-J. (2001). Effects of gravity wave drag induced by cumulus convection on the atmospheric general circulation. *J. Atmos. Sci.*, 58(3):302–319.

Clark, R. A., Ferziger, J. H., and Reynolds, W. C. (1979). Evaluation of subgrid-scale models using an accurately simulated turbulent flow. *J. Fluid Mech.*, 91(01):1–16.

Cot, C. (2001). Equatorial mesoscale wind and temperature fluctuations in the lower atmosphere. *J. Geophys. Res.*, 106(D2):1523–1532.

Dewan, E. M. (1979). Stratospheric wave spectra resembling turbulence. *Science*, 204(4395):832–835.

Dewan, E. M. (1997). Saturated-cascade similitude theory of gravity wave spectra. *J. Geophys. Res.*, 102(D25):29799–29817.

Domaradzki, J. A., Metcalfe, R. W., Rogallo, R. S., and Riley, J. J. (1987). Analysis of subgrid-scale eddy viscosity with use of results from direct numerical simulations. *Phys. Rev. Lett.*, 58(6):547–550.

Dörnbrack, A. (1998). Turbulent mixing by breaking gravity waves. *J. Fluid Mech.*, 375:113–141.

Drazin, P. G. (1977). On the instability of an internal gravity wave. *Proc. Roy. Soc. London A*, 356(1686):411–432.

Dunkerton, T. J. (1997a). The role of gravity waves in the quasi-biennial oscillation. *J. Geophys. Res.*, 102:26053–26076.

Dunkerton, T. J. (1997b). Shear instability of internal inertia-gravity waves. *J. Atmos. Sci.*, 54:1628–1641.

Eidson, T. M. (1985). Numerical simulation of the turbulent Rayleigh–Bénard problem using subgrid modelling. *J. Fluid Mech.*, 158:245–268.

Einaudi, F. and Hines, C. O. (1970). WKB approximation in application to acoustic-gravity waves. *Can. J. Phys.*, 48:1458–1471.

Fritts, D. C. and Alexander, M. J. (2003). Gravity wave dynamics and effects in the middle atmosphere. *Rev. Geophys.*, 41(1).

Fritts, D. C., Isler, J. R., and Andreassen, O. (1994). Gravity wave breaking in two and three dimensions 2. Three-dimensional evolution and instability structure. *J. Geophys. Res.*, 99:8109–8124.

Fritts, D. C. and Wang, L. (2013). Gravity wave-fine structure interactions. Part II: Energy dissipation evolutions, statistics, and implications. *J. Atmos. Sci.*, 70(12):3710–3734.

Fritts, D. C., Wang, L., Werne, J., Lund, T., and Wan, K. (2009a). Gravity wave instability dynamics at high reynolds numbers. Part I: Wave field evolution at large amplitudes and high frequencies. *J. Atmos. Sci.*, 66(5):1126–1148.

Fritts, D. C., Wang, L., Werne, J., Lund, T., and Wan, K. (2009b). Gravity wave instability dynamics at high reynolds numbers. Part II: Turbulence evolution, structure, and anisotropy. *J. Atmos. Sci.*, 66(5):1149–1171.

Fritts, D. C., Wang, L., and Werne, J. A. (2013). Gravity wave-fine structure interactions. Part I: Influences of fine structure form and orientation on flow evolution and instability. *J. Atmos. Sci.*, 70(12):3710–3734.

Fruman, M. D. and Achatz, U. (2012). Secondary instabilities in breaking inertia-gravity waves. *J. Atmos. Sci.*, 69:303–322.

Fruman, M. D., Remmler, S., Achatz, U., and Hickel, S. (2014). On the construction of a direct numerical simulation of a breaking inertia-gravity wave in the upper-mesosphere. *J. Geophys. Res.*, accepted for publication.

Gage, K. S. (1979). Evidence for a $k^{-5/3}$ law inertial range in mesoscale two-dimensional turbulence. *J. Atmos. Sci.*, 36:1950–1954.

Bibliography

Germano, M., Piomelli, U., Moin, P., and Cabot, W. H. (1991). A dynamic subgrid-scale eddy viscosity model. *Phys. Fluids A*, 3(7):1760–1765.

Godeferd, F. S. and Cambon, C. (1994). Detailed investigation of energy transfers in homogeneous stratified turbulence. *Phys. Fluids*, 6(6):2084–2100.

Godeferd, F. S. and Staquet, C. (2003). Statistical modelling and direct numerical simulations of decaying stably stratified turbulence. Part 2. Large-scale and small-scale anisotropy. *J. Fluid Mech.*, 486:115–159.

Grilli, M., Schmid, P. J., Hickel, S., and Adams, N. A. (2012). Analysis of unsteady behaviour in shockwave turbulent boundary layer interaction. *J. Fluid Mech.*, 700:16–28.

Grimsdell, A. W., Alexander, M. J., May, P. T., and Hoffmann, L. (2010). Model study of waves generated by convection with direct validation via satellite. *J. Atmos. Sci.*, 67(5):1617–1631.

Grinstein, F. F., Margolin, L. G., and Rider, W. J., editors (2007). *Implicit Large Eddy Simulation – Computing Turbulent Fluid Dynamics*. Cambridge University Press.

Heisenberg, W. (1948). Zur statistischen Theorie der Turbulenz. *Z Phys. A*, 124:628–657.

Herring, J. R. and Métais, O. (1989). Numerical experiments in forced stably stratified turbulence. *J. Fluid Mech.*, 202(1):97–115.

Hickel, S. and Adams, N. A. (2007). A proposed simplification of the adaptive local deconvolution method. *ESAIM*, 16:66–76.

Hickel, S., Adams, N. A., and Domaradzki, J. A. (2006). An adaptive local deconvolution method for implicit LES. *J. Comput. Phys.*, 213:413–436.

Hickel, S., Adams, N. A., and Mansour, N. N. (2007). Implicit subgrid-scale modeling for large-eddy simulation of passive scalar mixing. *Phys. Fluids*, 19:095102.

Hickel, S., Kempe, T., and Adams, N. A. (2008). Implicit large-eddy simulation applied to turbulent channel flow with periodic constrictions. *Theor. Comput. Fluid Dyn.*, 22:227–242.

Hines, C. O. (1965). Dynamical heating of the upper atmosphere. *J. Geophys. Res.*, 70(1):177–183.

Holton, J. R. (1982). The role of gravity wave induced drag and diffusion in the momentum budget of the mesosphere. *J. Atmos. Sci.*, 39:791–799.

Houghton, J. T. (1978). The stratosphere and mesosphere. *Quart. J. Roy. Meteor. Soc.*, 104(439):1–29.

Kawamura, T., Takami, H., and Kuwahara, K. (1986). Computation of high reynolds number flow around a circular cylinder with surface roughness. *Fluid Dynam. Res.*, 1(2):145–162.

Kim, Y.-J., Eckermann, S. D., and Chun, H.-Y. (2003). An overview of the past, present and future of gravity–wave drag parametrization for numerical climate and weather prediction models. *Atmosphere-Ocean*, 41(1):65–98.

Klein, R. (2009). Asymptotics, structure, and integration of sound-proof atmospheric flow equations. *Theor. Comput. Fluid Dyn.*, 23:161–195.

Klostermeyer, J. (1982). On parametric instabilities of finite-amplitude internal gravity waves. *J. Fluid Mech.*, 119:367–377.

Kolmogorov, A. N. (1941). The local structure of turbulence in incompressible viscous fluid at high Reynolds number. *C. R. Acad. Sci. URSS*, 30:301–305.

Kraichnan, R. H. (1967). Inertial ranges in two-dimensional turbulence. *Phys. Fluids*, 10(7):1417–1423.

Kraichnan, R. H. (1976). Eddy viscosity in two and three dimensions. *J. Atmos. Sci.*, 33:1521–1536.

Laprise, J. P. R. (1993). An assessment of the WKBJ approximation to the vertical structure of linear mountain waves: Implications for gravity-wave drag parameterization. *J. Atmos. Sci.*, 50:1469–1487.

Laval, J.-P., McWilliams, J. C., and Dubrulle, B. (2003). Forced stratified turbulence: Successive transitions with Reynolds number. *Phys. Rev. E*, 68(3):036308.

Lelong, M.-P. and Dunkerton, T. J. (1998). Inertia-gravity wave breaking in three dimensions. Parts I and II. *J. Atmos. Sci.*, 55:2473–2501.

Lilly, D. K. (1967). The representation of small scale turbulence in numerical simulation experiments. In *IBM Scientific Computing Symposium on environmental sciences*, pages 195–210.

Lilly, D. K. (1972). Wave momentum flux - A GARP problem. *Bull. Am. Meteor. Soc.*, 53:17–23.

Bibliography

Lilly, D. K. (1983). Stratified turbulence and the mesoscale variability of the atmosphere. *J. Atmos. Sci.*, 40(3):749–761.

Lilly, D. K. (1992). A proposed modification of the german subgrid-scale closure method. *Phys. Fluids A*, 4(3):633–635.

Lilly, D. K., Bassett, G., Droegemeier, K., and Bartello, P. (1998). Stratified turbulence in the atmospheric mesoscales. *Theor. Comput. Fluid Dyn.*, 11:139–153.

Lilly, D. K., Nicholls, J. M., Kennedy, P. J., Klemp, J. B., and Chervin, R. M. (1982). Aircraft measurements of wave momentum flux over the colorado rocky mountains. *Quart. J. Roy. Meteor. Soc.*, 108(457):625–642.

Lindborg, E. (2006). The energy cascade in a strongly stratified fluid. *J. Fluid Mech.*, 550(1):207–242.

Lindzen, R. S. (1981). Turbulence and stress owing to gravity wave and tidal breakdown. *J. Geophys. Res.*, 86:9707–9714.

Lund, T. S. and Fritts, D. C. (2012). Numerical simulation of gravity wave breaking in the lower thermosphere. *J. Geophys. Res.*, 117(D21105).

McFarlane, N. A. (1987). The effect of orographically excited gravity wave drag on the general circulation of the lower stratosphere and troposphere. *J. Atmos. Sci.*, 44:1775–1800.

McLandress, C. (1998). On the importance of gravity waves in the middle atmosphere and their parameterization in general circulation models. *J. Atmos. Sol.-Terr. Phy.*, 60(14):1357–1383.

Mied, R. P. (1976). The occurrence of parametric instabilities in finite-amplitude internal gravity waves. *J. Fluid Mech.*, 78(4):763–784.

Muraschko, J., Fruman, M. D., Achatz, U., Hickel, S., and Toledo, Y. (2014). On the application of Wentzel–Kramer–Brillouin theory for the simulation of the weakly nonlinear dynamics of gravity waves. *Q. J. R. Meteorol. Soc.*

Nappo, C. J. (2002). *An introduction to atmospheric gravity waves*. Academic Press.

Nastrom, G. D. and Gage, K. S. (1985). A climatology of atmospheric wavenumber spectra of wind and temperature observed by commercial aircraft. *J. Atmos. Sci.*, 42(9):950–960.

Orszag, S. A. (1970). Analytical theories of turbulence. *J. Fluid Mech.*, 41(02):363–386.

O'Sullivan, D. and Dunkerton, T. J. (1995). Generation of inertia-gravity waves in a simulated life cycle of baroclinic instability. *J. Atmos. Sci.*, 52(21):3695–3716.

Palmer, T. N., Shutts, G. J., and Swinbank, R. (1986). Alleviation of a systematic westerly bias in general circulation and numerical weather prediction models through an orographic gravity wave drag parametrization. *Quart. J. Roy. Meteor. Soc.*, 112(474):1001–1039.

Parker, S. P. (2003). *McGraw-Hill dictionary of scientific and technical terms*. The McGraw-Hill Companies, 6th edition.

Plougonven, R. and Snyder, C. (2007). Inertia gravity waves spontaneously generated by jets and fronts. Part I: Different baroclinic life cycles. *J. Atmos. Sci.*, 64(7):2502–2520.

Prusa, J. M., Smolarkiewicz, P. K., and Garcia, R. R. (1996). Propagation and breaking at high altitudes of gravity waves excited by tropospheric forcing. *J. Atmos. Sci.*, 53(15):2186–2216.

Remmler, S., Fruman, M. D., and Hickel, S. (2013). Direct numerical simulation of a breaking inertia-gravity wave. *J. Fluid Mech.*, 722:424–436.

Remmler, S. and Hickel, S. (2012). Direct and large eddy simulation of stratified turbulence. *Int. J. Heat Fluid Flow*, 35:13–24.

Remmler, S. and Hickel, S. (2013). Spectral structure of stratified turbulence: Direct numerical simulations and predictions by large eddy simulation. *Theor. Comput. Fluid Dyn.*, 27:319–336.

Remmler, S. and Hickel, S. (2014). Spectral eddy viscosity of stratified turbulence. *J. Fluid Mech.*, 755(R 6).

Remmler, S., Hickel, S., Fruman, M. D., and Achatz, U. (2015). Validation of large-eddy simulation methods for gravity-wave breaking. *J. Atmos. Sci.*, doi:10.1175/JAS-D-14-0321.1, in press.

Riley, J. J. and de Bruyn Kops, S. M. (2003). Dynamics of turbulence strongly influenced by buoyancy. *Phys. Fluids*, 15(7):2047–2059.

Sawyer, J. S. (1959). The introduction of the effects of topography into methods of numerical forecasting. *Quart. J. Roy. Meteor. Soc.*, 85(363):31–43.

Scinocca, J. F. and McFarlane, N. A. (2000). The parametrization of drag induced by stratified flow over anisotropic orography. *Quart. J. Roy. Meteor. Soc.*, 126(568):2353–2393.

Bibliography

Shu, C.-W. (1988). Total-variation-diminishing time discretizations. *SIAM J. Sci. Stat. Comput.*, 9(6):1073–1084.

Smagorinsky, J. (1963). General circulation experiments with the primitive equations. I: The basic experiment. *Mon. Wea. Rev.*, 91:99–164.

Smith, L. M. and Waleffe, F. (2002). Generation of slow large scales in forced rotating stratified turbulence. *J. Fluid Mech.*, 451(1):145–168.

Smith, R. B. (1979). The influence of mountains on the atmosphere. *Adv. Geophys.*, 21:87–230.

Smolarkiewicz, P. K. and Margolin, L. G. (1998). MPDATA: A finite-difference solver for geophysical flows. *J. Comput. Phys.*, 140(2):459–480.

Staquet, C. and Godeferd, F. S. (1998). Statistical modelling and direct numerical simulations of decaying stably stratified turbulence. Part 1. Flow energetics. *J. Fluid Mech.*, 360:295–340.

Sukoriansky, S., Galperin, B., and Staroselsky, I. (2005). A quasinormal scale elimination model of turbulent flows with stable stratification. *Phys. Fluids*, 17(8):085107.

van der Vorst, H. A. (1992). Bi-CGSTAB: A fast and smoothly converging variant of Bi-CG for the solution of nonsymmetric linear systems. *SIAM J. Sci. Stat. Comput.*, 13(2):631–644.

van Zandt, T. E. (1982). A universal spectrum of buoyancy waves in the atmosphere. *Geophys. Res. Lett.*, 9(5):575–578.

Vincze, M., Borchert, S., Achatz, U., von Larcher, T., Baumann, M., Liersch, C., Remmler, S., Beck, T., Alexandrov, K., Egbers, C., Fröhlich, J., Heuveline, V., Hickel, S., and Harlander, U. (2015). Benchmarking in a rotating annulus: a comparative experimental and numerical study of baroclinic wave dynamics. *Meteorol. Z.*, 23(6):611–635.

Waite, M. L. and Bartello, P. (2004). Stratified turbulence dominated by vortical motion. *J. Fluid Mech.*, 517:281–308.

Winters, K. B. and D'Asaro, E. A. (1994). Three-dimensional wave instability near a critical level. *J. Fluid Mech.*, 272:255–284.

A. Reprints of journal articles

In this appendix we reprint those journal articles on which the present dissertation is based. The following list is hyper-linked for navigation within in the PDF document.

- IJHFF12: Direct and large eddy simulation of stratified turbulence

- TCFD13: Spectral structure of stratified turbulence

- JFM13: Direct numerical simulation of a breaking inertia-gravity wave

- JFM14: Spectral eddy viscosity of stratified turbulence

- JGR14: On the construction of a direct numerical simulation of a breaking inertia-gravity wave in the upper-mesosphere

- JAS15: Validation of large-eddy simulation methods for gravity-wave breaking
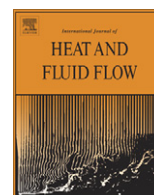
Direct and large eddy simulation of stratified turbulence

Sebastian Remmler *, Stefan Hickel

Institute of Aerodynamics and Fluid Mechanics, Technische Universität München, 85747 Garching bei München, Germany

ABSTRACT

Simulations of geophysical turbulent flows require a robust and accurate subgrid-scale turbulence modeling. To evaluate turbulence models for stably stratified flows, we performed direct numerical simulations (DNSs) of the transition of the three-dimensional Taylor–Green vortex and of homogeneous stratified turbulence with large-scale horizontal forcing. In these simulations we found that energy dissipation is concentrated within thin layers of horizontal tagliatelle-like vortex sheets between large pancake-like structures. We propose a new implicit subgrid-scale model for stratified fluids, based on the Adaptive Local Deconvolution Method (ALDM). Our analysis proves that the implicit turbulence model ALDM correctly predicts the turbulence energy budget and the energy spectra of stratified turbulence, even though dissipative structures are not resolved on the computational grid.

© 2012 Elsevier Inc. All rights reserved.

1. Introduction

To predict atmospheric and oceanic mesoscale flows, we need to understand and parametrize small scale turbulence that is strongly affected by the presence of stable density stratification. The stratification suppresses vertical motions and thus makes all scales of the velocity field strongly anisotropic. Using aircraft observations, the horizontal velocity spectrum in the atmosphere was analyzed by Nastrom and Gage (1985). They found a power-law behavior in the mesoscale range with an exponent of −5/3. In the vertical spectrum, on the other hand, Cot (2001) observed an exponent of −3 in the inertial range.

There has been a long an intensive discussion whether the observed spectra are due to a backward cascade of energy (Gage, 1979; Lilly, 1983; Herring and Métais, 1989) as in two-dimensional turbulence (Kraichnan, 1967), or due to breaking of internal waves, which means that a forward cascade is the dominant process (Dewan, 1979; van Zandt, 1982). In different numerical and theoretical studies, ambiguous or even conflicting results were obtained (Lilly et al., 1998).

During the last decade, a number of new simulations and experiments addressed the issue. Smith and Waleffe (2002) observed a concentration of energy in the lowest modes in their simulations. Other studies (Laval et al., 2003; Waite and Bartello, 2004) suggested that the character of the flow depends on the Reynolds number. Apparently, high Reynolds numbers are associated with stronger three-dimensionality and a forward cascade of energy. Riley and de Bruyn Kops (2003) suggested that the flow can be

strongly stratified but still turbulent if $Fr^2Re > 1$. Lindborg (2006) presented a scaling analysis of the Boussinesq equations for low Froude and high Reynolds number. His theory of strongly anisotropic, but still three-dimensional, turbulence explains the horizontal $k_h^{-5/3}$ spectrum as well as the vertical k_v^{-3} spectrum. On the basis of these findings, Brethouwer et al. (2007) showed that the relevant non-dimensional parameter controlling stratified turbulence must indeed be the buoyancy Reynolds number $\mathcal{R} = Fr^2Re$. For $\mathcal{R} \gg 1$, they predict stratified turbulence including local overturning and a forward energy cascade. In the opposite limit, for $\mathcal{R} \ll 1$, the flow is controlled by viscosity and does not contain small-scale turbulent motions. A detailed analysis of the spectral structure and spectral energy budget of homogeneous stratified turbulence based on direct numerical simulations is provided by Remmler and Hickel (in press).

Since a full resolution of all turbulence scales is only possible for very low Reynolds numbers, many groups performed large eddy simulations (LESs), which rely on a subgrid-scale model to represent effects of unresolved small-scale turbulence. For example, Métais and Lesieur (1992) used a spectral eddy viscosity model, based on the eddy damped quasi-normal Markovian (EDQNM) theory. This required a flow simulation in Fourier space and the cut-off wavenumber to be in the inertial range. For LES in physical space, Smagorinsky models are widely used, either in the classical formulation (Kaltenbach et al., 1994) or with certain modifications for stratified turbulence that are usually based on the local Richardson number (Dörnbrack, 1998). Better results can be obtained if the model constant of a Smagorinsky model is not prescribed, but computed by the dynamic procedure of Germano et al. (1991). This approach was successfully applied to stably stratified turbulent channel flow by Armenio and Sarkar (2002), Taylor et al. (2005), Basu and Porté-Agel (2006), and others. Staquet and Godeferd

---

* Corresponding author. Tel.: +49 89 289 16348.
E-mail address: remmler@tum.de (S. Remmler).

(1998) presented a two-point closure statistical EDQNM turbulence model, which was adapted for axisymmetric spectra about the vertical axis. Recently, many groups presented regularized direct numerical simulations (DNSs) of stratified turbulence, which means rather pragmatically stabilizing under-resolved DNS by removing the smallest resolved scales. This is usually achieved by a hyperviscosity approach (Lindborg, 2006) or by de-aliasing in spectral methods using the "2/3-rule" (Bouruet-Aubertot et al., 1996; Fritts et al., 2009).

In practice, all SGS turbulence models suffer from the problem that the computed SGS stresses are of the same order as the grid truncation error. This typically leads to interference between SGS model and numerical scheme, that can manifest in instability and lack of grid convergence. This issue can be solved by combining discretization scheme and SGS model in a single approach. This is usually referred to as "implicit" LES (ILES) in contrast to the traditional "explicit" SGS models. The idea of physically consistent ILES was realized by Hickel et al. (2006) in the Adaptive Local Deconvolution Method (ALDM) for neutrally stratified fluids. ALDM provides a framework for the design, analysis and optimization of numerical discretizations with an implicit SGS model that is consistent with turbulence theory. Based on this method and ALDM for passive scalar transport (Hickel et al., 2007), we developed an implicit SGS model for Boussinesq fluids. In the present paper, we evaluate the applicability of ALDM for stably stratified turbulence.

We simulated transition and decay of the three-dimensional Tailor–Green vortex as an example of a transitional stratified turbulent flow. For isotropic conditions, this flow was intensively studied by Brachet et al. (1983). Riley and de Bruyn Kops (2003) first simulated its evolution in a stably stratified background. The second test case to be considered is forced homogeneous stratified turbulence at different Froude and Reynolds numbers. For both cases, we present not only ILES, but also LES with a standard Smagorinsky model (SSM) and a dynamic Smarorinsky model (DSM) as well as high-resolution DNS as benchmark solutions.

2. Governing equations

The non-dimensional Boussinesq equations for a stably stratified fluid in Cartesian coordinates read

$$\nabla \cdot \mathbf{u} = 0 \tag{1a}$$

$$\partial_t \mathbf{u} + \nabla \cdot (\mathbf{uu}) = -\nabla p - \frac{\rho}{\mathrm{Fr}_0^2} \mathbf{e}_z + \frac{1}{\mathrm{Re}_0} \nabla^2 \mathbf{u} \tag{1b}$$

$$\partial_t \rho + \nabla \cdot (\rho \mathbf{u}) = -w + \frac{1}{\mathrm{Pr}\, \mathrm{Re}_0} \nabla^2 \rho \tag{1c}$$

where velocities $\mathbf{u} = [u, v, w]$ are made non-dimensional by $\mathcal{U}$, all spatial coordinates by the length scale $\mathcal{L}$, pressure by $\mathcal{U}^2$, time by $\mathcal{L}/\mathcal{U}$, and density fluctuation $\rho = \rho^* - \bar{\rho}$ (ρ^*: local absolute density, $\bar{\rho}$: background density) by the background density gradient $\mathcal{L}|d\bar{\rho}/dz|$. The non-dimensional parameters are

$$\mathrm{Fr}_0 = \frac{\mathcal{U}}{N\mathcal{L}}, \quad \mathrm{Re}_0 = \frac{\mathcal{U}\mathcal{L}}{\nu}, \quad \mathrm{Pr} = \frac{\nu}{\alpha}, \tag{2}$$

where $N = \sqrt{-g/\rho_0\, d\bar{\rho}/dz}$ is the Brunt–Väisälä frequency, ν is the kinematic viscosity and α is the thermal diffusivity. We chose a Prandtl number of Pr = 0.7, corresponding to values found in the atmosphere. Froude and Reynolds number are the parameters that control the flow regime. For given Fr_0 and Re_0, the dimensional length scale can be estimated from

$$\mathcal{L} = \sqrt{\frac{\mathrm{Re}_0}{\mathrm{Fr}_0}} \frac{\nu}{N}. \tag{3}$$

With the instantaneous values of kinetic energy E_k and kinetic energy dissipation ε_k, we find the local Froude and Reynolds number as well as the buoyancy Reynolds number $\mathcal{R}$, defined by Brethouwer et al. (2007):

$$\mathrm{Fr} = \frac{\mathrm{Fr}_0 \mathcal{L}}{\mathcal{U}} \frac{\varepsilon_k}{E_k}, \quad \mathrm{Re} = \frac{\mathrm{Re}_0}{\mathcal{U}\mathcal{L}} \frac{E_k^2}{\varepsilon_k}, \quad \mathcal{R} = \mathrm{Re}\,\mathrm{Fr}^2 \tag{4}$$

In ILES by construction we do not have direct access to the value of ε_k, as only a small part of it is resolved. For LES, we thus estimate ε_k from the total energy balance

$$\partial_t \langle E_t \rangle = \partial_t \langle E_k \rangle + \partial_t \langle E_p \rangle = P - \varepsilon_k - \varepsilon_p = P - (1 + \Gamma)\varepsilon_k, \tag{5}$$

where the temporal change of total energy in the flow $\partial_t \langle E_t \rangle$ can be computed from the energy levels at subsequent time steps, P is the power inserted into the system by the external forcing and $\Gamma = \varepsilon_p/\varepsilon_k$ is the mixing ratio assumed to be constant $\Gamma = 0.4$, which is an acceptable approximation for a wide range of parameters (Remmler and Hickel, in press). Here, ε_p is the dissipation rate of potential energy. The kinetic energy dissipation rate can then be computed from

$$\varepsilon_k = \frac{1}{1 + \Gamma}(P - \partial_t \langle E_t \rangle). \tag{6}$$

3. Numerical method

3.1. Flow solver

Our finite-volume solver INCA offers different discretization schemes depending on the application. For DNS and LES with SSM and DSM, we used a non-dissipative central difference scheme with 4th order accuracy for the convective terms and 2nd order central differences for the diffusive terms and the continuity equation (Poisson equation for pressure). For implicit LES, we replaced the central difference scheme for the convective terms by the implicit turbulence model ALDM. All computations were run on Cartesian staggered grids with uniform cell size.

For time integration, we used an explicit third-order accurate Runge–Kutta scheme, proposed by Shu (1988). The time step was dynamically adjusted to keep the CFL number smaller than unity.

The Poisson equation for the pressure is solved in every Runge–Kutta sub step. The Poisson solver employs fast Fourier-transform (FFT) in the vertical direction and a Stabilized Bi-Conjugate Gradient (BiCGSTAB) solver (van der Vorst, 1992) in the horizontal plane. By the FFT, the three-dimensional problem is transformed into a set of independent two-dimensional problems, which can be solved in parallel.

3.2. The adaptive local deconvolution method

Our approach to ILES is based on a nonlinear finite-volume scheme involving a solution adaptive reconstruction (deconvolution) of the numerical solution. The nonlinear discretization scheme generates a certain controllable spectral numerical viscosity. Using an evolutionary optimization algorithm, free parameters of the discretization scheme have been calibrated in such a way that the effective spectral numerical viscosity is identical to the spectral eddy viscosity from turbulence theory for asymptotic cases (Hickel et al., 2006). In the following we give a concise description of ALDM on the example of a one-dimensional generic transport equation

$$\partial_t u + \partial_x F(u) = 0. \tag{7}$$

For a more detailed description and the extension to the three-dimensional Navier–Stokes equations, we refer to Hickel et al. (2006).

We obtain the discretized form of Eq. (7) by a convolution with a homogeneous filter kernel G and a subsequent discretization of the filtered equations

$$\partial_t \bar{u}_N + G * \partial_x F_N(u_N) = -G * \partial_x \cdot \tau_{sgs} = \mathcal{G}_{sgs}, \tag{8}$$

where the overbar indicates spatial filtering and the subscript N denotes the discretized solution on a numerical grid. In Eq. (8) we use the unfiltered solution to compute the nonlinear term, which requires the deconvolution of the solution on the range of represented scales $u_N = G^{-1} * \bar{u}_N$.

The truncation error of a numerical reconstruction scheme can be written as:

$$\mathcal{G}_{num} = G * \partial_x F_N(u_N) - \widetilde{G} * \tilde{\partial}_x \widetilde{F}_N(\tilde{u}_N), \tag{9}$$

where the tilde indicates discrete numerical approximations: While the exact continuous solution u is unknown, we can obtain the numerical approximation $\tilde{u}_N$ of the grid function u_N by a regularized deconvolution of $\bar{u}_N$ (Domaradzki and Adams, 2002). The discrete filtered solution of a general numerical method then satisfies the modified differential equation

$$\partial_t \bar{u}_N + G * \partial_x F_N(u_N) = \mathcal{G}_{num} + \widetilde{\mathcal{G}}_{sgs}, \tag{10}$$

which is identical to Eq. (8) if $\mathcal{G}_{num} + \widetilde{\mathcal{G}}_{sgs} = \mathcal{G}_{sgs}$. Explicit SGS modeling is based on the assumption $\mathcal{G}_{num} = 0$. In implicit LES the numerical error acts as an implicit SGS model: $\mathcal{G}_{num} \doteq \mathcal{G}_{sgs}$ and no explicit SGS model is used, i.e., $\widetilde{\mathcal{G}}_{sgs} = 0$. The transport equation eventually to be solved is

$$\partial_t \bar{u}_N + \widetilde{G} * \tilde{\partial}_x \widetilde{F}_N(\tilde{u}_N) = 0, \tag{11}$$

where no model terms are computed explicitly.

Finite volume methods such as ALDM require a local approximation of the unfiltered solution at the cell faces (indicated by half-integer indices), which we find by a nonlinear combination

$$\tilde{u}_N^{\mp}(x_{j\pm 1/2}) = \sum_{k=1}^{K} \sum_{r=0}^{k-1} \omega_{k,r}^{\mp}(\bar{u}_N) \tilde{p}_{k,r}^{\mp}(x_{j\pm 1/2}), \tag{12}$$

of Harten-type reconstruction polynomials (Harten et al., 1987)

$$\tilde{p}_{k,r}^{\mp}(x_{j\pm 1/2}) = \sum_{l=0}^{k-1} c_{k,r,l}^{\mp}(x_N) \bar{u}_{j-r+l}. \tag{13}$$

The deconvolution is solution adaptive by weighting the contributions of the different polynomials by the coefficients $\omega_{k,r}^{\mp}(\bar{u}_N)$, which represent the smoothness of the solution $\bar{u}_N$, see Hickel et al. (2006). The grid-dependent coefficients $c_{k,r,l}^{\mp}(x_N)$ are chosen such that the polynomial $\tilde{p}_{k,r}^{\mp}$ is a k-th order approximation of the unfiltered solution. The reconstructed solution $\tilde{u}_N^{\mp}$ is used in a consistent numerical flux function

$$\widetilde{F}_N(x_{j\pm 1/2}) = F\left(\frac{\tilde{u}_{j\pm 1/2}^- + \tilde{u}_{j\pm 1/2}^+}{2}\right) - \sigma_{j\pm 1/2}\left(\tilde{u}_{j\pm 1/2}^+ - \tilde{u}_{j\pm 1/2}^-\right). \tag{14}$$

Both, reconstruction and flux function introduce free parameters, which can be used to control the truncation error. Our objective is not a maximum order of accuracy but a physically correct representation of the effects of unresolved turbulence. For this purpose, Hickel et al. (2006) performed a spectral space analysis of the effective viscosity of ALDM. They optimized the free parameters such that the spectral numerical viscosity of ALDM matches the spectral eddy viscosity from the eddy-damped quasinormal Markovian (EDQNM) theory for isotropic turbulence. This single set of parameters has not been changed since it was once settled and is also used for the computations we are presenting here. Although optimized for the asymptotic case of isotropic turbulence, ALDM has proven to yield good results for a large variety

of complex turbulent flows. This includes decaying turbulence (Hickel et al., 2006), boundary layer flows (Hickel and Adams, 2007; Hickel and Adams, 2008), separated flows (Hickel et al., 2008; Grilli et al., in press) and others. ALDM yields good results also for cases of anisotropic and inhomogeneous turbulence.

Hickel et al. (2007) extended ALDM to the turbulent transport of passive scalars. This basically employs the same framework, but a distinction is made between two different regimes depending on the Schmidt number. For high Schmidt numbers $Sc \gg 1$, the passive scalar spectrum has two distinct inertial ranges, which is taken into account by using a different set of optimized model parameters. For the case $Sc \lesssim 1$, which applies to the present simulations, the spectra of turbulence kinetic and potential energy are similar and thus the same set of parameters can be used for momentum and scalar transport equations. We adopted this implicit SGS model for passive scalar transport for the active scalar equation. This is possible since the feedback from the density field onto the velocity field does not originate from a nonlinear term but from the linear buoyancy term.

In the original formulation, Hickel et al. (2007) used the reconstructed velocity field $\tilde{u}$ to compute the numerical flux function for the scalar transport. Since the reconstructed velocity $\tilde{u}$ is in general not divergence-free, an additional divergence correction term is necessary to avoid the generation of artificial fluctuations in a uniform scalar field. In the present implementation we avoid this difficulty by using the filtered velocity field $\bar{u}_N$, which satisfies the continuity Eq. (1a), for the transport velocity in the buoyancy flux. The numerical flux function in the buoyancy transport equation then reads

$$\widetilde{F}_{j\pm 1/2}^s = \bar{u}_{j-1/2\pm 1/2} \frac{\tilde{c}_{j\pm 1/2}^- + \tilde{c}_{j\pm 1/2}^+}{2} - \sigma_C \left| \tilde{u}_{j\pm 1/2}^- - \tilde{u}_{j-1\pm 1/2}^+ \right| \left(\tilde{c}_{j\pm 1/2}^+ - \tilde{c}_{j\pm 1/2}^- \right). \tag{15}$$

This modified numerical flux function was validated against the original implementation for neutrally and stably stratified turbulence. As there was no recognizable effect on the flow energy spectra, we used the simplified formulation throughout the present study.

3.3. Standard Smagorinsky model

If we apply a generic spatial filter (denoted by an overbar) to the dimensional momentum equation, we obtain

$$\partial_t \bar{u}_i + \partial_{x_j}(\bar{u}_i \bar{u}_j) + \partial_{x_i} \bar{p} = \partial_{x_j}(2\nu \bar{S}_{ij}) - \partial_{x_j} \tau_{ij}. \tag{16}$$

where $\bar{S}_{ij} = 0.5(\partial_{x_i} \bar{u}_j + \partial_{x_j} \bar{u}_i)$ is the filtered strain rate tensor and $\tau_{ij} = \overline{u_i u_j} - \bar{u}_i \bar{u}_j$ is the unknown SGS stress tensor, which has to be modeled. With a Boussinesq approach the SGS stress tensor is modeled as

$$\tau_{ij}^{mod} = -2\nu_t \bar{S}_{ij}. \tag{17}$$

The eddy viscosity concept is common to many SGS turbulence models. Smagorinsky (1963) estimated the unknown eddy viscosity ν_t from

$$\nu_t = (C_S \bar{\Delta})^2 |\bar{S}|; \quad |\bar{S}| = \sqrt{2\bar{S}_{ij}\bar{S}_{ij}}, \tag{18}$$

where $\bar{\Delta} = (\Delta_x \Delta_y \Delta_z)^{1/3}$ is the grid or filter size, respectively. In this formulation, the unknown SGS fluxes can be computed directly from the resolved velocity field. There is no universal value for the model constant C_S; for different flow configurations different values of the constant have been found to be optimal. In our simulations we use a value of $C_S = 0.18$, which follows from theory of isotropic turbulence (Lilly, 1967) and has been found to yield good
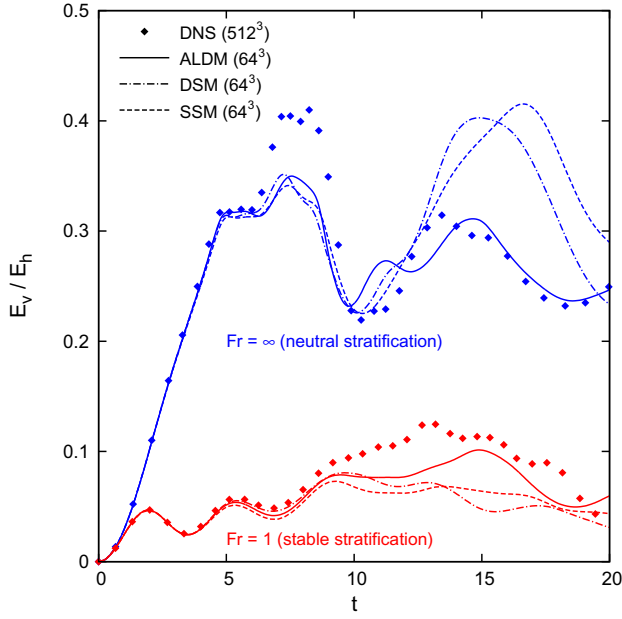
Fig. 1. Ratio of vertical to horizontal kinetic energy in the Taylor–Green vortex ($Re_0 = 1600$).

results in practice (Clark et al., 1979). The buoyancy equation is closed analogously by an eddy diffusivity model with $\alpha_t = \nu_t/\mathrm{Pr}_t$.

3.4. Dynamic Smagorinsky model

The case-dependence of the value for the model constant in the standard Smagorinsky model led to the idea of replacing the constant by a dynamic parameter, which automatically adjusts to the flow conditions. Germano et al. (1991) presented a general dynamic procedure for eddy viscosity models and applied it to the Smagorinsky model. The basic idea is a similarity between the interactions of the smallest resolved scales and unresolved scales compared to the interactions between medium scales and the smallest resolved scales.

The solution is available in its filtered form $\bar{u}$ with a grid filter width $\overline{\Delta}$. This filtered velocity field is explicitly filtered by a test

filter with a larger filter width $\hat{\Delta}$. As a test filter, we use a top-hat filter with $\hat{\Delta} = 2\overline{\Delta}$. The subfilter-scale stress tensor is $T_{ij} = \widehat{\overline{u_i u_j}} - \widehat{\overline{u}_i}\widehat{\overline{u}_j}$. It cannot be computed directly from the filtered velocity field, but one can compute the Leonard stress tensor $L_{ij} = \widehat{\overline{u}_i\,\overline{u}_j} - \widehat{\overline{u}}_i\,\widehat{\overline{u}}_j$. Using the Germano identity

$$T_{ij} = L_{ij} + \widehat{\tau_{ij}} \tag{19}$$

and the standard Smagorinsky model for τ_{ij} and T_{ji}, we can minimize the difference between L_{ij} and

$$
\begin{aligned}
L_{ij}^{mod} &= T_{ij}^{mod}(C,\hat{\Delta},\hat{\mathbf{u}}) - \widehat{\tau_{ij}^{mod}}(C,\overline{\Delta},\bar{\mathbf{u}}) \\
&\doteq -2C\hat{\Delta}^2|\widehat{\overline{S}}|\widehat{\overline{S}}_{ij} + 2C\widehat{(\overline{\Delta}^2|\widehat{\overline{S}}|\widehat{\overline{S}}_{ij})} \\
&\doteq 2CM_{ij}
\end{aligned}
\tag{20}
$$

by a least-squares procedure

$$C = \frac{1}{2}\frac{L_{ij}M_{ij}}{M_{ij}M_{ij}}. \tag{21}$$

We apply this dynamic procedure in every time step to obtain the model parameter $C_S^2 = C$ for the flow. Since the presently investigated flows are homogeneous in all spatial directions, numerator and denominator of Eq. (21) are averaged in space before evaluating Eq. (21). So finally, the parameter C_S is spatially constant, but can vary in time.

4. Results and discussion

4.1. Taylor–Green vortex (TGV)

Transitional flows are a challenging problem for turbulence subgrid-scale models. Their correct prediction is only possible if the subgrid-scale model does not affect the laminar flow and its instability modes. For most eddy-viscosity models, such as the Smagorinsky model without dynamic model-coefficient adaption, this requirement is not fulfilled. We used the transition of the three-dimensional Taylor–Green vortex (TGV) as a test for ALDM in laminar-to-turbulence transition. The velocity field in a triple-periodic box with side length $L_D = 2\pi\mathcal{L}$ is initialized with a set of large scale vortices varying vertically:

$$\mathbf{u}(t=0) = \mathcal{U}\cos(z/\mathcal{L})\begin{bmatrix} \cos(x/\mathcal{L})\,\sin(y/\mathcal{L}) \\ -\sin(x/\mathcal{L})\,\cos(y/\mathcal{L}) \\ 0 \end{bmatrix} \tag{22}$$

(a) neutral stratification   (b) stable stratification, $\mathrm{Fr}_0 = 1$
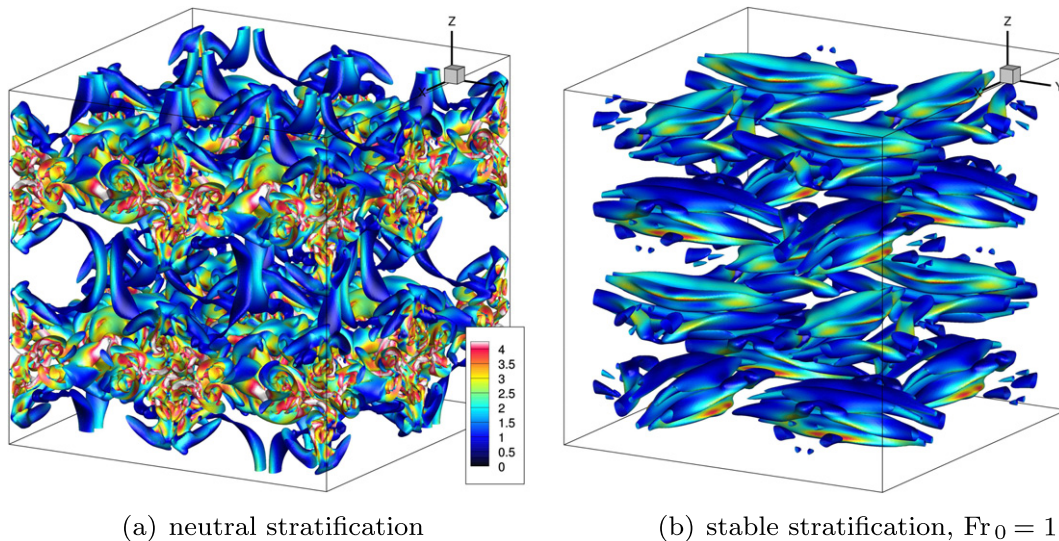
Fig. 2. Visualization of the TGV at $t = 10$ (DNS 256^3 cells at $Re_0 = 800$). Iso-surfaces at $Q = 0.5$, colored by the shear rate.
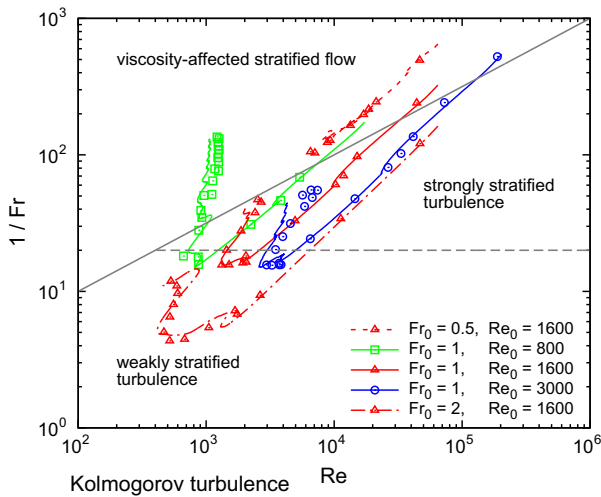
Fig. 3. Regime diagram (Brethouwer et al., 2007) for the transition of the TGV for different parameters; symbols: DNS, lines: LES with ALDM.


Fig. 5. Contributions to energy dissipation of the TGV ($Re_0 = 1600$, $Fr_0 = 2$).

Fig. 4. Total energy dissipation rate of the TGV ($Re_0 = 1600$).

Fig. 6. Contributions to energy dissipation of the TGV ($Re_0 = 1600$, $Fr_0 = 1$).

where $\mathcal{U}$ and $\mathcal{L}$ are characteristic velocity and length scales of the problem. The density field $\rho(t = 0) \equiv 0$ is initially unperturbed.

Initially, all flow energy is concentrated on the lowest wavenumbers. The flow is purely horizontal, laminar and strongly anisotropic. At later times, energy is transferred to smaller scales by vortex stretching. After approximately 10 non-dimensional time units, the flow is quasi-turbulent, keeping its determinism and spatial symmetry. At this time, the energy dissipation has a maximum due to the enhanced shear in the small scale vortices. If neutrally stratified, the energy of the vertical velocity component increases quickly, almost reaching the level of the horizontal components. In case of a stable background stratification, vertical motions are damped by the restoring buoyancy force and the flow remains highly anisotropic. In the linear limit of zero Froude number, the stratification completely prevents the transition to turbulence.

We show the temporal evolution of the ratio of vertical to horizontal kinetic energy in Fig. 1. We see, that contrary to common beliefs, the TGV never reaches a fully isotropic state. In the unstrat-

ified case, the maximum E_v/E_h observed is 0.4, whereas a value of 0.5 would correspond to isotropic turbulence. For the strongly stratified case ($Fr_0 = 1$), the vertical kinetic energy never exceeds 10% of the horizontal kinetic energy.
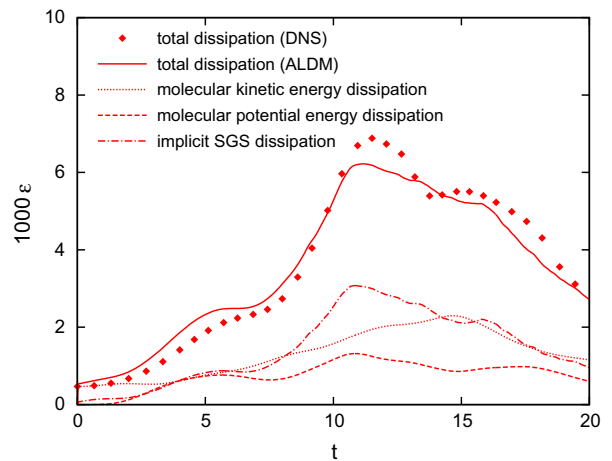
For DNS, the number of computational cells depends on the Reynolds number. We used 256^3 cells for $Re_0 = 800$, 512^3 cells for $Re_0 = 1600$, and 768^3 cells for $Re_0 = 3000$, to ensure proper representation of the smallest turbulence scales. With LES, the resolution is in principle Reynolds number independent. We used 64^3 cells for all LES.

The effect of a density stratification on turbulence is illustrated in Fig. 2, which shows a visualization of the turbulence structures approximately at the time of maximum dissipation. In a stratified medium, the coherent structures are larger and anisotropic and the shear rate magnitude is lower compared to neutral stratification.

The local Froude and Reynolds number in the TGV flow field are rapidly changing during the transition. To verify that the transition occurs in a relevant parameter space, we show the tracks of several
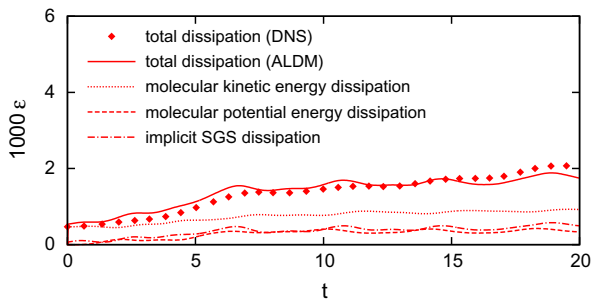
Fig. 7. Contributions to energy dissipation of the TGV ($Re_0 = 1600$, $Fr_0 = 0.5$).
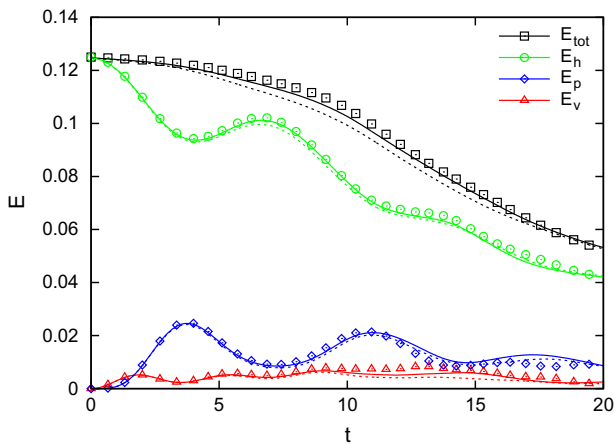

**Fig. 8.** Energy budget of the TGV ($Re_0 = 1600$, $Fr_0 = 1$); solid lines: ALDM, dashed lines: SSM.
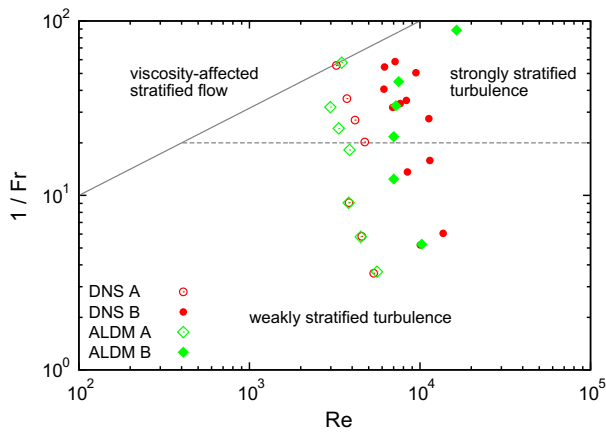
**Fig. 9.** Regime diagram for our simulations of stratified turbulence.

Fig. 10. Ratio of vertical to potential energy in HST as a function of local Froude number.
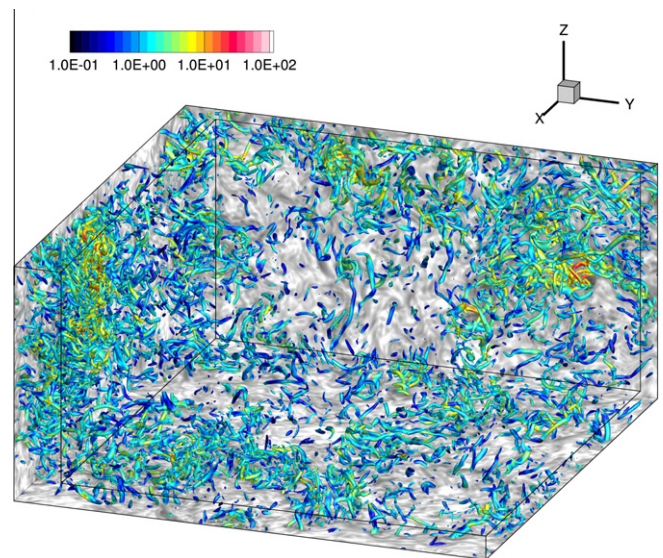
Fig. 11. DNS of neutrally stratified turbulence ($Re = 8440$). Iso-surface of Q, color of iso-surface and shading of domain faces by local molecular dissipation rate (normalized by the spatial average).

TGV simulations in Fig. 3. Indeed, most of the simulations are located in the regime of strongly stratified turbulence. Hence they are suitable for validation of an SGS model for stratified turbulence.

An LES must be able to correctly predict the temporal evolution of the total dissipation rate by modeling the effect of the small scale vortices on the larger scales. In Fig. 4, we show results for LES (64^3 cells) using ALDM as well as the SSM and DSM compared to DNS results (512^3 cells). The resolution of the LES can be characterized by comparing the grid size $\varDelta$ to the Kolmogorov length $\eta = \nu^{3/4}/\varepsilon_k^{1/4}$, computed from the corresponding DNS results. The maximum of the ratio $\varDelta/\eta$ is about 6.5 for the LES and correspond-

ingly about 0.8 for the DNS. Since the dependence of η on ε_k is weak, these numbers are basically the same for all turbulent cases. The LES predict the total dissipation very well, independent of the stratification. The differences between the results from ALDM, DSM and SSM are small, the best prediction being obtained with ALDM.

In Figs. 5–7, we show the contributions of molecular and implicit SGS dissipation to the total dissipation in LES with ALDM for three different intensities of stratification. The relative amount of implicit SGS dissipation decreases with increasing stratification, since the flow is better resolved in cases of strong stratification. For $Fr_0 = 2$ and $Fr_0 = 1$, the dissipation peaks are dominated by implicit SGS dissipation, which shows that the implicit model is automatically activated, when it is needed, and provides a good approximation of the unresolved stresses for different intensities of stratification.

The ratios of the different types of energy in the TGV vary throughout the temporal evolution. While initially there is only horizontal kinetic energy, at later times a certain fraction of this energy is converted to vertical kinetic energy as well as available potential energy. The energy budget for one representative case
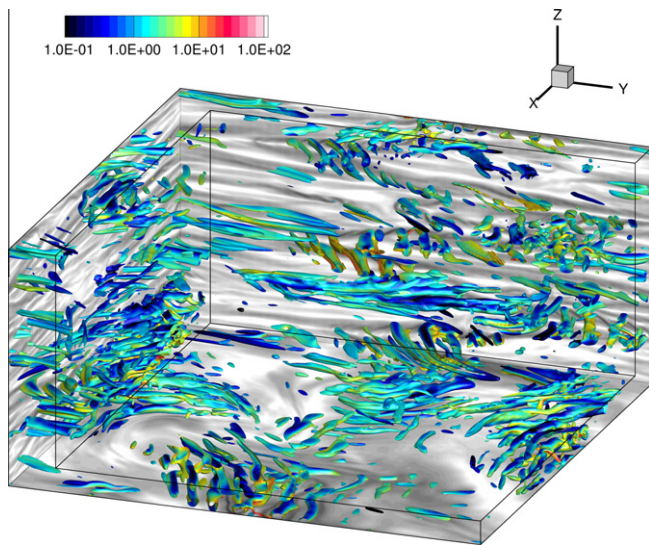
Fig. 12. DNS of strongly stratified turbulence (Re = 7110, Fr = 0.017). Coloring as in Fig. 11.

is shown in Fig. 8. Both LES, with implicit ALDM and with explicit SSM, predict the energy conversions with good accuracy. The best agreement is obtained for the horizontal kinetic energy component. The overall agreement with DNS data is slightly better if ALDM is used.

4.2. Homogeneous stratified turbulence (HST)

The second investigated test case is homogeneous stratified turbulence in a statistically steady state. The flow is maintained at an approximately constant energy level by a large scale vertically uniform forcing of the horizontal velocity components. This approach models the forcing by the synoptic scale flow in the atmosphere and was successfully applied by several authors before (Métais and Herring, 1989; Waite and Bartello, 2004; Lindborg, 2006).

We ran two series of DNS, series A with Re_0 = 6500 and series B with Re_0 = 13 000. The domain size was 320^3 cells for series A and 640^3 cells for series B. Within the single series, the Froude number was varied to cover different buoyancy Reynolds numbers. The basic domain size again was $2\pi\mathcal{L}$. For low Froude numbers, we used a flat domain with a height of only $\pi\mathcal{L}$, but keeping cubical cells. This is permitted since in stratified turbulence there is only a very small amount of energy contained in the large scale vertical modes.

The dimensional domain size can be computed from Eq. (3). If we, for example, assume a Brunt–Väisälä frequency of $N = 0.02 s^{-1}$ and a kinematic viscosity of $\nu = 1$ m^2/s (upper mesosphere), then we find dimensional domain sizes between 10 km and 40 km for the simulations of series B.

For both series, we performed LES, both with implicit ALDM and explicit SSM and DSM. For all these simulations, we used grid boxes with 64^3 cells. For the low Froude number simulations, the domain was flattened as well, leading to a doubled resolution in vertical direction. Fig. 9 shows the local Froude and Reynolds number of the simulations.
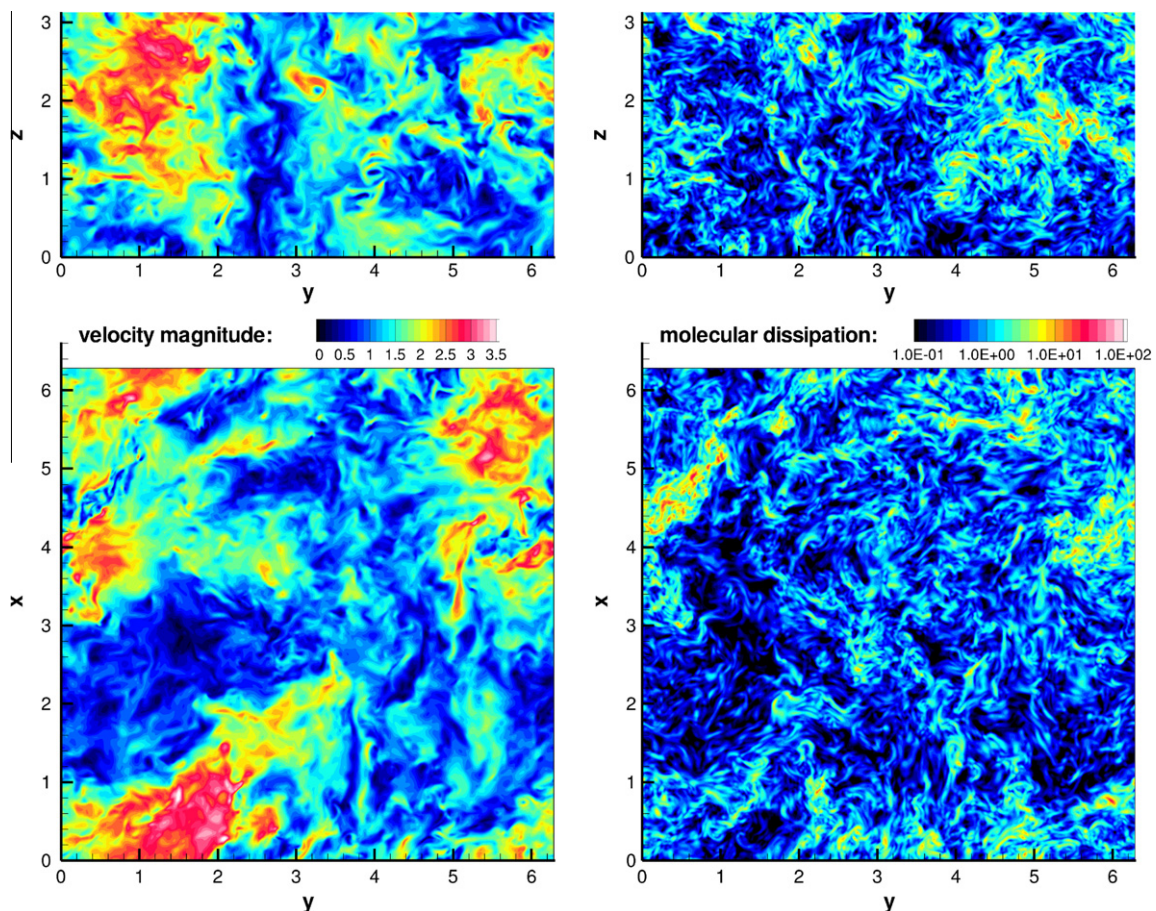
Fig. 13. Vertical ($x = 0$) and horizontal ($z = 2.4$) cuts through a DNS result of neutrally stratified turbulence. Left panels: velocity magnitude, right panels: molecular dissipation.
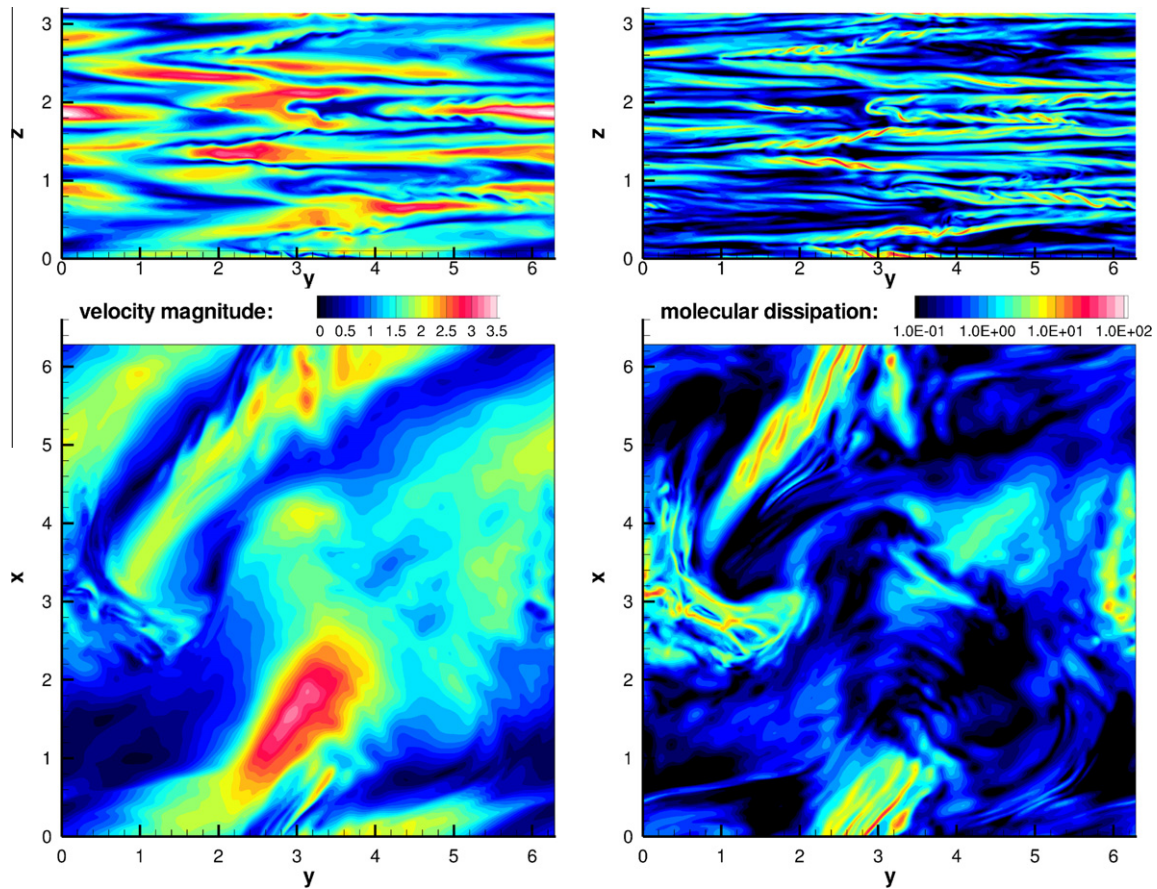
Fig. 14. Vertical ($x = 0$) and horizontal ($z = 0.1$) cuts through a DNS result of strongly stratified turbulence. Left panels: velocity magnitude, right panels: molecular dissipation.

Most important for the assessment of a parametrization scheme for stratified turbulence is its ability to correctly predict the amount of energy converted from horizontal kinetic energy to vertical kinetic energy and available potential energy before the energy is finally dissipated on the smallest represented scales. In Fig. 10, we show the ratio E_v/E_p as a function of local Froude number as predicted by DNS and LES with ALDM. The ratio E_v/E_p is not influenced by the forcing and can thus freely develop according to the dynamic interaction of convective, pressure and buoyancy term.

The vertical to potential energy ratio increases almost linearly with Froude number in the DNS. We find the same trend in our LES with ALDM. The agreement between DNS and LES is best in the region of high Froude numbers (weakly stratified turbulence), whereas for low Froude numbers the vertical kinetic energy is slightly underpredicted. Note that the difference between results from ALDM and SSM differ from each other most at the lowest Froude number. This is an indication for ALDM being better capable of handling the strong turbulence anisotropy in strongly stratified flows.

For a visual comparison of neutrally and stably stratified turbulence, we show the results of two computations from series B in Figs. 11 and 12. Both show snapshots of the developed turbulent flow at comparable Reynolds numbers. The turbulent structures are visualized by iso-surfaces of the Q-criterion (Hunt et al., 1988). For presentation purposes, the visualization includes only slices of finite thickness at the domain boundaries.

Fig. 11 shows a case with neutral stratification (Re = 8440). For better comparability with the stratified case, we show only the lower half of the cubical computational domain. The visualization shows that the turbulent structures have no preferred orientation. This proves that isotropic turbulence can be generated by the horizontal large-scale forcing that we used. Furthermore, we
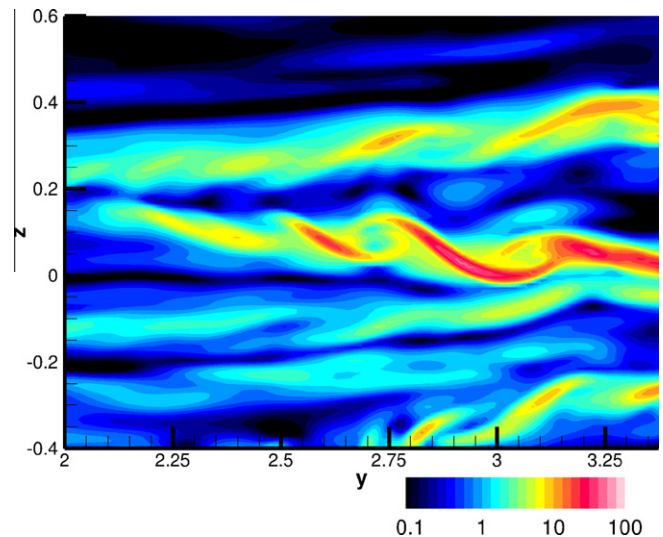

Fig. 15. Zoom into the vertical cut through a DNS result of strongly stratified turbulence (molecular dissipation).

observe a spatially intermittent field of turbulence which reflects the remaining large-scale anisotropy. There are regions of higher and lower density of turbulent vortices. The regions with strong turbulence activity are associated with much higher values of molecular dissipation rate. Note that the color scale of normalized dissipation rate is logarithmic. In the (rare) red[1] regions, the

---

[1] For interpretation of color in Figs. 1–18, the reader is referred to the web version of this article.
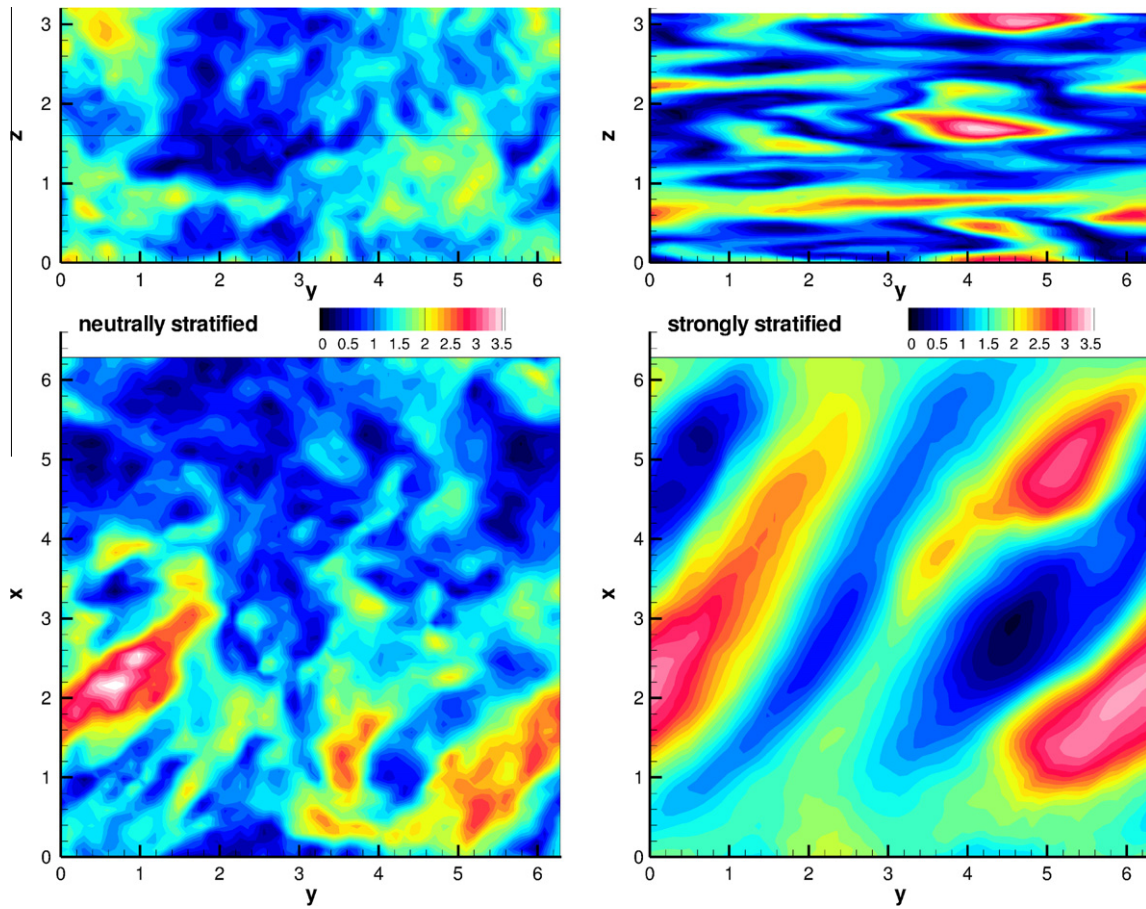
Fig. 16. Vertical ($x = 0$) and horizontal (left panel: $z = 1.6$, right panel: $z = 0.9$) cuts through ALDM results (velocity magnitude) of neutrally and strongly stratified turbulence.


(a) Horizontal spectra   (b) Vertical spectra
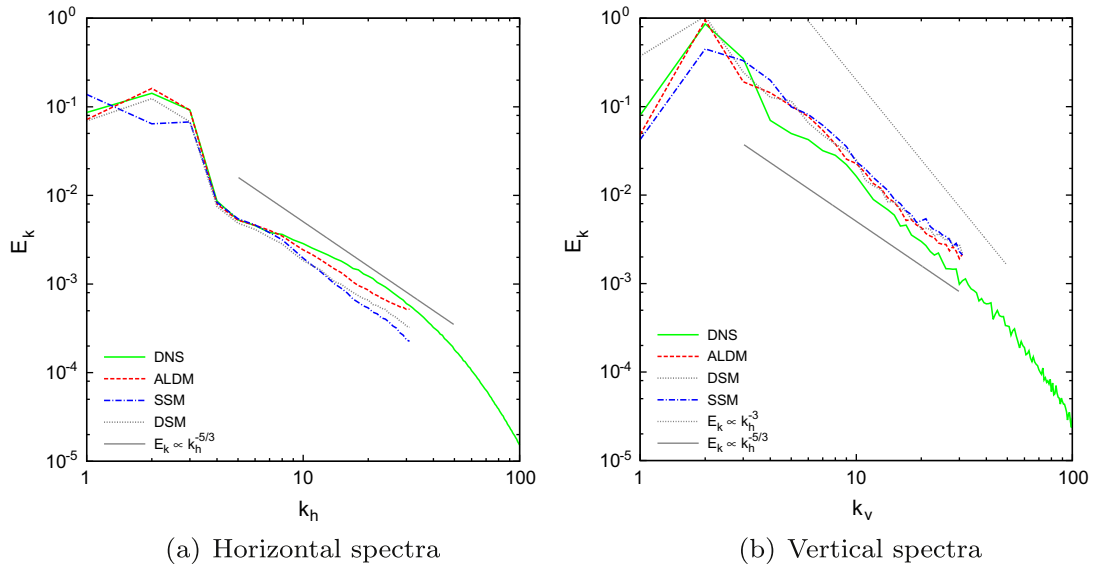
Fig. 17. Weakly stratified turbulence kinetic energy spectra ($\mathcal{R} = 41$).

dissipation rate is more than 30 times higher than the instantaneous spatial average in the whole domain.

In case of strongly stratified turbulence (Re = 7110, Fr = 0.017, $\mathcal{R} = 2.1$, cf. Fig. 12), the turbulence structures look completely different. Although Reynolds number and mean total energy dissipation are similar to the neutrally stratified case, the smallest eddies

are much larger. Additionally, all eddies are aligned horizontally. Despite the larger vortices, the molecular dissipation rates are comparable to the neutral case. This is due to the intensified shear between the horizontal layers.

We present vertical and horizontal cuts of the DNS domain in Figs. 13 and 14. In the neutrally stratified case, we can still see

(a) Horizontal spectra   (b) Vertical spectra
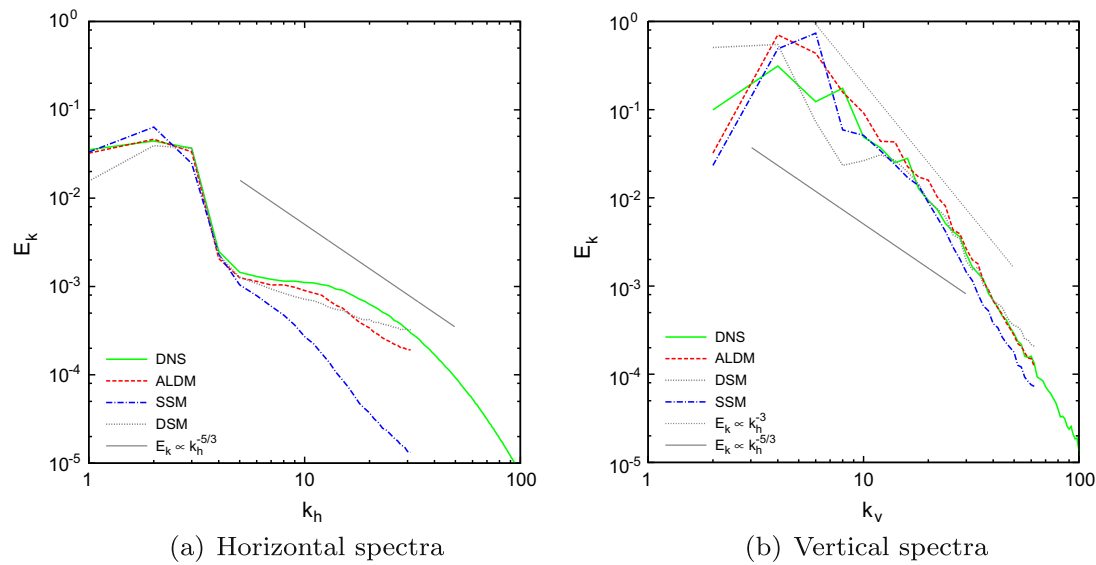
Fig. 18. Strongly stratified turbulence kinetic energy spectra ($\mathcal{R} = 6.3$).

the signature of the horizontal forcing in the velocity magnitude plots (left panels of Fig. 13). There are large-scale column-like regions of higher or lower velocity, superposed by a lot of small-scale variation. Apparently, this does not affect the behavior of the small scales. The signature of the column structures is missing in the contour plot of molecular dissipation (right panels). There is hardly any correlation between velocity magnitude and molecular dissipation. Small turbulence scales "forget" about the anisotropic large-scale forcing.

In case of strong stratification (Fig. 14), we find a strong horizontal layering, as described in many studies before. The flow is separated into thin layers of very different kinetic energy. The flow laminarization due to stratification reduces the amount of small-scale variations of velocity in horizontal planes compared to the neutrally stratified case. Neighboring layers can have strongly different (horizontal) velocities, which results in the formation of unstable shear layers. We observe a lot of Kelvin–Helmholtz-like structures all over the domain (cf. upper right panel of Fig. 14 and Fig. 15), which are responsible for the major part of energy dissipation. The signature of these Kelvin–Helmholtz layers can also be observed in the horizontal cut of the domain.

Many authors refer to the structures in stratified turbulence as "pancake" vortices. This popular image is used to describe large flat vortices rotating around a vertically oriented core. We observe large flat structures in the flow, but they are far from being coherent quasi-two-dimensional vortices. Instead, we find only very weak rotation around the vertical axis. The dominant turbulence structures are small-scale Kelvin–Helmholtz vortices, such as the ones shown in Fig. 15. These vortices are dominating the energy dissipation in the stratified turbulent flow. They appear in horizontal patches between two layers of strongly differing velocities, but their axis of rotation is basically horizontal. To stay within the culinary images, these vortices may better be described as "tagliatelle" rather than pancakes.

In Fig. 16 we present the contours of velocity magnitude for ALDM computations of the two cases presented before. The LES resolution was 64^3, so the total number of cells was three orders of magnitude lower than in the DNS. The global flow structure resembles well the DNS result, of course without the unresolved small scale content. In the strongly stratified case, we observe the same layering with large horizontal scales as in the DNS. Even the number and thickness of horizontal layers is similar. The major

difference between LES and DNS consists in the horizontal Kelvin–Helmholtz vortices. Their vertical extension, as found in the DNS, is of the same order of magnitude as the vertical resolution in the LES. Hence, they form a typical subgrid-scale problem and their dissipative effect is accounted for by the implicit turbulence model.

For comparison of kinetic energy spectra, we selected one DNS in the weakly stratified regime ($\mathcal{R} = 41$, Fr = 0.07, Re = 9300; cf. Fig. 17) and one DNS in the strongly stratified regime ($\mathcal{R} = 6.3$, Fr = 0.03, Re = 8300; cf. Fig. 18), both from series B. A more detailed analysis of these computations in spectral space is provided by Remmler and Hickel (in press). The corresponding LES have similar local Froude and Reynolds numbers.

In the horizontal spectra of kinetic energy, the differences between ALDM and the explicit SGS models are most obvious. In the weakly stratified case ($\mathcal{R} = 41$), the horizontal spectrum is still quite similar to the Kolmogorov spectrum of isotropic turbulence. In this case, all three SGS models predict the inertial range spectrum fairly well. The SSM and DSM are slightly too dissipative, but the difference to the DNS spectrum is acceptable. Things completely change for the stronger stratified case ($\mathcal{R} = 6.3$). The SSM dissipates too much energy and thus underpredicts the inertial range spectrum by more than one order of magnitude. Additionally, the predicted power-law exponent is significantly lower than $-5/3$. With the DSM, the overall prediction of the spectrum is much better than with the SSM, but the power-law exponent near the cut-off wavenumber is greater than $-5/3$. The spectrum predicted by ALDM agrees better with the DNS than results for both Smagorinsky models. Only ALDM correctly predicts the characteristic plateau region between the forcing scales and the inertial scales. Moreover, ALDM produces a power-law decay with an exponent of $-5/3$, corresponding to the DNS and theory derived from scaling laws (Brethouwer et al., 2007).

We note that the dynamic model coefficient in the DSM is approximately constant in time as soon as the statistically steady state is reached. The dynamic procedure is efficient in choosing a proper coefficient depending on the strength of the stratification, but cannot cure the more structural weakness of the isotropic eddy viscosity approach.

In the vertical spectra of kinetic energy, the inertial range decay exponent changes from $-5/3$ in neutrally stratified fluid to -3 in strongly stratified turbulence. We find this change in the DNS and it is well reproduced by the LES. All three SGS models predict

the turbulence inertial range decay well. At strong stratification, the ALDM result perfectly agrees with the DNS. The SSM result is slightly too dissipative in this region.

5. Conclusion

We presented a numerical investigation of turbulence in a stably stratified fluid to proof the reliability of implicit turbulence modeling with the Adaptive Local Deconvolution Method (ALDM). As benchmark results, we used high resolution DNS data and LES results obtained with an explicit standard (SSM) Smagorinsky model and a dynamic Smagorinsky model (DSM). The investigated test cases were the transition of the three-dimensional Taylor–Green vortex (TGV) and horizontally forced homogeneous stratified turbulence (HST). In most simulations, the buoyancy Reynolds number was larger than unity. The Froude and Reynolds number were chosen to cover the complete range from isotropic Kolmogorov turbulence up to strongly stratified turbulence.

For the transition of the TGV, we found good agreement between ALDM results and DNS in neutrally and stably stratified fluid. With ALDM, we generally obtained similar or better predictions of energy dissipation rates than with both explicit models. ALDM also predicts the ratio of vertical and horizontal kinetic energy much better than the SSM and the DSM. This demonstrates the ability of the implicit turbulence model ALDM to properly represent the effect of the SGS stresses in a transitional stratified flow.

We analyzed results from DNS of homogeneous turbulence with and without stable stratification. As in previous studies, we found a strong horizontal layering in the strongly stratified cases. Energy dissipation is concentrated within thin layers of Kelvin–Helmholtz vortices. Although these dominant vortices are not resolved in the LES, the LES results (with ALDM) agree well with the reference DNS, both in integral flow properties and energy spectra. This applies to the whole Froude number range from infinity down to very low values. Especially in the strongly stratified regime, ALDM performs better than the SSM. While the SSM is far too dissipative in this case, ALDM spectra agree very well with the reference DNS. With the DSM, the excessive dissipation of the SSM can be avoided, but the spectral slope near the cut-off wavenumber is still not correct. Among the investigated SGS models, only ALDM predicted the correct exponent of $-5/3$.

The results presented here were obtained without recalibrating the ALDM model constants for stratified turbulence. The good agreement with DNS data shows the ability of ALDM to automatically adapt to strongly anisotropic turbulence. Within the continuation of the project, we will investigate to which extend the results can be further improved by a recalibration of the model coefficients for stratified turbulence. But even without this possible improvements, ALDM provides a suitable parametrization of geophysical turbulence. After having applied ALDM successfully to rather simple model flows, we will continue working on more complex geophysical problems.

Acknowledgements

References

Armenio, V., Sarkar, S., 2002. An investigation of stably stratified turbulent channel flow using large-eddy simulation. J. Fluid Mech. 459, 1–42.

Basu, S., Porté-Agel, F., 2006. Large-eddy simulation of stably stratified atmospheric boundary layer turbulence: a scale-dependent dynamic modeling approach. J. Atmos. Sci. 63 (8), 2074–2091.

Bouruet-Aubertot, P., Sommeria, J., Staquet, C., 1996. Stratified turbulence produced by internal wave breaking: two-dimensional numerical experiments. Dyn. Atmos. Oceans 23 (1–4), 357–369 (stratified flow).

Brachet, M.E., Meiron, D., Orszag, S., Nickel, B., Morf, R., Frisch, U., 1983. Small-scale structure of the Taylor–Green vortex. J. Fluid Mech. 130, 411–452.

Brethouwer, G., Billant, P., Lindborg, E., Chomaz, J.-M., 2007. Scaling analysis and simulation of strongly stratified turbulent flows. J. Fluid Mech. 585, 343–368.

Clark, R.A., Ferziger, J.H., Reynolds, W.C., 1979. Evaluation of subgrid-scale models using an accurately simulated turbulent flow. J. Fluid Mech. 91 (01), 1–16.

Cot, C., 2001. Equatorial mesoscale wind and temperature fluctuations in the lower atmosphere. J. Geophys. Res. 106 (D2), 1523–1532.

Dewan, E.M., 1979. Stratospheric wave spectra resembling turbulence. Science 204 (4395), 832–835.

Domaradzki, J.A., Adams, N.A., 2002. Direct modelling of subgrid scales of turbulence in large eddy simulations. J. Turb. 3, 24.

Dörnbrack, A., 1998. Turbulent mixing by breaking gravity waves. J. Fluid Mech. 375, 113–141.

Fritts, D.C., Wang, L., Werne, J., Lund, T., Wan, K., 2009. Gravity wave instability dynamics at high reynolds numbers. Part I: wave field evolution at large amplitudes and high frequencies. J. Atmos. Sci. 66 (5), 1126–1148.

Gage, K.S., 1979. Evidence for a $k^{-5/3}$ law inertial range in mesoscale two-dimensional turbulence. J. Atmos. Sci. 36, 1950–1954.

Germano, M., Piomelli, U., Moin, P., Cabot, W.H., 1991. A dynamic subgrid-scale eddy viscosity model. Phys. Fluids A 3 (7), 1760–1765.

Grilli, M., Schmid, P.J., Hickel, S., Adams, N.A., in press. Analysis of unsteady behaviour in shockwave turbulent boundary layer interaction. J. Fluid Mech., doi:http://dx.doi.org/10.1017/jfm.2012.37.

Harten, A., Engquist, B., Osher, S., Chakravarthy, S.R., 1987. Uniformly high order accurate essentially non-oscillatory schemes, III. J. Comput. Phys. 71 (2), 231–303.

Herring, J.R., Métais, O., 1989. Numerical experiments in forced stably stratified turbulence. J. Fluid Mech. 202 (1), 97–115.

Hickel, S., Adams, N.A., 2007. On implicit subgrid-scale modeling in wall-bounded flows. Phys. Fluids 19, 105106.

Hickel, S., Adams, N.A., 2008. Implicit les applied to zero-pressure-gradient and adverse-pressure-gradient boundary-layer turbulence. Int. J. Heat Fluid Flow 29, 626–639.

Hickel, S., Adams, N.A., Domaradzki, J.A., 2006. An adaptive local deconvolution method for implicit LES. J. Comput. Phys. 213, 413–436.

Hickel, S., Adams, N.A., Mansour, N.N., 2007. Implicit subgrid-scale modeling for large-eddy simulation of passive scalar mixing. Phys. Fluids 19, 095102.

Hickel, S., Kempe, T., Adams, N.A., 2008. Implicit large-eddy simulation applied to turbulent channel flow with periodic constrictions. Theor. Comput. Fluid Dynam. 22, 227–242.

Hunt, J.C.R., Wray, A.A., Moin, P., 1988. Eddies, streams, and convergence zones in turbulent flows, 193–208.

Kaltenbach, H.-J., Gerz, T., Schumann, U., 1994. Large-eddy simulation of homogeneous turbulence and diffusion in stably stratified shear flow. J. Fluid Mech. 280 (1), 1–40.

Kraichnan, R.H., 1967. Inertial ranges in two-dimensional turbulence. Phys. Fluids 10 (7), 1417–1423.

Laval, J.-P., McWilliams, J.C., Dubrulle, B., 2003. Forced stratified turbulence: successive transitions with Reynolds number. Phys. Rev. E 68 (3), 036308.

Lilly, D.K., 1967. The representation of small scale turbulence in numerical simulation experiments. In: IBM Scientific Computing Symposium on Environmental Sciences, pp. 195–210.

Lilly, D.K., 1983. Stratified turbulence and the mesoscale variability of the atmosphere. J. Atmos. Sci. 40 (3), 749–761.

Lilly, D.K., Bassett, G., Droegemeier, K., Bartello, P., 1998. Stratified turbulence in the atmospheric mesoscales. Theor. Comput. Fluid Dynam. 11, 139–153.

Lindborg, E., 2006. The energy cascade in a strongly stratified fluid. J. Fluid Mech. 550 (1), 207–242.

Métais, O., Herring, J.R., 1989. Numerical simulations of freely evolving turbulence in stably stratified fluids. J. Fluid Mech. 202 (1), 117–148.

Métais, O., Lesieur, M., 1992. Spectral large-eddy simulation of isotropic and stably stratified turbulence. J. Fluid Mech. 239, 157–194.

Nastrom, G.D., Gage, K.S., 1985. A climatology of atmospheric wavenumber spectra of wind and temperature observed by commercial aircraft. J. Atmos. Sci. 42 (9), 950–960.

Remmler, S., Hickel, S., in press. Spectral structure of stratified turbulence: Direct numerical simulations and predictions by large eddy simulation. Theor. Comput. Fluid Dynam., doi:http://dx.doi.org/10.1007/s00162-012-0259-9.

Riley, J.J., de Bruyn Kops, S.M., 2003. Dynamics of turbulence strongly influenced by buoyancy. Phys. Fluids 15 (7), 2047–2059.

Shu, C.-W., 1988. Total-variation-diminishing time discretizations. SIAM J. Sci. Stat. Comput. 9 (6), 1073–1084.

Smagorinsky, J., 1963. General circulation experiments with the primitive equations. I: the basic experiment. Mon. Wea. Rev. 91, 99–164.

Smith, L.M., Waleffe, F., 2002. Generation of slow large scales in forced rotating stratified turbulence. J. Fluid Mech. 451 (1), 145–168.

Staquet, C., Godeferd, F.S., 1998. Statistical modelling and direct numerical simulations of decaying stably stratified turbulence. Part 1. Flow energetics. J. Fluid Mech. 360, 295–340.

Taylor, J.R., Sarkar, S., Armenio, V., 2005. Large eddy simulation of stably stratified open channel flow. Phys. Fluids 17 (11), 116602.

van der Vorst, H.A., 1992. Bi-CGSTAB: a fast and smoothly converging variant of Bi-CG for the solution of nonsymmetric linear systems. SIAM J. Sci. Stat. Comput. 13 (2), 631–644.

van Zandt, T.E., 1982. A universal spectrum of buoyancy waves in the atmosphere. Geophys. Res. Lett. 9 (5), 575–578.

Waite, M.L., Bartello, P., 2004. Stratified turbulence dominated by vortical motion. J. Fluid Mech. 517, 281–308.

ORIGINAL ARTICLE

Sebastian Remmler · Stefan Hickel

Spectral structure of stratified turbulence: direct numerical simulations and predictions by large eddy simulation

Abstract Density stratification has a strong impact on turbulence in geophysical flows. Stratification changes the spatial turbulence spectrum and the energy transport and conversion within the spectrum. We analyze these effects based on a series of direct numerical simulations (DNS) of stratified turbulence. To facilitate simulations of real-world problems, which are usually beyond the reach of DNS, we propose a subgrid-scale turbulence model for large eddy simulations of stratified flows based on the Adaptive Local Deconvolution Method (ALDM). Flow spectra and integral quantities predicted by ALDM are in excellent agreement with direct numerical simulation. ALDM automatically adapts to strongly anisotropic turbulence and is thus a suitable tool for studying turbulent flow phenomena in atmosphere and ocean.

Keywords Stratified turbulence · Direct numerical simulation · Large eddy simulation · Subgrid-scale modeling

1 Introduction

Density stratification is a common situation in geophysical fluid flows that affects turbulence strongly. Stratification suppresses vertical motions typically leading to a k_v^{-3} scaling of the vertical turbulence kinetic energy spectrum, while the horizontal spectrum shows a $k_h^{-5/3}$ inertial range. These different scaling laws render all scales of the velocity field strongly anisotropic, which poses a true challenge for turbulence models and parameterizations.

The horizontal velocity spectrum in the atmosphere was analyzed by Nastrom and Gage [31] using aircraft observations. They found a power-law behavior in the mesoscale range with an exponent of $-5/3$. There has been a long an intensive discussion whether this spectrum is due to a backward cascade of energy [13,16,26] as it is known for two-dimensional turbulence [24], or due to intermittent breaking of internal waves [7,8,36] and thus a forward cascade of energy. In different numerical and theoretical studies, ambiguous or even conflicting results were obtained [27]. Despite this discussion about its origin, the inertial range itself with an exponent of $-5/3$ in the horizontal spectrum has been confirmed by most authors.

During the last decade, a number of new simulations [25,33,38] suggested that the character of the flow depends on the Reynolds number. High Reynolds numbers are associated with stronger three-dimensionality and a forward cascade of energy. Lindborg [28] presented a scaling analysis of the Boussinesq

S. Remmler (✉) · S. Hickel
Institute of Aerodynamics and Fluid Mechanics, Technische Universität München, 85747 Garching bei München, Germany
E-mail: remmler@tum.de

S. Hickel
E-mail: sh@tum.de

equations for low Froude and high Reynolds number. His theory of strongly anisotropic, but still three-dimensional, turbulence explains the horizontal $k_h^{-5/3}$-spectrum as well as the vertical k_v^{-3}-spectrum observed by Cot [6]. On the basis of these findings, Brethouwer et al. [5] showed that the relevant non-dimensional parameter for stratified turbulence is the buoyancy Reynolds number $\mathcal{R} = Fr^2 Re$. For $\mathcal{R} \gg 1$, they predict stratified turbulence including local overturning and a forward energy cascade. In the opposite limit, for $\mathcal{R} \ll 1$, the flow is controlled by viscosity and does not contain small-scale turbulent motions.

Since a full resolution of all turbulence scales is only possible for very low Reynolds numbers, many groups resorted to large eddy simulations (LES) and used subgrid-scale (SGS) models in their computations. For example, Métais and Lesieur [30] used a spectral eddy viscosity model, based on the eddy-damped quasi-normal Markovian (EDQNM) theory. This required a flow simulation in Fourier space and the cut-off wavenumber to be in the inertial range. For classical LES in physical space, Smagorinsky models are widely used, either in the classical formulation [22] or with certain modifications for stratified turbulence based on the local Richardson number [11]. Staquet and Godeferd [35] presented a two-point closure statistical EDQNM turbulence model, which was adapted for axisymmetric spectra about the vertical axis. Recently, many groups presented regularized direct numerical simulations (DNS) of stratified turbulence, which means rather pragmatically stabilizing under-resolved DNS by removing the smallest resolved scales. This is often achieved by a hyperviscosity approach [28,29], which is frequently combined with rigorous de-aliasing in spectral methods using the 2/3-rule [4,12], or by explicit spectral filtering [9].

All explicit SGS turbulence closures for LES suffer from the problem that the computed SGS stresses are of the same order as the grid truncation error. This interference between SGS model and numerical scheme may lead to computational instability and a lack of grid convergence. A possible solution for this issue is a combination of discretization scheme and SGS model in a unified framework. Such approaches are usually referred to as "implicit" LES (ILES) in contrast to the traditional "explicit" SGS models. ILES methods are particularly appealing for the simulation of stratified flows, where the fundamental assumptions of conventional eddy viscosity-based turbulence models may not hold. Several approaches to ILES have been developed in the past, which led to a comprehensive textbook edited by Grinstein et al. [14]. First indications that the truncation error of linear upwind schemes in some cases may function as an implicit SGS model so that no explicit SGS model has to be added to the discretized flow equations were reported by Kawamura and Kuwahara [23]. The use of nonlinearly stable higher-order schemes (i.e., monotonic, monotonicity preserving, or total variation diminishing methods) for so-called Monotonically Integrated LES (MILES) has been proposed by Boris et al. [3]. Particularly noteworthy is the Multidimensional Positive Definite Advection Transport Algorithm (MPDATA) of Smolarkiewicz and Margolin [34], which has been applied widely to geophysical flows. However, when using nonlinearly stable schemes for ILES, one must be aware that most previously proposed methods only guarantee numerical stability, which is necessary, but not sufficient for the physically correct dynamics of the resolved scales. Employing implicit LES for predictive science requires that not only mathematical but also physical constraints have to be incorporated into the design of an implicit SGS model. The first ILES method which is not only based on numerical considerations but also involves physical constraints is the Adaptive Local Deconvolution Method (ALDM) for incompressible neutrally stratified fluids presented by Hickel et al. [19]. Based on this method and ALDM for passive scalar transport [20], we developed an implicit SGS model for Boussinesq fluids.

So far most numerical and experimental studies of stratified turbulence were concentrating on the purely horizontal or vertical spectra of turbulence. In the first part of the present study, we will extend this work and discuss the spatial structure of the turbulence energy spectrum. We shall show how stratification changes the shape of the spectrum with respect to the spherically symmetric spectrum known from isotropic turbulence. Stratified turbulence is called "pancake-turbulence" by several authors, because of the large horizontal and small vertical extension of flow structures in physical space. We will demonstrate how this translates into spectral space as well. Furthermore, we will analyze the contributions of the different terms in the energy transport equation on the total spectral energy balance. This will enable us to follow the flow energy from its injection into the flow through all transport and conversion mechanisms eventually to molecular dissipation.

Based on this detailed analysis of homogeneous stratified turbulence by direct numerical simulation, we will assess the applicability of the implicit SGS model ALDM to this type of flow in the second part of the paper. The comparison of spectra from ALDM simulations with results of DNS and of the standard Smagorinsky model (SSM) will be part of this analysis.

2 Governing equations

The non-dimensional Boussinesq equations for a stably stratified fluid in Cartesian coordinates read

$$\nabla \cdot \mathbf{u} = 0 \tag{1a}$$

$$\partial_t \mathbf{u} + \nabla \cdot (\mathbf{uu}) = -\nabla p - \frac{\rho}{Fr_0^2} \mathbf{e}_z + \frac{1}{Re_0} \nabla^2 \mathbf{u} \tag{1b}$$

$$\partial_t \rho + \nabla \cdot (\rho \mathbf{u}) = \mathbf{u} e_z + \frac{1}{Pr \, Re_0} \nabla^2 \rho \tag{1c}$$

where velocities are made non-dimensional by $\mathcal{U}$, all spatial coordinates by the length scale $\mathcal{L}$, pressure by $\mathcal{U}^2$, time by $\mathcal{L}/\mathcal{U}$, and density fluctuation $\rho = \rho^* - \overline{\rho}$ (ρ^*: local absolute density, $\overline{\rho}$: background density) by the background density gradient $\mathcal{L}|\mathrm{d}\overline{\rho}/\mathrm{d}z|$. The vertical unit vector is $\mathbf{e}_z$. The non-dimensional parameters are

$$Fr_0 = \frac{\mathcal{U}}{N\mathcal{L}}, \quad Re_0 = \frac{\mathcal{U}\mathcal{L}}{\nu}, \quad Pr = \frac{\nu}{\mu} \tag{2}$$

We chose a Prandtl number of $Pr = 0.7$, corresponding to typical values in the atmosphere. Froude and Reynolds number are parameters that control the flow regime.

Without loss of generality, we assume that all mean velocity components are zero (Galilean invariance) and define the turbulence kinetic energy

$$E_k = \frac{1}{2} u_i u_i \tag{3}$$

and the available potential energy

$$E_p = \frac{1}{2} \rho^2 / Fr_0^2. \tag{4}$$

The transport equations for the turbulence kinetic and the potential energy read

$$\partial_t E_k + \nabla \cdot (\mathbf{u} E_k) = \underbrace{-\mathbf{u} \cdot \nabla p}_{-\mathcal{T}} \underbrace{-\frac{\rho}{Fr_0^2} \mathbf{u} \cdot \mathbf{e}_z}_{\mathcal{P}} + \underbrace{\frac{1}{Re_0} \left[\nabla^2 E_k + (\nabla \mathbf{u})^2 \right]}_{\mathcal{D}} + \underbrace{\mathbf{F}}_{\mathcal{F}} \tag{5a}$$

$$\partial_t E_p + \nabla \cdot (\mathbf{u} E_p) = \underbrace{\frac{\rho}{Fr_0^2} \mathbf{u} \cdot \mathbf{e}_z}_{\mathcal{B}} + \underbrace{\frac{1}{Pr \, Re_0} \left[\nabla^2 E_p + \frac{(\nabla \rho)^2}{Fr_0^2} \right]}_{\mathcal{D}} \tag{5b}$$

where the single terms represent turbulent diffusion $\mathcal{T}$ (advection by turbulent velocity), pressure transport $\mathcal{P}$, buoyancy transport $\mathcal{B}$, molecular dissipation and diffusion $\mathcal{D}$, and external forces $\mathcal{F}$.

Our results will be presented in spectral space. The spectral kinetic energy density is defined as

$$\widehat{E_k} = \frac{1}{2} \widehat{u_i} \widehat{u_i}^*, \tag{6}$$

where $\widehat{u_i}$ are the Fourier-transformed velocity components and the asterisk $(\cdot)^*$ denotes the complex conjugate. The temporal rate of change of kinetic energy in spectral space is computed from

$$\widehat{\partial_t E_k} = \frac{1}{2} \left(\widehat{u_i} \widehat{\partial_t u_i}^* + \widehat{u_i}^* \widehat{\partial_t u_i} \right) = \widehat{\mathcal{T}}(E_k) + \widehat{\mathcal{P}}(E_k) + \widehat{\mathcal{B}}(E_k) + \widehat{\mathcal{D}}(E_k) + \widehat{\mathcal{F}}(E_k) \tag{7}$$

For evaluating the terms $\widehat{\mathcal{T}}$, $\widehat{\mathcal{P}}$, $\widehat{\mathcal{B}}$, $\widehat{\mathcal{D}}$, and $\widehat{\mathcal{F}}$, we use the respective term of the discretized transport equation to replace $\widehat{\partial_t u_i}$. The spectral buoyancy transport of kinetic energy, for example, is computed from

$$\widehat{\mathcal{B}}(E_k) = -\frac{\mathbf{e}_z}{2Fr_0^2} \cdot \left(\widehat{\mathbf{u}} \widehat{\rho}^* + \widehat{\mathbf{u}}^* \widehat{\rho} \right). \tag{8}$$

The spectral distribution of potential energy and its temporal derivative are defined accordingly.

With the spatial mean values of kinetic energy $\langle E_k \rangle$ and kinetic energy dissipation $\varepsilon_k = \langle \mathcal{D}(E_k) \rangle$, we define the integral flow scales

$$U_{\text{int}} = \langle E_k \rangle^{1/2} \,, \quad L_{\text{int}} = \frac{\langle E_k \rangle^{3/2}}{\varepsilon_k} \tag{9}$$

to find the local Froude and Reynolds number as well as the buoyancy Reynolds number $\mathcal{R}$, defined by Brethouwer et al. [5]:

$$Fr = \frac{Fr_0 \mathcal{L}}{\mathcal{U}} \frac{\varepsilon_k}{\langle E_k \rangle} \,, \quad Re = \frac{Re_0}{\mathcal{U}\mathcal{L}} \frac{\langle E_k \rangle^2}{\varepsilon_k} \,, \quad \mathcal{R} = Re \, Fr^2 = Re_0 \, Fr_0^2 \, \varepsilon_k \frac{\mathcal{L}}{\mathcal{U}^3} \tag{10}$$

In LES by construction, we do not have direct access to the values of ε_k and $\varepsilon_p = \langle \mathcal{D}(E_p) \rangle$, as they are unresolved small-scale quantities. For LES, we thus estimate ε_k from the total energy balance

$$\partial_t \langle E_t \rangle = \partial_t \langle E_k \rangle + \partial_t \langle E_p \rangle = P - \varepsilon_k - \varepsilon_p = P - (1 + \Gamma)\varepsilon_k, \tag{11}$$

where the temporal change of total energy in the flow $\langle E_t \rangle$ can be computed from the energy levels at subsequent time steps, P is the power inserted into the system by the external forcing and $\Gamma = \varepsilon_p / \varepsilon_k$ is the mixing ratio assumed to be constant $\Gamma = 0.4$, which is an acceptable approximation for a wide range of parameters (cp. our DNS results, Fig. 2).

3 Numerical method

3.1 The adaptive local deconvolution method

Our approach to ILES is based on a nonlinear finite volume scheme involving a solution adaptive reconstruction (deconvolution) of the numerical solution. The nonlinear discretization scheme generates a certain controllable spectral numerical viscosity. Using an evolutionary optimization algorithm, free parameters of the discretization scheme have been calibrated in such a way that the effective spectral numerical viscosity is identical to the spectral eddy viscosity from turbulence theory for asymptotic cases [19]. In the following, we give a concise description of ALDM on the example of a one-dimensional generic transport equation

$$\partial_t u + \partial_x F(u) = 0. \tag{12}$$

For a more detailed description and the extension to the three-dimensional Navier-Stokes equations, we refer to Hickel et al. [19].

We obtain the discretized form of Eq. 12 by a convolution with a homogeneous filter kernel G and a subsequent discretization of the filtered equations

$$\partial_t \overline{u}_N + G * \partial_x F_N(u_N) = -G * \partial_x \cdot \tau_{\text{sgs}} = \mathcal{G}_{\text{sgs}}, \tag{13}$$

where the overbar indicates spatial filtering and the subscript N denotes the discretized solution on a numerical grid. In Eq. 13 we use the unfiltered solution to compute the nonlinear term, which requires the deconvolution of the solution on the range of represented scales $u_N = G^{-1} * \overline{u}_N$.

The truncation error of a numerical reconstruction scheme can be written as

$$\mathcal{G}_{\text{num}} = G * \partial_x F_N(u_N) - \tilde{G} * \tilde{\partial}_x \tilde{F}_N(\tilde{u}_N), \tag{14}$$

where the tilde indicates discrete numerical approximations. While the exact continuous solution u is unknown, we can obtain the numerical approximation $\tilde{u}_N$ of the grid function u_N by a regularized deconvolution of $\overline{u}_N$ [10]. The discrete filtered solution of our numerical method then satisfies the modified differential equation

$$\partial_t \overline{u}_N + G * \partial_x F_N(u_N) = \mathcal{G}_{\text{num}} + \tilde{\mathcal{G}}_{\text{sgs}}, \tag{15}$$

which is identical to Eq. 13 if $\mathcal{G}_{\text{num}} + \tilde{\mathcal{G}}_{\text{sgs}} = \mathcal{G}_{\text{sgs}}$. Explicit SGS modeling is based on the assumption $\mathcal{G}_{\text{num}} = 0$. In implicit LES, the numerical error acts as an implicit SGS model: $\mathcal{G}_{\text{num}} = \mathcal{G}_{\text{sgs}}$ and no explicit SGS model is used, i.e., $\tilde{\mathcal{G}}_{\text{sgs}} = 0$. The transport equation eventually to be solved is

$$\partial_t \overline{u}_N + \tilde{G} * \tilde{\partial}_x \tilde{F}_N(\tilde{u}_N) = 0, \tag{16}$$

where no model terms are computed explicitly.

Finite volume methods such as ALDM require a local approximation of the unfiltered solution at the cell faces (indicated by half-integer indices), which we find by a nonlinear combination

$$\tilde{u}_N^{\mp}(x_{j\pm1/2}) = \sum_{k=1}^{K} \sum_{r=0}^{k-1} \omega_{k,r}^{\mp}(\overline{u}_N) \tilde{p}_{k,r}^{\mp}(x_{j\pm1/2}) \tag{17}$$

of Harten-type polynomials [15]

$$\tilde{p}_{k,r}^{\mp}(x_{j\pm1/2}) = \sum_{l=0}^{k-1} c_{k,r,l}^{\mp}(x_N) \overline{u}_{j-r+l}. \tag{18}$$

The deconvolution is solution adaptive by weighting the contributions of the different polynomials by the coefficients $\omega_{k,r}^{\mp}(\overline{u}_N)$, which represent the smoothness of the solution $\overline{u}_N$, see [19]. The grid-dependent coefficients $c_{k,r,l}^{\mp}(x_N)$ are chosen such that the polynomial $\tilde{p}_{k,r}^{\mp}(j \pm 1/2)$ is a k-th order approximation of the unfiltered solution. The reconstructed solution $\tilde{u}_N^{\mp}$ is used in a consistent numerical flux function

$$\tilde{F}_N(x_{j\pm1/2}) = F\left(\frac{\tilde{u}_{j\pm1/2}^- + \tilde{u}_{j\pm1/2}^+}{2}\right) - \sigma_{j\pm1/2}\left(\tilde{u}_{j\pm1/2}^+ - \tilde{u}_{j\pm1/2}^-\right). \tag{19}$$

Both the reconstruction scheme and the flux function introduce free parameters, which can be used to control the truncation error. Our objective is not a maximum order of accuracy but a physically correct representation of the effects of unresolved turbulence. For this purpose, Hickel et al. [19] performed a spectral space analysis of the effective viscosity of ALDM. They optimized the free parameters such that the spectral numerical viscosity of ALDM matches the spectral eddy viscosity from the eddy-damped quasi-normal Markovian (EDQNM) theory for isotropic turbulence. This single set of parameters has not been changed since it was once settled and is also used for the computations we are presenting here. Although optimized for the asymptotic case of isotropic turbulence, ALDM has proven to yield good results for a large variety of complex turbulent flows. This includes decaying turbulence [19], boundary layer flows [17,18], separated flows [21], and others. ALDM yields good results also for cases of anisotropic and inhomogeneous turbulence.

Hickel et al. [20] extended ALDM to the transport of passive scalars. This basically employs the same framework, but a distinction is made between two different regimes depending on the Schmidt number. For high Schmidt numbers Sc $\gg$ 1, the passive scalar spectrum has two distinct inertial ranges, which is taken into account by using a different set of optimized model parameters. For the case Sc $\lesssim$ 1, which applies to the present simulations, the spectra of turbulence kinetic and potential energy are similar and thus the same set of parameters can be used for momentum and scalar transport equations. We adopted this implicit SGS model for passive scalar transport for the active scalar equation. This is possible since the feedback from the density field onto the velocity field does not originate from a nonlinear term but from the linear buoyancy term.

In the original formulation, Hickel et al. [20] used the reconstructed velocity field $\tilde{u}$ to compute the numerical flux function for the scalar transport. Since the reconstructed velocity $\tilde{u}$ is in general not divergence-free, an additional divergence correction term is necessary to avoid the generation of artificial fluctuations in a uniform scalar field. In the present implementation, we avoid this difficulty by using the filtered (defined on a staggered Cartesian mesh and therefore divergence-free) velocity field $\overline{u}_N$ for the transport velocity in the scalar flux. The numerical flux function in the scalar transport equation then reads

$$\tilde{F}_{j\pm1/2}^s = \overline{u}_{j-1/2\pm1/2} \frac{\tilde{c}_{j\pm1/2}^- + \tilde{c}_{j\pm1/2}^+}{2} - \sigma_C \left|\tilde{u}_{j\pm1/2}^- - \tilde{u}_{j-1\pm1/2}^+\right| \left(\tilde{c}_{j\pm1/2}^+ - \tilde{c}_{j\pm1/2}^-\right). \tag{20}$$

This modified numerical flux function has been tested against the original implementation for neutrally and stably stratified turbulence. As there was no recognizable effect on the flow energy spectra, we used the simplified formulation throughout the present study.

3.2 Computational details

With our flow solver INCA, the Boussinesq equations are discretized by a fractional step method on a staggered Cartesian mesh. The code is parallelized both for shared and distributed memory systems and it offers different discretization schemes depending on the application. For time advancement, the explicit third-order Runge-Kutta scheme of Shu [32] is used. The time step is dynamically adapted to satisfy a Courant-Friedrichs-Lewy condition with CFL = 1.0. The spatial discretization is a finite volume method. For DNS and LES with explicit SGS model, we use a non-dissipative central difference scheme with fourth-order accuracy for the convective terms and second-order central differences for the diffusive terms and the pressure Poisson solver. For implicit LES, the central difference scheme for the convective terms is replaced by the implicit turbulence model ALDM. The Poisson equation for the pressure is solved at every Runge-Kutta substep. The Poisson solver employs fast Fourier-transform in the vertical direction and a Stabilized Bi-Conjugate Gradient (BiCG-STAB) solver [37] in the horizontal plane. By the FFT, the three-dimensional problem is transformed into a set of independent two-dimensional problems, which can be solved in parallel. All computations presented here were run on Cartesian grid blocks with uniform cell size.

3.3 Numerical set-up of homogeneous stratified turbulence

We simulate homogeneous turbulence with stable stratification in a triply-periodic box. The turbulence kinetic energy is maintained at an approximately constant level by a volume force at small wavenumbers. As proposed in [5,16,28,38], the forcing is only applied to horizontal wavenumbers of the horizontal velocity components. The time- and space-dependent forcing term reads [1]

$$\mathbf{F}(\mathbf{x}, t) = \sum_{k_i, k_j=1}^{2} \mathbf{a}_{i,j} \cos(2\pi k_i x + p_{i,j}) \cos(2\pi k_j y + q_{i,j}). \tag{21}$$

The random amplitudes $\mathbf{a}_{i,j}$ and phases $p_{i,j}$ and $q_{i,j}$ are recomputed at every time step so that no mean velocity is forced in any direction. Additionally, the forcing term is scaled with a spatially constant factor in such a way that the forcing power achieves a prescribed value. Thus, the amount of input energy per time unit is kept constant and variations of the total flow energy are only due to variations in the dissipation rate. The forcing is applied at wavenumbers $k_i, k_j \in [1, 2]$, which corresponds to lengthscales $L_f \in [0.5\mathcal{L}, \mathcal{L}]$, where $\mathcal{L} = 2\pi$ is an arbitrary length scale. In the statistically steady state, the mean dissipation rate becomes equal to the forcing power. Hence we can control the total energy dissipation rate by fixing the forcing power. We choose the forcing power to be $P = 1/(2\pi)$ and a unity velocity scale $\mathcal{U}$. Thus, the integral turbulence length scale $L_{\text{int}} = \mathcal{U}^3/\varepsilon$ is of the same order as $\mathcal{L}$.

The computations are initialized with low-level white noise. Due to the constant energy injection by the forcing, the flow energy increases linearly in time. Vertical vortices gain intensity until they break down due to the inherent instability of the flow [2]. This transition was completed in all computations after 30–40 time units. We usually computed the transition phase on a coarse grid. Then, we interpolated the results to the final fine grid and continued the computation on the fine grid. An example time series of energy and dissipation rate is displayed in Fig. 1.

We present the result of three series of direct numerical simulations. A detailed list with the parameters of the computations is given in Table 1. The series differ in their Reynolds number, which is approximately 5,000 for series A, 10,000 for series B, and 25,000 for series C. Within each series we chose a set of different Froude numbers between 0.01 and 0.2 and simulated also a neutrally stratified case, which corresponds to an infinite Froude number. To reduce the number of grid points, the domain size in the vertical direction is reduced by 50% the cases with $\mathcal{R} < 50$, except for the third series. This was possible since the vertical length scales are expected to be much smaller than the horizontal ones if the stratification has a considerable influence.

The LES were performed with the same set of parameters and domain size as the DNS. The LES resolution is 64^3 grid cells, unless stated otherwise.
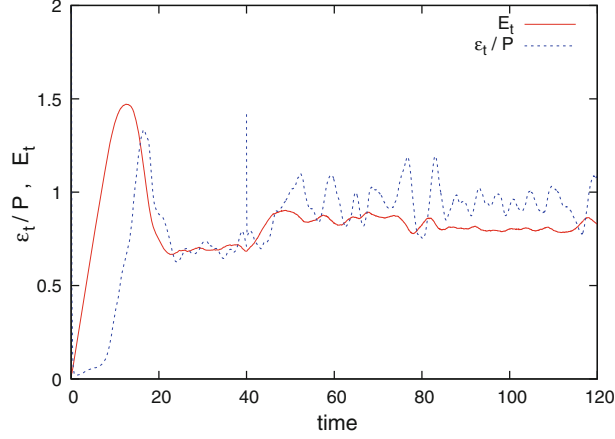
Fig. 1 Total energy and dissipation rate over time for a single DNS. At $t = 40$ we switched from the coarse to the fine grid, which generates a peak in the dissipation rate

Table 1 List of direct numerical simulations of forced stratified turbulence

#	Re	Fr	$\mathcal{R}$	N_h	N_v	L_v/π	$\eta k_{\max}$
A1	3,700	0.017	1.1	320	160	1	2.3
A2	3,700	0.028	2.8	320	160	1	2.3
A3	4,900	0.033	5.3	320	160	1	1.9
A4	5,300	0.044	10.4	320	160	1	1.8
A5	4,200	0.099	41.3	320	160	1	2.1
A6	4,900	0.162	126.7	320	320	2	1.9
A7	4,800	0.304	448.1	320	320	2	1.9
B1	7,100	0.017	2.1	640	320	1	2.8
B2	6,100	0.025	3.7	640	320	1	3.2
B3	8,300	0.027	6.3	640	320	1	2.6
B4	11,800	0.035	14.2	640	320	1	2.0
B5	9,300	0.067	41.4	640	640	2	2.4
B6	9,600	0.201	387.6	640	640	2	2.2
B7	8,400	∞	∞	480	480	2	1.7
C1	23,000	0.010	2.4	960	960	2	2.8
C2	22,700	0.020	9.5	960	960	2	3.2
C3	28,900	0.034	33.7	960	960	2	2.6

Within the series A, B, and C, the simulations have roughly the same Reynolds number. N_h and N_v are the number of cells in horizontal and vertical direction, respectively. L_v is the vertical domain size. The horizontal domain size was $L_h = 2\pi$ in all cases. The product of Kolmogorov length η and the maximum resolved wavenumber $k_{\max}$ is an indicator of the resolution of the smallest turbulent scales. It should be larger than one for any DNS

4 Results

4.1 Direct numerical simulations

4.1.1 Integral flow data

In Fig. 2, we show the mixing efficiency $\varepsilon_p/\varepsilon_k$ as well as the ratio of potential to kinetic energy E_p/E_k as functions of the buoyancy Reynolds number. These plots include the results from all three series of DNS. Additionally, we added the results from Brethouwer et al. [5]. For low $\mathcal{R}$, the mixing efficiency increases with increasing $\mathcal{R}$. This confirms the results of Brethouwer et al. [5]. In the region with $\mathcal{R} \gtrsim 100$, we find a decreasing mixing efficiency. The computations in the high $\mathcal{R}$ region all have a comparatively high Froude number (larger than 0.1), which means that they are only weakly affected by stratification effects and thus do not necessarily follow the same scaling as the stronger stratified cases. Thus, we cannot conclude with certainty whether the decreasing mixing efficiency is an effect of Froude or buoyancy Reynolds number. The peak value of $\varepsilon_p/\varepsilon_k$ is between 0.4 and 0.5, which agrees with common assumptions.

The ratio of potential to kinetic energy E_p/E_k is not a universal quantity as the mixing efficiency since it is directly influenced by the forcing, but still we can find a certain trend depending on the buoyancy Reynolds

(a) Mixing efficiency **(b)** Energy ratio
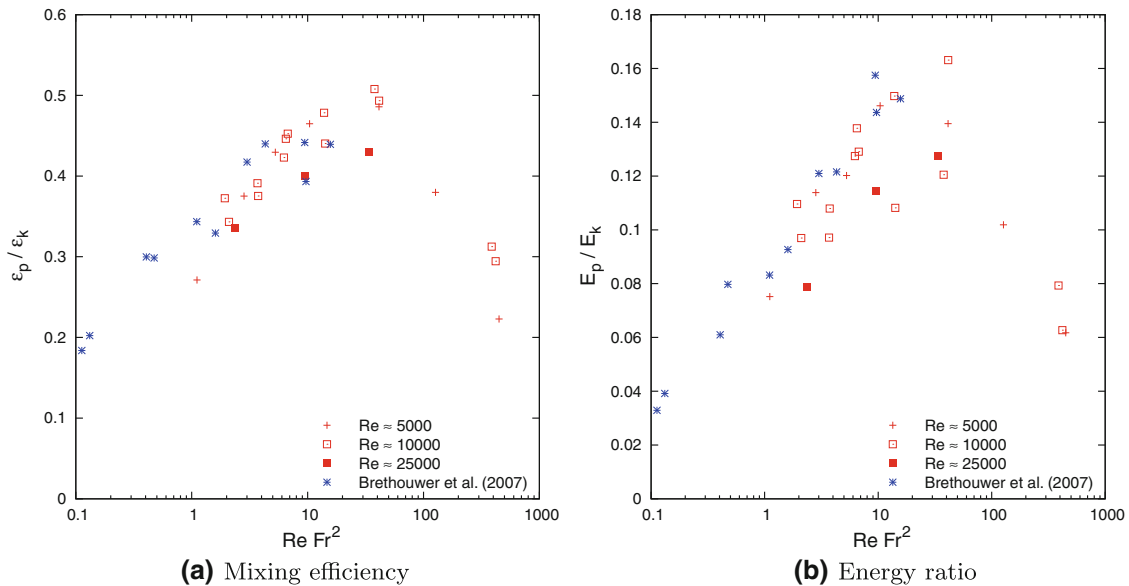
Fig. 2 Integral ratios of kinetic to potential energy and dissipation rates in stratified turbulence (DNS)

number. Similarly to the mixing efficiency, it has a peak in the region $10 < \mathcal{R} < 100$, although the results scatter a bit more than for the mixing efficiency. This shows that large-scale features (energy ratio) and small-scale features (mixing efficiency) evolve in a similar manner if the stratification is gradually increased.

4.1.2 Effects of stratification

The energy spectrum of homogeneous turbulence is a function of the three-dimensional wavenumber space. If we assume that the flow is isotropic in the horizontal plane, we can reduce this to a two-dimensional representation. We removed the second horizontal direction by averaging the spectrum on circles with constant distance from the vertical axis (k_h) and constant vertical wavenumber (k_v).

To illustrate the influence of stable stratification on the energy spectra, we show in Figs. 3, 4, 5, 6 results from the second series of DNS with Reynolds numbers of approximately 10,000. The three cases chosen include a strongly stratified case ($Fr = 0.017$, $\mathcal{R} = 2.1$), a moderately stratified case ($Fr = 0.035$, $\mathcal{R} = 14.2$), and a neutrally stratified case ($Fr = \infty$) for comparison.

The energy spectra of the three selected cases are presented in Fig. 3. In the neutral case, the horizontal kinetic energy is distributed quite isotropically, if we ignore the local influence of the large-scale horizontal forcing. For increasing stratification, the vertical modes of E_h contain increasingly more energy than the horizontal modes of the same absolute wavenumber. This corresponds to integral flow structures that have large horizontal and small vertical scales. Note that the peak energy density for the strongly stratified example is more than one order of magnitude higher than in the neutral case, while the integral amount of energy is similar in both cases.

The effect of stratification on the vertical kinetic energy is remarkably different. We find that the distribution of E_v is less anisotropic than E_h, especially for the strongly stratified case. Here, the peak energy density decreases, since the integral amount of vertical kinetic energy decreases for strong stratification. The potential energy spectrum has features of both kinetic energy spectra. It shows an agglomeration of energy near the vertical axis, just like the horizontal kinetic energy spectrum, but on the other hand, there is also a significant contribution on horizontal modes for medium wavenumbers.

To help understanding the mechanisms that lead to the mean energy spectra presented before, we analyze the spectra of the different terms in the transport equation of turbulence energy. To account for the fact that regions with large horizontal wavenumbers contribute more to the total change of energy than region close to the vertical axis, we show here spectra *integrated* over circles with constant horizontal and vertical wavenumber rather than averaged spectra.

We show the spectra of turbulent diffusion in Fig. 4. Horizontal kinetic energy is transported away from the region of forcing (which is not displayed in the double-logarithmic plot, since it has a zero vertical wavenumber)
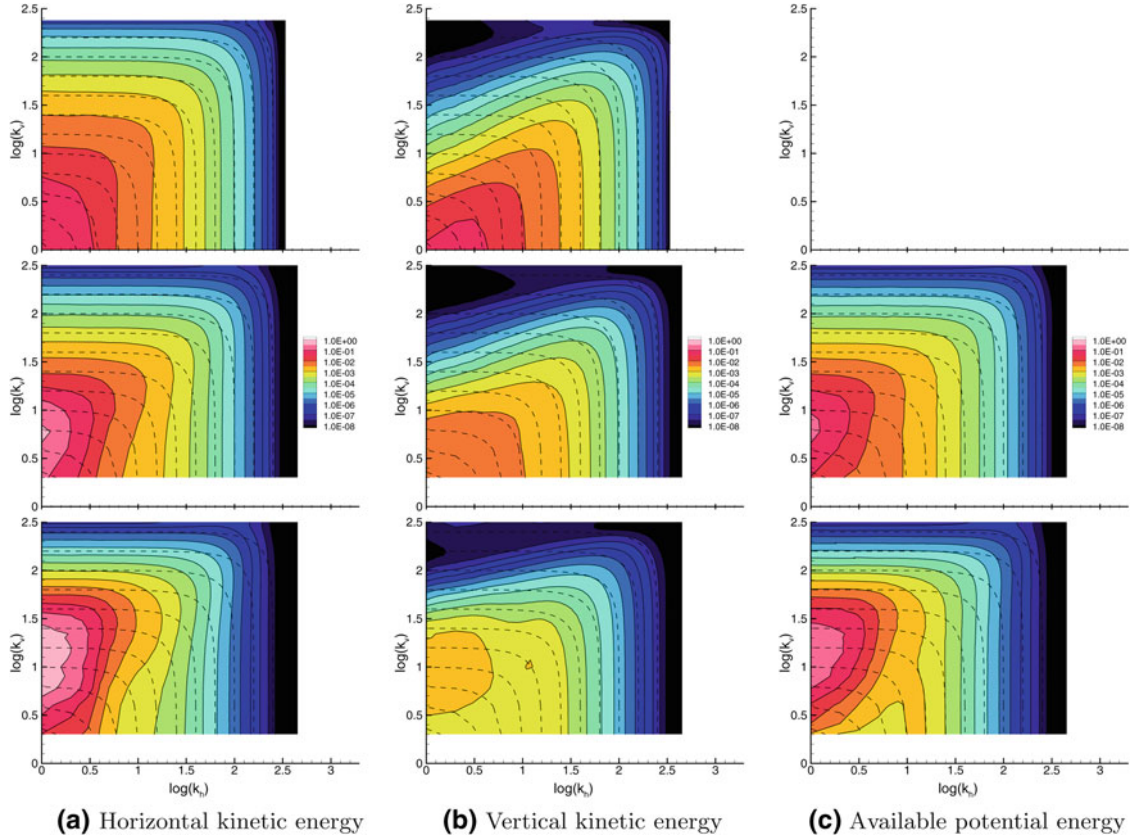
Fig. 3 Two-dimensional energy spectra of homogeneous stratified turbulence with $Re \approx 10{,}000$ (Simulations B1, B4, and B7). *Solid lines*: energy contours (adjacent contour lines are separated by a factor of $\sqrt{10}$), *dashed lines*: iso-lines of total wavenumber $\sqrt{k_h^2 + k_v^2}$. *First row*: neutral stratification ($Fr = \infty$), *second row*: weak stratification ($Fr = 0.035$), *third row*: strong stratification ($Fr = 0.017$)

to smaller scales. For vertical kinetic energy, we find a transport from large to small scales only in the neutrally stratified case. As soon as stable stratification comes into play, it is more a transport away from vertical or diagonal[1] modes to horizontal modes. This explains the isotropic distribution of E_v, we have seen in the preceding section.

The molecular diffusion and dissipation spectra in Fig. 5 show that for strong stratification the activity of molecular dissipation of horizontal kinetic energy and potential energy is concentrated in the vertical modes, where the peak values of the respective energy spectra are located. This does not apply to the vertical kinetic energy, which is dissipated more or less isotropically at small scales.

The gap between turbulent diffusion and molecular dissipation is closed by the pressure term, Fig. 6a, which basically converts horizontal kinetic energy into vertical kinetic energy and the buoyancy term, Fig. 6b, which converts vertical kinetic energy into available potential energy. Both terms act on similar medium scales.

We can summarize the evolution of energy in strongly stratified turbulence as follows: Horizontal turbulence kinetic energy E_h, being produced by a forcing on large horizontal scales, is transported to medium vertical and diagonal scales by turbulent diffusion (advection by the turbulent velocity field). A certain fraction, especially in the vertical modes, is directly dissipated by molecular viscosity, the rest is turned into vertical kinetic energy E_v by the pressure term. Turbulent diffusion equilibrates the distribution of E_v by transferring part of it to medium horizontal modes. A small amount of E_v is dissipated, the rest is converted into available potential energy E_p by buoyancy. E_p is transferred to small vertical scales by turbulent diffusion, where it is eventually extracted from the system by molecular dissipation.

---

[1] As diagonal modes we refer to the region where vertical and horizontal wavenumber are similar. This corresponds to isotropically shaped structures in real space.
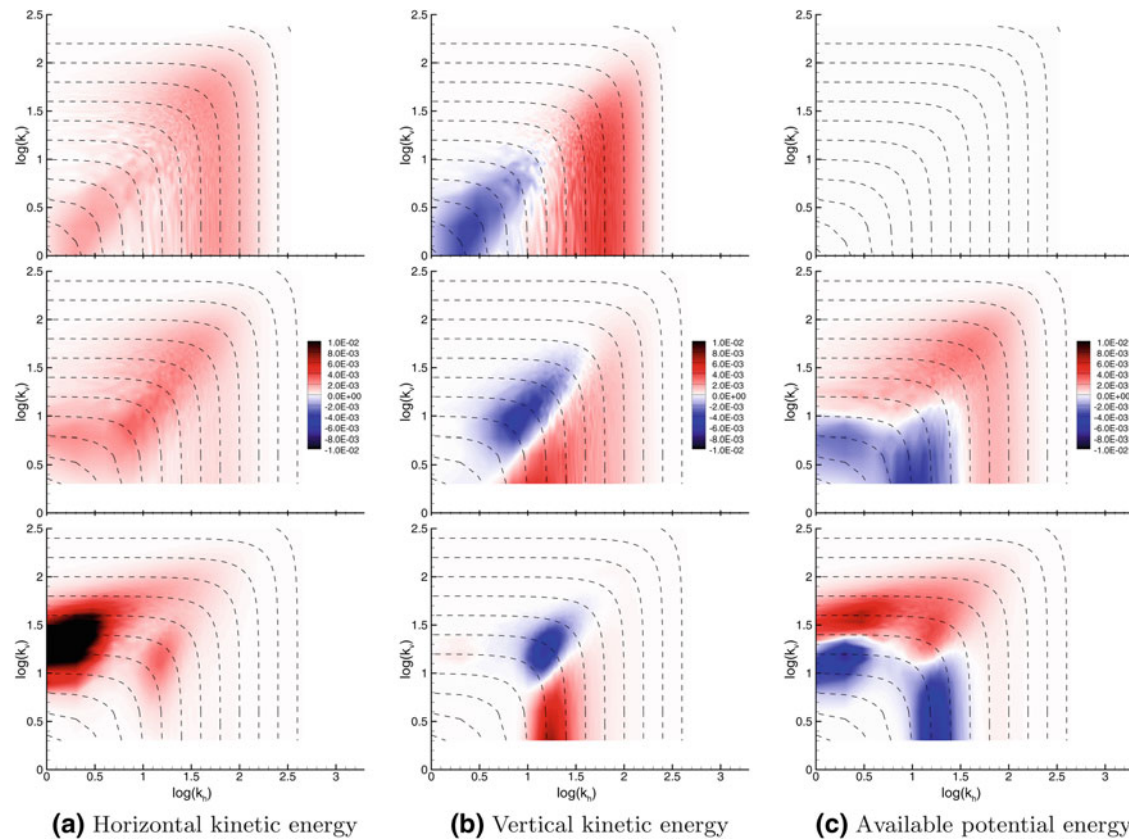
Fig. 4 Two-dimensional spectra of turbulent diffusion $\widehat{\mathcal{T}}$ in homogeneous stratified turbulence with $Re \approx 10,000$. *Dashed lines* indicate constant total wavenumber. $Fr = \infty, 0.035, 0.017$ (cf. Fig. 3)

4.1.3 Reynolds number effects

In the preceding section, we have discussed the effects of varying Froude number on the energy spectra. The second important issue is the influence of the Reynolds number. Certainly, increasing the Reynolds number will shift the dissipation range to smaller scales and increase the size of the inertial range. According to Brethouwer et al. [5], the spectra are self-similar at constant buoyancy Reynolds number. On the other hand, the anisotropy of turbulence is governed by the Froude number. The question is then how the spectra change if the Reynolds number is changed and the Froude number or buoyancy Reynolds number, respectively, are held constant.

In Fig. 7, we show the spectra of horizontal kinetic energy for cases with different Reynolds numbers. In the top row, the buoyancy Reynolds number is approximately held constant, while the Froude number is changed. In the bottom row, the Froude number is approximately constant. Generally, the dissipative range of the spectrum is shifted to higher wavenumbers as the Reynolds number increases, since the Kolmogorov length scale decreases. So the small-scale range of the spectra does not show any unexpected behavior. The energy containing region, however, looks different in the scenario with $\mathcal{R} \approx const$ compared to a constant Froude number. Only for the latter variation we find a similar peak region for all three Reynolds numbers. For constant buoyancy Reynolds number, on the other hand, the peak is shifted to larger vertical wavenumbers as the Reynolds number is increased (which means a decreased Froude number).

This observation is confirmed by studying the energy transfer spectra. As an example, we show the buoyancy transport spectrum of vertical kinetic energy in Fig. 8. For $\mathcal{R} \approx const$ we observe a shift of the main activity of the buoyancy term to smaller scales at higher Reynolds number. Especially, the separation of the activity into two distinct regions, one on vertical modes and one more on horizontal modes, only arises if the Froude number is sufficiently low. On the other hand, for $Fr \approx const$ the distribution of buoyancy fluxes looks similar for all Reynolds numbers. Only the "tail" of the horizontal region reaches to smaller horizontal scales.

In summary, we find that the relevant parameter determining the shape of the spectrum in the strongly stratified regime is the Froude number. It controls the distribution of the most energetic modes in the spectrum

(a) Horizontal kinetic energy **(b)** Vertical kinetic energy **(c)** Available potential energy
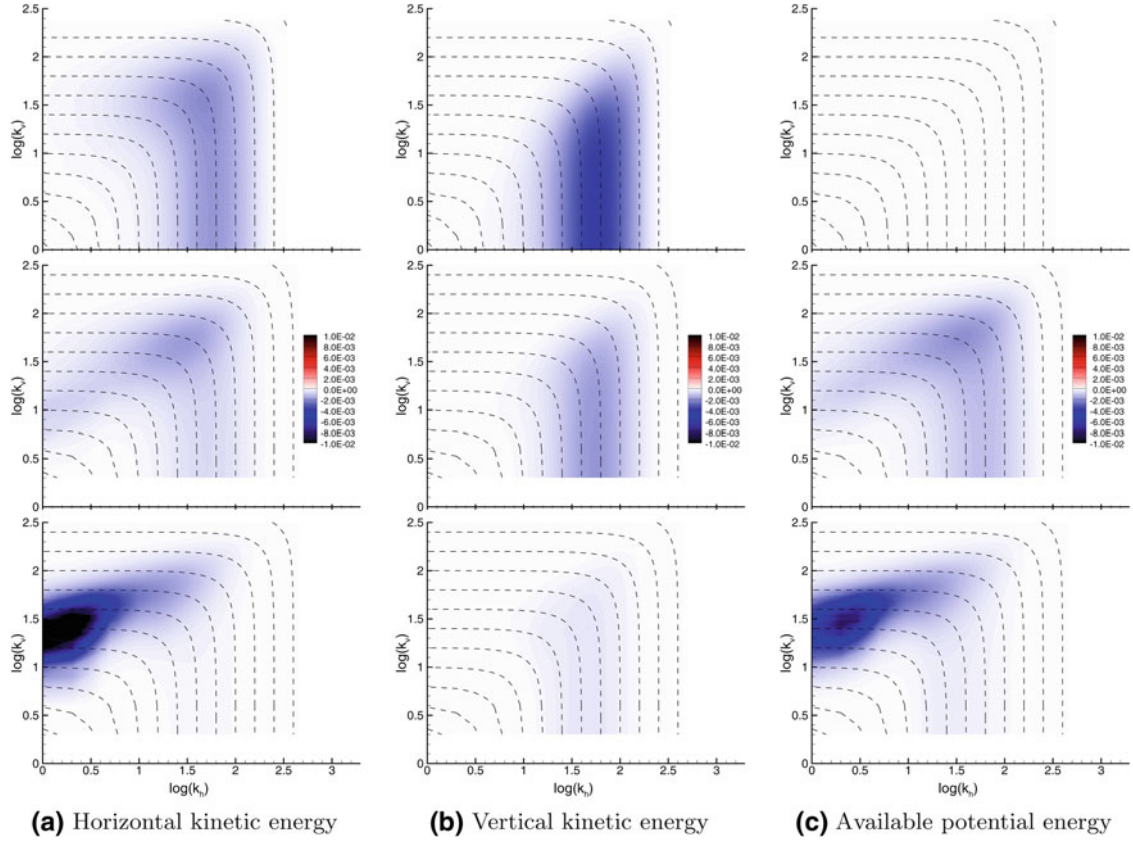
Fig. 5 Two-dimensional spectra of molecular diffusion and dissipation $\widehat{\mathcal{D}}$. *Dashed lines* indicate constant total wavenumber. $Fr = \infty, 0.035, 0.017$ (cf. Fig. 3)

and the anisotropy of turbulence. The Reynolds number, in the other hand, just changes the range of scales of turbulence but does not influence the large scales. This is in good agreement to common knowledge about isotropic turbulence.

4.2 Large eddy simulations

4.2.1 Integral flow data

The first criterion for the validation of an LES method is its ability to correctly reproduce the ratios of the different types of energy from the DNS. In Fig. 9a, we show again the ratio of potential to kinetic energy versus buoyancy Reynolds number. The results from a number of LES are included. They match very well with the DNS results for most of the parameter space. Just for the lowest buoyancy Reynolds number, the energy ratio is under-predicted by the LES. However, in this region the flow is not turbulent any more but in the transition to the "viscosity affected stratified" regime [5], which we presently do not want to address.

In Fig. 9b, we make the comparison for the ratio of vertical kinetic energy to potential energy. In our horizontally forced scenario, this ratio of energies is the only one which is not affected by the forcing. We thus can assume that it will follow a universal trend. E_v/E_p monotonically decreases if the Froude number decreases. This emphasizes the growing influence of the buoyancy transport with increasing stratification. In the DNS, the rate of change of the energy ratio is approximately $Fr^{0.82}$. If plotted over the Froude number, the results from all DNS with different Reynolds number are within a comparably narrow band. On the other hand, in a plot as a function of buoyancy Reynolds number, one could see a significant influence of Reynolds number. We conclude that the Froude number is also the relevant parameter to control the ratio E_v/E_p.
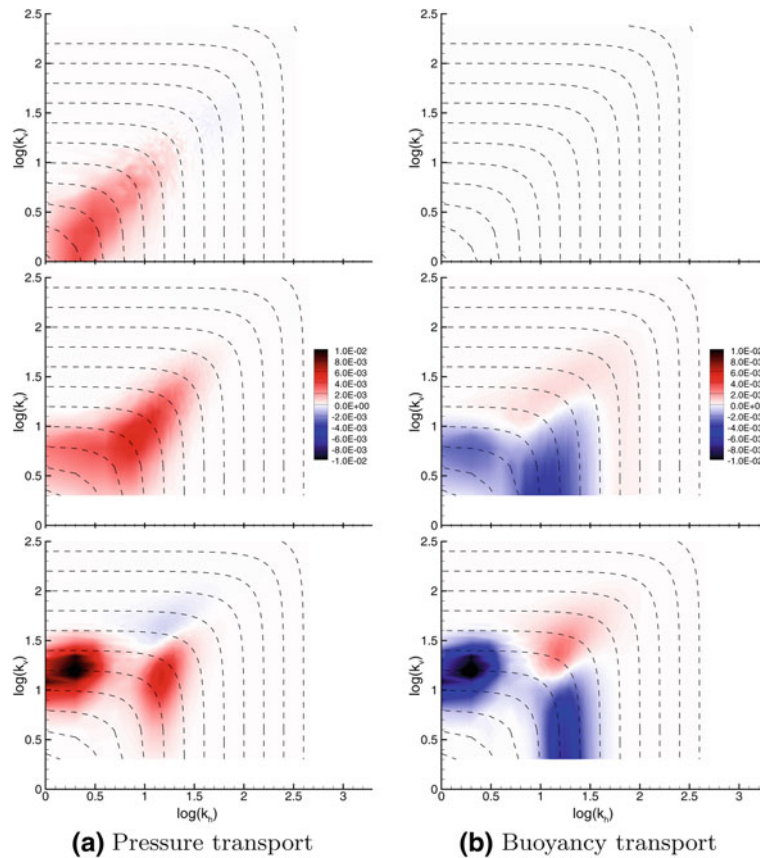
Fig. 6 Two-dimensional spectra of pressure transport $\widehat{\mathcal{P}}$ and buoyancy transport $\widehat{\mathcal{B}}$ of vertical kinetic energy. *Dashed lines* indicate constant total wavenumber. $Fr = \infty$, 0.035, 0.017 (cf. Fig. 3)

With the implicit LES model ALDM, we find the same trend for the energy ratio. For large Froude numbers, the agreement with DNS is very good, whereas for stronger stratification ALDM systematically under-predicts E_v/E_p. The exponent for the rate of change is slightly higher, i.e., approximately 0.95. This result is, however, still in much better agreement with the DNS than the results obtained with the standard Smagorinsky model (SSM). For high Froude numbers, the SSM predicts the energy ratio with good accuracy, but for stronger strat-ified flows the decay of vertical kinetic energy compared to potential energy is strongly over-predicted. The large eddy simulations with ALDM and SSM, respectively, were computed on the same computational grids. Hence, the different result is due to the different ability of both SGS models to adapt to strongly anisotropic conditions. ALDM clearly shows a better performance in strongly stratified cases.

4.2.2 One-dimensional energy spectra

For comparison of kinetic energy spectra, we selected one DNS in the weakly stratified regime ($\mathcal{R} = 41$, $Fr = 0.07$, $Re = 9,300$) in Fig. 10 and strongly stratified regime ($\mathcal{R} = 6.3$, $Fr = 0.03$, $Re = 8,300$) in Fig. 11. The corresponding LES have similar Froude and Reynolds numbers.

In the horizontal spectra of kinetic energy, the difference between ALDM and an explicit eddy viscosity model is most obvious. In the weakly stratified case ($\mathcal{R} = 41$), the horizontal spectrum is still quite simi-lar to the Kolmogorov spectrum of isotropic turbulence. In this case, both SGS models predict the inertial range spectrum fairly well. The SSM is slightly too dissipative, but the difference from the DNS spectrum is acceptable. Things completely change for the stronger stratified case ($\mathcal{R} = 6.3$). The SSM dissipates too much energy and thus under-predicts the inertial range spectrum by more than one order of magnitude. Additionally, the predicted power-law exponent is significantly lower than $-5/3$. The spectrum predicted by ALDM, on the other hand, agrees well with the DNS. It correctly predicts the characteristic plateau region between the
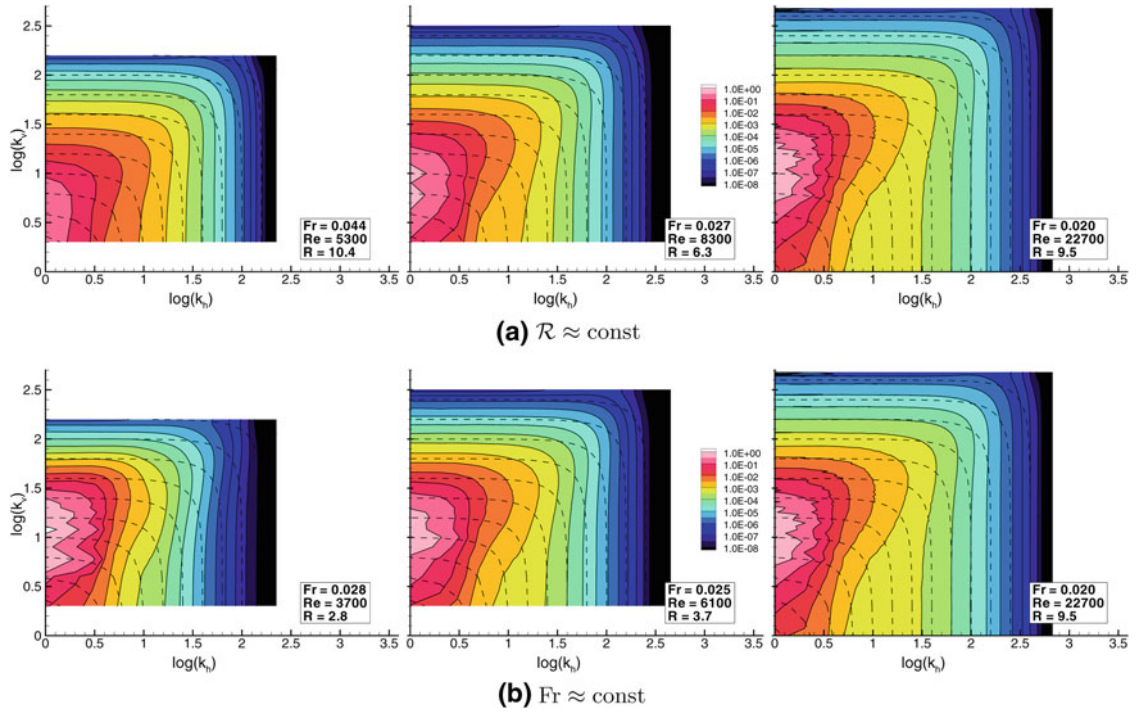
Fig. 7 Two-dimensional spectra of horizontal kinetic energy for different Reynolds numbers. *Dashed lines* indicate constant total wavenumber. **a** Simulations A4, B3, and C2; **b** simulations A2, B2, and C2
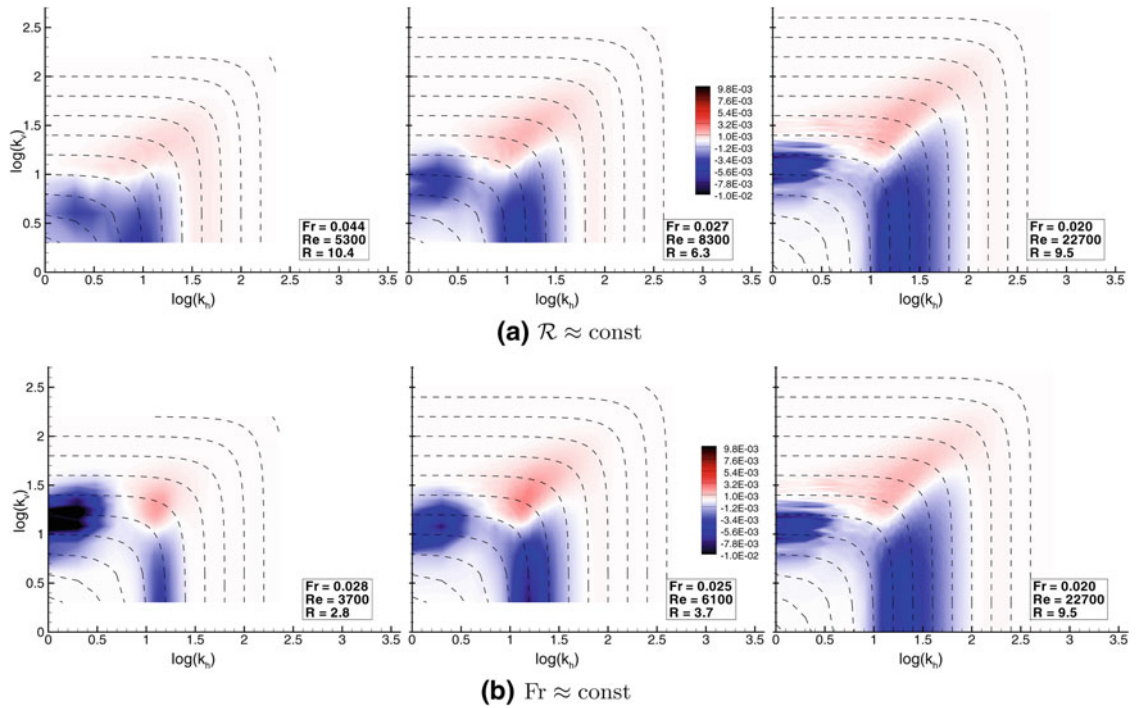

Fig. 8 Two-dimensional spectra of buoyancy transport $\widehat{\mathcal{B}}$ of vertical kinetic energy for different Reynolds numbers. *Dashed lines* indicate constant total wavenumber

(a) Ratio of potential energy to kinetic energy

(b) Ratio of vertical kinetic energy to potential energy
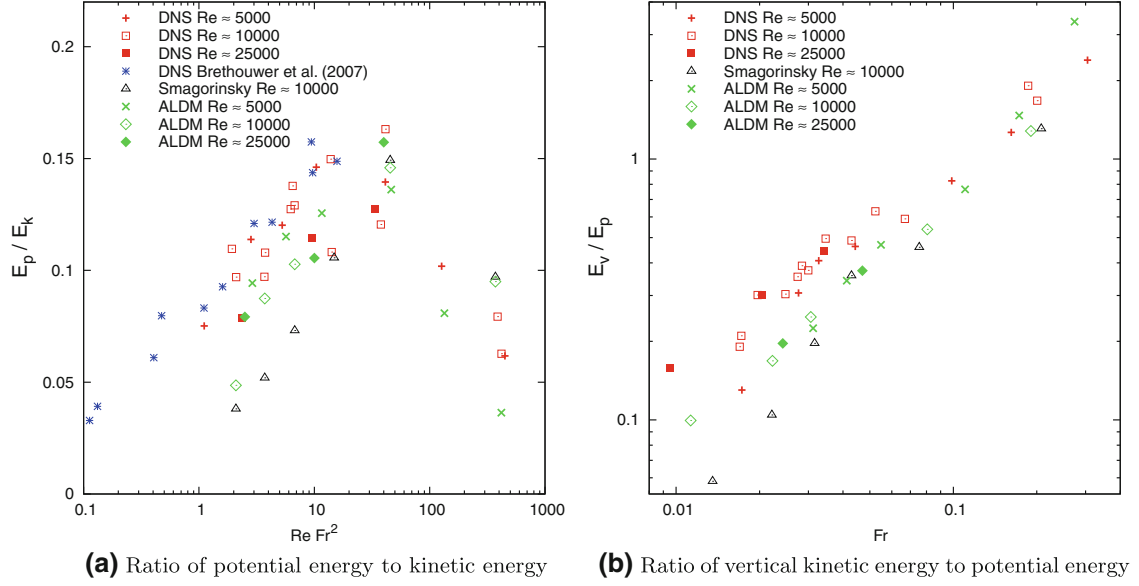
Fig. 9 Integral energy ratios in stratified turbulence. Comparison of DNS and LES results

(a) Horizontal spectra

(b) Vertical spectra
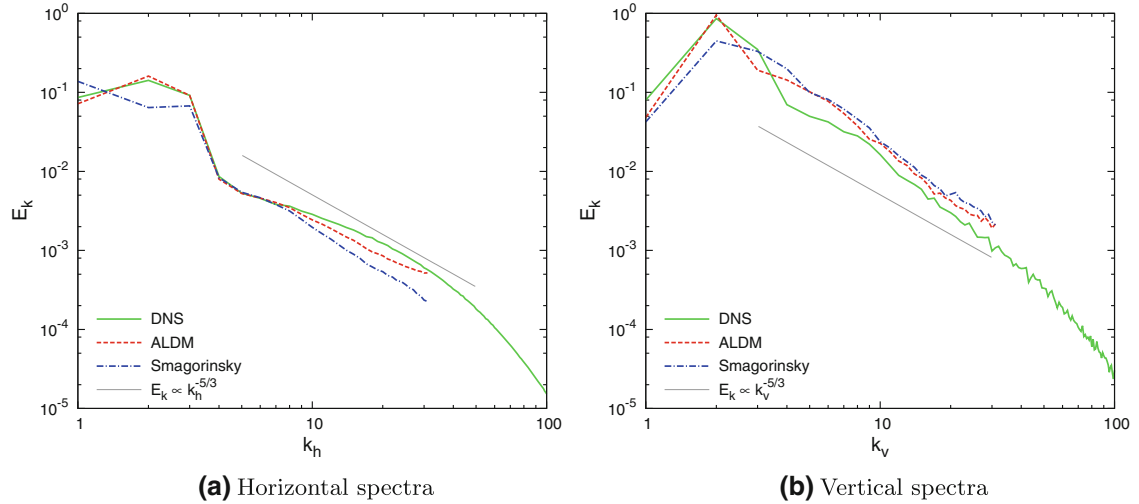
Fig. 10 Weakly stratified turbulence kinetic energy spectra ($\mathcal{R} = 41$)

forcing scales and the inertial scales. Moreover, it produces a power-law decay with an exponent of $-5/3$, corresponding to the DNS[2] and theory derived from scaling laws [5].

In the vertical spectra of kinetic energy, the inertial range decay exponent changes from $-5/3$ in neutrally stratified fluid to -3 in strongly stratified turbulence. We find this change in the DNS and it is well reproduced by the LES. Both SGS models predict the turbulence inertial range decay well. At strong stratification, the ALDM result perfectly agrees with the DNS. The SSM result is slightly too dissipative in this region.

4.2.3 Two-dimensional energy spectra

We compare the two-dimensional energy spectra of a strongly stratified case ($\mathcal{R} = 3.7$) in Fig. 12. In the DNS spectra, the LES domain is indicated by a black rectangle to simplify visual comparison with the LES results. The ILES spectra of all three types of energy compare well the corresponding DNS spectra, although the ILES

---

[2] In fact, the inertial range is not clearly visible in the DNS due to the low buoyancy Reynolds number $\mathcal{R}$. Similar spectra were, for example, reported by Brethouwer et al. [5].

(a) Horizontal spectra   **(b)** Vertical spectra
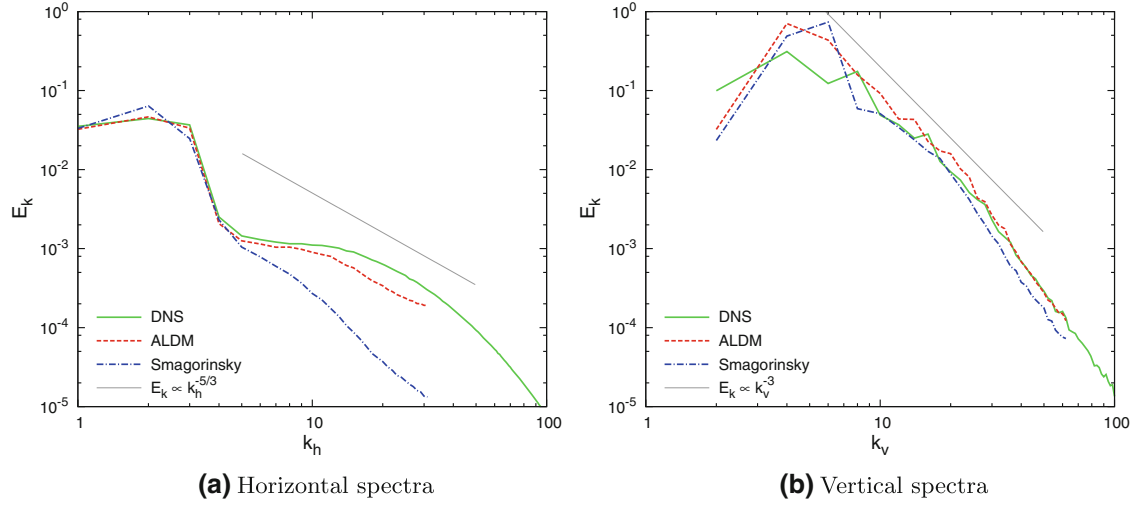
**Fig. 11** Strongly stratified turbulence kinetic energy spectra ($\mathcal{R} = 6.3$)
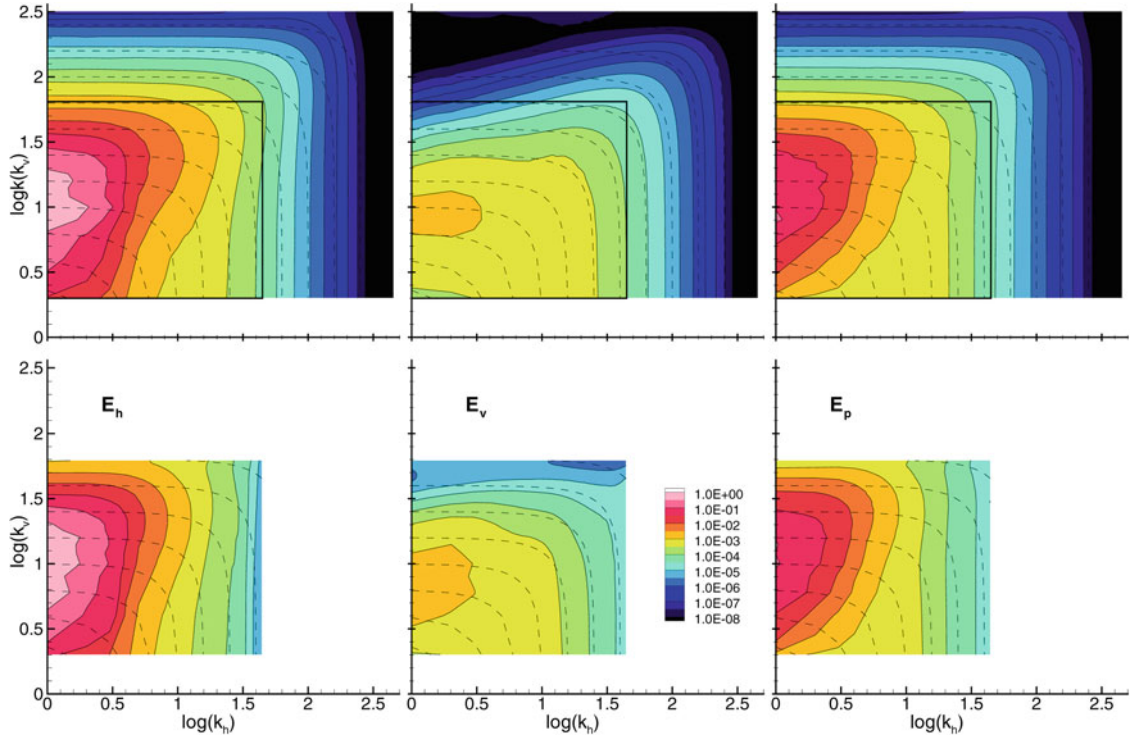
Fig. 12 Two-dimensional energy spectra of stratified turbulence ($Fr = 0.025$, $Re = 6{,}100$, $\mathcal{R} = 3.7$). DNS (*top row*) and ILES with ALDM (*bottom row*)

was computed on a coarse grid of only 64^3 cells, while the DNS needed $640^2 \times 320$ cells. The ILES resemble the large-scale features of the DNS very well and also correctly predict the vertical spectrum up to the cut-off wavenumber. At high horizontal wavenumbers, we observe a slight under-prediction of the energy levels, as we have already seen in the one-dimensional spectra (Figs. 10 and 11).

The ILES are also capable of accurately predicting the spectra of turbulent diffusion (Fig. 13). At high horizontal wavenumbers, the computed values of $\widehat{\mathcal{T}}$ are smaller in the ILES solution compared to the corresponding DNS results. This discrepancy is due to the lower energy level observed there. However, the anisotropic shape of the two-dimensional spectra and the relative intensities of energy are predicted in an excellent way.
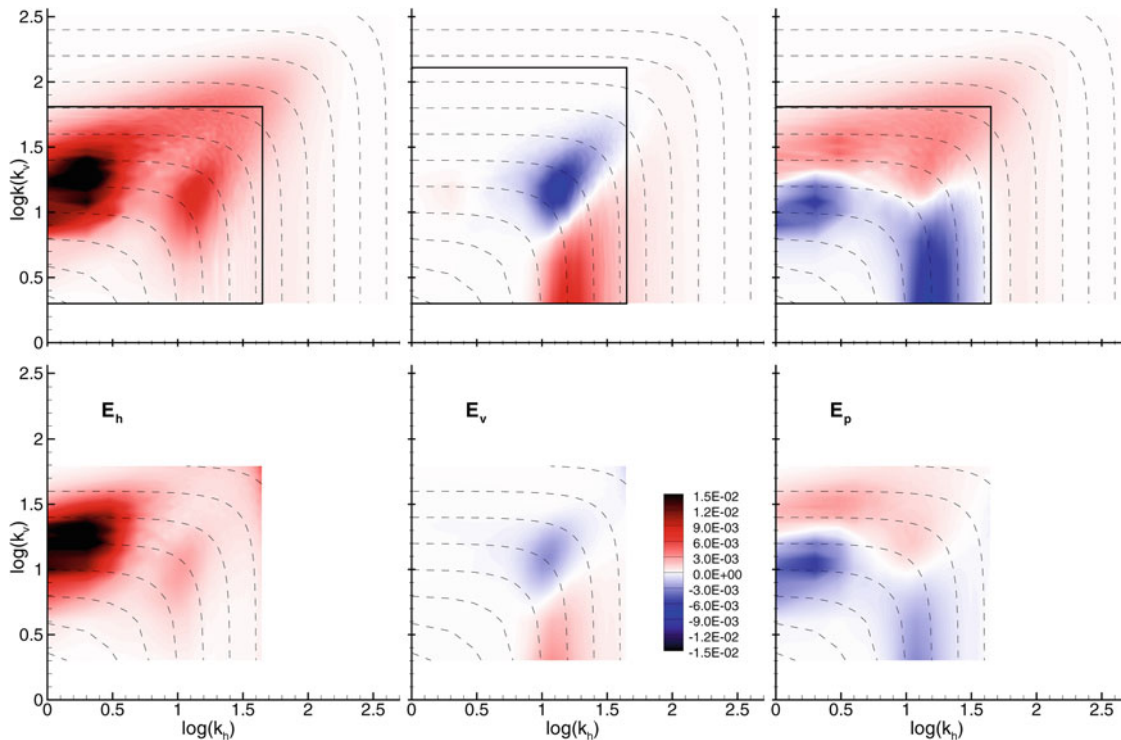
Fig. 13 Two-dimensional spectra of turbulent diffusion $\widehat{\mathcal{T}}$ in stratified turbulence ($Fr = 0.025$, $Re = 6,100$, $\mathcal{R} = 3.7$). DNS (*top row*) and ILES with ALDM (*bottom row*)

Since $\widehat{\mathcal{T}}$ is a pure energy transport term, its integral over all wavenumbers is zero for each individual energy form in the DNS. In the under-resolved ILES, the complete region of negative turbulent diffusion is resolved, but part of the region where it is positive (and energy is dissipated by molecular viscosity) is not included. Hence the integral of $\widehat{\mathcal{T}}$ over the ILES domain must be smaller than zero, corresponding to an effective dissipation of energy. The implicit SGS model automatically accounts for this effect. In the example presented in Fig. 13, the implicit SGS dissipation compared to the total (resolved molecular plus implicit) dissipation amounts to $\mathcal{T}_i(E_h)/\varepsilon_h = 0.63$, $\mathcal{T}_i(E_v)/\varepsilon_v = 0.48$, and $\mathcal{T}_i(E_p)/\varepsilon_p = 0.54$, respectively. About half of the total energy dissipation is provided by the implicit SGS model.

5 Conclusion

We presented new results from DNS of horizontally forced homogeneous stratified turbulence of a Boussinesq fluid at different Reynolds and Froude numbers. Our numerical set-up is similar to previous simulations, which allowed us to compare results with literature. In addition to the previously investigated cases, the parameter range of the new DNS data extends to significantly higher buoyancy Reynolds numbers and covers the strongly stratified regime as well as the transition to weak and neutral stratification. We thoroughly discussed two-dimensional spectra for all three forms of flow energy: horizontal and vertical kinetic energy and potential energy. A particular emphasis was put on identifying the mechanisms that govern the conversion of energy and its transport between different scales. This was achieved through analyzing the contributions of all terms of the Boussinesq energy budget equations in spectral space.

Confirming the findings of Brethouwer et al. [5], we observed that the ratio of potential to kinetic energy as well as the mixing efficiency decreases with increasing stratification. In extending previous studies to higher buoyancy Reynolds numbers, we found that both ratios also tend to decrease for very weak stratification, which means that there is a peak at about $10 < \mathcal{R} < 100$.

The horizontal kinetic energy accumulates in modes with high vertical and low horizontal wavenumber ("pancake-turbulence"), while the vertical kinetic energy is distributed much more isotropically in spectral space. The available potential energy distribution combines elements of both kinetic energy types. It has a

strong peak on vertical modes like the horizontal kinetic energy and it has some contribution on medium horizontal scales like the vertical kinetic energy. In analyzing the contributions of the different terms in the energy transport equations to the total energy balance, we could show in detail the various ways in which energy is transformed and transported. Furthermore, we found that with changing Reynolds number the relevant parameter for controlling the distribution of energy in the wavenumber space is the Froude number rather than the buoyancy Reynolds number. We observed similar spectra in simulations with comparable Froude number and strongly varying spectra if the buoyancy Reynolds number was fixed.

To reduce the computational costs of simulating stratified turbulent flows, we proposed an implicit SGS model for LES based on the ALDM [19,21]. In ALDM, the SGS stress term is not explicitly computed based on the available flow solution, but it is rather part of the non-linear numerical discretization. The implicit SGS model provided by this discretization can be interpreted as a combination of tensor dissipation and scale similarity modeling. When applying ALDM to homogeneous stratified turbulence, we found good agreement with the DNS results. ALDM correctly predicts trends and values of integral flow parameters, such as the ratios of different types of energy. Especially in cases of strong stratification, the ALDM predictions are much closer to the DNS results than simulations with a Smagorinsky model. The same observation is made for the prediction of energy spectra. We emphasize that ALDM does neither require ad hoc modifications nor a re-calibration of model parameters. We used the very same set of model parameters for our simulations of stratified turbulence that had been found to be optimal for isotropic neutrally stratified turbulence before. The implicit model automatically adapts to anisotropic conditions and predicts the spectra modified by strong stratification much better than a classical eddy viscosity model.

We conclude that ALDM is a suitable tool for simulating turbulent flows in stably stratified background. The applicability of ALDM to (neutrally stratified) engineering flows had already been shown in a number of previous studies. With the present investigations, we also qualified the implicit SGS model for use in geophysical applications. Future applications of ALDM include breaking of gravity waves, atmospheric boundary layers, mixing events in the ocean and other small and mesoscale phenomena.

References

1. Aspden, A.J., Nikiforakis, N., Dalziel, S.B., Bell, J.B.: Analysis of implicit les methods. Comm. App. Math. Comp. Sci. **3**(1), 103–126 (2008)
2. Billant, P., Chomaz, J.M.: Theoretical analysis of the zigzag instability of a vertical columnar vortex pair in a strongly stratified fluid. J. Fluid Mech. **419**(1), 29–63 (2000)
3. Boris, J., Grinstein, F., Oran, E., Kolbe, R.: New insights into large eddy simulation. Fluid Dynam. Res. **10**(4–6), 199–228 (1992)
4. Bouruet-Aubertot, P., Sommeria, J., Staquet, C.: Stratified turbulence produced by internal wave breaking: two-dimensional numerical experiments. Dyn. Atmos. Oceans **23**(1–4), 357–369 (1996). Stratified flows
5. Brethouwer, G., Billant, P., Lindborg, E., Chomaz, J.M.: Scaling analysis and simulation of strongly stratified turbulent flows. J. Fluid Mech. **585**, 343–368 (2007)
6. Cot, C.: Equatorial mesoscale wind and temperature fluctuations in the lower atmosphere. J. Geophys. Res. **106**(D2), 1523–1532 (2001)
7. Dewan, E.M.: Stratospheric wave spectra resembling turbulence. Science **204**(4395), 832–835 (1979)
8. Dewan, E.M.: Saturated-cascade similitude theory of gravity wave spectra. J. Geophys. Res. **102**(D25), 29799–29817 (1997)
9. Diamessis, P.J., Spedding, G.R., Domaradzki, J.A.: Similarity scaling and vorticity structure in high-reynolds-number stably stratified turbulent wakes. J. Fluid Mech. **671**, 52–95 (2011)
10. Domaradzki, J.A., Adams, N.A.: Direct modelling of subgrid scales of turbulence in large eddy simulations. J. Turb. **3**, 24 (2002)
11. Dörnbrack, A.: Turbulent mixing by breaking gravity waves. J. Fluid Mech. **375**, 113–141 (1998)
12. Fritts, D.C., Wang, L., Werne, J., Lund, T., Wan, K.: Gravity wave instability dynamics at high reynolds numbers. part i: wave field evolution at large amplitudes and high frequencies. J. Atmos. Sci. **66**(5), 1126–1148 (2009)
13. Gage, K.S.: Evidence for a $k^{-5/3}$ law inertial range in mesoscale two-dimensional turbulence. J. Atmos. Sci. **36**, 1950–1954 (1979)
14. Grinstein, F.F., Margolin, L.G., Rider, W.J. (eds.): Implicit Large Eddy Simulation—Computing Turbulent Fluid Dynamics. Cambridge University Press, Cambridge (2007)
15. Harten, A., Engquist, B., Osher, S., Chakravarthy, S.R.: Uniformly high order accurate essentially non-oscillatory schemes. III. J. Comput. Phys. **71**(2), 231–303 (1987)
16. Herring, J.R., Métais, O.: Numerical experiments in forced stably stratified turbulence. J. Fluid Mech. **202**(1), 97–115 (1989)

17. Hickel, S., Adams, N.A.: On implicit subgrid-scale modeling in wall-bounded flows. Phys. Fluids **19**, 105–106 (2007)
18. Hickel, S., Adams, N.A.: Implicit les applied to zero-pressure-gradient and adverse-pressure-gradient boundary-layer turbulence. Int. J. Heat Fluid Flow **29**, 626–639 (2008)
19. Hickel, S., Adams, N.A., Domaradzki, J.A.: An adaptive local deconvolution method for implicit LES. J. Comput. Phys. **213**, 413–436 (2006)
20. Hickel, S., Adams, N.A., Mansour, N.N.: Implicit subgrid-scale modeling for large-eddy simulation of passive scalar mixing. Phys. Fluids **19**, 095–102 (2007)
21. Hickel, S., Kempe, T., Adams, N.A.: Implicit large-eddy simulation applied to turbulent channel flow with periodic constrictions. Theor. Comput. Fluid Dyn. **22**, 227–242 (2008)
22. Kaltenbach, H.J., Gerz, T., Schumann, U.: Large-eddy simulation of homogeneous turbulence and diffusion in stably stratified shear flow. J. Fluid Mech. **280**(1), 1–40 (1994)
23. Kawamura, T., Kuwahara, K. (eds.): Computation of high Reynolds number flow around a circular cylinder with surface roughness (1984)
24. Kraichnan, R.H.: Inertial ranges in two-dimensional turbulence. Phys. Fluids **10**(7), 1417–1423 (1967)
25. Laval, J.P., McWilliams, J.C., Dubrulle, B.: Forced stratified turbulence: successive transitions with Reynolds number. Phys. Rev. E **68**(3), 036–308 (2003)
26. Lilly, D.K.: Stratified turbulence and the mesoscale variability of the atmosphere. J. Atmos. Sci. **40**(3), 749–761 (1983)
27. Lilly, D.K., Bassett, G., Droegemeier, K., Bartello, P.: Stratified turbulence in the atmospheric mesoscales. Theor. Comput. Fluid Dyn. **11**, 139–153 (1998)
28. Lindborg, E.: The energy cascade in a strongly stratified fluid. J. Fluid Mech. **550**(1), 207–242 (2006)
29. Lindborg, E., Brethouwer, G.: Stratified turbulence forced in rotational and divergent modes. J. Fluid Mech. **586**, 83–108 (2007)
30. Métais, O., Lesieur, M.: Spectral large-eddy simulation of isotropic and stably stratified turbulence. J. Fluid Mech. **239**, 157–194 (1992)
31. Nastrom, G.D., Gage, K.S.: A climatology of atmospheric wavenumber spectra of wind and temperature observed by commercial aircraft. J. Atmos. Sci. **42**(9), 950–960 (1985)
32. Shu, C.W.: Total-variation-diminishing time discretizations. SIAM J. Sci. Stat. Comput. **9**(6), 1073–1084 (1988)
33. Smith, L.M., Waleffe, F.: Generation of slow large scales in forced rotating stratified turbulence. J. Fluid Mech. **451**(1), 145–168 (2002)
34. Smolarkiewicz, P.K., Margolin, L.G.: MPDATA: a finite-difference solver for geophysical flows. J. Comput. Phys. **140**(2), 459–480 (1998)
35. Staquet, C., Godeferd, F.S.: Statistical modelling and direct numerical simulations of decaying stably stratified turbulence. Part 1. Flow energetics. J. Fluid Mech. **360**, 295–340 (1998)
36. van Zandt, T.E.: A universal spectrum of buoyancy waves in the atmosphere. Geophys. Res. Lett. **9**(5), 575–578 (1982)
37. van der Vorst, H.A.: Bi-CGSTAB: a fast and smoothly converging variant of Bi-CG for the solution of nonsymmetric linear systems. SIAM J. Sci. Stat. Comput. **13**(2), 631–644 (1992)
38. Waite, M.L., Bartello, P.: Stratified turbulence dominated by vortical motion. J. Fluid Mech. **517**, 281–308 (2004)

Direct numerical simulation of a breaking inertia-gravity wave

S. REMMLER[1], M. D. FRUMAN[2] AND S. HICKEL[1]

[1]Institute of Aerodynamics and Fluid Mechanics, Technische Universität München,
D-85747 Garching bei München, Germany

[2]Institute for Atmospheric and Environmental Sciences, Goethe-Universität Frankfurt,
D-60438 Frankfurt am Main, Germany

We performed fully resolved three-dimensional numerical simulations of a statically unstable monochromatic inertia-gravity wave using the Boussinesq equations on an f-plane with constant stratification. The chosen parameters represent a gravity wave with almost vertical direction of propagation and a wavelength of 3 km breaking in the middle atmosphere. We initialised the simulation with a statically unstable gravity wave perturbed by its leading transverse normal mode and the leading instability modes of the time-dependent wave breaking in a two-dimensional space. The wave was simulated for approximately 16 hours, which is twice the wave period. After the first breaking triggered by the imposed perturbation, two secondary breaking events are observed. Similarities and differences between the three-dimensional and previous two-dimensional solutions of the problem and effects of domain size and initial perturbations are discussed.

1. Introduction

Today there is no longer any doubt that gravity waves play an important role in the global circulation in the atmosphere. Sawyer (1959) was one of the first to note the necessity of taking gravity waves into account in numerical weather forecast models. Several authors (Bretherton 1969; Lilly 1972; Blumen & McGregor 1976) attempted to quantify the gravity wave drag exerted by orographic gravity waves on the mean flow, finding values of the order of 1 Pa, which can be sufficient to accelerate the mean flow by several m/s per day (Nappo 2002). Chun & Baik (1998) found even larger values of acceleration and deceleration due to gravity waves generated by thermal forcing in cumulus convection. The direct effects of gravity waves on the general circulation in the troposphere and lower stratosphere are only minor, although gravity wave breaking can lead to clear-air turbulence and locally enhanced turbulent diffusion in this region. On the other hand, gravity waves strongly influence the circulation in the mesosphere (the altitude range between 50 and 90km), where they are responsible for the cold summer pole mesopause (Houghton 1978), and in the stratosphere, where together with other equatorial waves they lead to the quasi-biennial oscillation in equatorial winds (Dunkerton 1997*a*).

Despite this unquestioned importance of gravity waves, their treatment in present general circulation models remains unsatisfactory. The major part of the gravity wave spectrum is not or is only marginally resolved by the numerical grids and must thus be explicitly parametrised. Various parametrisations have been proposed, e. g. by Lindzen (1981), Holton (1982) and others. Reviews of gravity wave parametrisation schemes are provided by McLandress (1998) and Fritts & Alexander (2003). Generally, the upward propagation of linear waves through the atmosphere is computed using the Wentzel-Kramers-Brillouin-Jeffreys (WKBJ) approximation, which is based on the assumption

of a slowly varying background flow field. During the upward propagation of the wave, the amplitude typically grows as the ambient density decreases. The wave becomes more nonlinear until it reaches the threshold of static stability (i. e. where the vertical gradient of total potential temperature becomes locally negative) and breaks. Most parametrisation schemes account for this effect by transferring some fraction of the wave momentum to the mean flow and reducing the wave amplitude accordingly.

All aspects of gravity wave parametrisation, i. e. sources, propagation and breaking are associated with large uncertainties. Consequently, the schemes have to be carefully tuned in order to obtain realistic results for the general circulation. An improvement of the gravity wave parametrisation (without ad-hoc tuning) requires a better understanding of the physical process of wave breaking, which can only be obtained through a detailed analysis of breaking events.

Theoretical analyses of inviscid (Mied 1976; Drazin 1977) and weakly viscous (Klostermeyer 1982) breaking gravity waves show that monochromatic high frequency gravity waves (HGWs), i. e. waves unaffected by rotation, are linearly unstable regardless of their amplitude, either through parametric subharmonic instability or convective instability. As opposed to HGWs, low frequency inertia-gravity waves (IGWs) are influenced by the Coriolis force and thus have a nonzero third velocity component perpendicular to the plane of the wave. Dunkerton (1997*b*) and Achatz & Schmitz (2006*b*) showed that this influences the orientation of the most unstable perturbations. Hence the breaking mechanism in IGWs differs fundamentally from HGWs and has to be investigated separately.

The onset of gravity wave breaking, i. e. the initial growth of some instability modes, can be treated as a two-dimensional problem with three velocity components. However, the breaking process itself is inherently three-dimensional, and the breaking dynamics in two- and three-dimensional simulations strongly differ from each other, as pointed out first by Andreassen *et al.* (1994) and later by Fritts *et al.* (1994, 2009).

The analysis of the breaking process of gravity waves in the atmosphere at realistic scales and Reynolds numbers requires highly resolved non-linear three-dimensional simulations. For IGWs, which are affected by rotation, no such simulations have yet been published. The high resolution simulations of Fritts *et al.* (2009) are restricted to HGWs, where the velocity vector of the base wave lies in the plane of the wave. Lelong & Dunkerton (1998) simulated breaking IGWs at a greatly reduced ratio of the Brunt-Väisälä frequency to the Coriolis parameter compared to atmospheric values. There and in many other studies (Winters & D'Asaro 1994; Andreassen *et al.* 1998; Dörnbrack 1998; Afanasyev & Peltier 2001, and others) no attempt is made to resolve all turbulence scales at realistic Reynolds numbers. Instead, either a subgrid-scale (SGS) parametrisation of turbulence or a hyperviscosity formulation is used. Alternatively, the Reynolds number is greatly reduced to match laboratory experiments. In none of the aforementioned studies have the used SGS parametrisations been validated using turbulence resolving reference simulations. Clearly, however, possible effects of the SGS parametrisation on the general breaking process can only by excluded by fully resolving all turbulence scales.

Since three-dimensional simulations are computationally expensive and thus not suitable for investigating a large space of parameters, the following multi-step approach for the simulation of IGW breaking was proposed by Fruman & Achatz (2012): First, they computed the leading primary instabilities of a given IGW. Second, they performed high-resolution nonlinear simulations initialised with the superposition of the IGW and its leading unstable modes. These simulations are restricted to a two-dimensional domain but contain three independent velocity components, so they are referred to as "2.5"-dimensional. Next, this 2.5-dimensional time dependent flow was analysed for stability
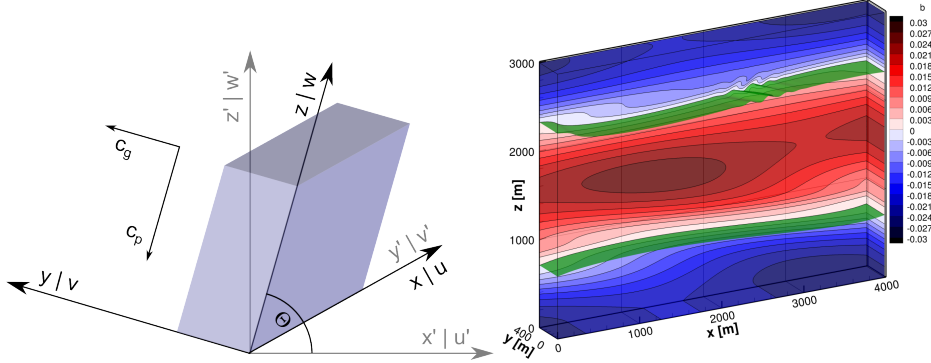
FIGURE 1. Left: Computational domain in the rotated coordinate system x, y, z. The earth coordinates are denoted as x', y', z'. c_p and c_g indicate the phase and group velocity. Right: Initial condition with secondary SV perturbation. Contours of buoyancy in colours and an iso-surface at $b = 0$ in green.

with respect to secondary perturbations varying in the remaining spatial direction. We will now extend this procedure by adding a fourth and last step: a fully three-dimensional nonlinear integration of the breaking event. The initial condition is the same as that of the 2.5-dimensional simulations, but perturbed by the fastest growing secondary perturbation. The resulting initial flow field is then fully three-dimensional. The domain size is determined by the wavelength of the base wave and by the scales of the primary and secondary perturbations.

2. Physical and mathematical model

Inertia-gravity waves have a horizontal wavelength that can easily reach some hundreds of kilometres. We can avoid simulating in such a large domain by rotating the coordinate system so that one coordinate axis is aligned with the direction of propagation of the wave. Figure 1 shows the unrotated and rotated coordinate systems for the case of a *transverse* primary perturbation. We obtain the wave coordinates x, y, z by rotating the earth coordinates x', y', z' first by $90° - \Theta$ about the y' axis and then by $90°$ about the z axis. Then x is the direction of the primary perturbation, y is the direction of the secondary perturbation and the base wave varies in the z direction. In this coordinate system the true vertical direction is described by the unit vector $\mathbf{e}_{z'} = [0, \sin\Theta, \cos\Theta]$.

We can write the non-dimensional Boussinesq equations on an f-plane as

$$\nabla \cdot \mathbf{u} = 0 \tag{2.1a}$$

$$\partial_t \mathbf{u} + \nabla \cdot (\mathbf{uu}) = -\frac{\mathbf{e}_{z'} \times \mathbf{u}}{Ro} - \nabla p + \frac{b}{Fr^2}\mathbf{e}_{z'} + \frac{1}{Re}\nabla^2 \mathbf{u} \tag{2.1b}$$

$$\partial_t b + \nabla \cdot (b\mathbf{u}) = -\hat{N}^2 \mathbf{u} \cdot \mathbf{e}_{z'} + \frac{1}{Pr\, Re}\nabla^2 b, \tag{2.1c}$$

where velocities $\mathbf{u}$ are made non-dimensional by $\mathcal{U}$, all spatial coordinates $\mathbf{x}$ by the length scale $\mathcal{L}$, normalised pressure p by $\mathcal{U}^2$, and time t by $\mathcal{L}/\mathcal{U}$. Density deviations from the background mean are measured by the buoyancy $b = (\theta^* - \bar{\theta})/\theta_0$ ($\bar{\theta}$: background potential temperature, θ^*: local potential temperature, θ_0: reference potential temperature). The non-dimensional parameters are

$$Ro = \frac{\mathcal{U}}{f\mathcal{L}}, \quad Fr = \frac{\mathcal{U}}{\sqrt{g\mathcal{L}}}, \quad Re = \frac{\mathcal{U}\mathcal{L}}{\nu}, \quad \hat{N}^2 = \frac{\partial \bar{b}}{\partial z'} = N^2\frac{\mathcal{L}}{g}, \quad Pr = \frac{\nu}{\alpha}, \tag{2.2}$$

where f is the Coriolis parameter, g is the gravitational acceleration, ν is the kinematic viscosity, $N^2 = (g/\theta_0)d\bar{\theta}/dz'$ is the Brunt-Väisälä frequency and α is the thermal diffusivity.

If we use the rotated coordinates as defined above, we find that the monochromatic gravity wave is an exact solution to the Boussinesq equations 2.1:

$$[u, v, w, b] = a \left[\frac{f/K}{\cos\Theta}\cos\varphi, -\frac{\Omega/K}{\sin\Theta\cos\Theta}\sin\varphi, 0, -\frac{N^2/K}{g\sin\Theta}\cos\varphi \right], \qquad (2.3)$$

where $K = 2\pi/\lambda$ is the base wave number, $\varphi = Kz - \Omega t$ is the phase angle of the wave and the wave frequency Ω is determined by the dispersion relation

$$\Omega^2 = N^2\cos^2\Theta + f^2\sin^2\Theta. \qquad (2.4)$$

The non-dimensional wave amplitude a is defined such that the wave is statically unstable for $a > 1$ and statically stable for $a < 1$. For the detailed derivation of the wave solution in the rotated coordinate system and for the primary and secondary instability analysis, see the work of Achatz (2005, 2007) and Fruman & Achatz (2012).

The flow under investigation is highly three-dimensional and thus requires appropriate definitions for quantifying turbulent mixing. Fully resolved DNS allow for a direct evaluation of the local dissipation rates ε_k and ε_p of kinetic energy $\frac{1}{2}u_i u_i$ and available potential energy $\frac{1}{2}b^2/\hat{N}^2 Fr^2$ from the velocity and buoyancy fields:

$$\varepsilon_k = \frac{1}{Re}\left\langle \left(\partial_{x_j}u_i + \partial_{x_i}u_j\right)\left(\partial_{x_j}u_i + \partial_{x_i}u_j\right)\right\rangle \qquad (2.5)$$

$$\varepsilon_p = \frac{1}{Pr\,Re\,\hat{N}^2\,Fr^2}\left\langle \left(\partial_{x_i}b\right)\left(\partial_{x_i}b\right)\right\rangle\ , \qquad (2.6)$$

where $\langle...\rangle$ indicates an appropriate spatial average. These definitions fully exploit the three-dimensional information available in DNS and, in particular, they do not involve any assumptions about the ratio of horizontal to vertical scales, as sorting procedures (Thorpe 1977) generally do. For a detailed analysis of the energy transfer and dissipation in a stably stratified turbulent flow we refer to Remmler & Hickel (2012b).

The Boussinesq equations are discretised by a finite-volume fractional-step method on a staggered Cartesian mesh. For time advancement the explicit third-order Runge-Kutta scheme of Shu (1988) is used. The time-step is dynamically adapted to satisfy a Courant-Friedrichs-Lewy condition with $CFL \leqslant 1.0$. The spatial discretization is based on non-dissipative central schemes with 4th order accuracy for the advective terms and 2nd order accuracy for the diffusive terms and the pressure Poisson solver. The Poisson equation for the pressure is solved at every Runge-Kutta sub step, using a direct method (based on the Fast Fourier Transform and modified wavenumbers consistent with the underlying staggered grid method) in the z direction and an iterative Stabilised Bi-Conjugate Gradient (BiCGSTAB) solver in the x-y planes. For more details on our flow solver INCA (www.inca-cfd.org), its performance and validation for atmospheric flows we refer to Remmler & Hickel (2012a,b).

3. Test case definition

We consider a statically unstable monochromatic inertia-gravity wave whose parameters are chosen such that inertial and buoyancy forces have similar magnitudes. All physical parameters are summarised in table 1. A comparable 2.5-D case was already investigated by Achatz (2007) and Fruman & Achatz (2012) at a wavelength of $\lambda = 6\,\text{km}$. To reduce the necessary domain size, we repeated their analysis for a wavelength of

wavelength	λ	$= 3\,\mathrm{km}$						
wave vector orientation	Θ	$= 89.5°$						
dimensional wave amplitudes	$\hat{u}$	$= 8.97\,\mathrm{m/s}$	;	$\hat{v}$	$= 14.56\,\mathrm{m/s}$;	$\hat{b}$	$= 0.0234$	
non-dimensional wave amplitude	a	$= 1.2$						
kinematic viscosity	ν	$= 1\,\mathrm{m^2/s}$	;	Re	$= 43665$			
Coriolis parameter	f	$= 1.367 \cdot 10^{-4}\,\mathrm{s^{-1}}$	;	Ro	$= 35.5$			
Brunt-Väisälä frequency	N	$= 0.02\,\mathrm{s^{-1}}$	;	$\hat{N}$	$= 6.12$			
gravitational acceleration	g	$= 9.81\,\mathrm{m/s^2}$	;	Fr	$= 0.0848$			
thermal diffusivity	α	$= 1\,\mathrm{m^2/s}$	;	Pr	$= 1$			
horizontal wavelength	$\lambda_{x'}$	$= 343\,\mathrm{km}$						
(downward) phase velocity	c_p	$= 0.106\,\mathrm{m/s}$						
wave oscillation period	T	$= 7.87\,\mathrm{h}$						

TABLE 1. Physical parameters of the investigated inertia-gravity wave. The non-dimensional numbers were computed based on the wavelength $\mathcal{L} = \lambda = 3\,\mathrm{km}$ and the maximum velocity $\mathcal{U} = \hat{v} = 14.56\,\mathrm{m/s}$.

only $\lambda = 3\,\mathrm{km}$ and found that the wavelengths of the perturbations scale with the base wavelength without changing the general character of the breaking event. The kinematic viscosity used here and in the preceding 2.5-D studies corresponds to a geopotential altitude of 81 km in the US Standard Atmosphere, which is in the upper part of the range where gravity wave breaking occurs and affects the middle-atmosphere circulation. We refrain from using a lower kinematic viscosity (corresponding to lower altitudes) to limit the computational costs and to keep our results comparable to the previous work.

The base wave as described by equation 2.3 is initially disturbed by its leading transverse normal mode (Achatz 2007), which has a wavelength of 3891 m. This wavelength determines the domain size in the x direction. The perturbed wave field is further perturbed by the fastest growing singular vector (SV) of the equations 2.1 linearised about the time dependent nonlinear 2.5-D solution (Fruman & Achatz 2012). This singular vector has a wavelength of 400 m, which determines the domain size in the y direction. The amplitude of the SV perturbation is somewhat arbitrary. We chose the amplitude such that the maximum energy density in the SV is 1% of the maximum initial energy density in the wave and primary normal mode. The initial condition is displayed in figure 1. The domain size for the simulations presented here was $3981\,\mathrm{m} \times 400\,\mathrm{m} \times 3000\,\mathrm{m}$. We conducted two simulations on different grids: a fine simulation designed to fully resolve all turbulence scales and a second, coarser simulation at approximately half the resolution. The grid of the fine simulation had $1350 \times 128 \times 1000$ cells, which corresponds to a uniform cell size $\Delta \approx 3\,\mathrm{m}$ in all directions. The coarse grid had a resolution of $\Delta \approx 6\,\mathrm{m}$ ($640 \times 64 \times 500$). The governing equations were integrated in time for 34000 s (fine) and 60000 s (coarse).

4. Results and discussion

We verified the chosen grid resolution by computing the Kolmogorov length $\eta = \nu^{3/4}\varepsilon_k^{-1/4}$ with the maximum of the kinetic energy dissipation rate in the domain, see figure 2(a). According to Yamazaki *et al.* (2002), the low-order statistics of turbulence are basically unaffected by the resolution as long as $k_{max}\eta \gtrsim 1$, i. e. $\Delta < \pi\eta$. By this criterion, we find that the fine simulation is fully resolved and the coarse simulation is insufficiently resolved. Nevertheless, the coarse simulation remains free of unphysical oscillations with-
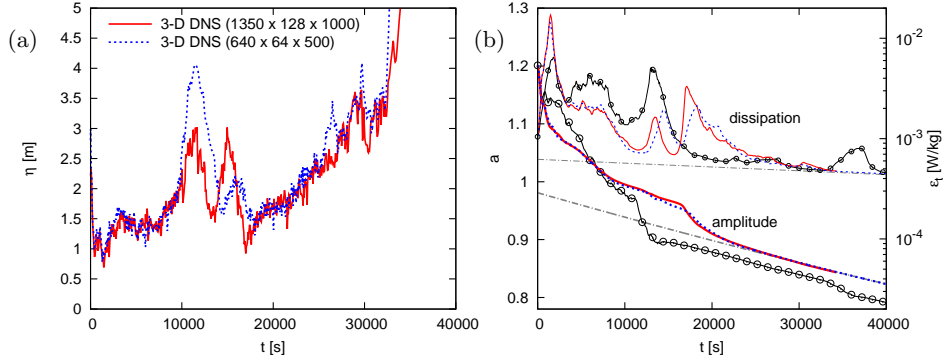
FIGURE 2. Time series for (a) Kolmogorov length and (b) nondimensional amplitude of the primary wave and total energy dissipation. Solid lines: full resolution 3-D DNS; dashed lines: half resolution 3-D DNS; symbols: 2.5-D DNS; dash-dotted lines: laminar decay.
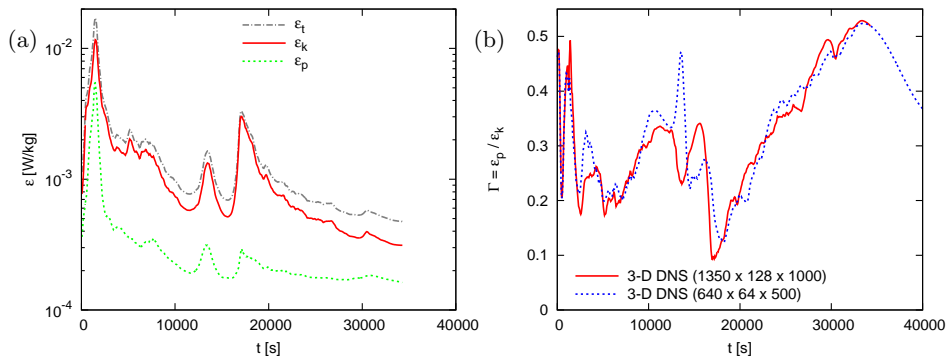

FIGURE 3. Spatial mean values of energy dissipation: (a) contributions to the energy dissipation for the fine grid, (b) $\Gamma = \varepsilon_p/\varepsilon_k$ in coarse and fine simulation.

out requiring any artificial numerical dissipation, which we attribute to the good spectral resolution properties (modified wavenumber) of staggered-grid methods.

The most important quantities extracted from the simulations are the amplitude of the primary wave and the spatially averaged energy dissipation rate, shown in figure 2(b). For comparison, we added the curves for a purely laminar wave decaying like $a(t) = a_0 e^{-\nu K^2 t}$ with the parameter a_0 fitted to match the final (laminar) state of the original wave.

During the first wave period ($T = 28342\,\mathrm{s}$), there are three distinct occurrences of wave breaking characterised by a rapid decrease of the wave amplitude and a strongly increased total dissipation rate. After $t = 35000\,\mathrm{s}$ the wave has become laminar and no longer shows signs of turbulence and enhanced dissipation.

Both 3-D simulations predict basically the same temporal development of the amplitude. There are some differences in the dissipation rate between the fine and coarse simulations, especially during the second and third breaking events. However, the overall agreement between the two simulations is very good. This indicates that the full resolution simulation yields a grid-converged solution.

We compare the 3-D DNS to a 2.5-D simulation performed with the model of Achatz (2007) initialised with just the IGW and the leading transverse normal mode. The wave amplitude from the 2.5-D simulation with $\Delta \approx 3\,\mathrm{m}$ is also plotted in figure 2(b). While the temporal evolution of the wave amplitude is not exactly the same in the 2.5-D and
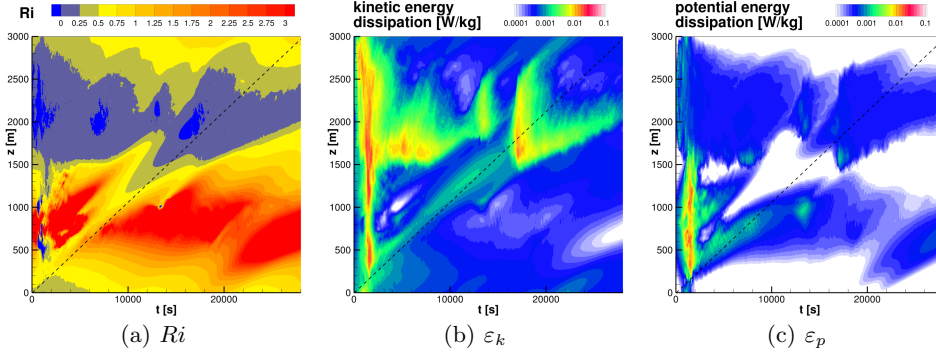
FIGURE 4. Hovmöller plots of Richardson number (a) and energy dissipation (b and c). The dashed lines indicate a fixed position in space while the coordinate system is moving downward with the phase speed of the wave.

3-D simulations, the duration of the breaking event and the total energy decrease due to the breaking are similar. Details, such as the secondary breaking events observed in the 3-D simulations are not reproduced by the 2.5-D simulation and the breaking lasts longer in the 3-D simulations.

We decomposed the energy dissipation into kinetic ε_k and potential energy dissipation ε_p in figure 3(a). Both show peaks during the three breaking events, but the peaks of ε_k are much more pronounced, so that the ratio $\Gamma = \varepsilon_p/\varepsilon_k$ is temporally reduced during these events (figure 3(b)). The strongest reduction is observed during the third event. This means that the energy dissipation is caused by strong gradients in the velocity field rather than the buoyancy field during this event.

The dissipation rates averaged in the x-y plane (perpendicular to the wave vector) are plotted against time in figure 4. The coordinate system is moving with the phase speed of the primary wave, so the most unstable region is always in the upper half of the domain and the most stable part in the lower half. An indicator for stability is the Richardson number

$$Ri = \frac{\hat{N}^2 + \langle \partial_{z'} b \rangle}{Fr^2 \left\langle (\partial_{z'} u')^2 + (\partial_{z'} v')^2 \right\rangle} = \frac{\hat{N}^2 + \langle \sum_i \partial_{x_i} b \; e_{z',i} \rangle}{Fr^2 \left\langle \sum_k \left(\sum_j \partial_{x_k} u'_{h,j} e_{z',k} \right)^2 \right\rangle} \, , \qquad (4.1)$$

where $u'_{h,j} = u_j - (\mathbf{u} \cdot \mathbf{e}_{z'}) e_{z',j}$ is the horizontal velocity in the earth frame and $\langle ... \rangle$ indicates an average in the x-y plane. The Richardson number is shown in figure 4(a). Blue regions indicate static instability, because the Richardson number is negative there. Violet regions correspond to $0 < Ri < 0.25$ and hence dynamic instability. Comparison of figures 4(a) and 4(b) shows that turbulent dissipation of kinetic energy is spatially and temporally correlated with static and dynamic instability of the mean state. Note that this is an average Richardson number in the x-y-plane, so locally the value of Ri can strongly differ from this average.

The first breaking event triggered by the initial perturbation is spread over the whole domain. Turbulence (indicated by enhanced kinetic energy dissipation, figure 4(b)) is generated in the stable and unstable regions of the wave, but only in the stable region does this lead to strong potential energy dissipation, see figure 4(c). Both secondary breaking events (around $t = 12000\,\mathrm{s}$ and $t = 16000\,\mathrm{s}$) have hardly any signature in ε_p. Most energy is dissipated mechanically in the unstable half of the domain.

Figure 5 shows some snapshots of the wave field during the first breaking event. The
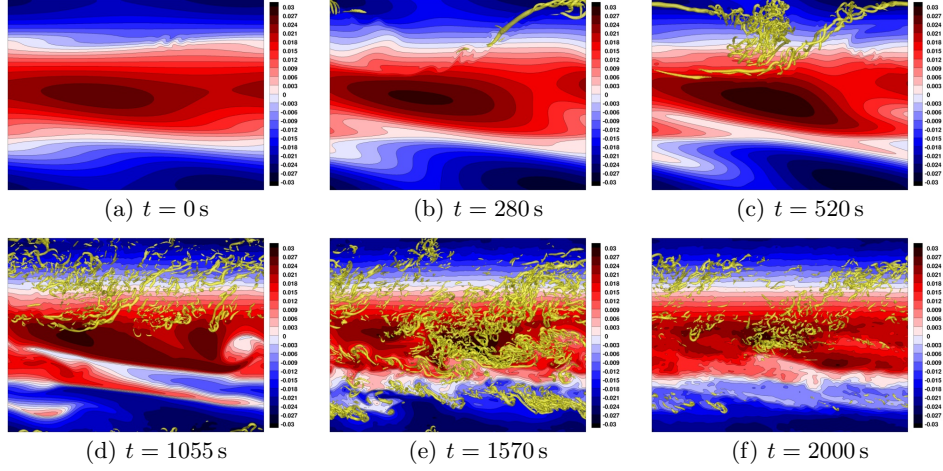
FIGURE 5. Temporal evolution of the first breaking event. Background: plane at $y = 400\,\mathrm{m}$ coloured by buoyancy; foreground: iso-surface of $Q = 0.004\,\mathrm{s}^{-2}$, indicating turbulent vortices.
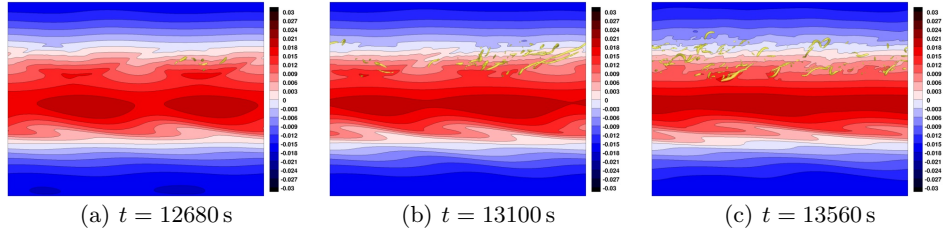

FIGURE 6. Temporal evolution of the second breaking event. Colouring as in figure 5.
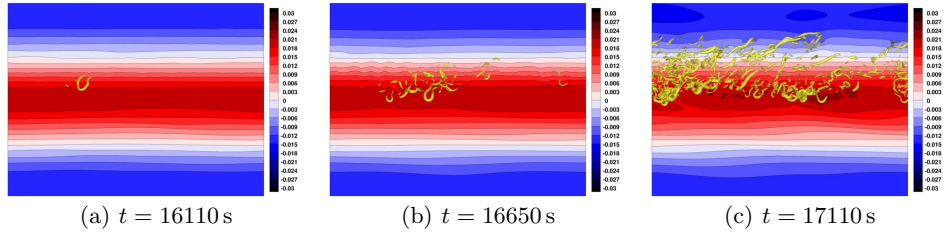

FIGURE 7. Temporal evolution of the third breaking event. Colouring as in figure 5.

yellow iso-surface of $Q = \frac{1}{2}\left(|\mathbf{\Omega}|^2 - |\mathbf{S}|^2\right) = \frac{1}{8}\left(|\partial_{x_j}u_i - \partial_{x_i}u_j|^2 - |\partial_{x_j}u_i + \partial_{x_i}u_j|^2\right)$ is used to visualise turbulent vortices. During the first $1000\,\mathrm{s}$ strongly three-dimensional turbulence structures develop in the unstable half. The strong perturbations of the isopycnals quickly vanish. In the meantime a strong two-dimensional overturning develops in the stable region, eventually breaking and generating three-dimensional turbulence around $t = 1500\,\mathrm{s}$. While turbulence is sustained for a long time in the unstable half of the wave, it decays quickly through the damping effect of stratification in the stable half. In the 2.5-D simulations, the turbulence in the stable half of the wave is much longer lived. Achatz & Schmitz (2006a) and Achatz (2007) attribute this turbulence to small scale waves excited near the level of maximum static instability encountering a critical level associated with the zero in the v component of the original wave. This effect appears to be less important in 3D.
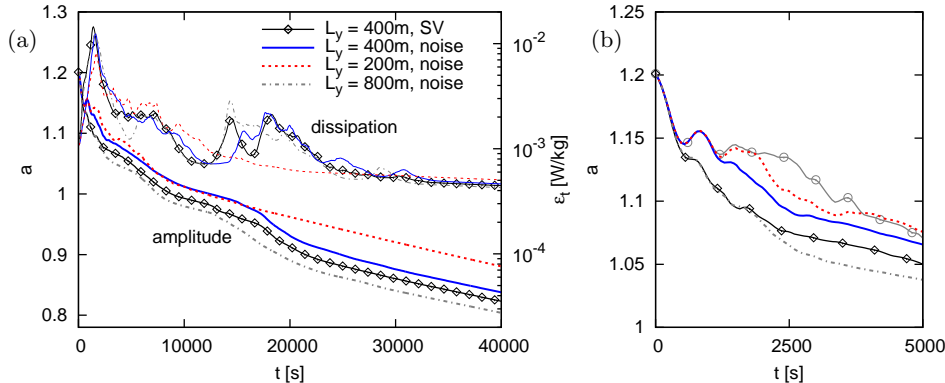
FIGURE 8. Time series for the non-dimensional amplitude of the primary wave and total energy dissipation for different secondary perturbations and domain sizes. (a) full time range, (b) amplitude during the first 5000 s (circles: 2.5-D simulation)

The second breaking event (figure 6) is much weaker than the first. It is initiated by a growing instability of the large-scale wave that spans both the statically stable and unstable regions. Note that the nondimensional amplitude of the wave drops below the threshold of static instability right before the event becomes visible. Unlike the first event, the instability is too weak to generate turbulence in the stable region, but some turbulence appears in the unstable region.

The third breaking event (figure 7) is stronger than the second, but still much weaker than the first. It is not preceded by a visible instability of the primary wave. The isopycnals in figure 7(a) are almost perfectly horizontal. The turbulence emerges "out of nothing" in the unstable region, causes some mixing there and eventually decays. An explanation can be found in figure 4(b). By the time of the third breaking event, the primary wave has propagated about half a wavelength downwards, so the unstable region of the wave has arrived at the fixed point in space where the wave was most stable at the beginning of the simulation. There seems to be some "leftover" turbulence generated by the first breaking, which is amplified as soon as the stability in this region has decreased sufficiently. Therefore, the third event is not really a third breaking event, but rather a burst of turbulence triggered by the arrival of the dynamically unstable part of the wave in a region preconditioned by the first breaking event.

In order to investigate the effect of the particular choice of secondary perturbation on the three-dimensionalisation and overall evolution of the flow, we conducted additional simulations at the 6 m resolution with the SV perturbation replaced by low level white noise and with the domain size L_y in the direction of the secondary perturbation varied between 200 m and 800 m. Since white noise is a superposition of perturbations with all possible scales, it also contains contributions of the SV that leads to maximum energy growth, as long as the domain size is large enough. For $L_y = 400$ m and $L_y = 800$ m, the wave amplitude decay and energy dissipation are similar to those of the SV initialization, but for the smaller domain size the initial peak of the dissipation rate is smaller and the second and third breaking events are missing completely, see figure 8(a). A close look at the first hour of the integrations in figure 8(b) reveals that the quick three-dimensionalisation seen in the SV simulation occurs only in the simulation with $L_y = 800$ m, while the other two white noise simulations follow the 2.5-D solution, and three-dimensional effects take longer to emerge. This reassures us that the SV is physically

meaningful and representative of the perturbations that grow spontaneously even in a larger domain with many more degrees of freedom.

5. Conclusion

We have presented the first turbulence resolving three-dimensional simulations of an inertia-gravity wave breaking under environmental conditions realistic for the middle atmosphere. The breaking was stimulated by optimal perturbations of the wave derived from linear theory.

The primary breaking of the unstable wave stretches over the complete space of the wave and is responsible for a strong reduction of the wave amplitude by more than 12% within less than 10000 s (on the order of half a wave period). A pure laminar decay of the wave would take three times as long for the same amplitude reduction.

We observed a second and a third burst of turbulence after the first breaking event. During these secondary events turbulence appears only in the unstable region of the wave and most energy is dissipated mechanically rather than thermally. The second event is negligible with regard to its reduction of the amplitude of the primary wave. It is preceded by a weak instability of the wave, which has an amplitude close to the threshold of static instability at that time. During the third event the reduction of the primary wave amplitude is more severe, amounting to about 5% of the amplitude. However, the third event is not really a breaking event, but rather a burst of turbulence in the unstable region of the wave triggered by disturbances created during the first breaking of the wave.

As previous simulations of breaking IGWs employed a 2.5-D approximation, i.e. a two-dimensional domain and three velocity components, we conducted a 2.5-D simulation of the same wave breaking case to investigate the effects of three-dimensionality. Details such as the secondary breaking events observed in the 3-D DNS are not reproduced by the 2.5-D simulation and the breaking lasts longer in the 3-D simulations. However, the overall results in terms of total amplitude reduction and breaking duration are similar between the 3-D and 2.5-D simulations. This similarity is important to note, since the singular vector analysis that we used to determine the domain size for the 3-D DNS was based on the 2.5-D simulation.

DNS where we replaced the secondary SV perturbation by white noise and varied the domain size, showed that a SV initialization is both physically meaningful and efficient, as it leads to a realistic three-dimensionalisation of the flow in the smallest possible domain.

With these first fully resolved three-dimensional direct numerical simulations of a breaking IGW we hope to present a valuable reference case for testing and validation of models involving less brute-force resolution and more physics-based parameterisation. This may include large eddy simulations as well as more abstract methods like WKBJ models, which can lead to efficient and more reliable representation of gravity waves in atmospheric circulation models.

REFERENCES

ACHATZ, U. 2005 On the role of optimal perturbations in the instability of monochromatic gravity waves. *Phys. Fluids* **17** (9), 094107.

ACHATZ, U. 2007 The primary nonlinear dynamics of modal and nonmodal perturbations of monochromatic inertia gravity waves. *J. Atmos. Sci.* **64**, 74.

ACHATZ, U. & SCHMITZ, G. 2006a Optimal growth in inertia-gravity wave packets: Energetics, long-term development, and three-dimensional structure. *J. Atmos. Sci.* **63**, 414–434.

ACHATZ, U. & SCHMITZ, G. 2006b Shear and static instability of inertia-gravity wave packets: Short-term modal and nonmodal growth. *J. Atmos. Sci.* **63**, 397–413.

AFANASYEV, Y. D. & PELTIER, W. R. 2001 Numerical simulations of internal gravity wave breaking in the middle atmosphere: The influence of dispersion and three-dimensionalization. *J. Atmos. Sci.* **58**, 132–153.

ANDREASSEN, Ø., ØYVIND HVIDSTEN, P., FRITTS, D. C. & ARENDT, S. 1998 Vorticity dynamics in a breaking internal gravity wave. Part 1. Initial instability evolution. *J. Fluid Mech.* **367**, 27–46.

ANDREASSEN, Ø., WASBERG, C. E., FRITTS, D. C. & ISLER, J. R. 1994 Gravity wave breaking in two and three dimensions 1. Model description and comparison of two-dimensional evolutions. *J. Geophys. Res.* **99**, 8095–8108.

BLUMEN, W. & MCGREGOR, C. D. 1976 Wave drag by three-dimensional mountain lee-waves in nonplanar shear flow. *Tellus* **28** (4), 287–298.

BRETHERTON, F. P. 1969 Waves and turbulence in stably stratified fluids. *Radio Sci.* **4** (12), 12791287.

CHUN, H.-Y. & BAIK, J.-J. 1998 Momentum flux by thermally induced internal gravity waves and its approximation for large-scale models. *J. Atmos. Sci.* **55**, 3299–3310.

DÖRNBRACK, A. 1998 Turbulent mixing by breaking gravity waves. *J. Fluid Mech.* **375**, 113–141.

DRAZIN, P. G. 1977 On the instability of an internal gravity wave. *Proc. Roy. Soc. London A* **356** (1686), 411–432.

DUNKERTON, T. J. 1997a The role of gravity waves in the quasi-biennial oscillation. *J. Geophys. Res.* **102**, 26053–26076.

DUNKERTON, T. J. 1997b Shear instability of internal inertia-gravity waves. *J. Atmos. Sci.* **54**, 1628–1641.

FRITTS, D. C. & ALEXANDER, M. J. 2003 Gravity wave dynamics and effects in the middle atmosphere. *Rev. Geophys.* **41**, 1003.

FRITTS, D. C., ISLER, J. R. & ANDREASSEN, Ø. 1994 Gravity wave breaking in two and three dimensions 2. Three-dimensional evolution and instability structure. *J. Geophys. Res.* **99**, 8109–8124.

FRITTS, D. C., WANG, L., WERNE, J., LUND, T. & WAN, K. 2009 Gravity wave instability dynamics at high reynolds numbers. Parts I and II. *J. Atmos. Sci.* **66** (5), 1126–1171.

FRUMAN, M. D. & ACHATZ, U. 2012 Secondary instabilities in breaking inertia-gravity waves. *J. Atmos. Sci.* **69**, 303–322.

HOLTON, J. R. 1982 The role of gravity wave induced drag and diffusion in the momentum budget of the mesosphere. *J. Atmos. Sci.* **39**, 791–799.

HOUGHTON, J. T. 1978 The stratosphere and mesosphere. *Quart. J. Roy. Meteor. Soc.* **104** (439), 1–29.

KLOSTERMEYER, J. 1982 On parametric instabilities of finite-amplitude internal gravity waves. *J. Fluid Mech.* **119**, 367–377.

LELONG, M.-P. & DUNKERTON, T. J. 1998 Inertia-gravity wave breaking in three dimensions. Parts I and II. *J. Atmos. Sci.* **55**, 2473–2501.

LILLY, D. K. 1972 Wave momentum flux - A GARP problem. *Bull. Am. Meteor. Soc.* **53**, 17–23.

LINDZEN, R. S. 1981 Turbulence and stress owing to gravity wave and tidal breakdown. *J. Geophys. Res.* **86**, 9707–9714.

MCLANDRESS, C. 1998 On the importance of gravity waves in the middle atmosphere and their parameterization in general circulation models. *J. Atmos. Sol.-Terr. Phy.* **60** (14), 1357 – 1383.

MIED, R. P. 1976 The occurrence of parametric instabilities in finite-amplitude internal gravity waves. *J. Fluid Mech.* **78** (4), 763–784.

NAPPO, C. J. 2002 *An introduction to atmospheric gravity waves*. Academic Press.

S. Remmler, M. D. Fruman and S. Hickel

REMMLER, S. & HICKEL, S. 2012*a* Direct and large eddy simulation of stratified turbulence. *Int. J. Heat Fluid Flow* **35**, 13–24.

REMMLER, S. & HICKEL, S. 2012*b* Spectral structure of stratified turbulence: Direct numerical simulations and predictions by large eddy simulation. *Theor. Comput. Fluid Dyn.* Published online: DOI 10.1007/s00162-012-0259-9.

SAWYER, J. S. 1959 The introduction of the effects of topography into methods of numerical forecasting. *Quart. J. Roy. Meteor. Soc.* **85** (363), 31–43.

SHU, C.-W. 1988 Total-variation-diminishing time discretizations. *SIAM J. Sci. Stat. Comput.* **9(6)**, 1073–1084.

THORPE, S. A. 1977 Turbulence and mixing in a scottish loch. *Philos. Trans. Roy. Soc. London A* **286** (1334), pp. 125–181.

WINTERS, K. B. & D'ASARO, E. A. 1994 Three-dimensional wave instability near a critical level. *J. Fluid Mech.* **272**, 255–284.

YAMAZAKI, Y., ISHIHARA, T. & KANEDA, Y. 2002 Effects of wavenumber truncation on high-resolution direct numerical simulation of turbulence. *J. Phys. Soc. Jpn.* **71**, 777.

JFM RAPIDS

journals.cambridge.org/rapids
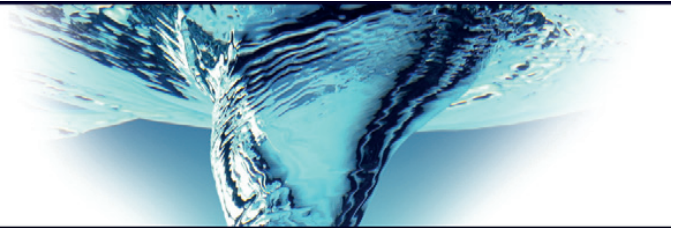
Spectral eddy viscosity of stratified turbulence

Sebastian Remmler† and Stefan Hickel

Institute of Aerodynamics and Fluid Mechanics, Technische Universität München,
85747 Garching bei München, Germany

The spectral eddy viscosity (SEV) concept is a handy tool for the derivation of large-eddy simulation (LES) turbulence models and for the evaluation of their performance in predicting the spectral energy transfer. We compute this quantity by filtering and truncating fully resolved turbulence data from direct numerical simulations (DNS) of neutrally and stably stratified homogeneous turbulence. The results qualitatively confirm the plateau–cusp shape, which is often assumed to be universal, but show a strong dependence on the test filter size. Increasing stable stratification not only breaks the isotropy of the SEV but also modifies its basic shape, which poses a great challenge for implicit and explicit LES methods. We find indications that for stably stratified turbulence it is necessary to use different subgrid-scale (SGS) models for the horizontal and vertical velocity components. Our data disprove models that assume a constant positive effective turbulent Prandtl number.

Key words: homogeneous turbulence, stratified turbulence, turbulence modelling

1. Introduction

In large-eddy simulation (LES) the unresolved part of the turbulent velocity field is modelled by a subgrid-scale (SGS) model. This SGS turbulence model is supposed to modify the flow energy balance in the same way as the small-scale structures of fully resolved turbulence would do. Most SGS models are, at least to some extent, based on an eddy viscosity hypothesis. This means that the SGS model dissipates turbulence energy, especially at the smallest resolved scales, but also on larger scales. Heisenberg (1948) introduced the concept of modelling nonlinear interactions in turbulence by a scale-dependent spectral eddy viscosity (SEV). The underlying theory has since been refined by Kraichnan (1976) and others. Although impractical in real-space-based numerical simulations, the SEV as a function of wavenumber can be used to verify the correct behaviour of SGS models in a set-up of homogeneous (but not necessarily isotropic) turbulence.

† Email address for correspondence: remmler@tum.de

Algebraic expressions for the SEV have been derived based on the eddy-damped quasi-normal Markovian (EDQNM) theory (Orszag 1970) for isotropic turbulence. A different approach was pursued by Domaradzki *et al.* (1987), who computed the SEV from direct numerical simulations (DNS) of fully resolved turbulence by truncating the results in spectral space. They found some agreement with the theoretical results of Kraichnan (1976), but also differences due to the finite inertial range in their simulations. Despite these discrepancies, the behaviour of isotropic turbulence is quite well understood. On the other hand, corresponding numerical studies for anisotropic turbulence are still rare.

Semi-analytical expressions for the eddy-viscosity and eddy-diffusivity spectra for stratified turbulence are given by Godeferd & Cambon (1994), Staquet & Godeferd (1998) and Godeferd & Staquet (2003) in the framework of the EDQNM approximation. Another form was obtained by Sukoriansky, Galperin & Staroselsky (2005) and Galperin & Sukoriansky (2010) through quasi-normal scale elimination (QNSE). These theoretical results show that turbulence anisotropy can significantly affect SGS energy dissipation in flows dominated by stable stratification, solid body rotation or shear.

In validating an SGS model for stably stratified flows, we have generated an extensive database of DNS results for homogeneous stratified turbulence. The simulations cover a wide range of Froude numbers from the neutrally stratified to the strongly stratified regime (Remmler & Hickel 2012, 2013). We now analyse these results with respect to the anisotropic, i.e. direction-dependent, SEV. To achieve this, we follow Domaradzki *et al.* (1987) and filter the DNS results to coarser resolutions in several steps and compute the SGS stress necessary to obtain the same large-scale result on the coarse grid as on the full DNS grid. Similar studies were presented by Kitsios, Frederiksen & Zidikheri (2012, 2013) for the quasi-geostrophic equations and by Khani & Waite (2013) for the Boussinesq equations using one-dimensional SEV spectra based on grid truncation in the horizontal or vertical direction.

In the following section, we will briefly outline the governing equations, review the concept of SEV and diffusivity and comment on our flow solver. A short overview of the computational set-up follows. The results section presents results for isotropic turbulence in comparison to the work of Kraichnan (1976) and Domaradzki *et al.* (1987) as well as SEV data in a two-dimensional spectral space for stably stratified homogeneous turbulence. Furthermore, we use these newly obtained reference data to evaluate the performance of different existing LES methods. One model follows the implicit LES paradigm, i.e. the discretisation scheme and the SGS model are merged. The other models combine an explicit approximation of the SGS tensor with a non-dissipative central discretisation.

2. Computational methods

2.1. *Boussinesq equations*

The flows to be investigated are characterised by a stable background stratification, so the density is not constant. However, the density differences are small and the flow velocities are much smaller than the speed of sound, which justifies the Boussinesq approximation. The non-dimensional Boussinesq equations for a stably stratified fluid in Cartesian coordinates read

$$\nabla \cdot \boldsymbol{u} = 0, \tag{2.1a}$$

$$\partial_t \boldsymbol{u} + \nabla \cdot (\boldsymbol{u}\boldsymbol{u}) = -\nabla p - \frac{\rho}{Fr_0^2}\hat{\boldsymbol{e}}_z + \frac{1}{Re_0}\nabla^2 \boldsymbol{u} + \boldsymbol{F}, \tag{2.1b}$$

$$\partial_t \rho + \nabla \cdot (\rho \boldsymbol{u}) = \boldsymbol{u} \cdot \hat{\boldsymbol{e}}_z + \frac{1}{Pr\,Re_0} \nabla^2 \rho, \tag{2.1c}$$

where the velocities are made non-dimensional by a reference velocity $\mathscr{U}$, all spatial coordinates by the length scale $\mathscr{L}$, pressure by $\overline{\rho}\mathscr{U}^2$, time by $\mathscr{L}/\mathscr{U}$ and density fluctuation $\rho = \rho^* - \overline{\rho}$ (ρ^* is the local absolute density, $\overline{\rho}$ is the background density) by the background density gradient $\mathscr{L}|\mathrm{d}\overline{\rho}/\mathrm{d}z|$. The vertical unit vector is $\hat{\boldsymbol{e}}_z$ and $\boldsymbol{F}$ denotes a large-scale forcing, see (3.1). The non-dimensional flow parameters are

$$Fr_0 = \frac{\mathscr{U}}{N\mathscr{L}}, \quad Re_0 = \frac{\mathscr{U}\mathscr{L}}{\nu}, \quad Pr = \frac{\nu}{D}, \tag{2.2a–c}$$

where ν is the kinematic viscosity, $N = \sqrt{-g/\overline{\rho}\,\mathrm{d}\overline{\rho}/\mathrm{d}z}$ is the Brunt–Väisälä frequency and D is the thermal diffusivity of the fluid. We chose a Prandtl number of $Pr = 0.7$, corresponding to typical values in the atmosphere.

The local dissipation rates ε_k and ε_p of kinetic energy $E_k = (1/2)\sum_i u_i u_i$ and available potential energy $E_p = (1/2)\rho^2/Fr_0^2$ can be computed directly from the velocity and density field,

$$\varepsilon_k = \frac{\boldsymbol{u} \cdot \nabla^2 \boldsymbol{u}}{Re_0}, \quad \varepsilon_p = \frac{\rho \nabla^2 \rho}{Pr\,Re_0\,Fr_0^2}. \tag{2.3a,b}$$

With the spatial mean values of kinetic energy $\langle E_k \rangle$ and kinetic energy dissipation $\langle \varepsilon_k \rangle$, we define the local Froude and Reynolds number as well as the buoyancy Reynolds number $\mathscr{R}$, (Brethouwer *et al.* 2007)

$$Fr = \frac{Fr_0 \mathscr{L}}{\mathscr{U}} \frac{\langle \varepsilon_k \rangle}{\langle E_k \rangle}, \quad Re = \frac{Re_0}{\mathscr{U}\mathscr{L}} \frac{\langle E_k \rangle^2}{\langle \varepsilon_k \rangle}, \quad \mathscr{R} = Re\,Fr^2, \tag{2.4a–c}$$

which are used to characterise the flow regime. The overturning wavenumber (Dougherty 1961; Ozmidov 1965)

$$k_O = \frac{N^{3/2}}{\varepsilon_k^{1/2}} \tag{2.5}$$

approximately separates small scales which are practically isotropic and large scales which are affected by buoyancy.

2.2. *Spectral eddy viscosity*

The momentum equation for incompressible homogeneous turbulence in spectral space reads

$$\left(\partial_t + \nu k^2\right) \hat{u}_i(\boldsymbol{k}) = \hat{S}_i(\boldsymbol{k}) - \mathrm{i} \sum_{j,q} k_q P_{ij}(\boldsymbol{k}) \sum_{\boldsymbol{m}} \hat{u}_j(\boldsymbol{m}) \hat{u}_q(\boldsymbol{k} - \boldsymbol{m}), \tag{2.6}$$

where $P_{ij}(\boldsymbol{k}) = \delta_{ij} - k_i k_j/k^2$ is the projection tensor onto a divergence-free velocity field, δ_{ij} is the Kronecker symbol, $k^2 = |\boldsymbol{k}|^2 = k_1^2 + k_2^2 + k_3^2$ is the wavenumber and $\hat{S}_i$ contains all forces on the fluid. The kinetic energy of a single mode $\boldsymbol{k}$ is

$$e_i(\boldsymbol{k}) = \tfrac{1}{2}\hat{u}_i(\boldsymbol{k})\hat{u}_i^{\star}(\boldsymbol{k}), \tag{2.7}$$

where $(\cdot)^{\star}$ denotes the complex conjugate. Implicit summation over repeated indices does not apply throughout this paper. If required, summation is directly indicated. We refer to $e(\boldsymbol{k}) = \sum_i e_i(\boldsymbol{k})$ as the total kinetic energy and to $e_h(\boldsymbol{k}) = e_1(\boldsymbol{k}) + e_2(\boldsymbol{k})$ and

$e_v(\boldsymbol{k}) = e_3(\boldsymbol{k})$ as the horizontal and vertical kinetic energy, respectively (assuming for simplicity that the vertical direction coincides with the x_3 direction).

The temporal evolution of $e_i(\boldsymbol{k})$ is governed by

$$\left(\partial_t + 2\nu k^2\right) e_i(\boldsymbol{k}) - \mathrm{Re}\left\{\hat{S}_i \hat{u}_i^\star(\boldsymbol{k})\right\} = T_i(\boldsymbol{k}), \tag{2.8}$$

with the transfer term

$$T_i(\boldsymbol{k}) = \sum_{j,q} k_q P_{ij}(\boldsymbol{k}) \mathrm{Im}\left\{\sum_{\boldsymbol{m}} \hat{u}_i^\star(\boldsymbol{k})\hat{u}_j(\boldsymbol{m})\hat{u}_q(\boldsymbol{k}-\boldsymbol{m})\right\}. \tag{2.9}$$

If the numerical discretisation acts as a perfect low-pass filter, only wavenumbers $|\boldsymbol{k}| < k_c$ are resolved and we can split the transfer term $T(\boldsymbol{k})$ into

$$T(\boldsymbol{k}) = \sum_i T_i(\boldsymbol{k}) = T^-(\boldsymbol{k}, k_c) + T^+(\boldsymbol{k}, k_c); \quad |\boldsymbol{k}| < k_c, \tag{2.10}$$

where $T^-(\boldsymbol{k}, k_c)$ involves only interactions of wavenumbers $|\boldsymbol{k}| < k_c$, $|\boldsymbol{m}| < k_c$, $|\boldsymbol{k} - \boldsymbol{m}| < k_c$ and is thus resolved by the numerical grid. The SGS transfer $T^+(\boldsymbol{k}, k_c)$ represents all unresolved interactions and has to be modelled in an LES.

We can model the average SGS transfer by using the SEV hypothesis

$$\nu_t(k, k_c) = \frac{\left\langle T^+(\boldsymbol{k}, k_c)\right\rangle_s}{2k^2 \left\langle e(\boldsymbol{k})\right\rangle_s} \quad \text{or} \quad \nu_t(\boldsymbol{k}', k_c) = \frac{\left\langle T^+(\boldsymbol{k}, k_c)\right\rangle_c}{2k^2 \left\langle e(\boldsymbol{k})\right\rangle_c}. \tag{2.11a,b}$$

The average $\langle \cdots \rangle_s$ is taken over time and on thin spherical shells with radius $|\boldsymbol{k}|$ for isotropic turbulence, which reduces the wavenumber space to one dimension k. For flows with spectra symmetric about the k_z-axis, such as rotating or stratified turbulence, we average $\langle \cdots \rangle_c$ over thin cylindrical shells with radius $k_h = |\boldsymbol{k}_h| = \sqrt{k_x^2 + k_y^2}$. The result is defined in a two-dimensional wavenumber space $\boldsymbol{k}' = (k_h, k_z)$. We compute the SEV for the horizontal and vertical kinetic energy by

$$\nu_{t,h} = \frac{1}{4k^2}\left[\frac{\left\langle T_1^+\right\rangle}{\left\langle e_1\right\rangle} + \frac{\left\langle T_2^+\right\rangle}{\left\langle e_2\right\rangle}\right]; \quad \nu_{t,v} = \frac{\left\langle T_3^+\right\rangle}{2k^2 \left\langle e_3\right\rangle}. \tag{2.12a,b}$$

For isotropic turbulence the SEV is generally normalised by the cutoff wavenumber and the kinetic energy at this wavenumber

$$\nu_t^+(k/k_c) = \nu_t(k, k_c)\sqrt{\frac{k_c}{E(k_c)}}, \tag{2.13}$$

where the integral kinetic energy is $E(k) = 4\pi k^2 \langle e(\boldsymbol{k})\rangle$. This is only a useful definition if the energy spectrum is known (e.g. $E(k) = C_K \varepsilon^{2/3} k^{-5/3}$) at the cutoff wavenumber. Otherwise, it is helpful to use the original formulation of Kraichnan (1976),

$$\nu_t^*(k/k_c) = \nu_t(k, k_c)\varepsilon_k^{-1/3} k_c^{4/3}. \tag{2.14}$$

For isotropic turbulence with an infinite inertial range, ν_t^+ and ν_t^* are simply related by $\nu_t^* = \sqrt{C_K}\nu_t^+$, where C_K is the Kolmogorov constant. An algebraic model equation for $\nu_t^+(k/k_c)$ in isotropic turbulence is given by Chollet (1984).

As we have a fully resolved simulation of homogeneous turbulence, we can extract the full transfer term $T(\boldsymbol{k})$. By filtering the solution to a coarser test grid, we find the resolved term $T^-(\boldsymbol{k}, k_c)$ for the test grid resolution and then compute the SGS transfer $T^+(\boldsymbol{k}, k_c)$ from (2.10).

We can derive an expression for the spectral eddy diffusivity (SED) of any conserved scalar, such as the density fluctuation

$$D_t(\boldsymbol{k}', k_c) = \frac{\left\langle T_p^+(\boldsymbol{k}, k_c) \right\rangle_c}{2k^2 \left\langle e_p(\boldsymbol{k}) \right\rangle_c}, \quad (2.15)$$

where T_p^+ is the SGS transfer term in the density equation and

$$e_p(\boldsymbol{k}) = \tfrac{1}{2}\hat{\rho}(\boldsymbol{k})\hat{\rho}^\star(\boldsymbol{k}) \quad (2.16)$$

is the spectral potential energy density. We normalise the SED by

$$D_t^*(k/k_c) = D_t(k, k_c)\varepsilon_k^{-1/3}k_c^{4/3} \quad (2.17)$$

using the kinetic energy dissipation rate ε_k as for the SEV. This normalisation follows from the common belief that the eddy diffusivity can roughly be modelled with a turbulent Prandtl number, which is backed by spectral turbulence theory for high Reynolds numbers and Prandtl numbers of order unity (see equation (23) in Hickel, Adams & Mansour 2007).

We define the effective turbulent Prandtl number for a certain cutoff wavenumber k_c in the spectral space,

$$Pr_t(\boldsymbol{k}, k_c) = \frac{\nu_t(\boldsymbol{k}, k_c)}{D_t(\boldsymbol{k}, k_c)}. \quad (2.18)$$

2.3. *Flow solver*

With our flow solver INCA, the Boussinesq equations are discretised by a fractional-step method on a staggered Cartesian mesh. For time advancement the explicit third-order Runge–Kutta scheme of Shu (1988) is used. The time step is dynamically adapted to satisfy a Courant–Friedrichs–Lewy condition (including the limits for advective, diffusive and buoyancy terms) with CFL $\leqslant$ 1.0. The Poisson equation for the pressure is solved at every Runge–Kutta substep.

2.4. *Spatial discretisation and SGS models*

The spatial discretisation is based on a finite-volume method. We use a non-dissipative central-difference scheme with second-order accuracy for the diffusive terms and the pressure Poisson solver. The discretisation of the advective terms depends on the application. For the DNS we use a non-dissipative fourth-order central difference scheme (CDS4).

For LES on much coarser grids a turbulence SGS model is required. In the present study we tested four different SGS models. The first model is the Adaptive Local Deconvolution Method (ALDM). It is an implicit SGS model, i.e. the numerical discretisation of the advective terms acts as a sink of energy by providing a suitable amount of numerical dissipation. This is achieved by a reconstruction of the unfiltered solution through an approximate deconvolution and a regularisation based on a tailored numerical flux function. ALDM was developed by Hickel, Adams & Domaradzki (2006) and Hickel *et al.* (2007) and successfully applied to stably stratified turbulent flows by Remmler & Hickel (2012, 2013).

Alternatively, an explicit SGS model can be applied on top of the non-dissipative central discretisation scheme. We use the Smagorinsky (1963) model with a fixed

No.	Re	Fr	$\mathscr{R}$	Re_λ	ηk_{max}	k_O
1	20 800	∞	∞	372	0.95	0.0
2	23 150	0.089	184.0	393	0.97	6.4
3	28 250	0.025	17.2	434	0.83	38.4
4	33 480	0.008	2.1	472	0.71	192.0

TABLE 1. List of the presented DNS ordered by the strength of the stable stratification. No. 1 is neutrally stratified, No. 4 is strongly stratified.

model coefficient of $C_S = 0.18$ ('standard Smagorinsky model', SSM) or a dynamic version of this model ('dynamic Smagorinsky model', DSM) based on the dynamic procedure proposed by Germano *et al.* (1991) and improved by Lilly (1992). The dynamic procedure is used to compute the Smagorinsky model coefficient based on test filtering the numerical solution assuming scale similarity between the smallest resolved scales and the largest unresolved scales. The test filter size is twice the grid size. For numerical stability reasons the computed model coefficient is usually averaged in homogeneous directions. Since we investigate a flow field that is homogeneous in all three directions, the method reduces to the computation of a spatially constant but temporally varying model coefficient. We also investigated the case without spatial averaging; this is denoted 'DSM2' in §4. In order to prevent numerical instability, the Smagorinsky model coefficient is clipped if negative values are computed. The turbulent Prandtl number is assumed to be $Pr_t = 0.4$ for both the SSM and the DSM.

3. Numerical set-up

We simulated homogeneous stratified turbulence in a triply periodic box with side length $\mathscr{L} = 2\pi$ and a resolution of 512^3 cells. A fluctuating large-scale horizontal volume force is applied to the fluid, which injects a constant forcing power into the domain. The time- and space-dependent forcing term reads (Aspden *et al.* 2008)

$$\boldsymbol{F}(\boldsymbol{x}, t) = \sum_{i,j=1}^{2} \boldsymbol{a}_{i,j} \cos(2\pi k_i x + p_{i,j}) \; \cos(2\pi k_j y + q_{i,j}). \tag{3.1}$$

The random amplitudes $\boldsymbol{a}_{i,j}$ and phases $p_{i,j}$ and $q_{i,j}$ are recomputed at every time step. After an initial transient phase, the turbulence kinetic energy remains at a constant level, as soon as the forcing power $P = 1/(2\pi)$ is balanced by the mean molecular dissipation $\varepsilon_k + \varepsilon_p$. A more detailed description of the simulations is provided by Remmler & Hickel (2013). We sampled the SEV and SED in time intervals $\Delta T = 5\mathscr{L}/\mathscr{U}$ sufficiently large to ensure decorrelated velocity and density fields. With an average computational time step of $\Delta t = 1.6 \times 10^{-3} \mathscr{L}/\mathscr{U}$ we needed ~ 3125 time steps for each sample. To limit computational costs, we restricted ourselves to 20 samples per simulation. All figures presented below are averages of these samples.

A list of the simulations can be found in table 1, where we provide the non-dimensional parameters for each case as well as the Reynolds number based on the Taylor microscale (see, e.g. Pope 2000), computed using the kinetic energy E_k and kinetic energy dissipation ε_k,

$$Re_\lambda = E_k \sqrt{\frac{20 Re_0}{3 \mathscr{U} \mathscr{L} \varepsilon_k}}. \tag{3.2}$$
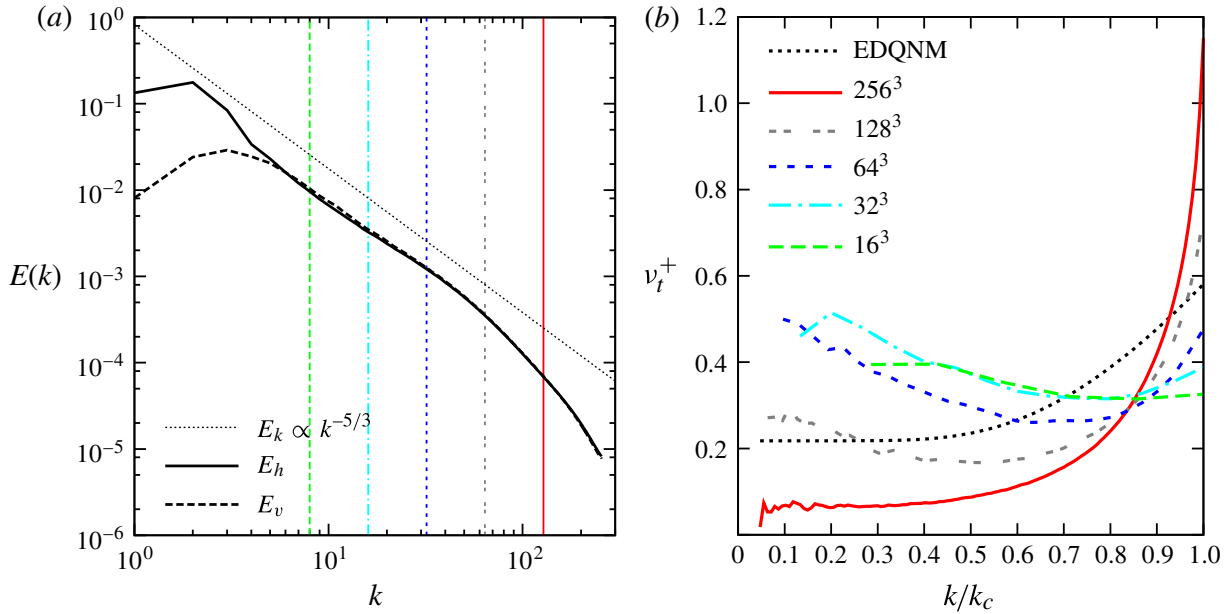
FIGURE 1. Integrated spectra of neutrally stratified turbulence DNS (512^3 cells). (*a*) Horizontal and vertical kinetic energy spectra. The vertical lines indicate cutoff wavenumbers for SEV computation. (*b*) SEV at different test grid levels. The EDQNM prediction (Kraichnan 1976) is also shown for comparison.

The product of the Kolmogorov length η and the maximum resolved wavenumber k_{max} is $\eta k_{max} \approx 1$, which indicates sufficient resolution of the smallest scales of turbulence.

The Ozmidov wavenumber k_O indicates the smallest scales of motion that are affected by buoyancy. For case No. 2 only the largest scales are affected by buoyancy; in case No. 4 almost the complete spectrum is influenced by buoyancy forces. (It should be noted that the grid cutoff wavenumber is $k_c = 256$.)

4. Results and discussion

4.1. *Neutrally stratified turbulence*

For neutrally stratified turbulence we can compare our results directly with the EDQNM prediction. The spectra of horizontal and vertical kinetic energy shown in figure 1(*a*) confirm that the turbulence is fully isotropic for wavenumbers $k > 5$. In figure 1(*b*) we show the results of spherically averaged SEV for five different coarse test grids together with the algebraic law of Kraichnan. It turns out that in our simulations the values of ν_t^+ are similar to the theoretical ones and the plateau–cusp shape of the curve is reproduced. However, the cusp is sharper than in the theoretical curve and its maximum value increases with the test grid resolution. Moreover, the plateau at low wavenumbers is tilted, its level rises with decreasing test grid resolution and it saturates for the test grid with 64^3 cells and the coarser grids.

Domaradzki *et al.* (1987) already observed a lower level of the SEV at low wavenumbers compared with theory, when they analysed DNS of isotropic turbulence at very low Reynolds number. Therefore the low-level plateau is probably due to the high cutoff wavenumbers which are close to the dissipative range.

The dependence of the cusp maximum and sharpness on the test grid was also observed and quantified by Kitsios *et al.* (2012). Our observations confirm their findings.
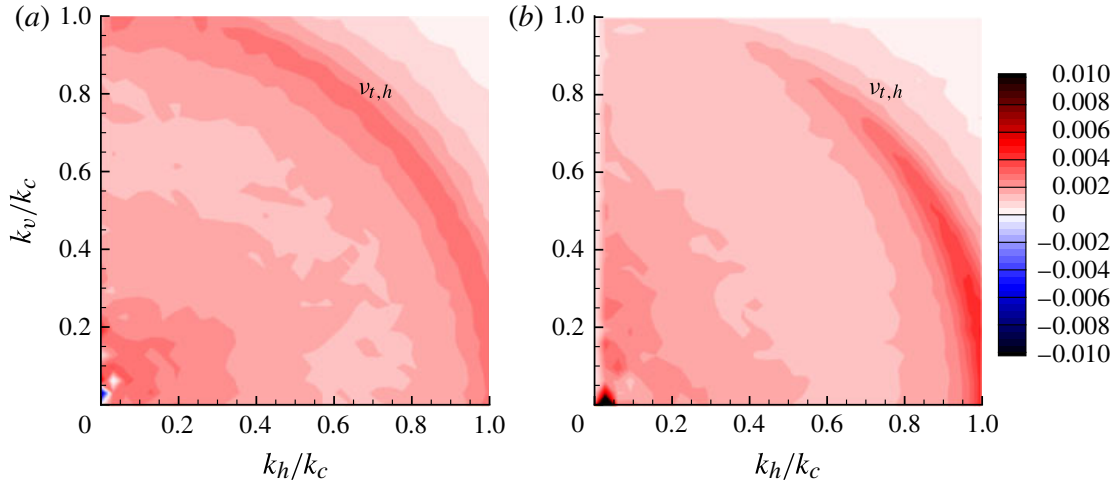
FIGURE 2. Two-dimensional SEV of neutrally stratified horizontally forced turbulence (test grid with 64^3 cells). Horizontal (*a*) and vertical (*b*) kinetic energy.

In figure 2 we present the SEV in a two-dimensional spectral space. Averaging was performed on circles with constant distance from the vertical axis. The analysis was carried out separately for the horizontal and vertical kinetic energy components. It turns out that, as expected, the horizontal eddy viscosity spectrum $\nu_{t,h}$ shows an isotropic distribution. The SEV of the vertical kinetic energy component $\nu_{t,v}$ is not isotropic, which is due to the anisotropic spectrum of any single-direction kinetic energy in a divergence-free velocity field.

4.2. *Stably stratified turbulence*

We applied the same analysis to the simulations with stable stratification, see figure 3. In this case, a third type of energy has to be considered, the available potential energy and hence the SED D_t. In the following, it is sometimes helpful to discuss the results not in Cartesian spectral coordinates but in terms of the absolute wavenumber k and the angle ϕ, which has the range $0 \leqslant \phi \leqslant \pi/2$ for the horizontal and vertical directions, respectively.

The cutoff wavenumber for the spectra presented in figure 3 is $k_c = 32$. This means that it is larger than the Ozmidov wavenumber k_O in case No. 2, approximately equal to k_O in case No. 3 and significantly smaller than k_O in case No. 4. As pointed out by Khani & Waite (2013), this has a large influence on the SEV and SED spectra.

The SEV of the horizontal kinetic energy is still almost isotropic in case No. 2 with $\mathscr{R} = 184$. At lower Froude numbers the cusp no longer appears in all directions, but only at medium angles ϕ. At the lowest Froude number investigated, it almost completely vanishes.

For the vertical kinetic energy, there is no visible difference between the neutral and the weakly stratified case. With increasing stable stratification, the overall level of $\nu_{t,v}$ decreases and a region with negative values appears. This could be explained by an inverse energy cascade or by the effect of 'pancake' vortices elongated in the horizontal direction and layered in the vertical direction. Remmler & Hickel (2013) indeed observed a transport of vertical kinetic energy from small to larger vertical scales in the case of strong stable stratification (cf. their figure 4*b*), which supports this view.

The SED differs quite strongly from the SEV described above. In the weakly stratified case, there is a clear plateau–cusp behaviour, but the plateau level depends
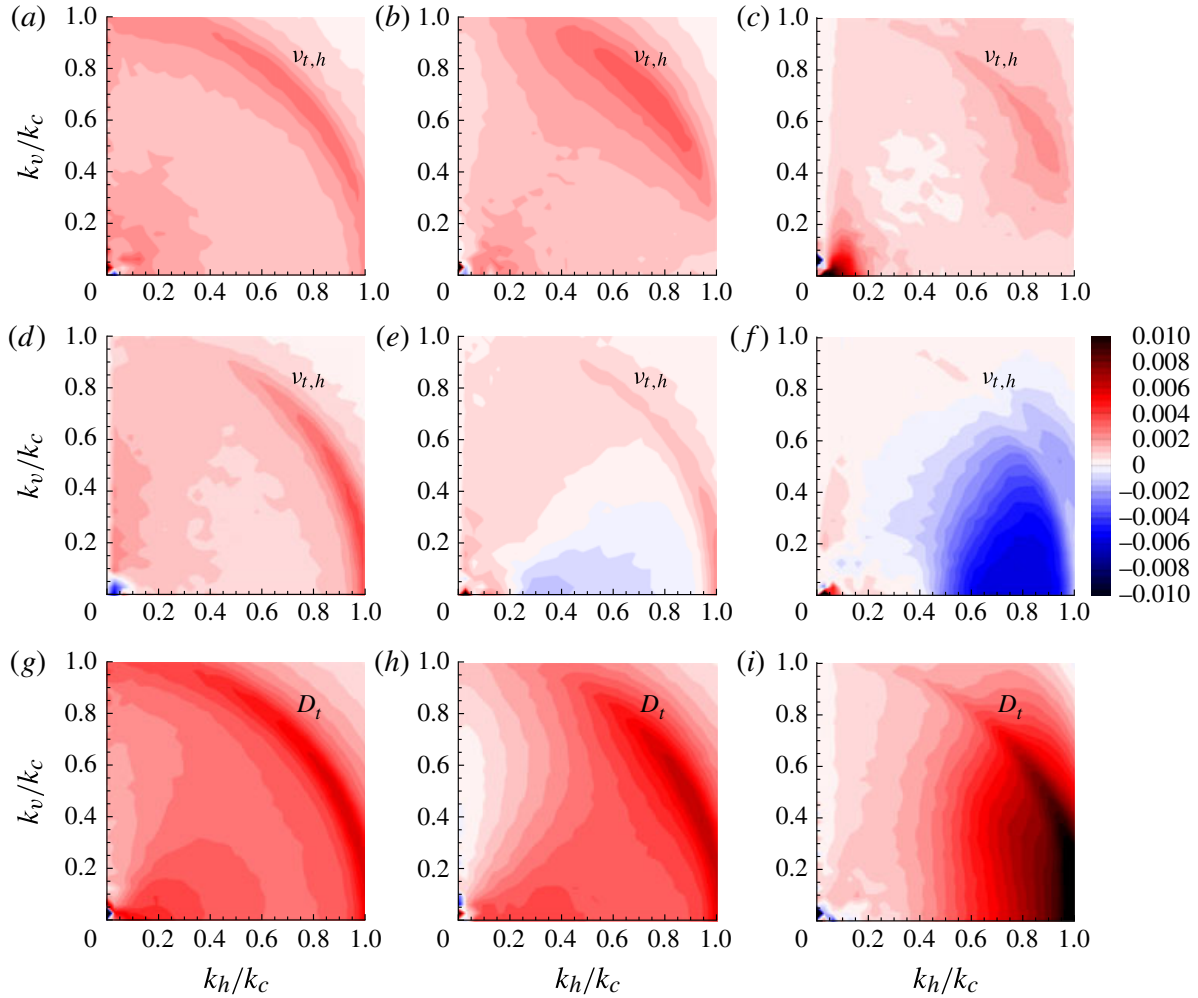
FIGURE 3. SEV and diffusivity of stably stratified turbulence (test grid with 64^3 cells) at different Froude numbers (corresponding to weak, medium and strong stratification). Horizontal (*a–c*) and vertical (*d–f*) kinetic energy as well as potential energy (*g–i*). (*a,d,g*) $\mathscr{R} = 184$, $Fr = 0.089$; (*b,e,h*) $\mathscr{R} = 17.2$, $Fr = 0.025$; (*c,f,i*) $\mathscr{R} = 2.1$, $Fr = 0.008$.

on the spectral direction. It strongly decreases when ϕ is increased. The cusp level, in contrast, is almost unaffected by the spectral direction. It decreases only slightly at $\phi \approx \pi/2$. Case No. 3 ($\mathscr{R} = 17.2$) looks very similar, just the plateau level is decreased and the drop of the cusp level at high ϕ is more pronounced than in the previous case. For the strongest stratification, the picture changes significantly. There is a peak at high horizontal wavenumbers and no plateau region as in the previous cases.

According to Galperin & Sukoriansky (2010), the horizontal viscosity and diffusivity should grow in the case of increased stratification while the vertical counterparts decrease. Our results confirm this for the vertical viscosity and diffusivity, but show a different trend for the horizontal direction.

The effective turbulent Prandtl number (figure 4) is homogeneously distributed in the spectrum in the case of weak stratification. In the horizontal direction there is a plateau at $Pr_t \approx 0.35$ and a cusp near the cutoff wavenumber with a maximum value of $Pr_t = 0.55$. For the vertical direction $Pr_t > 1$. In the case of stronger stratification the difference in the horizontal and vertical directions is increased, leading to a large region with negative values in our most strongly stratified case. The growth of the vertical turbulent Prandtl number with increasing stratification, at least for cases Nos 2 and 3, is in agreement with the findings of Galperin & Sukoriansky (2010).
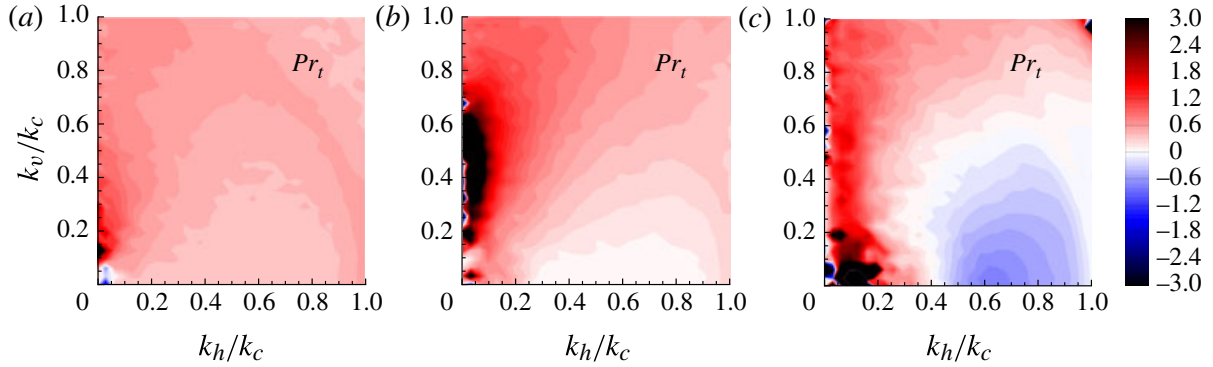
FIGURE 4. Effective turbulent Prandtl number in stably stratified turbulence (test grid with 64^3 cells) at different Froude numbers (corresponding to weak, medium and strong stratification). (*a*) $\mathscr{R} = 184$, $Fr = 0.089$; (*b*) $\mathscr{R} = 17.2$, $Fr = 0.025$; (*c*) $\mathscr{R} = 2.1$, $Fr = 0.008$.

Based on the observed inhomogeneity of the effective turbulent Prandtl number in spectral space we conclude that traditional SGS models assuming a constant positive turbulent Prandtl number are certainly unsuitable for simulations of strongly stratified turbulence.

4.3. *Analysis of LES schemes*

The reference data obtained from filtering the DNS can now be used to analyse LES methods. We computed the effective SEV and SED in LES from an ensemble of statistically independent snapshots of the flow field (see Hickel *et al.* 2006). The SEV and SED are both affected by the numerical discretisation and the turbulence SGS model. Both interfere with each other and cannot be judged independently, which motivates the idea of implicit LES where the discretisation and the SGS model are fully merged. Since quantitative comparison of two-dimensional plots as in figures 2 and 3 is difficult, we show the SEV and SED of different LES methods in figure 5 in a one-dimensional graph that is a cut through the spectral space at $\phi = \pi/4$ (the 'diagonal' modes). As a test case we selected case No. 3 with a medium stable stratification. The cutoff wavenumber $k_c = 16$ is slightly smaller than the Ozmidov wavenumber $k_O = 38.4$, so the SGS turbulence is, to a certain degree, influenced by buoyancy forces. Together with the EDQNM prediction and the DNS reference result, we show the results obtained with the ALDM, pure CDS4 without an SGS model and CDS4 with explicit models, namely SSM, DSM and DSM2.

It turns out that none of the tested methods are able to correctly reproduce all three SEV and SED spectra at the same time. The ALDM does on average a good job, which is remarkable since the method was optimised to reproduce the EDQNM curve as closely as possible (Hickel *et al.* 2006). The averaged DSM gives good results for the SEV of the horizontal kinetic energy and the SED of the available potential energy, but fails for the SEV of the vertical kinetic energy. The SEV of the vertical kinetic energy, on the other hand, is well predicted by the pure CDS4 discretisation without a turbulence SGS model. The DSM2 model, which allows for local variations in the model coefficient, does not improve the result over the averaged DSM, but rather makes it worse.

5. Summary and conclusions

We have computed the SEV and diffusivity of homogeneous turbulence with and without stable stratification. This was achieved by filtering fully resolved DNS results
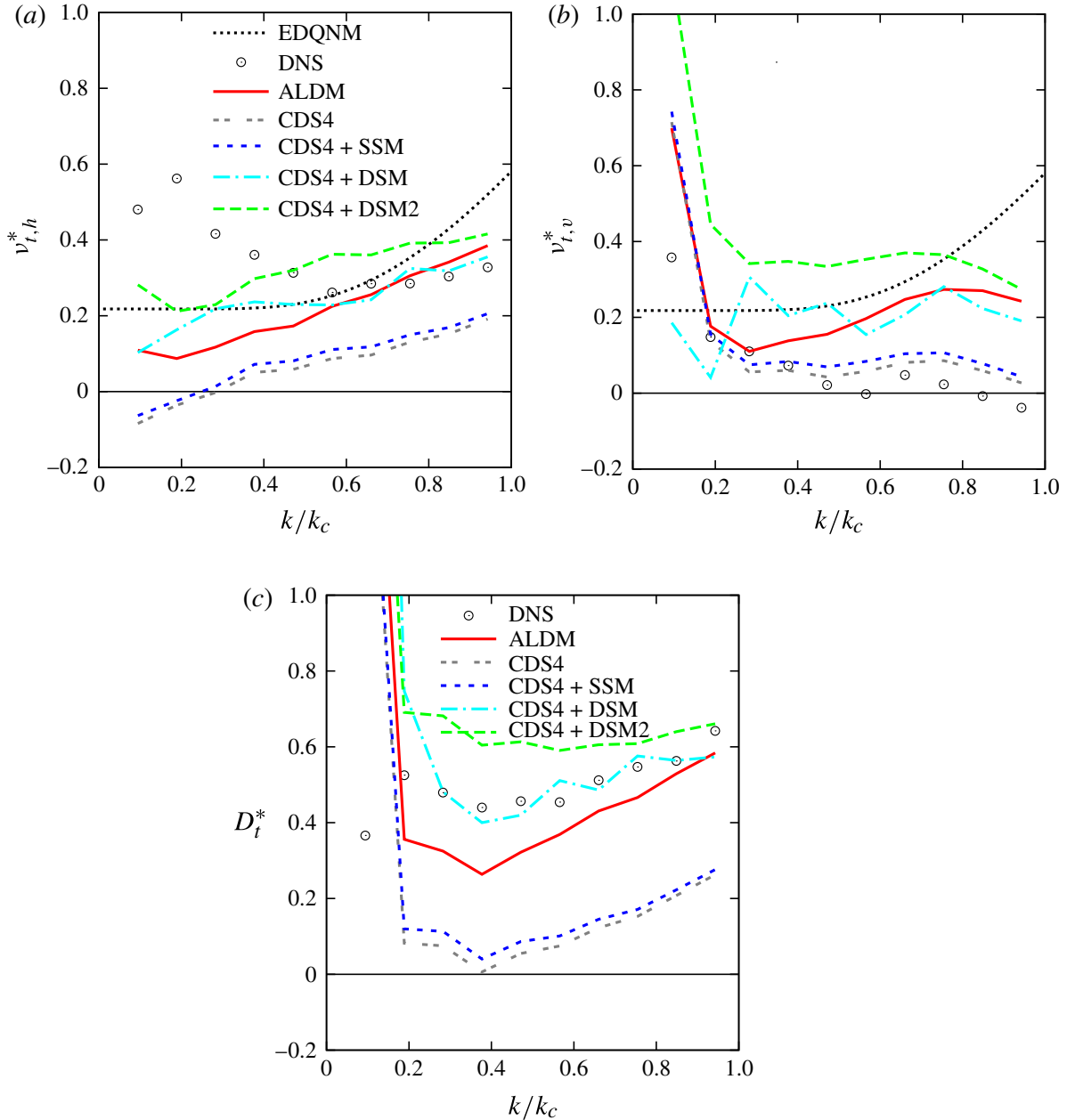
FIGURE 5. Diagonal SEV and SED of stably stratified turbulence at $\mathscr{R} = 17.2$ (32^3 cells) computed with different discretisation schemes and turbulence SGS models. (a) $v_{t,h}^*$; (b) $v_{t,v}^*$; (c) D_t^*.

and by computing the additional spectral energy flux that is necessary to obtain the same total flux in the coarse-grained flow field as in the fully resolved case.

For neutrally stratified turbulence we found eddy viscosity spectra that are, in general, similar to the EDQNM prediction of Kraichnan (1976) showing the well-known plateau–cusp behaviour. However, the amplitude of the cusp at the cutoff wavenumber depends on the test filter size, as described by Kitsios *et al.* (2012), and at low wavenumbers we find a pronounced linear decrease of the SEV instead of a flat plateau.

If the stable stratification is increased, the SEV and SED spectra become more and more anisotropic. For the most stable case investigated, the spectral space topology has completely changed. This illustrates that the characteristics of the flow change significantly as soon as the buoyancy Reynolds number approaches $\mathscr{R} \approx 1$. Strong

stratification leads to negative values of the effective turbulent Prandtl number at large horizontal and small vertical wavenumbers. Such results contradict the widespread assumption of a constant positive effective turbulent Prandtl number in SGS modelling. The treatment of SGS stresses in such cases must generally be different from that in fully turbulent flows with higher values of $\mathcal{R}$.

We used the results from the filtered DNS to test the implicit SGS model ALDM and a central discretisation scheme with and without the Smagorinsky model, either in the standard form or in the dynamic form. We found that the ALDM, despite being calibrated for the SEV from EDQNM theory, yields acceptable results for all three forms of flow energy. The DSM does a good job except for the vertical kinetic energy, which is best matched by the central discretisation without any SGS model. These results suggest that a potentially better model could be obtained by applying the DSM only to the horizontal velocity components and leaving the vertical momentum equation unmodified.

Acknowledgements

References

ASPDEN, A. J., NIKIFORAKIS, N., DALZIEL, S. B. & BELL, J. B. 2008 Analysis of implicit LES methods. *Commun. Appl. Math. Comput. Sci.* **3** (1), 103–126.

BRETHOUWER, G., BILLANT, P., LINDBORG, E. & CHOMAZ, J.-M. 2007 Scaling analysis and simulation of strongly stratified turbulent flows. *J. Fluid Mech.* **585**, 343–368.

CHOLLET, J.-P. 1984 Two-point closures as a subgrid scale modeling for large eddy simulations. In *4th Symposium on Turbulent Shear Flows* (ed. H. Viets, R. J. Bethke & D. Bougine), p. 9.

DOMARADZKI, J. A., METCALFE, R. W., ROGALLO, R. S. & RILEY, J. J. 1987 Analysis of subgrid-scale eddy viscosity with use of results from direct numerical simulations. *Phys. Rev. Lett.* **58** (6), 547–550.

DOUGHERTY, J. P. 1961 The anisotropy of turbulence at the meteor level. *J. Atmos. Sol.-Terr. Phys.* **21**, 210–213.

GALPERIN, B. & SUKORIANSKY, S. 2010 Geophysical flows with anisotropic turbulence and dispersive waves: flows with stable stratification. *Ocean Dyn.* **60**, 1319–1337.

GERMANO, M., PIOMELLI, U., MOIN, P. & CABOT, W. H. 1991 A dynamic subgrid-scale eddy viscosity model. *Phys. Fluids* A **3** (7), 1760–1765.

GODEFERD, F. S. & CAMBON, C. 1994 Detailed investigation of energy transfers in homogeneous stratified turbulence. *Phys. Fluids* **6** (6), 2084–2100.

GODEFERD, F. S. & STAQUET, C. 2003 Statistical modelling and direct numerical simulations of decaying stably stratified turbulence. Part 2. Large-scale and small-scale anisotropy. *J. Fluid Mech.* **486**, 115–159.

HEISENBERG, W. 1948 Zur statistischen Theorie der Turbulenz. *Z. Phys.* A **124**, 628–657.

HICKEL, S., ADAMS, N. A. & DOMARADZKI, J. A. 2006 An adaptive local deconvolution method for implicit LES. *J. Comput. Phys.* **213**, 413–436.

HICKEL, S., ADAMS, N. A. & MANSOUR, N. N. 2007 Implicit subgrid-scale modeling for large-eddy simulation of passive scalar mixing. *Phys. Fluids* **19**, 095102.

KHANI, S. & WAITE, M. L. 2013 Effective eddy viscosity in stratified turbulence. *J. Turbul.* **14** (7), 49–70.

KITSIOS, V., FREDERIKSEN, J. S. & ZIDIKHERI, M. J. 2012 Subgrid model with scaling laws for atmospheric simulations. *J. Atmos. Sci.* **69** (4), 1427–1445.

KITSIOS, V., FREDERIKSEN, J. S. & ZIDIKHERI, M. J. 2013 Scaling laws for parameterisations of subgrid eddy–eddy interactions in simulations of oceanic circulations. *Ocean Model.* **68**, 88–105.

KRAICHNAN, R. H. 1976 Eddy viscosity in two and three dimensions. *J. Atmos. Sci.* **33**, 1521–1536.

LILLY, D. K. 1992 A proposed modification of the German subgrid-scale closure method. *Phys. Fluids* A **4** (3), 633–635.

ORSZAG, S. A. 1970 Analytical theories of turbulence. *J. Fluid Mech.* **41** (02), 363–386.

OZMIDOV, R. V. 1965 On the turbulent exchange in a stably stratified ocean. *Izv., Atmos. Ocean. Phys.* **1**, 493–497.

POPE, S. B. 2000 *Turbulent Flows*. Cambridge University Press.

REMMLER, S. & HICKEL, S. 2012 Direct and large eddy simulation of stratified turbulence. *Intl J. Heat Fluid Flow* **35**, 13–24.

REMMLER, S. & HICKEL, S. 2013 Spectral structure of stratified turbulence: direct numerical simulations and predictions by large eddy simulation. *Theor. Comput. Fluid Dyn.* **27**, 319–336.

SHU, C.-W. 1988 Total-variation-diminishing time discretizations. *SIAM J. Sci. Stat. Comput.* **9** (6), 1073–1084.

SMAGORINSKY, J. 1963 General circulation experiments with the primitive equations. I: The basic experiment. *Mon. Weath. Rev.* **91**, 99–164.

STAQUET, C. & GODEFERD, F. S. 1998 Statistical modelling and direct numerical simulations of decaying stably stratified turbulence. Part 1. Flow energetics. *J. Fluid Mech.* **360**, 295–340.

SUKORIANSKY, S., GALPERIN, B. & STAROSELSKY, I. 2005 A quasinormal scale elimination model of turbulent flows with stable stratification. *Phys. Fluids* **17** (8), 085107.

On the construction of a direct numerical simulation of a breaking inertia-gravity wave in the upper mesosphere

Mark D. Fruman[1], Sebastian Remmler[2], Ulrich Achatz[1], and Stefan Hickel[2]

[1]Institute for Atmosphere and Environment, Goethe University Frankfurt, Frankfurt, Germany, [2]Institute of Aerodynamics and Fluid Mechanics, Technische Universität München, Munich, Germany

Abstract A systematic approach to the direct numerical simulation (DNS) of breaking upper mesospheric inertia-gravity waves of amplitude close to or above the threshold for static instability is presented. Normal mode or singular vector analysis applied in a frame of reference moving with the phase velocity of the wave (in which the wave is a steady solution) is used to determine the most likely scale and structure of the primary instability and to initialize nonlinear "2.5-D" simulations (with three-dimensional velocity and vorticity fields but depending only on two spatial coordinates). Singular vector analysis is then applied to the time-dependent 2.5-D solution to predict the transition of the breaking event to three-dimensional turbulence and to initialize three-dimensional DNS. The careful choice of the computational domain and the relatively low Reynolds numbers, on the order of 25,000, relevant to breaking waves in the upper mesosphere, makes the three-dimensional DNS tractable with present-day computing clusters. Three test cases are presented: a statically unstable low-frequency inertia-gravity wave, a statically and dynamically stable inertia-gravity wave, and a statically unstable high-frequency gravity wave. The three-dimensional DNS are compared to ensembles of 2.5-D simulations. In general, the decay of the wave and generation of turbulence is faster in three dimensions, but the results are otherwise qualitatively and quantitatively similar, suggesting that results of 2.5-D simulations are meaningful if the domain and initial condition are chosen properly.

1. Introduction

Inertia-gravity waves are a ubiquitous feature of the dynamics in the atmosphere and play a pivotal role in the global circulation. They are forced mostly by flow over orography [e.g., *Smith*, 1979; *Lilly et al.*, 1982; *McFarlane*, 1987], by convection [e.g., *Chun et al.*, 2001; *Grimsdell et al.*, 2010], and by spontaneous imbalance of the mean flow in the troposphere [*O'Sullivan and Dunkerton*, 1995; *Plougonven and Snyder*, 2007], and they transport energy and momentum from the region where they are forced to the region where they are dissipated (e.g., through breaking), often thousands of kilometers away. Since the waves are filtered and refracted by the environment through which they propagate, their effects are highly nonuniform. Various phenomena, such as the cold summer mesopause [*Hines*, 1965; *Lindzen*, 1973] and the quasi-biennial oscillation in the equatorial stratosphere [e.g., *Baldwin et al.*, 2001], cannot be explained nor reproduced in weather and climate simulations without accounting for the effect of gravity waves (see *Fritts and Alexander* [2003] for an overview of gravity waves in the middle atmosphere). In almost all cases, this is done through rather crude and extensively tuned *parameterizations* based on combinations of linear wave theory (beginning with *Lindzen* [1981]), empirical observations of time-mean energy spectra [e.g., *Hines*, 1997], and very simplified treatments of the breaking process. See *Kim et al.* [2003] and *McLandress* [1998] for reviews of the various standard parameterization schemes.

Inertia-gravity wave breaking involves time scales from seconds to hours and spatial scales from meters to tens of kilometers. It is therefore a demanding problem for both observational and computational investigation. The representation of small-scale turbulence in wave-breaking simulations and of wave breaking in weather and climate simulations represent two important but separate parameterization problems in atmospheric science. The former is the goal of large-eddy simulation (LES). To be trusted, an LES scheme must be tested against turbulence-resolving direct numerical simulation (DNS). The purpose of the present study is to describe a systematic strategy for constructing such DNS and to provide DNS for a selection of waves

with different characteristics. To qualify as DNS, a simulation of a turbulent flow must resolve scales smaller than the Kolmogorov length η, which depends on the kinematic viscosity ν and the maximum rate of kinetic energy dissipation; η represents the scale below which molecular viscosity and diffusion dominate over inertial effects and energy is removed from the system or converted to heat. For realistic flows in the troposphere, η is on the order of millimeters [*Vallis*, 2006], so for gravity waves with wavelengths on the order of kilometers, DNS is impossible. One case where DNS is possible is waves in the upper mesosphere (about 80 km altitude), where due to the extremely low ambient density, ν is about 1 m^2 s^{-1} in the U.S. Standard Atmosphere [*NOAA et al.*, 1976]. *Remmler et al.* [2013] found from simulation of a breaking statically unstable 3 km inertia-gravity wave a Kolmogorov length of between 1 m and 3 m so that a 3-D DNS could be achieved with on the order of 10^9 grid cells.

There have been a number of recent numerical studies of breaking gravity waves. *Fritts et al.* [2009a, 2009b] performed high-resolution DNS of high-frequency gravity waves (with periods of a few times the background buoyancy period) with amplitudes slightly above and slightly below the threshold for convective instability. They found that both waves break down to about a third of their initial amplitude within one or two wave periods and that the early phase of wave breaking is dominated by turbulent three-dimensional motion, while wave-wave interactions between the primary wave and secondary waves excited by the breaking persist for many wave periods. *Fritts et al.* [2013] and *Fritts and Wang* [2013] performed highly resolved, high Reynolds number DNS of a monochromatic gravity wave breaking due to interaction with a vertically varying "fine-structure" shear flow, finding that the direction of the fine-structure flow relative to the plane of the wave strongly affected the degree to which the gravity wave broke down into turbulence.

The above studies neglect the Coriolis effect, and thus, the velocity field of the primary gravity wave is strictly in the plane of phase propagation. The propagation of inertia-gravity waves, on the other hand, is maintained by both the vertical restoring force due to the stratification and the horizontal restoring force due to the Coriolis effect (the vertical component of the Coriolis force is typically neglected). Since in the atmosphere the former is much stronger than the latter, waves with steep phase propagation, with their nearly horizontal fluid parcel motions strongly influenced by the Coriolis force, have much lower frequency than waves with shallow phase propagation. Instability and breaking are very different for inertia-gravity waves of different frequencies [*Achatz*, 2005, 2007a, 2007b; *Lelong and Dunkerton*, 1998], so it is difficult to extrapolate any conclusions from a DNS study to waves with higher or lower frequency. *Remmler et al.* [2013] produced a DNS of a statically unstable low-frequency inertia-gravity wave (referred to as case I later in this paper). The low-frequency wave decays much less than a high-frequency wave, only to about three quarters of its initial amplitude within one wave period, about 8 h in that case. Also, the distribution of turbulent energy dissipation is much more inhomogeneous and intermittent than for a high-frequency wave.

Other recent studies have simulated not just one wavelength of a monochromatic wave in a triply periodic domain (as is done in the present work), but the more realistic case of a train of waves propagating through a variable background as they break. *Lund and Fritts* [2012] considered waves propagating through the thermosphere, their amplitude growing due to the decreasing density and changing due to the height-dependent stratification and chemical composition. *Liu et al.* [2010] considered waves excited at the surface of the ocean propagating downward through the thermocline. These studies must inevitably sacrifice model resolution to accommodate multiple wavelengths but are essential if conclusions from the more fully resolved idealized DNS are to be applied to more practical problems such as the parameterization of wave breaking in general circulation models, where a monochromatic inertia-gravity wave is unlikely to occur in isolation, especially at the amplitude necessary for convective instability.

Since a DNS of a breaking inertia-gravity wave is computationally expensive, time consuming, and produces a dauntingly complex and nonlinear result, it is important to choose the domain and parameters carefully. The present work describes a systematic, hierarchical approach to analyzing an inertia-gravity wave breaking event, combining linear modal analysis with two- and three-dimensional nonlinear simulation. Aspects of this procedure have already been published in *Achatz* [2007a, 2007b], *Fruman and Achatz* [2012], and *Remmler et al.* [2013]. Three test cases were chosen, representing waves with different inherent time scales and breaking behavior.

The analysis is greatly simplified if one works with the Boussinesq approximation on an f plane with a constant background Brunt-Väisälä frequency, enabling the use of periodic boundary conditions in any three orthogonal directions, one of which is usually chosen parallel to the direction of phase-propagation of

the wave. While obviously not realistic for a general description of the dynamics in the mesosphere, one might justify the Boussinesq approximation as long as the wavelength of the wave is small compared to the density scale height and the breaking process is fast compared to the vertical group propagation of the wave.

The method proceeds in four stages: (1) solution (in the form of normal modes or singular vectors) of the Boussinesq equations linearized about the basic state wave, determining the primary instability structures, (2) nonlinear two-dimensional (in space) numerical solution of the full equations using the result of stage 1 as initial condition, (3) solution in the form of singular vectors (varying in the remaining spatial direction) of the equations linearized about the time-dependent result of stage 2, and (4) three-dimensional DNS using the linear solutions from stages 1 and 3 as initial condition and their wavelengths for the size of the computational domain. In some cases the resulting computational domain is relatively narrow in either the streamwise or the spanwise direction, and therefore, the three-dimensional DNS is comparatively very efficient. Implicit in the strategy is that there is a temporal- and/or spatial-scale separation between the primary and secondary instabilities so that the nonlinear two-dimensional solution (stage 2) resembles the realistic (three-dimensional) evolution for a short time while secondary instabilities—different in scale and character from the primary instabilities calculated in stage 1—develop. This is the advantage of the approach over simply initializing three-dimensional DNS with mutually orthogonal primary perturbations.

The paper is organized as follows. Section 2 presents the governing equations, the monochromatic inertia-gravity wave solution, and the rotated coordinate system used. Section 3 describes in detail the four-stage approach to gravity wave breaking analysis. Section 4 presents the three test cases. The numerical methods used are explained in section 5. The results of the analyses are presented in section 6. Appendices elaborate on the calculation of normal modes and singular vectors, on projection of the evolving solution onto the original wave, and on the computing resources used for the 3-D DNS.

2. Governing Equations and the Gravity Wave Solution

Without loss of generality, we may assume that the monochromatic inertia-gravity wave is propagating in the x-z plane and let Θ be its angle of phase propagation with respect to the x axis. The problem is best solved in a reference frame (ξ, y, ζ) rotated about the y axis through an angle $\pi/2 - \Theta$ so that the wave vector of the gravity wave is parallel to the ζ axis (see Figure 1 (left)). That is,

$$\xi = x \, \sin\Theta - z \, \cos\Theta, \tag{1a}$$

$$\zeta = x \, \cos\Theta + z \, \sin\Theta. \tag{1b}$$

The Boussinesq equations may be written

$$\frac{\partial \boldsymbol{v}}{\partial t} + (\boldsymbol{v} \cdot \nabla)\boldsymbol{v} = b\hat{\boldsymbol{e}}_z - f\hat{\boldsymbol{e}}_z \times \boldsymbol{v} - \nabla p + \nu\nabla^2\boldsymbol{v}, \tag{2a}$$

$$\frac{\partial b}{\partial t} + (\boldsymbol{v} \cdot \nabla)b = -N^2\hat{\boldsymbol{e}}_z \cdot \boldsymbol{v} + \mu\nabla^2 b, \tag{2b}$$

$$\nabla \cdot \boldsymbol{v} = 0, \tag{2c}$$

where $\boldsymbol{v} = (u_\xi, v, w_\zeta)$ is the fluid velocity, b is buoyancy, p is pressure normalized by a constant background density, $\hat{\boldsymbol{e}}_z$ is the unit vector in the true vertical direction, N is the Brunt-Väisälä frequency, f is the Coriolis parameter, and ν and μ are the kinematic viscosity and thermal diffusivity, respectively.

An inertia-gravity wave propagating in the x-z plane at an angle Θ to the x axis and with upward group velocity may be written in the form

$$[u_\xi, v, w_\zeta, b] = [U_{\xi 0}, V_0, W_{\zeta 0}, B_0]$$
$$\equiv Re\left\{ a \left[\frac{iK\omega}{km}, \frac{f}{k}, 0, -\frac{N^2}{m} \right] e^{i\phi} \right\}, \tag{3}$$

where K is the magnitude of the wave vector and $k = K\cos\Theta$ and $m = K\sin\Theta$ are its horizontal and vertical components in the Earth frame,

$$\omega = -\sqrt{f^2\sin^2\Theta + N^2\cos^2\Theta} \tag{4}$$
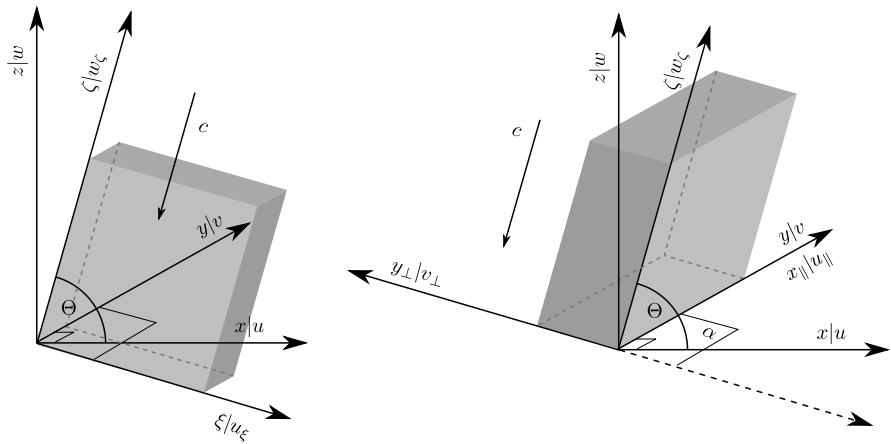
**Figure 1.** (left and right) Rotated coordinate systems for primary and secondary instability analyses [after *Remmler et al.*, 2013]. *c* indicates the direction of the phase velocity of the wave.

is the frequency, and $\phi = K\zeta - \omega t$ is the wave phase. The nondimensional (complex) wave amplitude a is defined such that a wave with $|a| = 1$ is neutral with respect to static instability at its least stable point, namely, where the vertical gradient of total potential temperature is least. Equation (3) is an exact solution to (2a) in the inviscid ($\nu = \mu = 0$) limit. When the Prandtl number is unity (i.e., $\nu = \mu$), the solution decays exponentially with time such that

$$a(t) = a(0)e^{-\nu K^2 t}.$$ (5)

In the midlatitude mesosphere, N is about 100 times larger than f, so the properties of the wave are very sensitive to Θ. A wave with Θ close to 90° has a relatively low frequency—close to f—and elliptically polarized velocity in the streamwise-spanwise (ξ-y) plane, i.e., u_ξ and v are of similar amplitude. Since f strongly affects the form of these waves, we call them inertia-gravity waves (IGW). A wave with shallower phase propagation has much higher frequency, approximately equal to $N \cos \Theta$, and a linearly polarized transverse velocity field ($|v| \ll |u|$). We call such waves high-frequency gravity waves (HGW) (strictly speaking, these are also inertia-gravity waves, but rotation plays a negligible role). *Lelong and Dunkerton* [1998] and *Achatz* [2005] showed that the nature of the instabilities of the two categories of waves are markedly different. This is primarily because of the influence of the transverse velocity component, large in the IGW and small in the HGW, which has maximum vertical shear at the levels of maximum buoyancy gradient, and because of the important role played by horizontal buoyancy gradients and horizontal velocity shear in the HGW.

3. Four-Stage Approach to the Simulation of Gravity Wave Breaking

In order to quantify the temporal and spatial scales of gravity wave breaking and to design a meaningful but still computationally tractable (and economical) 3-D DNS, we employ the following four-stage combination of linear and nonlinear analysis.

3.1. Primary Instability Analysis and 2.5-Dimensional DNS

The first step is to perform a large number of one-dimensional linear calculations to determine the wavelength, orientation, and spatial structure of the most unstable perturbations to the gravity wave.

The Boussinesq equations (2a) are linearized about the gravity wave (3) to yield the system

$$\frac{D'u'_\xi}{Dt} + w'_\zeta \frac{dU_{\xi 0}}{d\phi} + \cos \Theta\, b' - f \sin \Theta\, v' + \frac{\partial p'}{\partial \xi} = \nu \nabla^2 u'_\xi,$$ (6a)

$$\frac{D'v'}{Dt} + w'_\zeta \frac{dV_0}{d\phi} + f \left(\sin \Theta\, u'_\xi + \cos \Theta\, w'_\zeta \right) + \frac{\partial p'}{\partial y} = \nu \nabla^2 v',$$ (6b)

$$\frac{D' w'_\zeta}{Dt} - \sin\Theta \, b' - f \cos\Theta \, v' + K \frac{\partial p'}{\partial \phi} = \nu \nabla^2 w'_\zeta, \tag{6c}$$

$$\frac{D' b'}{Dt} + w'_\zeta \frac{dB_0}{d\phi} + N^2 \left(-\cos\Theta \, u'_\xi + \sin\Theta \, w'_\zeta \right) = \mu \nabla^2 b', \tag{6d}$$

$$\frac{\partial u'_\xi}{\partial \xi} + \frac{\partial v'}{\partial y} + K \frac{\partial w'_\zeta}{\partial \phi} = 0, \tag{6e}$$

where $[u'_\xi, v', w'_\zeta, b']$ is a small departure from (3) and

$$\frac{D'}{Dt} \equiv \frac{\partial}{\partial t} + U_{\xi 0} \frac{\partial}{\partial \xi} + V_0 \frac{\partial}{\partial y} - \omega \frac{\partial}{\partial \phi}. \tag{7}$$

Since the coefficients of u'_ξ, v', w'_ζ, and b' in (6) are independent of streamwise and spanwise position (ξ, y), solutions may be sought in the form

$$[u'_\xi, v', w'_\zeta, b'] = \Re \left\{ [\hat{u}'_\xi(\phi, t), \hat{v}'(\phi, t), \hat{w}'_\zeta(\phi, t), \hat{b}'(\phi, t)] \exp\left[i(k_\xi \xi + k_y y) \right] \right\}, \tag{8}$$

where k_ξ and k_y are constants. The ansatz (8) is inserted in (6), and the resulting system of equations for $[\hat{u}'_\xi, \hat{v}', \hat{w}'_\zeta, \hat{b}']$ are solved numerically (see section 5).

Note that the dissipation of the gravity wave solution is neglected in (6) so that the system of equations for $[\hat{u}'_\xi, \hat{v}', \hat{w}'_\zeta, \hat{b}']$ is homogeneous and autonomous and therefore admits normal mode analysis. The approximation is valid for our test cases since the time scale of the decay of the wave, $(\nu K^2)^{-1} \approx 2$ days, is long compared to the time for which the linear model is run (5 or 7.5 min) and the inverse growth rates of the fastest growing modes (about 100 s).

Normal modes are solutions of (6) in which the time dependence of $[u'_\xi, v', w'_\zeta, b']$ is a complex exponential function. For statically unstable waves ($|a| > 1$), there typically exist exponentially *growing* solutions, and the normal mode with largest growth factor is the dominant linear mode. For statically and dynamically stable waves, by which we mean that the Richardson number corresponding to the solution (3), viz

$$Ri_{\text{IGW}} = \frac{N^2(1 + a \sin\phi)}{a^2 \tan^2\Theta(\omega^2 \cos^2\phi + f^2 \sin^2\phi)}, \tag{9}$$

is greater than one fourth (the sufficient condition for linear stability of a steady, stratified shear flow) [see *Howard*, 1961; *Miles*, 1961], there are typically no exponentially growing normal modes, so the leading singular vector for a given optimization time is calculated instead. The leading singular vector [*Farrell and Ioannou*, 1996a, 1996b] for a given perturbation wavelength $\lambda_\parallel$ and orientation angle α is defined as the perturbation whose energy (or another norm) grows by the largest factor in the given optimization time (as governed by the linearized equations). Although singular vectors necessarily consist of superpositions of normal modes, they can have large growth factors even when all normal modes are exponentially decaying, since the latter are not orthogonal (i.e., "nonnormal") with respect to the energy scalar product. Details of the computation of normal modes and singular vectors are given in Appendix A [see also *Achatz*, 2005, 2007a].

The second stage is to perform nonlinear two-dimensional simulations initialized with the original gravity wave and one of the "more interesting" normal modes (or singular vectors), by which is meant those with the highest linear growth rate (or growth factor). In order to perform these simulations, a second rotation of the coordinate system, this time through an angle α about the ζ axis (Figure 1 (right)) is required, leading to the new coordinates

$$x_\parallel = \xi \, \cos\alpha + y \, \sin\alpha, \tag{10a}$$

$$y_\perp = -\xi \, \sin\alpha + y \, \cos\alpha. \tag{10b}$$

and corresponding velocity components $u_\parallel$ and $v_\perp$.

Since the dynamics—in terms of, for example, the energy exchange processes—are so different for *transverse* ($\alpha = 90°$) and *parallel* ($\alpha = 0°$) perturbations [*Andreassen et al.*, 1994; *Lelong and Dunkerton*, 1998; *Achatz*, 2007a; *Fruman and Achatz*, 2012], both the leading transverse and parallel perturbations are tried even when one has a much lower linear growth rate (or growth factor) than the other. As we will see, perturbation by the mode with smaller linear growth rate (or growth factor) can have a much more profound effect on the breaking of the original wave in nonlinear simulations. These simulations are called here "2.5-dimensional" (2.5-D) because although there are only two independent spatial coordinates, the velocity and vorticity fields are three dimensional. Since there is no conservation of enstrophy in this system (due to the vortex-tilting mechanism being active), the turbulent energy cascade is *direct* as in three-dimensional turbulence rather than inverse as in classical two-dimensional turbulence [e.g., *Kraichnan and Montgomery*, 1980].

For each 2.5-D simulation, the projection of the solution onto the original gravity wave mode (see Appendix B and *Achatz* [2007b] for details) is plotted versus time and compared to the laminar decay of an unperturbed wave (see equation (5)). A breaking wave decays faster, at first due to energy exchange with the growing linear mode and later due to interaction with the turbulence excited by the breaking. The latter process can last much longer than the time scale of the linear perturbation and as long as the period of the original wave. The decay of the gravity wave amplitude is the quantity most relevant to parameterizations of gravity wave drag in atmospheric models.

Other diagnostics used are the sum of the kinetic energy dissipation rate ϵ_k and the potential energy dissipation rate ϵ_p, where

$$\epsilon_k = \frac{\nu}{2}\left(\frac{\partial v_i}{\partial x_j} + \frac{\partial v_j}{\partial x_i}\right)\left(\frac{\partial v_i}{\partial x_j} + \frac{\partial v_j}{\partial x_i}\right) \tag{11a}$$

$$\epsilon_p = \frac{\mu}{N^2}\frac{\partial b}{\partial x_i}\frac{\partial b}{\partial x_i} \tag{11b}$$

(summation over repeated indices is implied) and the streamwise-spanwise-averaged energy wavelength spectra. Note that in nature, the dissipation of kinetic energy leads to localized frictional heating, an effect not considered in the present study.

3.2. Secondary Instability Analysis and Three-Dimensional DNS
The 2.5-D solution, which we write

$$[u_\parallel, v_\perp, w_\zeta, b] = \left[U_\parallel(x_\parallel, \phi, t), V_\perp(x_\parallel, \phi, t), W_\zeta(x_\parallel, \phi, t), B(x_\parallel, \phi, t)\right], \tag{12}$$

remains two-dimensional in space if not perturbed, but in nature the breaking of a gravity wave is inherently three dimensional. Therefore, in the next stage, the 2.5-D simulations in which the gravity wave amplitude decreased by the largest amount are subjected to a secondary instability analysis. The full equations (2a) are linearized about the time-dependent 2.5-D solution (12) to yield

$$\frac{D''u''_\parallel}{Dt} + \frac{\partial U_\parallel}{\partial x_\parallel}u''_\parallel + K\frac{\partial U_\parallel}{\partial \phi}w''_\zeta + \cos\alpha\cos\Theta\, b'' - f\left(\sin\Theta\, v''_\perp + \sin\alpha\cos\Theta\, u''_\parallel\right) + \frac{\partial p''}{\partial x_\parallel} = \nu\nabla^2 u''_\parallel, \tag{13a}$$

$$\frac{D''v''_\perp}{Dt} + \frac{\partial V_\perp}{\partial x_\parallel}u''_\parallel + K\frac{\partial V_\perp}{\partial \phi}w''_\zeta - \sin\alpha\cos\Theta\, b'' + f\left(\sin\Theta\, u''_\parallel + \cos\alpha\cos\Theta\, w''_\zeta\right) + \frac{\partial p''}{\partial y_\perp} = \nu\nabla^2 v''_\perp, \tag{13b}$$

$$\frac{D''w''_\zeta}{Dt} + \frac{\partial W_\zeta}{\partial x_\parallel}u''_\parallel + K\frac{\partial W_\zeta}{\partial \phi}w''_\zeta - \sin\Theta\, b'' - f\left(\sin\alpha\cos\Theta\, u''_\parallel + \cos\alpha\cos\Theta\, v''_\perp\right) + K\frac{\partial p''}{\partial \phi} = \nu\nabla^2 w''_\zeta, \tag{13c}$$

$$\frac{D''b''}{Dt} + N^2\left(-\cos\alpha\cos\Theta\, u''_\parallel + \sin\alpha\cos\Theta\, v''_\perp + \sin\Theta\, w''_\zeta\right) = \mu\nabla^2 b'', \tag{13d}$$

$$\frac{\partial u''_\parallel}{\partial x_\parallel} + \frac{\partial v''_\perp}{\partial y_\perp} + K\frac{\partial w''_\zeta}{\partial \phi} = 0, \tag{13e}$$

where

$$\frac{D''}{Dt} \equiv \frac{\partial}{\partial t} + U_\parallel\frac{\partial}{\partial x_\parallel} + V_\perp\frac{\partial}{\partial y_\perp} + \left(KW_\zeta - \omega\right)\frac{\partial}{\partial \phi}, \tag{14}$$

and $u_\parallel''$, $v_\perp''$, w_ζ'', and b'' are small perturbations from the 2.5-D basic state (12). Solutions are sought in the form

$$[u_\parallel'', v_\perp'', w_\zeta'', b''] = \Re\left\{ [\hat{u}_\parallel''(x_\parallel, \phi, t), \hat{v}_\perp''(x_\parallel, \phi, t), \hat{w}_\zeta''(x_\parallel, \phi, t), \hat{b}''(x_\parallel, \phi, t)] \times \exp(ik_\perp y_\perp) \right\}, \qquad (15)$$

where $k_\perp$ is the wave number in the $y_\perp$ direction (perpendicular to the plane defined by the wave vectors of the gravity wave and the primary perturbation).

Since the coefficients in (13) are time dependent; normal mode solutions of the form (15), i.e., solutions with complex exponential time dependence, do not exist. Instead, the leading singular vectors are computed for various wavelengths $\lambda_\perp$. This entails calculating eigenvectors involving tens to hundreds of 2.5-D linear integrations for each value of $\lambda_\perp$ (see *Fruman and Achatz* [2012] for more details). An alternative approach, used by *Klaassen and Peltier* [1985] for the related problem of secondary instabilities in Kelvin-Helmholtz billows, is to neglect the time dependence of the basic state and calculate secondary normal modes, but such an implicit assumption of time scale separation is not necessary for computing singular vectors.

The optimization time used for the calculation of the secondary singular vectors must necessarily be relatively short, because if at the optimization time the 2.5-D solution has already become turbulent and filamented, the fastest growing linear modes will be dominated by very small-scale shear instabilities which would quickly saturate in a nonlinear simulation and in any case are not well resolved by the numerics.

The final step is to perform three-dimensional simulations initialized with the sum of the gravity wave, the primary perturbation associated with the most significant wave decay in the 2.5-D simulations, and the initial condition of a leading secondary perturbation. The wavelengths of the primary wave and the perturbations determine the size of the triply periodic domain. The required grid size Δ depends on the intensity of the turbulence generated during the breaking process and the corresponding Kolmogorov length

$$\eta = \min\left(\nu^{3/4}\epsilon_k^{-1/4}\right), \qquad (16)$$

where the minimum is over the computational domain, by the condition $\Delta < \pi\eta$ (discussed by *Yamazaki et al.* [2002] for the case of isotropic turbulence). Since the resolved dissipation rate ϵ_k in turn depends on the grid resolution, the necessary grid resolution must be found by repeated simulations with increasingly fine meshes until the maximum dissipation rate does not change and the condition $\Delta < \pi\eta$ is fulfilled. The results of the 3-D DNS are compared with those of the 2.5-D simulations in terms of the time-dependent projection of the full solution onto the basic wave, the global mean dissipation of kinetic and potential energy in the system, and the streamwise-spanwise-averaged energy spectra.

4. Test Cases

Results are presented for three test cases: two low-frequency inertia-gravity waves (IGW), one of amplitude above and the other of amplitude below the static stability threshold, and a statically unstable high-frequency gravity wave (HGW). All waves have wavelength 3 km, and in all three cases, the f plane is centered at 70°N ($f = 1.4 \times 10^{-4}$ s); the constant Brunt-Väisälä frequency of $N = 2 \times 10^{-2}$ s^{-1} is used. A value of 1 m^2 s^{-1}, realistic for the upper mesosphere, is used for the kinematic viscosity ν and thermal diffusivity μ.

The low-frequency test cases use an IGW with propagation angle $\Theta = 89.5°$, corresponding to a period of 8 h and phase speed 0.1 m s^{-1}. Case I is a statically unstable wave with initial amplitude $a_0 \equiv |a(t_0)| = 1.2$, and case II is a statically and dynamically stable wave with $a_0 = 0.86$. The basic wave for case III is a statically unstable HGW with angle of phase-propagation $\Theta = 70°$ and initial amplitude $a_0 = 1.2$. It has a period of 15 min and phase speed 3.3 m s^{-1}. Due to its short period and small horizontal spatial scale, rotational effects do not play an important role in the dynamics of the HGW.

The Reynolds number, defined following *Fritts and Wang* [2013] as $Re \equiv \lambda_z^2 N/2\pi\nu$, where λ_z is the vertical wavelength of the wave, is about 28,000 for cases I and II and about 25,000 for case III.

The atmosphere and wave parameters for the three test cases are summarized in Tables 1 and 2.

5. Numerical Methods

The 2.5-D nonlinear simulations and the linear integrations required for determining the primary and secondary instability modes are performed with the numerical models developed by *Achatz* [2005, 2007a] and *Fruman and Achatz* [2012].

Table 1. Atmosphere Parameters

Kinematic viscosity	ν	$1\ \mathrm{m^2\,s^{-1}}$
Thermal diffusivity	μ	$1\ \mathrm{m^2\,s^{-1}}$
Latitude for Coriolis parameter	ϕ_C	70°N
Coriolis parameter	f	$1.37 \times 10^{-4}\ \mathrm{s^{-1}}$
Brunt-Väisälä frequency	N	$2 \times 10^{-2}\ \mathrm{s^{-1}}$
Acceleration due to gravity	g	$9.81\ \mathrm{m\,s^{-2}}$

As described in section 3.1 and in *Achatz* [2005], primary perturbations in the form of normal modes are computed using the one-dimensional linear system (6), constructed by linearizing (2a) about (3), and substituting the ansatz (8). The independent variables are the real and imaginary parts of $\hat{u}'_\xi$, $\hat{v}'$, $\hat{w}'_\zeta$, and $\hat{b}'$ evaluated on a discretized ϕ axis (ϕ being the phase of the wave). Singular vectors additionally require the corresponding adjoint model, which was developed using the Tangent linear and Adjoint Model Compiler (TAMC) utility [*Giering and Kaminski*, 1998]. The time integration is performed using a fourth-order Runge-Kutta scheme for the first two time steps and a third-order Adams-Bashforth scheme for the rest [see *Durran*, 2010, section 2.4].

The 2.5-D nonlinear simulations are performed at high enough resolution to resolve scales down to the Kolmogorov scale, here a few meters. The time integration of the system (2a) is performed using the third-order Runge-Kutta scheme of *Williamson* [1980].

The secondary singular vectors are computed using a two-dimensional model to solve the system (13) with solutions of the form (15) inserted. The dependent variables are the real and imaginary parts of $\hat{u}''_\parallel$, $\hat{v}''_\perp$, $\hat{w}''_\zeta$, and $\hat{b}''$ evaluated on a discrete $x_\parallel$-ϕ grid. Again, the corresponding adjoint model required for finding singular vectors was developed with the help of TAMC.

The 3-D DNS are performed with the INCA model (http://www.inca-cfd.com; for details see *Remmler and Hickel* [2012, 2013]) which solves the Boussinesq equations by means of a finite-volume fractional-step method in a triply periodic domain. For time advancement the explicit third-order Runge-Kutta scheme of *Shu* [1988] is used. The time step is dynamically adapted to satisfy a Courant-Friedrichs-Lewy condition. The spatial discretization is based on nondissipative central schemes with fourth-order accuracy for the advective terms and second-order accuracy for the diffusive terms and the pressure Poisson-equation solver.

For all models, the spatial discretization is a staggered one-, two-, or three-dimensional C grid, with each velocity component evaluated at a point displaced by one-half grid interval in the corresponding direction relative to the buoyancy and pressure. Eigenvalues for the primary and secondary instability analyses are computed iteratively using a variant of the Arnoldi process with the Fortran library ARPACK [*Lehoucq et al.*, 1998].

In the one- and two-dimensional models, the discrete pressure Poisson equation (obtained by setting the time derivative of the divergence constraint (2c) to zero) is solved using the discrete Fourier transform. For the 3-D multiblock simulations, the Poisson equation is solved by a Krylov subspace solver with algebraic-multigrid preconditioning.

Table 2. Parameters of the Initial Conditions for the 3-D DNS Test Cases[a]

Case	Amplitude	Propagation Angle Θ	Primary Perturbation	Secondary Perturbation
I. Unstable IGW	$a_0 = 1.2$ $\Delta u_\xi = 14.6\ \mathrm{m\,s^{-1}}$ $\Delta b = 0.23\ \mathrm{m\,s^{-2}}$	89.5°	NM, $\alpha = 90°$ $\lambda_\parallel = 3.98\mathrm{km}$ $A_1 = 0.05$	$\lambda_\perp = 0.4\mathrm{km}$ $A_2 = 0.02$
II. Stable IGW	$a_0 = 0.86$ $\Delta u_\xi = 10.4\ \mathrm{m\,s^{-1}}$ $\Delta b = 0.16\ \mathrm{m\,s^{-2}}$	89.5°	SV, $\alpha = 90°$ $\lambda_\parallel = 2.12\ \mathrm{km}$ $A_1 = 0.1$	$\lambda_\perp = 0.3\ \mathrm{km}$ $A_2 = 0.01$
III. Unstable HGW	$a_0 = 1.2$ $\Delta u_\xi = 12.2\ \mathrm{m\,s^{-1}}$ $\Delta b = 0.24\ \mathrm{m\,s^{-2}}$	70°	NM, $\alpha = 90°$ $\lambda_\parallel = 2.93\ \mathrm{km}$ $A_1 = 0.05$	$\lambda_\perp = 3.0\ \mathrm{km}$ $A_2 = 0.01$

[a]A_1 and A_2 are the amplitudes of the primary and secondary perturbations in terms of the maximum perturbation energy density compared to the maximum energy density in the basic state. Δu_ξ and Δb are the amplitudes of the u_ξ velocity component and buoyancy in the original wave.
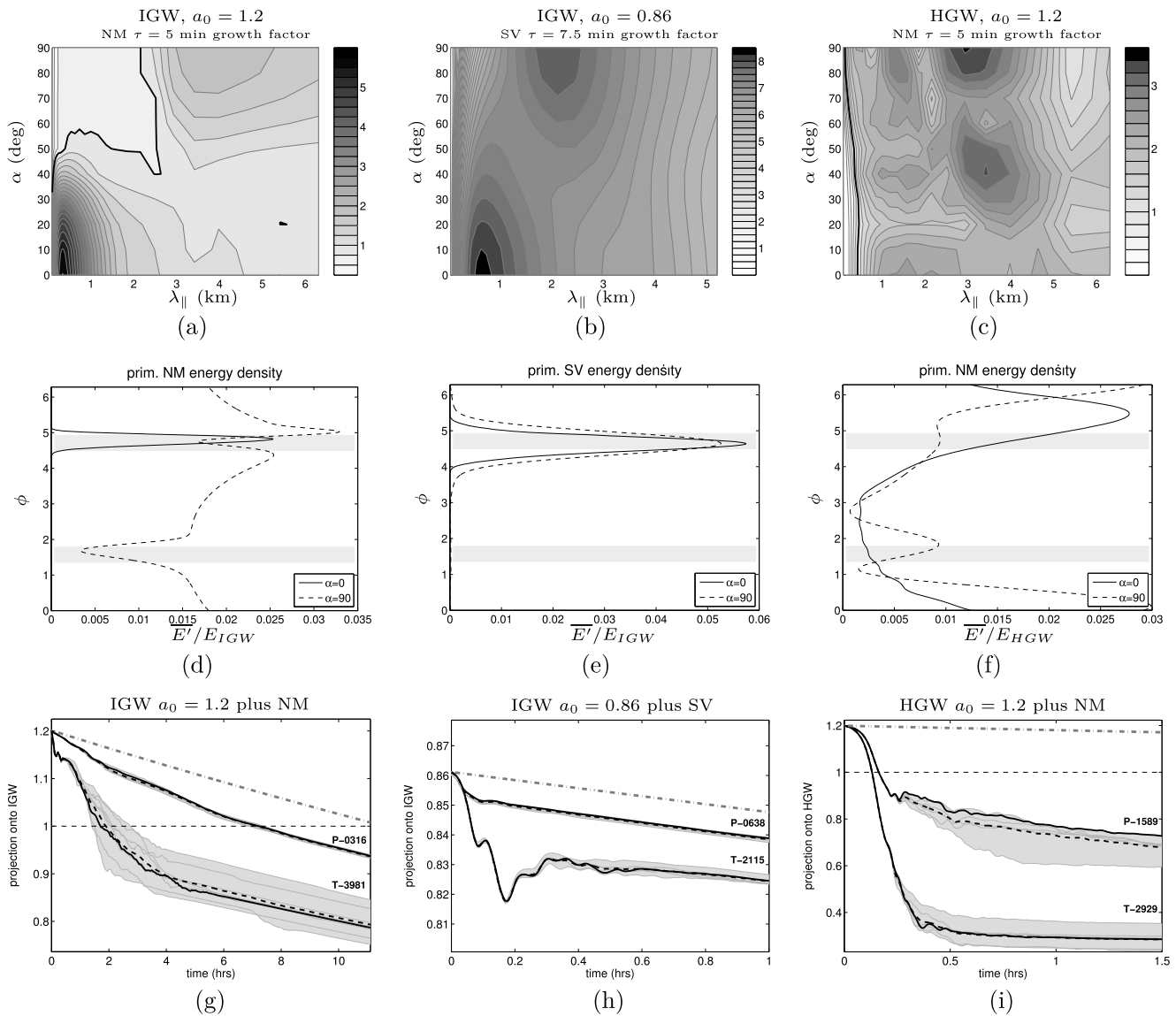
Figure 2. (a–c) Growth factors of leading primary linear modes as functions of perturbation wavelength and orientation angle: normal modes of unstable IGW (Figure 2a), $\tau = 7.5$ min singular vectors of stable IGW (Figure 2b), and normal modes of unstable HGW (Figure 2c). (d–f) Streamwise-spanwise mean perturbation energy density in initial condition of 2.5-D simulations, normalized by the mean energy density in the IGW (E_{IGW}) or HGW (E_{HGW}), for leading transverse ($\alpha = 90°$) and parallel ($\alpha = 0$) NM of unstable IGW (Figure 2d), leading transverse and parallel SV of stable IGW (Figure 2e), and leading transverse and parallel NM of unstable HGW (Figure 2f). Shaded regions in Figures 2d–2f are for reference, indicating levels of maximum ($\phi = \pi/2$) and minimum ($\phi = 3\pi/2$) static stability in the basic state wave. (g–i) Time-dependent projection of 2.5-D nonlinear solution onto the unstable IGW (Figure 2g), stable IGW (Figure 2h), and unstable HGW (Figure 2i). Grey-shaded regions in Figures 2g–2i represent the range of values from integrations with additional small-amplitude initial noise (ensemble average indicated by dashed lines), and dash-dotted line represents the viscous decay of the unperturbed wave.

See Appendix C for the computing resources required for the 3-D DNS and the technical specifications of the machines used to perform them.

6. Results

6.1. Case I: Statically Unstable IGW

The first test case is a statically unstable inertia-gravity wave with initial amplitude $a_0 = 1.2$, propagation angle 89.5°, and wavelength 3 km. The wave period is 8 h and the phase speed is 0.1 m s^{-1}.

Figure 2a shows the 5 min growth factors for the leading normal modes as a function of perturbation wavelength $\lambda_{\parallel} \equiv 2\pi \left(k_\xi^2 + k_y^2 \right)^{-1/2}$ and orientation angle $\alpha \equiv \tan^{-1}(k_y/k_\xi)$. The peaks in the growth factor occur
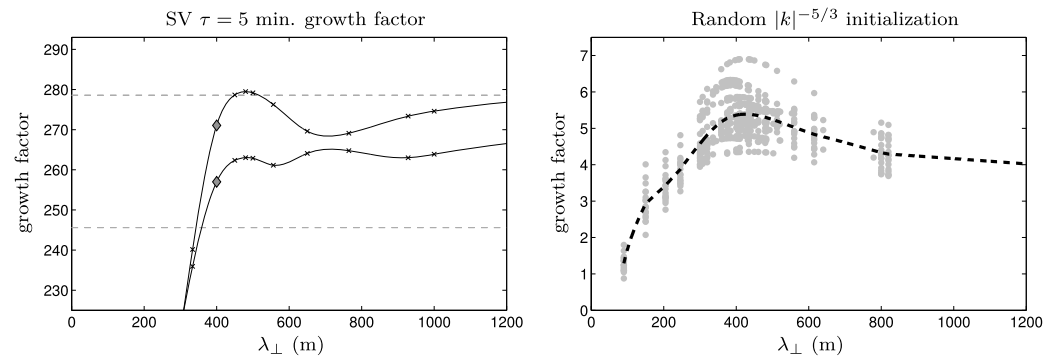
Figure 3. Linear growth factors (left) of leading and second-leading 5 min secondary singular vectors and (right) of randomly initialized perturbations versus secondary perturbation wavelength $\lambda_\perp$ for the unstable IGW perturbed by its leading transverse primary normal mode. Dashed horizontal lines in Figure 3 (left) are growth factors of leading SV for $\lambda_\perp = \infty$; filled diamonds indicate growth factors at $\lambda_\perp = 400$ m. Heavy dashed line in Figure 3 (right) represents ensemble mean growth factor at each wavelength.

for the limiting cases of parallel ($\alpha = 0$) and transverse ($\alpha = 90°$) perturbations. Their spatial structure can be gleaned from Figure 2d, showing the perturbation energy density as a function of ϕ. The perturbations are normalized such that the ratio A_1 of the maximum perturbation energy density in the domain to the (uniform) energy density in the basic state is 0.05. The faster growing of the two modes (indeed the fastest growing mode overall) is the leading parallel normal mode. It has very short wavelength (316 m), and its energy is very localized near the level of maximum static instability $\phi = 3\pi/2$. The leading transverse normal mode has wavelength longer than that of the original wave ($\lambda_\parallel = 3.981$ km), and its energy is distributed throughout the domain.

Figure 2g shows the projection of the 2.5-D nonlinear solution on the original gravity wave as a function of time for simulations initialized with the wave plus either the leading parallel or the leading transverse normal mode, as well as the range of results from ensembles of simulations with additional small amplitude random noise (white noise smoothed with a running mean with window of width 50 m in the $x_\parallel$ and ζ directions). For comparison, the curve showing the viscous amplitude decay of the unperturbed wave (see equation (5)) is plotted with a dash-dotted line. Despite the smaller linear growth rate of the initial perturbation, the wave perturbed by the transverse normal mode decays more than the wave perturbed by the parallel normal mode. The wave breaking lasts on the order of one half of a wave period and involves intermittent sharp drops in amplitude (these correspond to "bursts" of enhanced total energy dissipation discussed below; see Figure 6). The intermittency seems to be associated with the phase propagation of the wave (especially the layer of weakest static stability) through the inhomogeneous field of turbulence excited by the initial instability. Because it showed the most significant wave breaking, we focus on the simulation initialized with the transverse normal mode for the secondary instability analysis and 3-D DNS.

Figure 3 shows the growth factors of the leading 5 min secondary singular vectors versus perturbation wavelength $\lambda_\perp$. Also shown are the 5 min growth factors for an ensemble of linear integrations initialized with a random perturbation with a $k^{-5/3}$ energy spectrum. The ensemble mean has a peak near $\lambda_\perp = 400$ m. The leading secondary singular vector has a somewhat longer wavelength, but for $\lambda_\perp > 400$ m, the growth factor does not change much with wavelength. The $\lambda_\perp = 400$ m singular vector was therefore used to initialize the 3-D DNS. Figure 4 shows the structure of the real part of the $\hat{w}''_\zeta$ field of the 400 m secondary singular vector at the initial and optimization time ($\tau = 5$ min) plotted over the time-dependent basic state velocity and buoyancy fields. Note that the energy associated with the secondary singular vector—like the parallel primary normal mode—is initially concentrated near the level of maximum negative basic state buoyancy gradient. Unlike the primary normal mode, the structure of the singular vector evolves with time to extract most efficiently both potential energy (through interaction with the buoyancy gradient) and kinetic energy (through interaction with the wind shear) from the basic state. At the optimization time, the region of maximum energy density in the secondary singular vector straddles the line of maximum $V_\perp$ in the basic state. It is growing through the Orr mechanism associated with shear in the background velocity component parallel to the direction in which the perturbation varies (in this case $y_\perp$). See *Fruman and Achatz* [2012, Figures 8 and 9] for details.
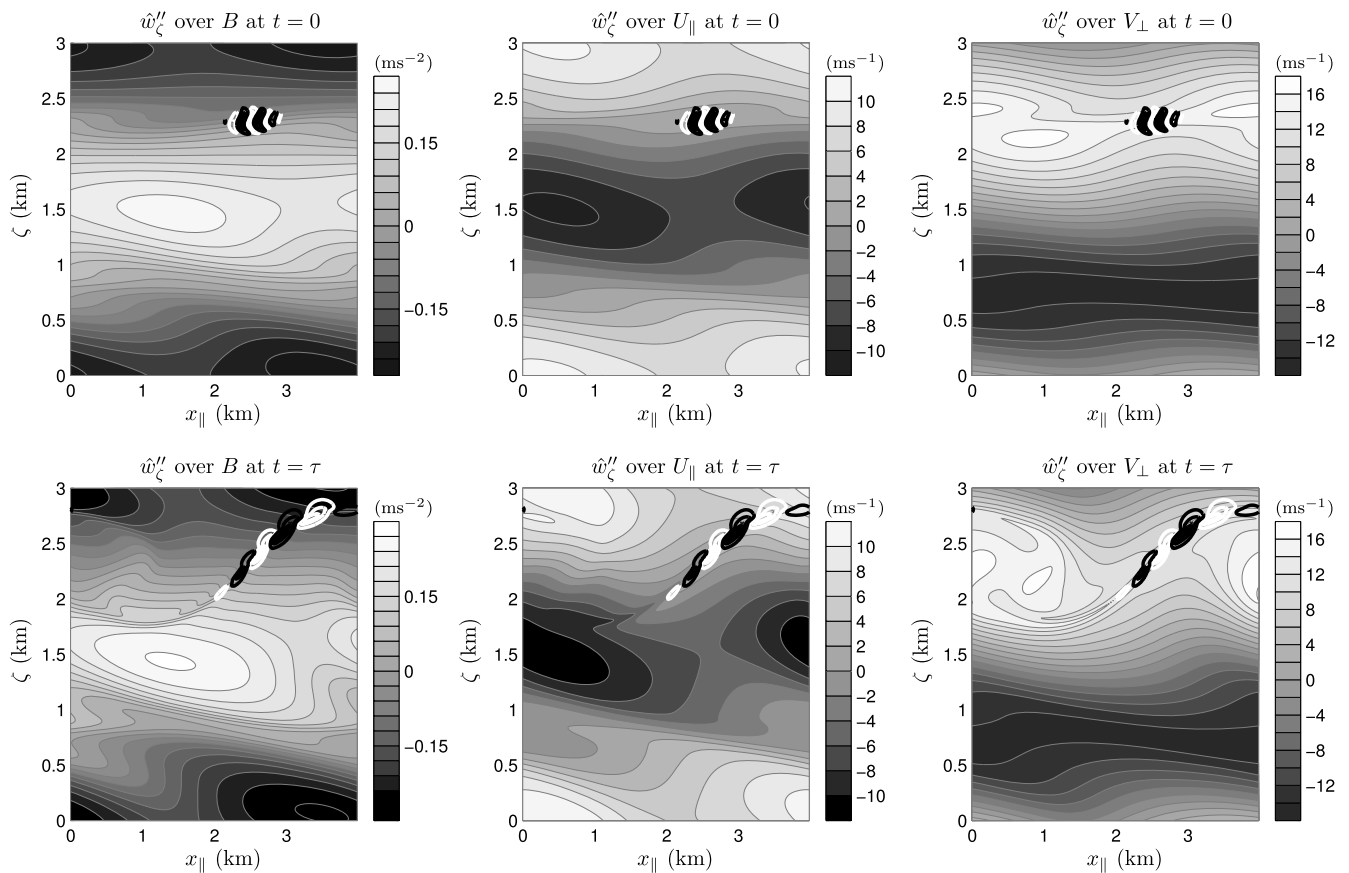
Figure 4. Contours of the real part of perturbation vertical velocity amplitude $\hat{w}''_\zeta$ (top row) at initial and (bottom row) at optimization times for 5 min secondary singular vector superimposed on the basic state buoyancy (left column) B and horizontal velocity fields (middle column) $U_\parallel$ and (right column) $V_\perp$ (shading) for statically unstable IGW perturbed by leading transverse normal mode.

Three-dimensional DNS initialized with the IGW ($\lambda = 3$ km), the leading transverse primary normal mode ($\lambda_\parallel = 3.981$ km) and the leading secondary singular vector with $\lambda_\perp = 400$ m were run with a grid spacing Δ of about 3 m (full resolution) and 6 m (coarse) in all three directions. The amplitude for the secondary singular vector A_2, defined here as the maximum perturbation energy density divided by the maximum basic state energy density, was 0.02. It was shown by *Remmler et al.* [2013] that only in the fully resolved simulation was the Kolmogorov length never smaller than Δ/π and that the results of the two simulations were otherwise extremely similar (hence grid converged). Figure 5 shows the initial buoyancy field from the full-resolution simulation and a snapshot at $t = 695$ s of the buoyancy field together with the kinetic energy dissipation ϵ_k. At the instant shown, very early in the simulation, turbulence has already developed in the upper half of the wave (i.e., the less stable half) and not in the lower half, but the energy density is not strongly correlated with the buoyancy gradient (velocity shear has a strong influence). Note that the figure is plotted in the reference frame moving with the wave. The decay of the wave amplitude with time and the global mean of the total energy dissipation $\epsilon_k + \epsilon_p$ from the ensemble of 2.5-D simulations and from the 3-D DNS are shown in Figure 6. The initial burst of turbulence is more intense in the 3-D DNS, and the wave decays more rapidly. On the other hand, in the 2.5-D simulations the initial turbulence is more sustained, the energy decay rate is greater for $t \gtrsim 30$ min, and the total reduction in wave amplitude over the length of the whole simulation is greater. Figure 7 shows the streamwise and spanwise averaged total energy dissipation as a function of ζ and time from the fully resolved 3-D DNS and the 2.5-D simulations without additional noise. Again, the plot is in the reference frame moving with the phase velocity of the wave. In the first 40 min of the 3-D simulation the turbulent dissipation is distributed throughout the domain after which it dies out in the statically stable half. In the 2.5-D simulation dissipation is sustained also in the stable half. In analyzing 2.5-D simulations of a similar unstable IGW, *Achatz* [2005, 2007a]
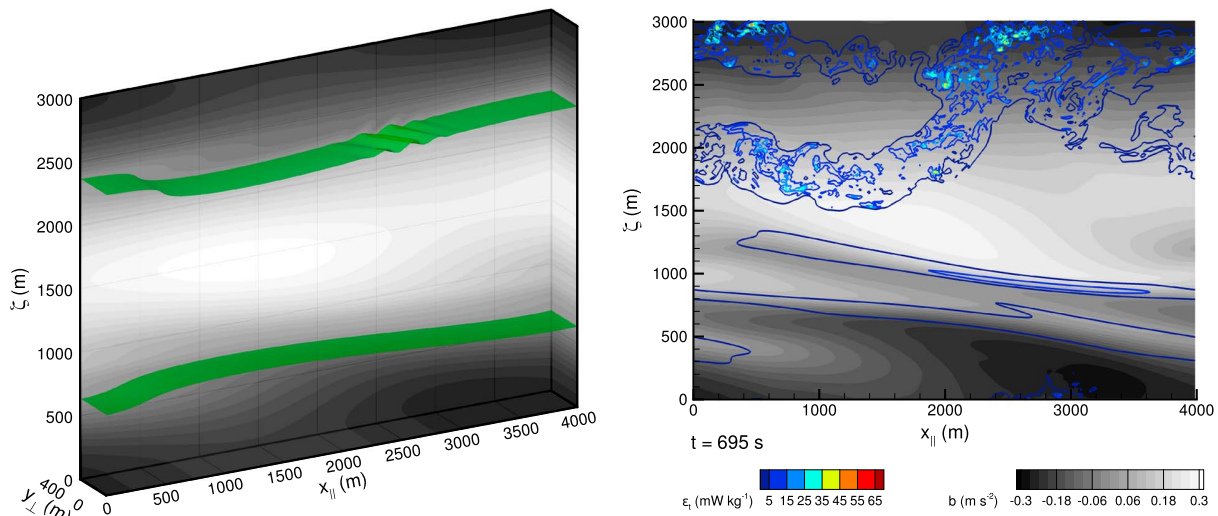
Figure 5. Snapshots of the buoyancy field from fine 3-D DNS (1350 × 128 × 1000 cells) of the statically unstable IGW: (left) 3-D initial condition with an iso-surface at $b = -0.02 \, \mathrm{m \, s^{-2}}$ (green color). (right) Flow field averaged in the $y_\perp$ direction at $t = 11.6 \, \mathrm{min}$ (grey scale contours: buoyancy, colored lines: total energy dissipation).

attributed the dissipation in the stable region to small-scale waves propagating away from the unstable region and encountering a critical level. After about one half of a wave period (about 4 h), there is an episode of enhanced energy dissipation in the 3-D DNS and a corresponding dip in the wave amplitude (cf. Figure 6). At this time the point of minimum static stability in the original wave has propagated down to the level initially occupied by the most stable point. The dashed black line in Figure 7 represents a point fixed in space. Evidently, residual turbulence in the stable part of the wave left over from the early phase of the breaking is stirred up when it interacts with the unstable part of the wave. This is discussed in more depth in *Remmler et al.* [2013]. The dark grey contours in Figure 7 show the isoline $Ri = 1/4$, where

$$Ri = \frac{N^2 + \overline{\partial b / \partial z}}{(\partial u / \partial z)^2 + (\partial v / \partial z)^2} \tag{17}$$
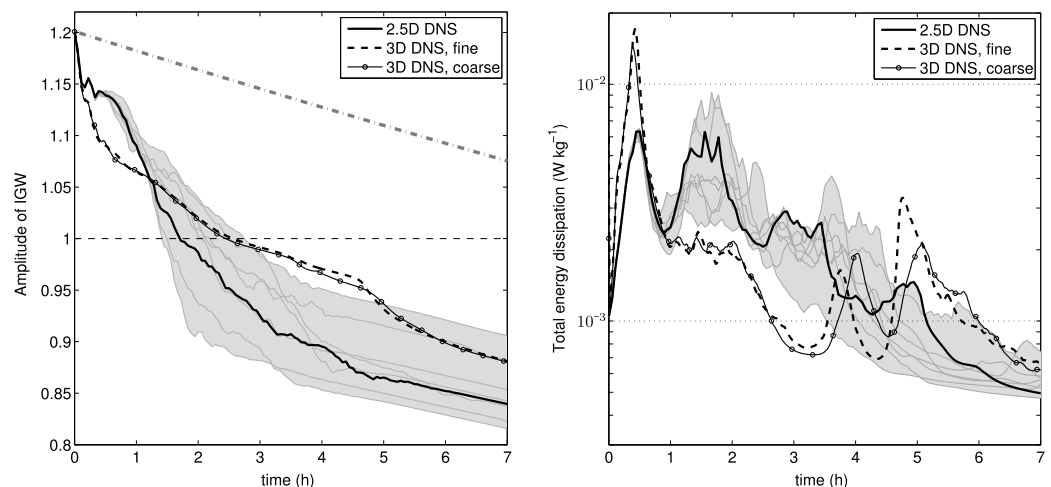
Figure 6. Comparison of (left) wave amplitude decay and (right) total energy dissipation in 2.5-D and 3-D DNS of statically unstable IGW. Dash-dotted line indicates amplitude decay due to laminar viscous decay of the unperturbed wave.
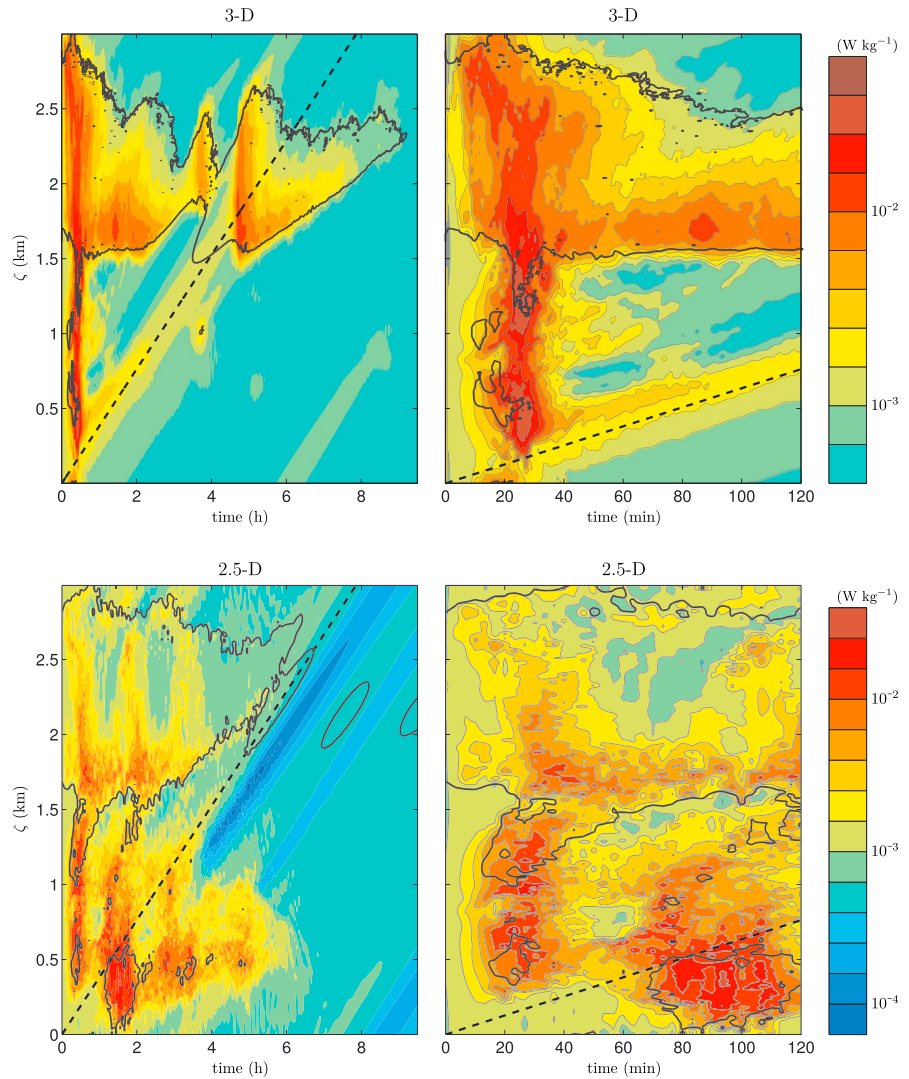
Figure 7. Spanwise and streamwise averaged total energy dissipation from (top row) 3-D and (bottom row) 2.5-D DNS of unstable IGW. Contours equally spaced on a logarithmic (base 10) scale. Dashed black line represents a fixed point in the Earth frame. Results of the (left column) entire run and (right column) closeups of the first 2h of model time. Solid dark grey lines represent contours of $Ri = 1/4$ (see equation (17)).

is the Richardson number (the overbars indicate the streamwise-spanwise mean,

$$u = u_{\parallel} \cos\alpha \sin\Theta - v_{\perp} \sin\alpha \sin\Theta + w_{\zeta} \cos\Theta \tag{18a}$$

$$v = u_{\parallel} \sin\alpha + v_{\perp} \cos\alpha \tag{18b}$$

are the horizontal velocity components in the Earth frame, and

$$\frac{\partial}{\partial z} = -\cos\alpha\cos\Theta\frac{\partial}{\partial x_{\parallel}} + \sin\alpha\cos\Theta\frac{\partial}{\partial y_{\perp}} + \sin\Theta\frac{\partial}{\partial \zeta} \tag{19}$$

is the vertical derivative in the Earth frame). Most of the dissipation occurs in regions of $Ri < 1/4$. This does not necessarily indicate a causal relationship (along the lines of a Kelvin-Helmholtz type instability) since turbulence necessarily entails large local velocity shear, which implies small values of Ri.

Figure 8 shows the streamwise and spanwise averaged energy spectra at times of peak energy dissipation in the 2.5-D (ensemble) and coarse-resolution 3-D simulations and near the end of the simulations. Also shown are the spectra from the initial conditions, which are identical in 2.5-D and 3-D except for the
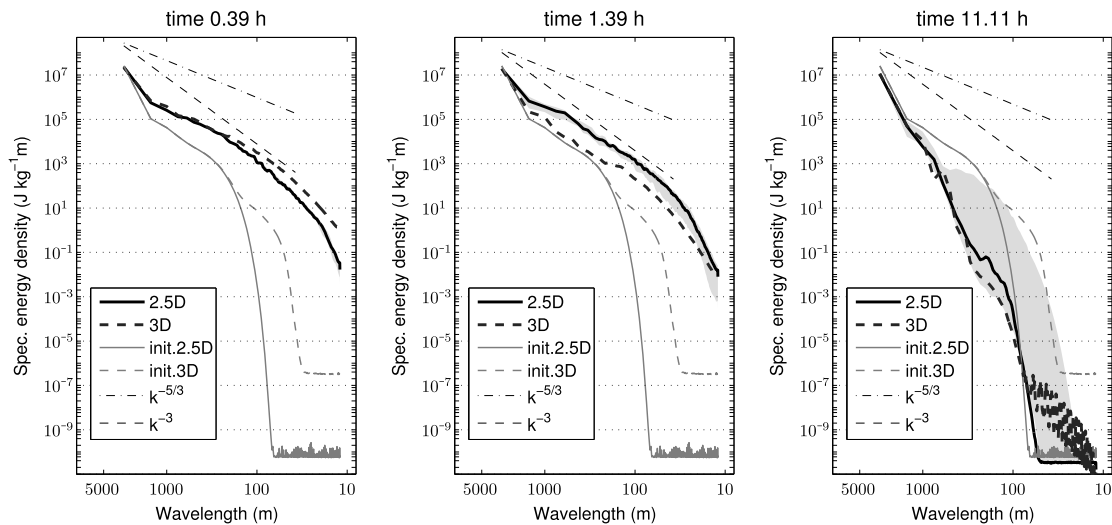
Figure 8. Spanwise and streamwise averaged energy spectra from times of peak energy dissipation in the 2.5-D and coarse-resolution (640 × 64 × 500 cells) 3-D DNS of the unstable IGW. Shaded regions show the range of values from the ensemble of 2.5-D simulations. Also plotted on all panels are the spectra from the initial conditions of 2.5-D and 3-D simulations.

effect of the secondary singular vector perturbation. At the moment of maximum energy dissipation in 3-D (0.39 h), the 2.5-D and 3-D spectra are very similar, both showing energy having moved to small scales and a $k^{-5/3}$ inertial range forming, characteristic of 3-D isotropic turbulence. The 3-D spectrum shows more energy at the smallest scales, which is what one would expect, given it has more possibilities for vortex tilting and stretching and therefore a more efficient downscale energy cascade.

The spectra at the time of the second burst of dissipation in 2.5-D (1.39 h) are quite different in 2.5-D and 3-D. There is much more energy in the smaller scales in the 2.5-D simulation, the 3-D simulation having "burned itself out" more quickly. The energy in the largest scale (which contains the original wave) is, however, almost the same in the two simulations. Both of these observations are consistent with Figure 6: the dissipation at 1.39 h is much less in 3-D (Figure 6, right), but the graphs of the projection onto the IGW intersect at about that time (Figure 6, left).

The 2.5-D spectra at 1.39 h exhibit a clear k^{-3} inertial range behavior. This spectral slope has been found in observations of the atmosphere [*Cot*, 2001] and in numerical studies [e.g., *Carnevale et al.*, 2001; *Brethouwer et al.*, 2007; *Remmler and Hickel*, 2013] to be characteristic of the "buoyancy range" in stratified turbulence. The 3-D spectral slope at the same time is something in between k^{-3} and $k^{-5/3}$, representing neither completely isotropic nor fully stratified turbulence. In the 2.5-D ensemble the spectra remain close to k^{-3} in the range between 100 m and 1000 m until about $t \approx 4.5$ h (not shown), which is about as long as the turbulent dissipation persists in the stable half of the domain (compare with Figure 7). This causes the turbulence to be, on average, much more strongly affected by stratification than in the 3-D DNS, where significant turbulence persists only in the unstable half of the domain. Consequently, the spectral slope in the 3-D DNS changes multiple times between $k^{-5/3}$ in times of strong turbulent dissipation ($t < 2$ h, $t \approx 4$ h, $t \approx 5$ h) and k^{-3} in times of weak dissipation ($t \approx 3.5$ h, $t \approx 4.5$ h, $t > 6$ h).

At the end of the simulations (11.11 h), the turbulence has died out and there is very little energy in the smaller scales. Notice that there is a wide variation in the spectra between 2.5-D ensemble members. Indeed, after the first burst of turbulence, the ensemble members begin to diverge in all three of the diagnostics presented. It is natural that such a long simulation of a highly nonlinear process like a breaking wave be sensitive to the addition of initial noise.

6.2. Case II: Statically Stable IGW

The second case is a statically stable inertia-gravity wave, identical to the first case but with $a_0 = 0.86$. The Richardson number Ri_{IGW} in the wave solution (equation (9)) is greater than $1/4$, and the linear model has been used to verify that no exponentially growing normal mode solutions exist for any perturbation wavelength or orientation (not shown). As such, the primary perturbation analysis in this case involves calculating
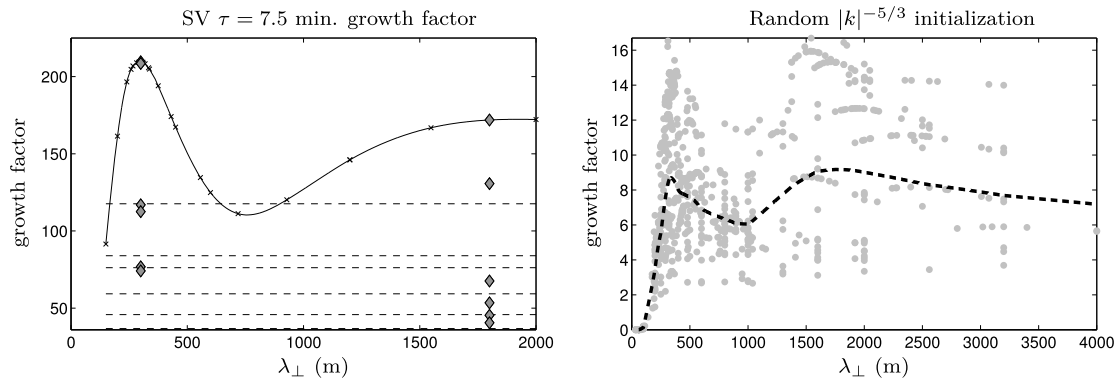
**Figure 9.** As in Figure 3 but for optimization time 7.5 min and the statically stable IGW perturbed by its leading transverse singular vector. The filled diamonds mark the growth factors of the leading 12 (note that they come in degenerate pairs) singular vectors for $\lambda_\perp = 300$ m and $\lambda_\perp = 1800$ m.

the leading singular vectors for a range of perturbation wavelengths and orientations. An optimization time of $\tau = 7.5$ min, chosen a posteriori, ensures that the primary and secondary singular vector analyses both yield a finite scale for the most amplified mode. The singular vector growth factors as functions of $\lambda_\parallel$ and α are shown in Figure 2b. Again, the leading parallel perturbation has shorter wavelength ($\lambda_\parallel = 0.638$ km) than the leading transverse perturbation ($\lambda_\parallel = 2.115$ km) and a larger growth factor, but only slightly so.

Figure 2e shows the energy density as a function of ϕ in the initial condition for the 2.5-D nonlinear simulations for the parallel and transverse singular vectors. Again, the transverse perturbation is less focused near the level of lowest static stability in the original wave. The amplitude A_1 of the initial perturbation was
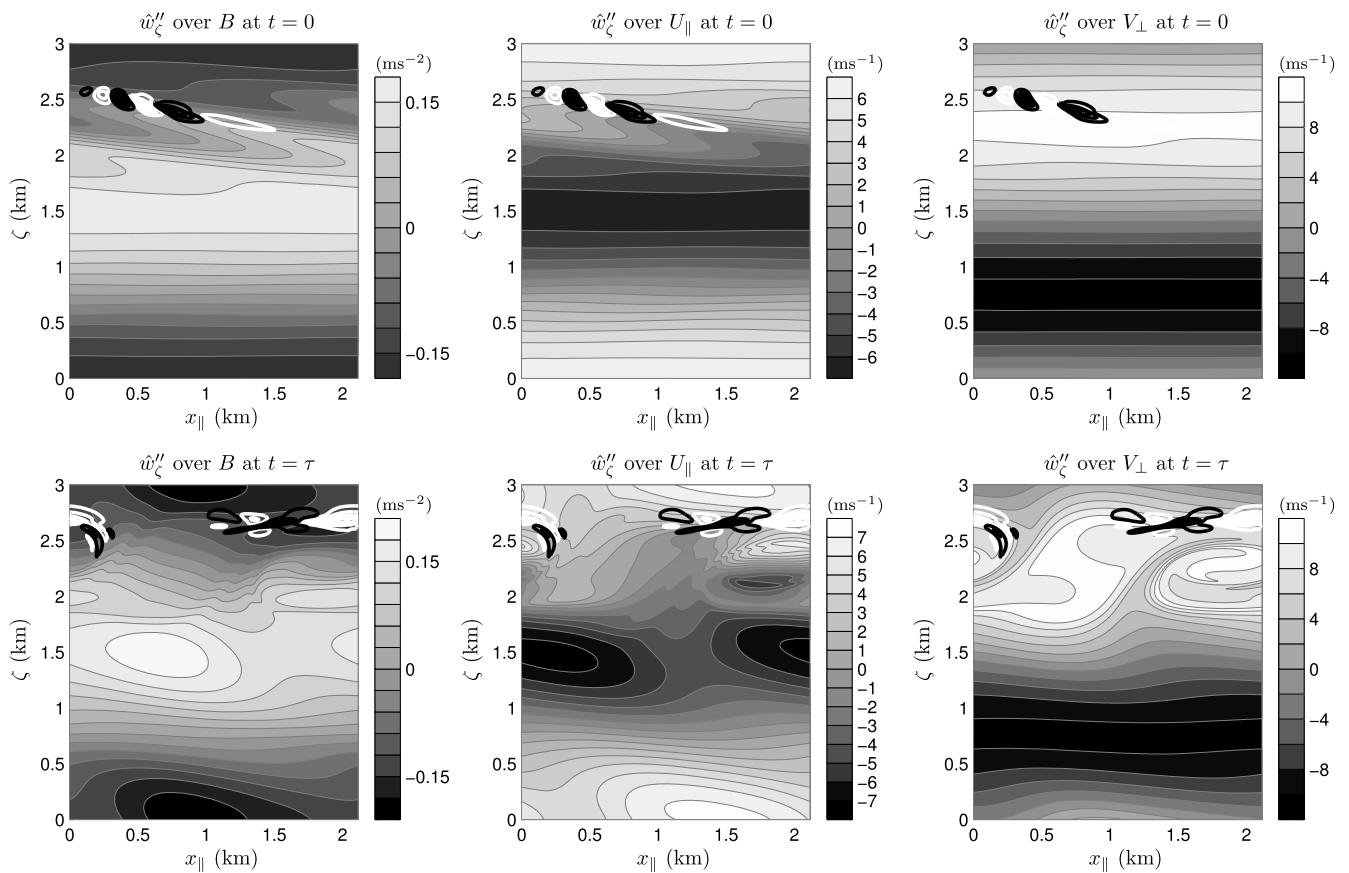
Figure 10. As in Figure 4 but for optimization time $\tau = 7.5$ min and the statically stable IGW perturbed by its leading 7.5 min transverse primary singular vector.

Table 3. Parameters of Numerical Calculations of Primary and Secondary Instability Growth Factors and of 2.5-D and 3-D Direct Numerical Simulations

	I. Unstable IGW	II. Stable IGW	III. Unstable HGW
Primary Instability			
n_ϕ $(\Delta\zeta)$	1024 (3 m)	1024 (3 m)	1024 (3 m)
Time step Δt	0.025 s	0.025 s	0.025 s
Integration time τ	5 min	7.5 min	5 min
2.5-D DNS			
$n_{x_\parallel} \times n_\zeta$ $(\Delta x_\parallel, \Delta\zeta)$	660 × 500 (6 m, 6 m)	350 × 500 (6 m, 6 m)	500 × 500 (6 m, 6 m)
Time step Δt	0.05 s	0.05 s	0.05 s
Integration time τ	666 min	60 min	90 min
Secondary Instability			
$n_{x_\parallel} \times n_\phi$ $(\Delta x_\parallel, \Delta\zeta)$	128 × 512 (31 m, 6 m)	128 × 512 (17 m, 6 m)	256 × 256 (11 m, 12 m)
Time step Δt	0.05 s	0.05 s	0.05 s
Integration time τ	5 min	7.5 min	5 min
Coarse-Resolution 3-D DNS			
$n_{x_\parallel} \times n_{y_\perp} \times n_\zeta$	640 × 64 × 500	512 × 64 × 768	768^3 / 384^3
Cell size Δ	6.2 m, 6.3 m, 6.0 m	4.1 m, 4.7 m, 3.9 m	3.9 m / 7.8 m
Integration time τ	1000 min	100 min	91 min / 157 min
Full-Resolution 3-D DNS			
$n_{x_\parallel} \times n_{y_\perp} \times n_\zeta$	1350 × 128 × 1000	720 × 96 × 1024	1536 × 1536 × 1536
Cell size Δ	2.9 m, 3.1 m, 3.0 m	2.9 m, 3.1 m, 2.9 m	1.9 m
Integration time τ	572 min	100 min	46 min

chosen such that the maximum energy density in the perturbation is 10% that of the original wave. Unlike a normal mode, which in the linear regime has a fixed spatial structure as its amplitude grows and oscillates, the structure of a singular vector changes with time (since its constituent normal modes each have a different decay rate and frequency). The choice of initial amplitude is therefore more consequential here in that it affects the spatial structure of the solution at the moment when nonlinear effects become important. Figure 2h shows the amplitude as a function of time for the 2.5-D simulations initialized with the leading parallel and transverse singular vectors, including results for an ensemble of simulations further perturbed by small-amplitude noise at $t = 0$. The wave perturbed by the transverse singular vector decays more than the wave perturbed by the parallel singular vector. The breaking is modest, in general, in this case, as the original wave is statically and dynamically stable.

Again, we chose the transverse perturbation for the rest of the analysis. Figure 9 shows the 7.5 min growth factors for the leading secondary singular vectors as functions of perturbation wavelength $\lambda_\perp$. The most amplifying perturbation has wavelength $\lambda_\perp = 300$ m. Also shown (filled diamonds) are the growth factors of the trailing singular vectors for $\lambda_\perp = 300$ m and $\lambda_\perp = 1800$ m (where the growth factor curve reaches a local maximum) and the growth factors for $\lambda_\perp = \infty$ (dashed lines). Figure 9 (right) shows the growth factors from ensembles of randomly initialized (with a $k^{-5/3}$ energy spectrum) linear integrations with a range of perturbation wavelengths. The ensemble mean of the latter also has peaks near $\lambda_\perp = 300$ m and $\lambda_\perp = 1800$ m, suggesting that the secondary singular vectors are representative of modes likely to emerge spontaneously. Figure 10 shows the spatial structure of the secondary singular vector with $\lambda_\perp = 300$ m at the initial and optimization times. Notice that the spatial scale in the $(x_\parallel, \zeta)$ plane roughly matches the wavelength (300 m) in the $y_\perp$ direction. This seems to be a generic feature of the early time unstable modes (primary and secondary; see *Fruman and Achatz* [2012]). As in the case of the unstable IGW, it is through interaction with the $V_\perp$ component of the basic state that the secondary singular vector is growing at the optimization time.

The initial condition for the 3-D DNS is composed of the original IGW ($\lambda = 3$ km), the leading 7.5 min transverse primary singular vector ($\lambda_\parallel = 2.115$ km) and the leading 7.5-min secondary singular vector ($\lambda_\perp = 300$ m). Simulations were run with average grid spacing $\Delta \approx 3$ m ("fine") and $\Delta \approx 4.2$ m ("coarse") (see third column of Table 3). The initial buoyancy field from the fine 3-D DNS is shown in Figure 11a. Note that although the base wave is statically stable, due to the finite amplitude primary perturbation, there is a region of static instability at the level of weakest stability in the base wave (as evidenced by the fold in the $b = -0.03$ m s^{-2} surface of the initial condition). The temporal development of the flow field is visualized

(a) $t = 0\,\mathrm{min}$ (initial condition) (b) $t = 4\,\mathrm{min}$ (c) $t = 7.5\,\mathrm{min}$ (optimization time)

(d) $t = 11\,\mathrm{min}$ (max. dissipation) (e) $t = 26\,\mathrm{min}$ (f) $t = 50\,\mathrm{min}$
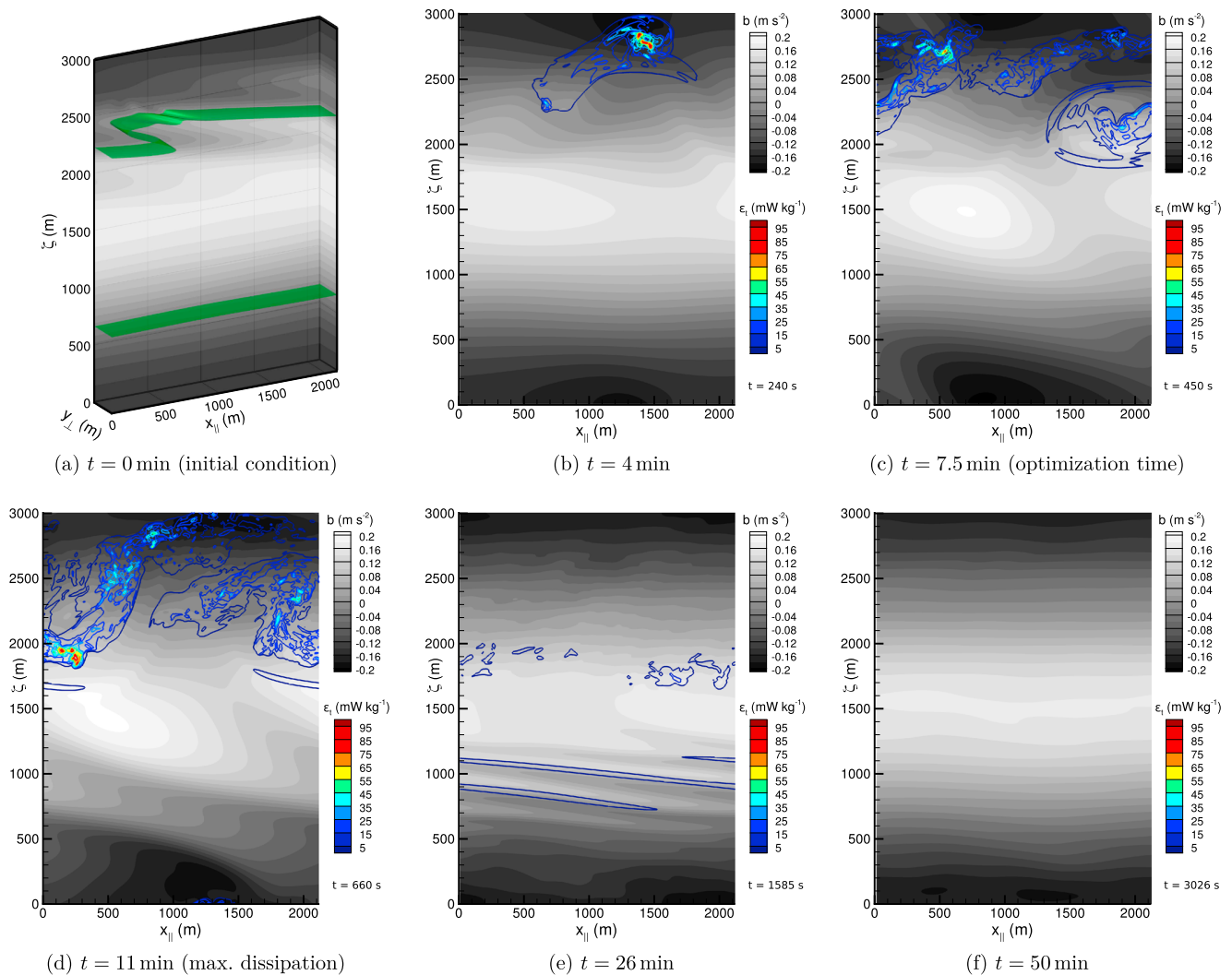
Figure 11. Snapshots of the buoyancy field from 3-D DNS ($720 \times 96 \times 1024$ cells) of the statically stable IGW: (a) 3-D initial condition with the isosurface $b = -0.03\,\mathrm{m\,s^{-2}}$ (green color). (b–f) Flow field averaged in the $y_\perp$ direction (grey scale contours: buoyancy, colored lines: total energy dissipation).

in Figures 11b–11f by contours of streamwise-averaged buoyancy and kinetic energy dissipation ϵ_k. The perturbation grows during the first minutes and generates turbulence in the least stable part of the wave. The turbulence remains confined to this region and is dissipated quickly. The peak dissipation is reached at $t = 11\,\mathrm{min}$, and after 40 min the turbulence has basically vanished. During this period of turbulent decay, some overturning occurs in the most stable part of the wave, similar to the case of the unstable IGW. Here, however, the overturning is too weak to create a negative vertical buoyancy gradient and breaking. It is thus simply dissipated by molecular heat transport.

Figure 12 shows the evolution of the wave amplitude and total energy dissipation from the 3-D DNS and the ensemble of 2.5-D simulations. The decay (and partial rebound) of the wave amplitude is very similar in 3-D and 2.5-D, but the onset of turbulence and the associated energy dissipation occur earlier in 3-D. The lower portion of Figure 12 (left) shows the maximum and mean perturbation energy density from a linear 2.5-D integration initialized with the primary singular vector. The mean energy in the singular vector is maximum at the optimization time and then decays. The drops in the maximum perturbation energy density from the linear integration approximately coincide in time with the rebounds of the IGW amplitude from the non-linear simulations. The spatial distribution of the dissipation (Figure 13) is very similar in 2.5-D and 3-D. The energy dissipation is strongly correlated with the region of $Ri < 1/4$ (bounded by the dark grey contour), particularly in the upper half of the domain in the 2.5-D simulation.
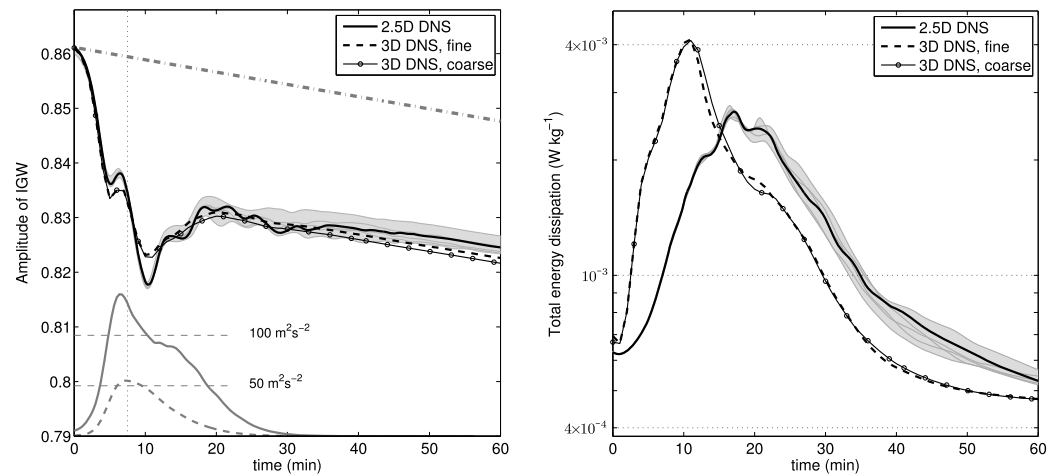
Figure 12. As in Figure 6 but for the statically stable IGW. The resolutions used for the 3-D DNS were 720 × 96 × 1024 (fine) and 512 × 64 × 768 (coarse). The curves in the lower part of Figure 12 (left) show the maximum (solid line) and mean (dashed line) energy in the linear 2.5-D integration initialized with the primary SV, and the vertical dotted line marks the optimization time (7.5 min). For reference, the energy density in the unperturbed IGW is 54.5 m^2 s^{-2}.

The base wave in this case being stable, it is not surprising that the peak in global mean dissipation is weaker than in case I (compare Figures 6 and 12). Nevertheless, the kinetic energy dissipation can be locally more intense during the early phase of the simulation (compare the colored contours in Figures 5 and 11). This can be attributed to the difference between a primary normal mode, used in case I, and a primary singular vector with short optimization time, used in case II. The latter extracts maximum energy in the early phase of the simulation.

The Kolmogorov length as a function of time from the two 3-D DNS is plotted in Figure 14a. In the fine simulation, η is always larger than Δ/π (indicated by the horizontal line), so all turbulence scales are resolved. Although η is briefly below Δ/π in the coarse simulation, the results are almost indistinguishable from the fine simulation (compare the projection and dissipation diagnostics shown in Figure 12), so the simulations are grid converged.
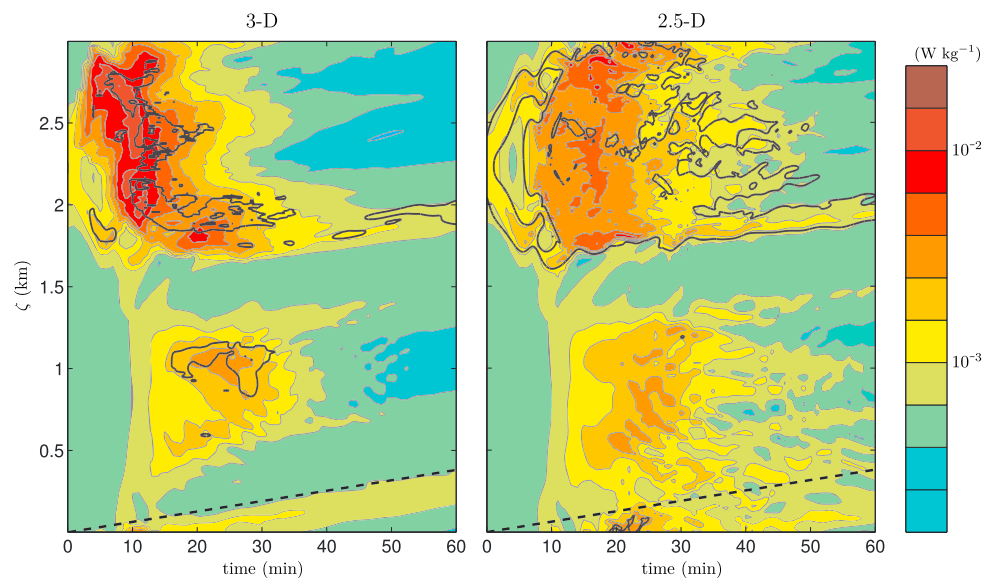
Figure 13. Spanwise and streamwise averaged total energy dissipation from the fully resolved (left) 3-D and (right) 2.5-D DNS of the statically stable IGW. Contours equally spaced on a logarithmic (base 10) scale. Solid light grey line is the contour $Ri = 1/4$ (see equation (17)), and the heavy dashed black line represents a fixed point in the Earth frame.

(a) stable IGW (case II)   (b) unstable HGW (case III)
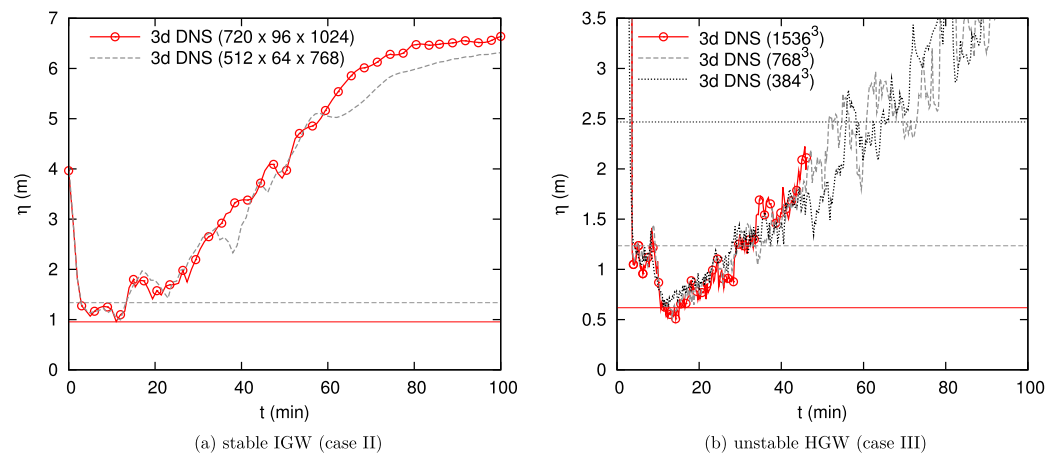
Figure 14. Kolmogorov length in the 3-D DNS of (a) the stable IGW and (b) the unstable HGW. The threshold where the simulation is supposed to be fully resolved is indicated by a horizontal line for each simulation.

6.3. Case III: Statically Unstable HGW

The third and final test case is the statically unstable ($a_0 = 1.2$) high-frequency gravity wave ($\Theta = 70°$, period 15 min, phase speed 3.3 m s^{-1}).

The 5 min growth factors of the leading normal modes for a range of wavelengths $\lambda_\parallel$ and orientation angles α are shown in Figure 2c. The fastest growing normal mode overall is the leading transverse ($\alpha = 90°$) mode with $\lambda_\parallel = 2929$ m. The wavelength of maximum growth rate is not very sensitive in this case to the orientation of the perturbation, with the peak for most orientation angles near $\lambda_\parallel = 3$ km (which happens to be the wavelength of the original wave). The leading parallel ($\alpha = 0$) normal mode is an exception, having a shorter wavelength of $\lambda_\parallel = 1589$ m. Figure 2c is comparable to Figure 5 of *Fritts et al.* [2013] showing growth rates computed using the Floquet theory method of *Lombard and Riley* [1996] for a HGW with $a_0 = 1.1$. For example, the growth factor of the leading transverse normal modes ($\alpha = 90$, or $k_i = 0$ in their notation) exhibits multiple peaks with the largest growth factor for primary perturbation wavelength close to the wavelength of the original wave.

The energy density in the leading transverse and parallel normal modes and the wave amplitude decay in the respectively initialized 2.5-D simulations are shown in Figures 2f and 2i. The high-frequency and significant horizontal gradients in the HGW make it less similar to a steady stratified shear flow than the IGW. It is not surprising then that the energy density in the leading normal modes is not as strongly correlated in space with the level of lowest static stability. Once again, it is the longer-wavelength transverse normal mode that leads to the most profound breaking of the original wave. The HGW decays more com-


SV $\tau = 5$ min. growth factor   Random $|k|^{-5/3}$ initialization
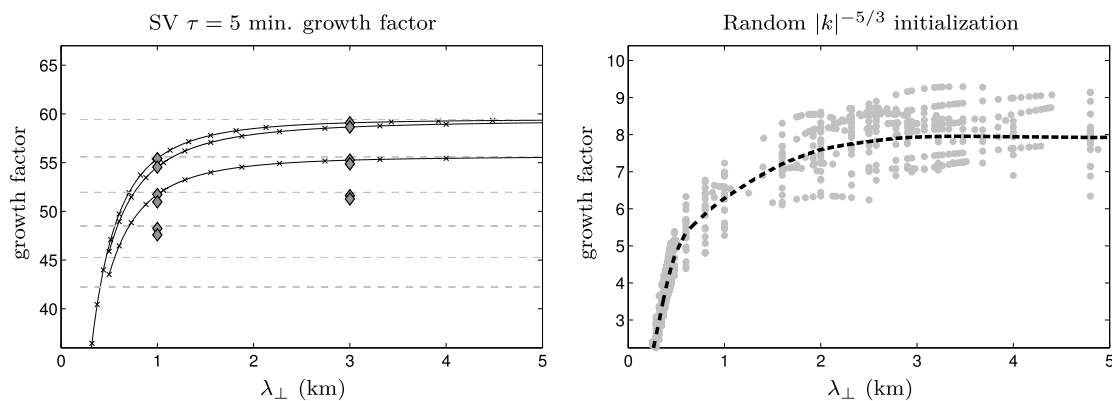
Figure 15. As in Figure 3 but for the statically unstable HGW perturbed by its leading transverse singular vector. Filled diamonds in Figure 15 (left) indicate growth factors of leading twelve singular vectors with $\lambda_\perp = 1000$ m and $\lambda_\perp = 3000$ m.
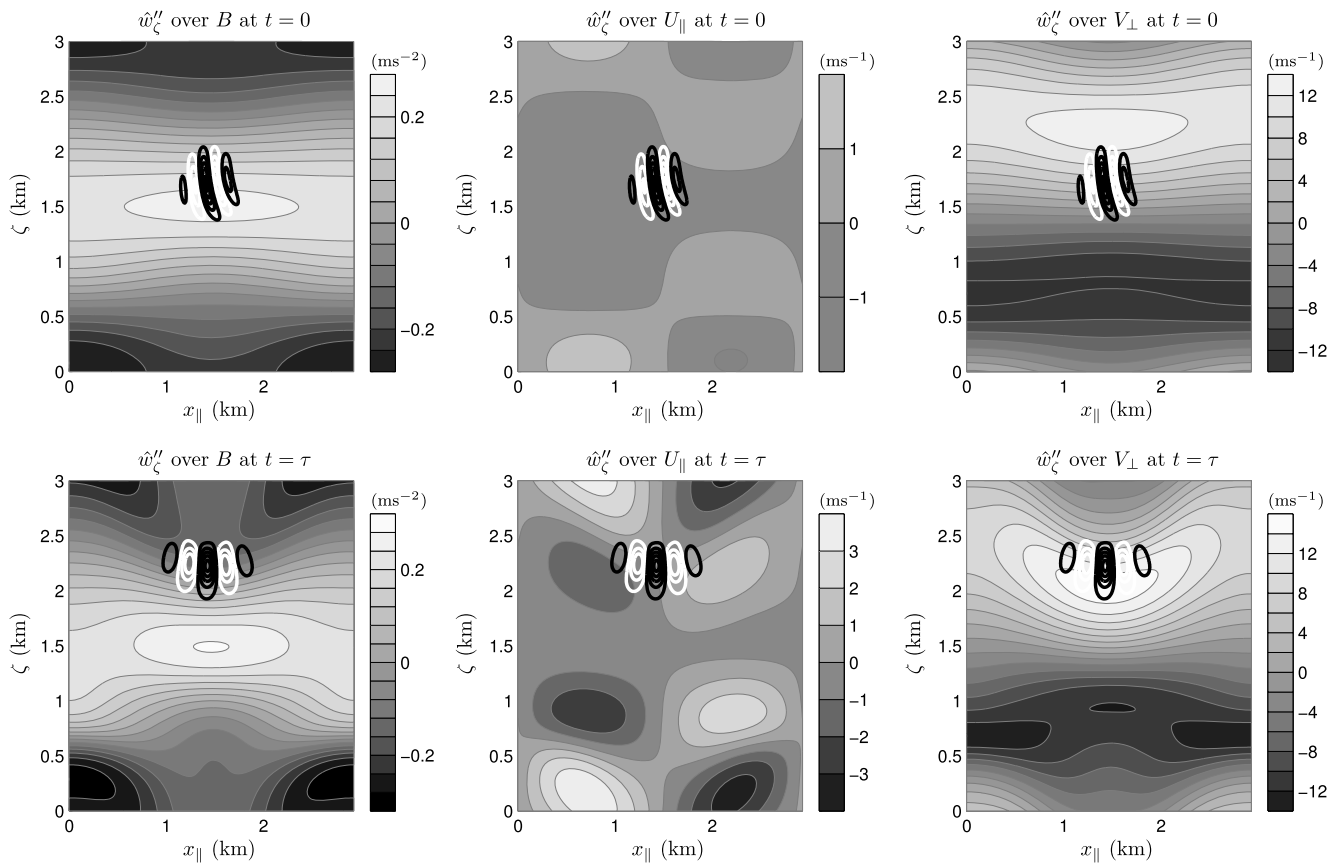
Figure 16. As in Figure 4 but for the statically unstable HGW perturbed by the leading transverse normal mode.

pletely and more vigorously than does the unstable IGW (cf. Figure 2g); its amplitude is reduced to about 0.3 within 30 min.

The 5 min growth factors of the leading secondary singular vectors as functions of perturbation wavelength $\lambda_\perp$ are shown in Figure 15. The basic state is the 2.5-D simulation initialized with the wave and the leading transverse primary normal mode. Also shown are the 5 min growth factors of randomly initialized integrations. There is no clear peak in either case, but the growth factor does not increase much beyond $\lambda_\perp = 3$ km. Figure 16 shows the structure of the secondary singular vector with $\lambda_\perp = 3$ km at the initial and optimization times. Notice that the singular vector appears to have "propagated" up through the domain. In fact, it is the original wave (and hence the entire reference frame) that has propagated downward about one third of a wavelength. Notice also that unlike for the elliptically polarized IGW, the transverse velocity in the basic state ($U_\parallel$ in the twice-rotated reference frame) is initially about an order of magnitude weaker than the parallel ($V_\perp$) component, but at the optimization time, it has grown due to interaction with the velocity shear in the HGW. *Achatz* [2007b] found that transverse primary perturbations to statically unstable HGW grow more through interaction with the shear in the wave than with the unstable buoyancy gradient.

The 3-D DNS was initialized with the original HGW ($\lambda = 3$ km), the leading transverse primary normal mode ($\lambda_\parallel = 2.929$ km) and the 5 min secondary singular vector with $\lambda_\perp = 3$ km. Three simulations were performed, with grid spacing Δ of 1.9 m (fine resolution), 3.9 m (coarse 1), and 7.8 m (coarse 2). The initial buoyancy field from the fine-resolution simulation is shown in Figure 17 together with snapshots of the streamwise-averaged buoyancy and kinetic energy dissipation at a sequence of later times. The dissipation at early times is localized where the secondary singular vector energy is concentrated (cf. Figure 16) but soon fills the domain. Comparisons of the amplitude decay and total energy dissipation are shown in Figure 18. Both diagnostics are quite similar in 2.5-D and 3-D, although as in the previous cases the onset of turbulent dissipation occurs slightly earlier in 3-D. The distribution in space and time of the energy

(a) $t = 0$ min (initial condition)

(b) $t = 3$ min

(c) $t = 5$ min (optimization time)

(d) $t = 8$ min

(e) $t = 15$ min (maximum dissipation)

(f) $t = 32$ min
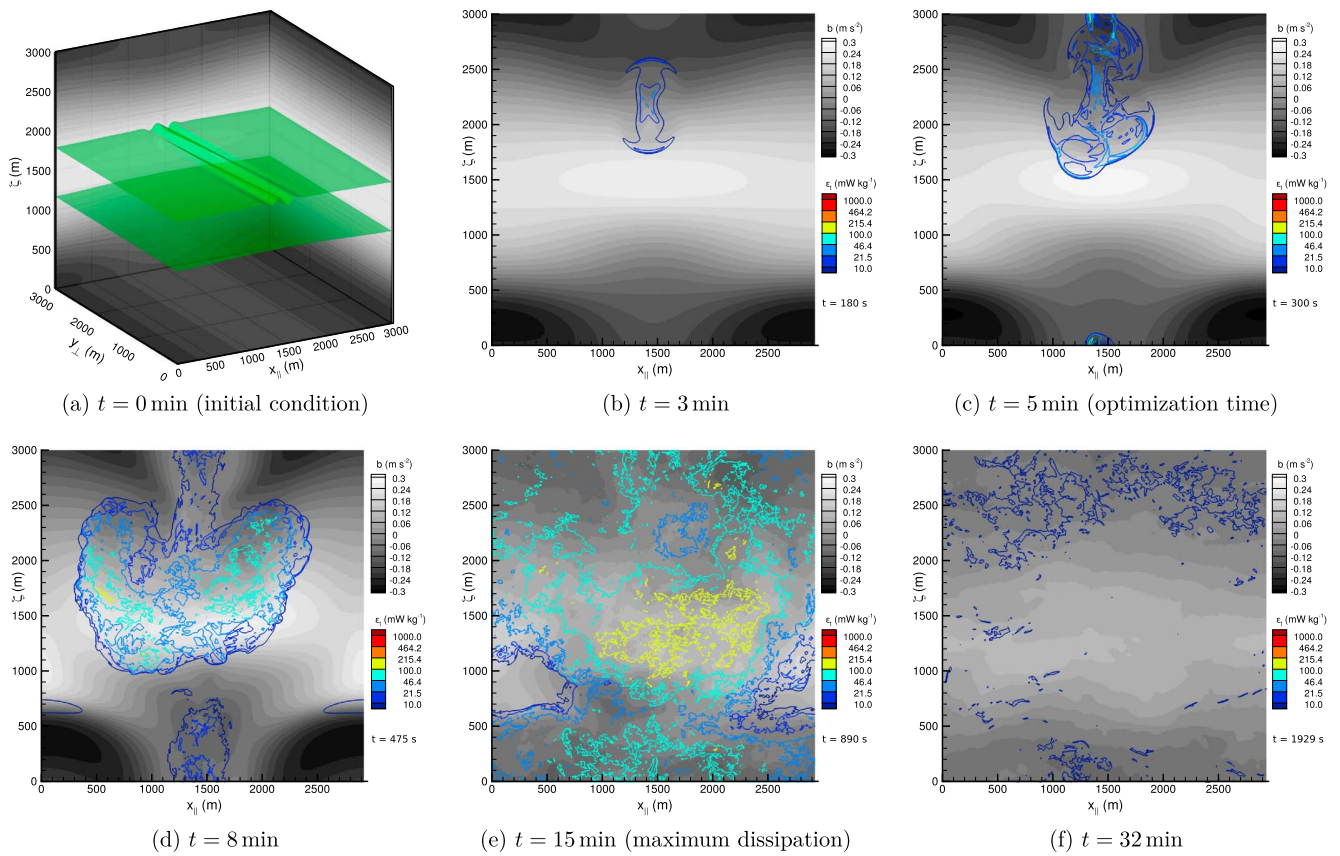
Figure 17. Snapshots of the buoyancy field from the fine 3-D DNS (1536^3 cells) of the statically unstable HGW: (a) 3-D initial condition with the isosurface $b = 0.2$ m s^{-2} (green color). (b–f) Flow field averaged in the $y_\perp$-direction (grey scale contours: buoyancy, colored lines: total energy dissipation).
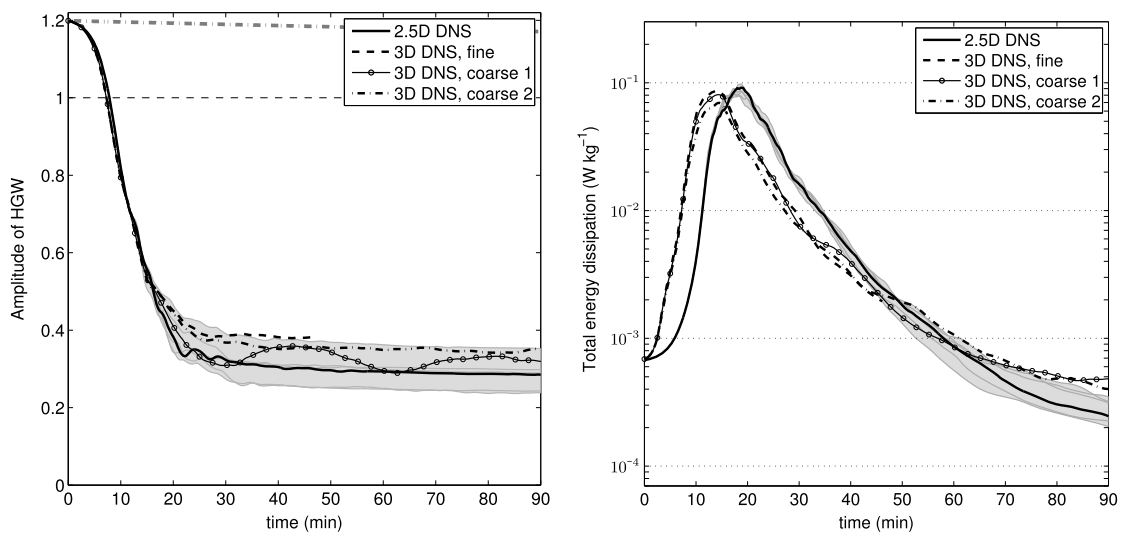

Figure 18. As in Figure 6 but for the statically unstable HGW. The 3-D DNS were performed with 1536^3 (fine), 768^3 (coarse 1), and 384^3 (coarse 2) grid cells.
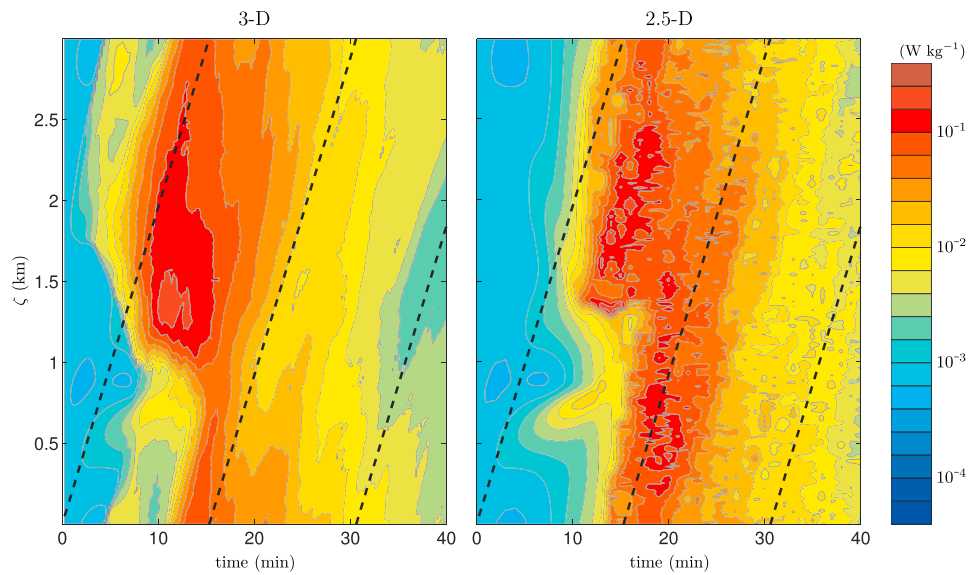
Figure 19. As in Figure 13 but for the unstable HGW. The fine-resolution simulation (1536^3 cells) was used for the 3-D plot.

dissipation from the medium-resolution (coarse 1) run is shown in Figure 19. The regions of intense energy dissipation are approximately fixed in space (parallel to the heavy dashed black lines), particularly in the 2.5-D simulation.

Spanwise and streamwise averaged energy spectra from the 2.5-D ensemble and the medium (coarse 1) resolution 3-D DNS are plotted in Figure 20 (computation of spectra for the fine simulation was too memory intensive). Spectra from two times during the period of strong energy dissipation (15 and 30 min) and at the end of the simulation are shown. During the period of maximum turbulence, energy moves to smaller scales and close to a $k^{-5/3}$ spectrum forms. At the end of the simulation the spectrum has steepened as the energy in smaller scales has been lost to friction and thermal diffusion. The cascade of energy to the smallest scales is more efficient in the 3-D simulations, but the difference between the 2.5-D and 3-D spectra seems to be
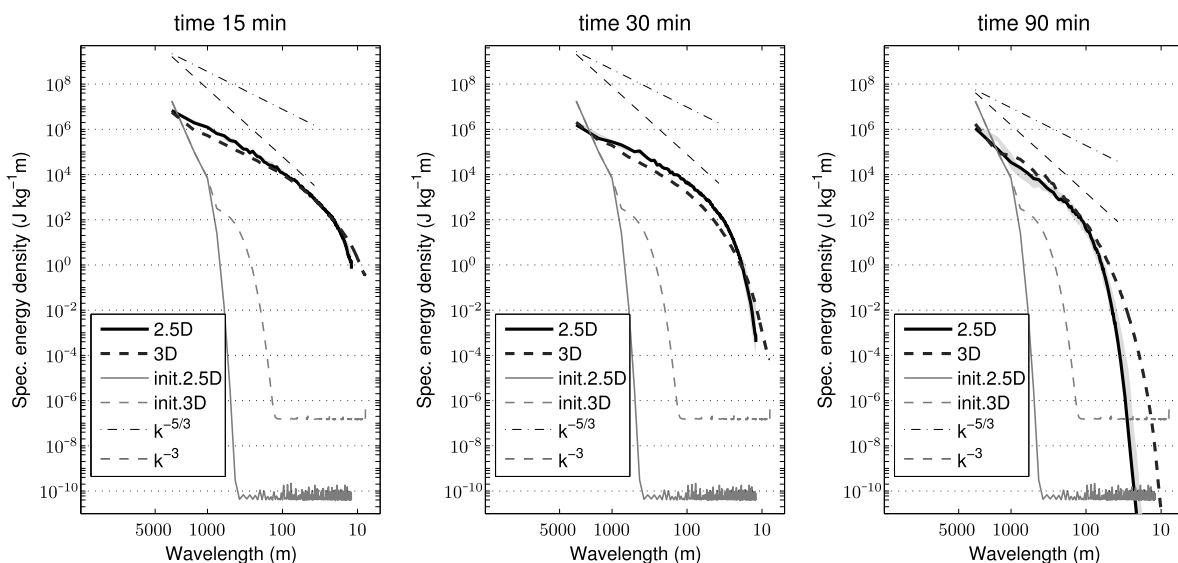

Figure 20. As in Figure 8 but for the unstable HGW. Plot times correspond to the moment of maximum energy dissipation in the 3-D simulation (15 min), a time after which the wave has decayed to near its saturation level (30 min) and the end of the simulations (90 min). The 3-D spectra were computed using the medium (coarse 1) resolution DNS.

small in this case. Like in the intermediate-time spectra from case I (Figure 8), the spectra at 90 min are close to the k^{-3} spectrum characteristic of anisotropic, buoyancy-dominated turbulence.

There is much less variation between ensemble members in the dissipation and spectra diagnostics than in the (much longer) unstable IGW simulations, and in the projection diagnostic there is much less variation relative to the amount of decay.

The Kolmogorov length η from the 3-D DNS with the three different resolutions is plotted as a function of time in Figure 14b. In the fine simulation, η is always approximately equal to or larger than Δ/π (indicated by the horizontal lines) and can hence be considered fully resolved. Nevertheless, there is not much difference in terms of the wave amplitude and dissipation rates (Figure 18) in the intense early phase (up to about 15 min) of the fine and coarse 1 simulations, so it is probably acceptable to use the latter for computing the spectra for Figure 20. The coarse 2 simulation, on the other hand, has a slightly lower dissipation peak than the other two and is thus not quite resolving the smallest relevant scales.

7. Conclusion

A systematic but flexible method for constructing an efficient three-dimensional (3-D) direct numerical simulation (DNS) of a breaking inertia-gravity wave has been presented. The method consists of four stages, which can be summarized as follows:

1. Normal mode (NM) or singular vector (SV) analysis of the Boussinesq equations linearized about the inertia-gravity wave solution (equation (6)). This entails a large number of one-dimensional linear calculations in the once-rotated coordinate system (ξ, y, ζ).
2. "2.5-dimensional" (2.5-D) nonlinear simulation of the full Boussinesq equations (equation (2a)) initialized with the inertia-gravity wave plus a leading NM or SV from step 1. These simulations are performed in the twice-rotated coordinate system $(x_\parallel, y_\perp, \zeta)$ and are supplemented by ensembles of simulations with additional small-amplitude initial noise.
3. SV analysis on the full equations linearized about the particular time-dependent 2.5-D solution from step 2 that resulted in the greatest reduction in the gravity wave amplitude. Uses equation (13).
4. Three-dimensional DNS initialized with the inertia-gravity wave, the leading NM or SV from step 1 and a leading secondary SV from step 3. The dimensions of the integration domain are equal to the wavelengths of the wave and the leading perturbations.

The characteristics of the initial wave are completely determined by the atmosphere parameters N and f and the wavelength and propagation angle Θ of the wave (see Tables 1 and 2). The primary instability structures (NM or SV) further depend on the viscosity ν and diffusivity μ and are characterized by the orientation angle α and wavelength $\lambda_\parallel$ and in the case of the singular vector the optimization time τ. The secondary singular vectors are characterized by their wavelength $\lambda_\perp$ and the optimization time, which may or may not be the same as that used for computing the primary singular vector.

The method has been applied to three test cases, resulting in the following initial conditions for the 3-D DNS:

Case I. A statically unstable inertia-gravity wave (IGW) with wavelength $\lambda = 3$ km, propagation angle $\Theta = 89.5°$ (period 8 h, phase speed 0.1 m s^{-1}), and amplitude $a_0 = 1.2$ (streamwise velocity amplitude $\Delta u_\xi = 14.6$ m s^{-1}) perturbed by the leading transverse primary normal mode with $\lambda_\parallel = 3.9$ km and the leading 5 min secondary singular vector with $\lambda_\perp = 400$ m.

Case II. A statically stable IGW with parameters identical to case I except the amplitude $a_0 = 0.86$ ($\Delta u_\xi = 10.4$ m s^{-1}), perturbed by the leading 7.5 min transverse primary singular vector with $\lambda_\parallel = 2.115$ km and the leading 7.5 min secondary singular vector with $\lambda_\perp = 300$ m.

Case III. A statically unstable high-frequency gravity wave (HGW) with wavelength $\lambda = 3$ km, propagation angle $\Theta = 70°$ (period 15 min, phase speed 3.3 m s^{-1}) and amplitude $a_0 = 1.2$ ($\Delta u_\xi = 12.2$ m s^{-1}) perturbed by the leading transverse normal mode with $\lambda_\parallel = 2.9$ km and the leading secondary singular vector with $\lambda_\perp = 3$ km.

The breaking of the unstable IGW (case I, also discussed in *Remmler et al.* [2013]) was perhaps the richest of the three cases. The turbulence and wave decay was intermittent and persisted for almost the period of the wave (8 h). The preliminary linear instability analysis and nonlinear 2.5-D simulations indicated that this case could be treated in a domain relatively narrow in the $y_\perp$ direction, making such a long integration possible.

After the first approximately 30 min, most of the energy dissipation in the 3-D simulation occurred near the level of static instability in the original wave, while in 2.5-D there is significant energy dissipation also in the stable part of the wave. In general, it was the only case with significant differences between the 2.5-D and 3-D DNS and with significant variation between members of the ensemble in 2.5-D.

The unstable HGW (case III) resulted in a rapid and almost total breakdown of the wave, its amplitude decaying to about 30% of the threshold amplitude for static instability within just over a single wave period (15 min). The breaking of this wave seems to be relatively isotropic, with scales in all three directions comparable to the wavelength of the original wave, and the dissipation occurs in one powerful burst (as opposed to being intermittent) and does not appear to be very spatially correlated with the distributions of velocity and buoyancy in the original wave. The results of this test case were similar to those of *Fritts et al.* [2009a, 2009b]. Although those authors did not include the Coriolis force in their calculations, it plays almost no role in the dynamics of high-frequency waves.

Probably, the least interesting of the three cases (from the point of view of wave breaking) was the statically stable IGW (case II). The wave amplitude is reduced by about 5%, from $a_0 = 0.86$ to about $|a| = 0.82$ before rebounding slightly after the optimization time of the primary singular vector (at which time its energy, in the linear solution, begins to decrease). *Achatz* [2007a] discussed a similar case (but for a wave with 6 km wavelength) and found that perturbation by a primary SV with 10 times larger relative amplitude than that considered here could lead, in nonlinear simulations, to significant reduction in the amplitude of the IGW. Such a large perturbation, however, makes the initial condition locally exceed the static instability threshold.

Overall, the results of the 2.5-D simulations are remarkably similar to those of the 3-D DNS in terms of the projection and resolved-energy dissipation diagnostics. The initial phase of wave breaking tends to be more rapid and more intense in the 3-D simulations—understandable since it provides more degrees of freedom and avenues to exchange energy between spatial scales. The spatial and temporal distribution of the energy dissipation are similar in 2.5-D and 3-D.

A possible objection to the approach advocated here is that the computational domain and initial condition are too carefully chosen for the results to be relevant to a wave breaking spontaneously in nature. For that reason, *Remmler et al.* [2013] performed additional simulations with the inertia-gravity wave from case I, in domains half as wide (200 m) and twice as wide (800 m) in the $y_\perp$ direction and with small amplitude noise instead of the secondary singular vector. It was found that the breaking of the wave in the narrow domain was more like in the 2.5-D simulations, while the breaking in the wider domain was more like the optimally initialized 3-D DNS, suggesting that the optimal initialization might be a closer approximation to nature than a randomly initialized simulation in a bounded domain. Since the breaking of the HGW (case III) was so similar in 2.5-D and in 3-D, this test was not deemed necessary.

While simulation of realistic breaking waves in the upper mesosphere is becoming tractable with improved computing technology, it remains an expensive and time-consuming undertaking and is still out of reach for waves in the ocean and most of the atmosphere. For that, one must rely on large-eddy simulation (LES) models. An immediate application of the results presented here is in the validation of LES schemes against a reliable properly resolved solution. The LES can then serve as an essential intermediate tool for the testing of gravity wave drag parameterizations, which are needed by every weather forecast and climate model, or simply for extending the parameter range (higher Reynolds numbers, larger simulation domains) that can be explored in monochromatic wave-breaking studies of the type presented here. We would be happy to share the data from the 3-D DNS with other researchers. Summaries of the data will be made available on the World Wide Web.

Appendix A: Normal Modes and Singular Vectors

Consider a system of coupled linear ordinary differential equations

$$\frac{\mathrm{d}}{\mathrm{d}t}\mathbf{x} = \mathbf{A}\mathbf{x}, \tag{A1}$$

where $\mathbf{x}$ is a vector and $\mathbf{A}$ is a matrix which may depend on time. In the context of the primary instability analysis (section 3.1), $\mathbf{x}$ consists of the real and imaginary parts of the perturbation velocity and buoyancy

amplitudes at a discrete set of ϕ values (where $\phi \in (0, 2\pi)$ is the phase of the original gravity wave) and $\mathbf{A}$ depends on ϕ through the basic state fields but is independent of time. For the secondary instability analysis (section 3.2), $\mathbf{x}$ consists of the same fields at discrete points on the $(x_\parallel, \phi)$ grid and $\mathbf{A}$ is time dependent.

The *normal modes* of (A1) are solutions of the form

$$\mathbf{x}(t) = \mathbf{x}_0 e^{\gamma t}, \tag{A2}$$

where $\mathbf{x}_0$ is an eigenvector of $\mathbf{A}$ and γ the corresponding eigenvalue. The *leading* normal mode is the one with the largest *growth rate* (the real part of γ). In general, $\mathbf{A}$ is a very large matrix, and one is interested only in the fastest growing normal modes, so it is convenient to use an iterative eigenvector solution method like the Arnoldi method, but these methods find the eigenvalue with the largest magnitude rather than the eigenvalue with the largest real part. The answer is to instead find the eigenvalues of the propagator matrix Φ_τ defined by

$$\mathbf{x}(\tau) = \Phi_\tau \mathbf{x}(0). \tag{A3}$$

When $\mathbf{A}$ is time independent, $\Phi_\tau \equiv \exp(\tau \mathbf{A})$ and has the same eigenvectors as $\mathbf{A}$ and eigenvalues of the form $\Gamma = \exp(\gamma \tau)$. Since $|\Gamma| = \exp(\mathrm{Re}(\gamma)t)$, the eigenvalues of Φ_τ with the largest magnitude correspond to the eigenvalues of $\mathbf{A}$ with the largest real part. Note that the matrix Φ_τ need not be known explicitly in order to calculate its eigenvalues and eigenvectors using a tool such as the ARPACK library [*Lehoucq et al.*, 1998]. One need only have a way of calculating $\mathbf{x}(\tau)$ from $\mathbf{x}_0$, i.e., the linear model.

It is often required to find the initial perturbations $\mathbf{x}_0$ for which the *growth factor* after time τ,

$$\sigma \equiv \sqrt{\frac{\mathbf{x}(\tau)^\dagger \mathbf{M} \mathbf{x}(\tau)}{\mathbf{x}_0^\dagger \mathbf{M} \mathbf{x}_0}} = \sqrt{\frac{\mathbf{x}_0^\dagger \Phi_\tau^\dagger \mathbf{M} \Phi_\tau \mathbf{x}_0}{\mathbf{x}_0^\dagger \mathbf{M} \mathbf{x}_0}} \tag{A4}$$

is maximized. Here $\mathbf{M}$ is a positive-definite matrix which defines a norm (such as the total energy) and its associated inner product, and $\mathbf{x}^\dagger$ is the conjugate-transpose of $\mathbf{x}$. It can be shown that σ is maximized when $\mathbf{x}_0$ is the eigenvector of the matrix $\mathbf{M}^{-1} \Phi_\tau^\dagger \mathbf{M} \Phi_\tau$ with the largest (in magnitude) eigenvalue. The eigenvectors $\{\mathbf{x}_k\}$ of $\mathbf{M}^{-1} \Phi_\tau^\dagger \mathbf{M} \Phi_\tau$ are called the *singular vectors* of the system described by $\mathbf{A}$ with respect to the optimization time τ.

It is simpler to find the vectors $\mathbf{q}_k = \mathbf{N} \mathbf{x}_k$, where $\mathbf{M} = \mathbf{N}^\dagger \mathbf{N}$ is the Cholesky factorization of $\mathbf{M}$, because the $\mathbf{q}_k$ satisfy the Hermitian eigenvector equation

$$(\mathbf{N} \Phi_\tau \mathbf{N}^{-1})^\dagger (\mathbf{N} \Phi_\tau \mathbf{N}^{-1}) \mathbf{q}_k = \sigma^2 \mathbf{q}_k. \tag{A5}$$

The singular vectors $\mathbf{x}_k$ can then be recovered by computing $\mathbf{x}_k = \mathbf{N}^{-1} \mathbf{q}_k$. In order to calculate the $\mathbf{q}_k$, both the linear model, to compute $\mathbf{y} = \Phi_\tau \mathbf{x}$, and its *adjoint*, to compute $\Phi_\tau^\dagger \mathbf{y}$, are required. In the present study, the adjoint models were constructed using the tool TAMC [*Giering and Kaminski*, 1998].

When $\mathbf{A}$ is time dependent (such as in the calculation of the secondary instabilities), the normal mode problem is not well-defined, but singular vectors can be calculated for any linear system. Furthermore, since the vectors $\mathbf{q}_k$ are the eigenvectors of a positive definite, Hermitian matrix, they form an orthonormal set. It follows that the singular vectors $\mathbf{x}_k$ are orthonormal with respect to the norm $\mathbf{M}$. It is easily shown that they are orthogonal also at the optimization time τ, i.e.,

$$(\Phi_\tau \mathbf{x}_j)^\dagger \mathbf{M} (\Phi_\tau \mathbf{x}_k) = \mathbf{x}_j^\dagger \Phi_\tau^\dagger \mathbf{M} \Phi_\tau \mathbf{x}_k = \sigma_k^2 \mathbf{x}_j^\dagger \mathbf{M} \mathbf{x}_k = \delta_{jk} \sigma_k^2. \tag{A6}$$

Appendix B: Projection Onto Free Gravity Waves

An important diagnostic quantity for simulations of the breaking of an inertia-gravity wave is the projection of the solution onto the inertia-gravity wave as a function of time. See the appendix of *Achatz* [2007b] for the more general problem of projecting the solution onto all free inertia-gravity waves and vortical modes.

The projection onto just the original inertia-gravity wave may be extracted from the streamwise-spanwise mean fields $\overline{u}_\parallel$, $\overline{v}_\perp$, $\overline{w}_\zeta$, and $\overline{b}$, where for the quantity X,

$$\overline{X}(\phi, t) = \frac{1}{\lambda_\parallel \lambda_\perp} \int_0^{\lambda_\perp} \int_0^{\lambda_\parallel} X(x_\parallel, y_\perp, \phi, t) \mathrm{d}x_\parallel \mathrm{d}y_\perp. \tag{B1}$$

The free linear modes depending only on ζ and t and periodic in ζ with period λ consist of the geostrophically balanced vortical modes

$$
\begin{aligned}
V_n &\equiv [\overline{u}_\parallel, \overline{v}_\perp, \overline{w}_\zeta, \overline{b}]_n^0 \\
&\equiv \frac{\sqrt{2}N}{\sqrt{N^2 \cos^2 \Theta + f^2 \sin^2 \Theta}} \left[\cos \Theta \sin \alpha, \cos \Theta \cos \alpha, 0, f \sin \Theta \right] \exp(inK\zeta),
\end{aligned}
\tag{B2}
$$

and the upward and downward propagating inertia-gravity waves

$$
\begin{aligned}
G_n^\pm &\equiv [\overline{u}_\parallel, \overline{v}_\perp, \overline{w}_\zeta, \overline{b}]_n^\pm \\
&\equiv \left[i \cos \alpha + \frac{f \sin \Theta}{\omega^\pm} \sin \alpha, -i \sin \alpha + \frac{f \sin \Theta}{\omega^\pm} \cos \alpha, 0, -\frac{N^2 \cos \Theta}{\omega^\pm} \right] \exp\left[i \left(nK\zeta - \omega^\pm t \right) \right].
\end{aligned}
\tag{B3}
$$

Here Θ is the angle of phase propagation of the original wave, α is the orientation of the primary perturbation, n is an integer, and

$$\omega^\pm = \pm \sqrt{f^2 \sin^2 \Theta + N^2 \cos^2 \Theta}. \tag{B4}$$

In addition, there is the "mode" $W \equiv [\overline{u}_\parallel, \overline{v}_\perp, \overline{w}_\zeta, \overline{b}]^w = [0, 0, \sqrt{2}, 0]$ representing the streamwise and spanwise mean of w_ζ (it follows from the continuity equation averaged over $x_\parallel$ and $y_\perp$ that $\overline{w}_\zeta$ is independent of ζ).

It is readily shown that the set $\{V_n^0, G_n^+, G_n^-, W\}$, where $n = 1, 2, 3, \ldots$, forms an orthonormal basis in the energy norm

$$||[\overline{u}_\parallel, \overline{v}_\perp, \overline{w}_\zeta, \overline{b}]||^2 \equiv \frac{1}{2\lambda} \int_0^\lambda \left(|\overline{u}_\parallel|^2 + |\overline{v}_\perp|^2 + |\overline{w}_\zeta|^2 + \frac{|\overline{b}|^2}{N^2} \right) \mathrm{d}\zeta \tag{B5}$$

for periodic functions of ζ with period λ. The original inertia-gravity wave, which had upward vertical group speed and therefore downward vertical phase speed, is the mode G_1^-.

Defining the discrete Fourier transform according to

$$\hat{X}_j = \frac{1}{N_\zeta} \sum_{l=1}^{N_\zeta} \overline{X}_l \exp\left(-i \frac{2\pi j l}{N_\zeta} \right), \tag{B6}$$

where N_ζ is the number of grid points in the ζ direction, the (complex) amplitude of the inertia-gravity wave at a given time is then the scalar product of the transformed discrete fields with G_1^-

$$
\begin{aligned}
A(t) &= \frac{1}{2} \left(\hat{u}_{\parallel_1^*} \hat{u}_{\parallel_1^-} + \hat{v}_{\perp_1^*} \hat{v}_{\perp_1^-} + \frac{1}{N^2} \hat{b}_1^* \hat{b}_1^- \right) \\
&= \frac{1}{2} \left[\left(i \cos \alpha + \frac{f \sin \Theta}{\omega^-} \sin \alpha \right) \hat{u}_{\parallel_1^*} + \left(-i \sin \alpha + \frac{f \sin \Theta}{\omega^-} \cos \alpha \right) \hat{v}_{\perp_1^*} - \frac{N^2 \cos \Theta}{\omega^-} \hat{b}_1^* \right],
\end{aligned}
\tag{B7}
$$

where $[\hat{u}_{\parallel_1}^-, \hat{v}_{\perp_1}^-, 0, \hat{b}_1^-]$ is the complex amplitude of the mode G_1^- (from equation (B3)). The magnitude of the amplitude normalized relative to the threshold for static instability $|\hat{b}_C| = N^2/(K \cos \Theta)$ is then

$$|a(t)| = \frac{|\hat{b}_1^-|}{|\hat{b}_C|} |A(t)| = \frac{2 \cos \Theta \sin \Theta}{(\lambda/2\pi)|\omega^-|} |A(t)|. \tag{B8}$$

Appendix C: Computational Resources Used for the 3-D DNS

The 3-D direct numerical simulations for the three test cases were performed at different high-performance computing centers.

For the unstable IGW, a resolution of $\Delta = 3$ m and therefore 172.8 million grid cells were required for the solution to be fully resolved. The simulation was run on the NEC SX-9 vector computer at the High Performance Computing Center in Stuttgart, Germany (HLRS). A single node of this machine (500 GB memory, 16 vector processors with 100 GFLOP/s peak performance each) had sufficient memory to store the complete flow field. Hence, we could avoid domain decomposition and relied on shared memory parallelization only. The efficient Poisson solver employs a discrete Fourier transform in one direction in combination with a Bi-Conjugate Gradient Stabilized solver [*van der Vorst*, 1992] in the plane perpendicular to the chosen direction. The Fourier transform converts the three-dimensional problem into a set of independent two-dimensional problems, which are solved in parallel. The simulation of a flow time of 35,000 s (270,000 time steps) required a *wall time* of 1100 h, which corresponds to 85.7×10^{-9} node seconds per time step and cell.

The simulations of the stable IGW were carried out on the LOEWE cluster at CSC Frankfurt, Germany. This machine consists of nodes with two AMD Opteron 6172 CPUs (12 cores per CPU, 8.4 GFlop/s per core peak performance) and 64 GB memory. The fully resolved DNS with 71 million grid cells was decomposed into 192 blocks and simulated on eight nodes. The integration up to $t = 100$ min (38 600 time steps) took 183 h, i.e., 1.93×10^{-6} node seconds per time step and cell.

The simulations of the unstable HGW were the most demanding and were run on the Cray XE6 cluster at HLRS Stuttgart, consisting of nodes with two AMD Opteron 6276 (Interlagos) CPUs (16 cores per CPU, 9.2 GFlop/s per core peak performance) and 32 GB memory. The fully resolved DNS with 3624 million grid cells was decomposed into 4096 blocks and simulated on 512 nodes using eight processor cores per node. The integration up to $t = 46.2$ min (49,460 time steps) required a wall time of about 288 h. Hence, the computational performance was 2.96×10^{-6} node seconds per time step and cell.

References

Achatz, U. (2005), On the role of optimal perturbations in the instability of monochromatic gravity waves, *Phys. Fluids*, *17*, 1–27.

Achatz, U. (2007a), The primary nonlinear dynamics of modal and nonmodal perturbations of monochromatic inertia-gravity waves, *J. Atmos. Sci.*, *64*, 74–95.

Achatz, U. (2007b), Modal and nonmodal perturbations of monochromatic high-frequency gravity waves: Primary nonlinear dynamics, *J. Atmos. Sci.*, *64*, 1977–1994.

Andreassen, O., C. E. Wasberg, D. C. Fritts, and J. R. Isler (1994), Gravity wave breaking in two and three dimensions. 1. Model description and comparison of two-dimensional evolutions, *J. Geophys. Res.*, *99*, 8095–8108.

Baldwin, M. P., et al. (2001), The quasi-biennial oscillation, *Rev. Geophys.*, *39*, 179–229, doi:10.1029/1999RG000073.

Brethouwer, G., P. Billant, E. Lindborg, and J. M. Chomaz (2007), Scaling analysis and simulation of strongly stratified turbulent flows, *J. Fluid Mech.*, *585*, 343–368.

Carnevale, F. G., M. Briscolini, and P. Orlandi (2001), Buoyancy to inertial range transition in forced stratified turbulence, *J. Fluid Mech.*, *427*, 205–239.

Chun, H. Y., M. D. Song, J. W. Kim, and J. J. Baik (2001), Effects of gravity wave drag induced by cumulus convection on the atmospheric general circulation, *J. Atmos. Sci.*, *58*, 302–319.

Cot, C. (2001), Equatorial mesoscale wind and temperature fluctuations in the lower atmosphere, *J. Geophys. Res.*, *106*, 1523–1532.

Durran, D. R. (2010), *Numerical Methods for Fluid Dynamics*, 516 pp., Springer, New York.

Farrell, B. F., and P. J. Ioannou (1996a), Generalized stability theory. Part I: Autonomous operators, *J. Atmos. Sci.*, *53*, 2025–2040.

Farrell, B. F., and P. J. Ioannou (1996b), Generalized stability theory. Part II: Nonautonomous operators, *J. Atmos. Sci.*, *53*, 2041–2053.

Fritts, D. C., and M. J. Alexander (2003), Gravity wave dynamics and effects in the middle atmosphere, *Rev. Geophys.*, *41*(1), 1003, doi:10.1029/2001RG000106.

Fritts, D. C., and L. Wang (2013), Gravity wave-fine structure interactions. Part II: Energy dissipation evolutions, statistics, and implications, *J. Atmos. Sci.*, *70*, 3735–3755.

Fritts, D. C., L. Wang, J. Werne, T. Lund, and K. Wan (2009a), Gravity wave instability dynamics at high Reynolds numbers. Part I: Wave field evolution at large amplitudes and high frequencies, *J. Atmos. Sci.*, *66*, 1126–1148.

Fritts, D. C., L. Wang, J. Werne, T. Lund, and K. Wan (2009b), Gravity wave instability dynamics at high Reynolds numbers. Part II: Turbulence evolution, structure, and anisotropy, *J. Atmos. Sci.*, *66*, 1149–1171.

Fritts, D. C., L. Wang, and J. A. Werne (2013), Gravity wave-fine structure interactions. Part I: Influences of fine structure form and orientation on flow evolution and instability, *J. Atmos. Sci.*, *70*, 3710–3734.

Fruman, M. D., and U. Achatz (2012), Secondary instabilities in breaking inertia-gravity waves, *J. Atmos. Sci.*, *69*, 303–322.

Giering, R., and T. Kaminski (1998), Recipes for adjoint code construction, *ACM Trans. Math. Software*, *24*, 437–474.

Grimsdell, A. W., M. J. Alexander, P. T. May, and L. Hoffmann (2010), Waves generated by convection with direct validation via satellite, *J. Atmos. Sci.*, *67*, 1617–1631.

Hines, C. O. (1965), Dynamical heating of the upper atmosphere, *J. Geophys. Res.*, *70*, 177–183.

Hines, C. O. (1997), Doppler-spread parameterization of gravity-wave momentum deposition in the middle atmosphere. Part I: Basic formulation, *J. Atmos. Sol. Terr. Phys.*, *59*, 371–386.

Howard, L. N. (1961), Note on a paper of John W. Miles, *J. Fluid Mech.*, *10*, 509–512.

Kim, Y.-J., S. D. Eckermann, and H.-Y. Chun (2003), An overview of the past, present and future of gravity-wave drag parameterization for numerical climate and weather prediction models, *Atmos. Ocean*, *41*(1), 65–98.

Klaassen, G. P., and W. R. Peltier (1985), The onset of turbulence in finite-amplitude Kelvin-Helmholtz billows, *J. Fluid Mech.*, *155*, 1–35.

Kraichnan, R. H., and D. Montgomery (1980), Two-dimensional turbulence, *Rep. Prog. Phys.*, *43*, 547–619.

Lehoucq, R. B., D. C. Sorensen, and C. Yang (1998), *ARPACK Users' Guide: Solution of Large-Scale Eigenvalue Problems With Implicitly Restarted Arnoldi Methods*, 160 pp., SIAM, Philadelphia, Pa.

Lelong, M.-P., and T. J. Dunkerton (1998), Inertia-gravity wave breaking in three dimensions. Part I: Convectively stable waves, *J. Atmos. Sci.*, *55*, 2473–2488.

Lilly, D. K., J. M. Nicholls, R. M. Chervin, P. J. Kennedy, and J. B. Klemp (1982), Aircraft measurements of wave momentum flux over the Colorado Rocky Mountains, *Q. J. R. Meteorol. Soc.*, *108*, 625–642.

Lindzen, R. S. (1973), Wave-mean flow interactions in the upper atmosphere, *Boundary Layer Meteorol.*, *4*, 327–343.

Lindzen, R. S. (1981), Turbulence and stress owing to gravity wave and tidal breakdown, *J. Geophys. Res.*, *86*, 9707–9714.

Liu, W., F. P. Bretherton, Z. Liu, L. Smith, H. Lu, and C. J. Rutland (2010), Breaking of progressive internal gravity waves: Convective instability and shear instability, *J. Phys. Oceanogr.*, *40*, 2243–2263.

Lombard, P. N., and J. J. Riley (1996), Instability and breakdown of internal gravity waves. I. Linear stability analysis, *Phys. Fluids*, *8*, 3271–3287.

Lund, T. S., and D. C. Fritts (2012), Numerical simulation of gravity wave breaking in the lower thermosphere, *J. Geophys. Res.*, *117*, D21105, doi:10.1029/2012JD017536.

McFarlane, N. (1987), The effect of orographically excited gravity wave drag on the general circulation of the lower stratosphere and troposphere, *J. Atmos. Sci.*, *44*, 1775–1800.

McLandress, C. (1998), On the importance of gravity waves in the middle atmosphere and their parameterization in general circulation models, *J. Atmos. Sol. Terr. Phys.*, *60*, 1357–1383.

Miles, J. W. (1961), On the stability of heterogeneous shear flows, *J. Fluid Mech.*, *10*, 496–508.

NOAA, US Air Force, and US Air (1976), US standard atmosphere, *Tech. Rep. NOAA-S/T76-1562*, Natl. Oceanic Atmos. Admin., Natl. Aeronaut. and Space Admin., and U.S. Air Force, Washington, D. C.

O'Sullivan, D., and T. J. Dunkerton (1995), Generation of inertia-gravity waves in a simulated life cycle of baroclinic instability, *J. Atmos. Sci.*, *52*, 3695–3716.

Plougonven, R., and C. Snyder (2007), Inertia-gravity waves spontaneously generated by jets and fronts. Part I: Different baroclinic life cycles, *J. Atmos. Sci.*, *64*, 2502–2520.

Remmler, S., and S. Hickel (2012), Direct and large eddy simulation of stratified turbulence, *Intl. J. Heat Fluid Flow*, *35*, 13–24.

Remmler, S., and S. Hickel (2013), Spectral structure of stratified turbulence: Direct numerical simulation and predictions by LES, *Theor. Comput. Fluid Dyn.*, *27*, 319–336.

Remmler, S., M. D. Fruman, and S. Hickel (2013), Direct numerical simulation of a breaking inertia-gravity wave, *J. Fluid Mech.*, *722*, 424–436.

Shu, C.-W. (1988), Total-variation-diminishing time discretizations, *SIAM J. Sci. Stat. Comput.*, *9*(6), 1073–1084.

Smith, R. B. (1979), The influence of mountains on the atmosphere, *Adv. Geophys.*, *21*, 87–230.

Vallis, G. K. (2006), *Atmospheric and Oceanic Fluid Dynamics*, Cambridge Univ. Press, Cambridge, U. K.

van der Vorst, H. A. (1992), Bi-CGSTAB: A fast and smoothly converging variant of Bi-CG for the solution of nonsymmetric linear systems, *SIAM J. Sci. Stat. Comput.*, *13*(2), 631–644.

Williamson, J. H. (1980), Low-storage Runge–Kutta schemes, *J. Comput. Phys.*, *35*(1), 48–56.

Yamazaki, Y., T. Ishihara, and Y. Kaneda (2002), Effects of wavenumber truncation on high-resolution direct numerical simulation of turbulence, *J. Phys. Soc. Jpn.*, *71*, 777–781.

Validation of Large-Eddy Simulation Methods for Gravity Wave Breaking

SEBASTIAN REMMLER* AND STEFAN HICKEL[+]

Institute of Aerodynamics and Fluid Mechanics, Technische Universität München, Munich, Germany

MARK D. FRUMAN AND ULRICH ACHATZ

Institute for Atmosphere and Environment, Goethe University Frankfurt, Frankfurt, Germany

ABSTRACT

To reduce the computational costs of numerical studies of gravity wave breaking in the atmosphere, the grid resolution has to be reduced as much as possible. Insufficient resolution of small-scale turbulence demands a proper turbulence parameterization in the framework of a large-eddy simulation (LES). The authors validate three different LES methods—the adaptive local deconvolution method (ALDM), the dynamic Smagorinsky method (DSM), and a naïve central discretization without turbulence parameterization (CDS4)—for three different cases of the breaking of well-defined monochromatic gravity waves. For ALDM, a modification of the numerical flux functions is developed that significantly improves the simulation results in the case of a temporarily very smooth velocity field. The test cases include an unstable and a stable inertia–gravity wave as well as an unstable high-frequency gravity wave. All simulations are carried out both in three-dimensional domains and in two-dimensional domains in which the velocity and vorticity fields are three-dimensional (so-called 2.5D simulations). The results obtained with ALDM and DSM are generally in good agreement with the reference direct numerical simulations as long as the resolution in the direction of the wave vector is sufficiently high. The resolution in the other directions has a weaker influence on the results. The simulations without turbulence parameterization are only successful if the resolution is high and the level of turbulence is comparatively low.

1. Introduction

Gravity waves are a common phenomenon in any stably stratified fluid, such as found in the atmosphere of Earth. They can be excited by flow over orography (e.g., Smith 1979; McFarlane 1987), by convection (e.g., Chun et al. 2001; Grimsdell et al. 2010), and by spontaneous imbalance of the mean flow in the troposphere (O'Sullivan and Dunkerton 1995; Plougonven and Snyder 2007). Gravity waves transport energy and momentum from the region where they are forced to the region where they are dissipated (e.g., through breaking), possibly far away from the source region. Various

phenomena, such as the cold summer mesopause (Hines 1965) and the quasi-biennial oscillation in the equatorial stratosphere (e.g., Baldwin et al. 2001), cannot be explained nor reproduced in weather and climate simulations without accounting for the effect of gravity waves. See Fritts and Alexander (2003) for an overview of gravity waves in the middle atmosphere. Prusa et al. (1996) found in numerical experiments that (because of wave dispersion) gravity waves generated in the troposphere at a broad wavelength spectrum reach the upper mesosphere as an almost monochromatic wave packet with a horizontal wavelength between a few kilometers and more than 100 km, depending on the horizontal scale of the forcing and the background conditions.

Since most gravity waves have a wavelength that is not well resolved in general circulation models, the effect of gravity waves on the global circulation is usually accounted for by parameterizations based on combinations of linear wave theory (Lindzen 1981), empirical observations of time-mean energy spectra (e.g., Hines 1997), and simplified treatments of the breaking process.

---

* Current affiliation: AUDI AG, Ingolstadt, Germany.

[+] Current affiliation: Technische Universiteit Delft, Delft, Netherlands.

Corresponding author address: Stefan Hickel, Aerodynamics Group, Faculty of Aerospace Engineering, Technische Universiteit Delft, Kluyverweg 1, 2629 HS Delft, Netherlands.
E-mail: S.Hickel@tudelft.nl

See Kim et al. (2003) and McLandress (1998) for reviews of the various standard parameterization schemes.

A common weakness of most parameterization schemes is the oversimplified treatment of the wave breaking process. Improving this point requires a deeper insight into the breaking process that involves generation of small-scale flow features through wave–wave interactions and through wave–turbulence interactions. Since the gravity wave wavelength and the turbulence that eventually leads to energy dissipation into heat span a wide range of spatial and temporal scales, the breaking process is challenging both for observations and numerical simulations. Direct numerical simulations (DNSs) must cover the breaking wave with a wavelength of a few kilometers as well as the smallest turbulence scales (the Kolmogorov length η). The Kolmogorov length depends on the kinetic energy dissipation and the kinematic viscosity. It is on the order of millimeters in the troposphere (Vallis 2006) and approximately 1 m at 80-km altitude (Remmler et al. 2013).

The necessity of resolving the Kolmogorov scale can be circumvented by applying the approach of a large-eddy simulation (LES): that is, by parameterizing the effect of unresolved small eddies on the resolved large-scale flow. This can be necessary in cases where DNS would be too expensive [e.g., in investigating the dependence of the gravity wave breaking on several parameters (propagation angle, wavelength, amplitude, viscosity, and stratification) at the same time]; for problems in which many wavelengths need to be resolved, such as propagation of a wave packet or wave train through a variable background (Lund and Fritts 2012) or modeling realistic cases of waves generated by topography or convection; for validating quasi-linear wave-propagation theory (Muraschko et al. 2014); or for validating gravity wave–drag parameterization schemes.

The subgrid-scale parameterization of turbulence is, of course, a source of uncertainty and, where possible, should be validated against fully resolved DNSs or observations for every type of flow for which it is to be used. Many numerical studies of breaking gravity waves rely on the LES principle without such a validation (e.g., Winters and D'Asaro 1994; Lelong and Dunkerton 1998a,b; Andreassen et al. 1998; Dörnbrack 1998; Afanasyev and Peltier 2001).

Recent studies (Fritts et al. 2009a,b, 2013; Fritts and Wang 2013) have presented highly resolved, high Reynolds number DNSs of a monochromatic gravity wave breaking. However, they do not take into account the Coriolis force, which has a large influence on the dynamics of breaking for low-frequency gravity waves (Dunkerton 1997; Achatz and Schmitz 2006b), often referred to as inertia–gravity waves (IGWs), as opposed to high-frequency gravity waves (HGWs). The Coriolis force induces an elliptically polarized transverse velocity field in IGWs, and the velocity component normal to the plane of propagation of the wave has its maximum shear at the level of minimum static stability. Dunkerton (1997) and Achatz and Schmitz (2006b) showed that this strongly influences the orientation of the most unstable perturbations.

An important aspect in setting up a simulation of a gravity wave breaking event is the proper choice of the domain size and initial conditions. While the gravity wave itself depends on one spatial coordinate and has a natural length scale given by its wavelength, the breaking process and the resulting turbulence are three-dimensional, and proper choices have to be made for the domain sizes in the two directions perpendicular to the wave vector. Achatz (2005) and Achatz and Schmitz (2006a) analyzed the primary instabilities of monochromatic gravity waves of various amplitudes and propagation directions using normal-mode and singular-vector analysis, and Fruman and Achatz (2012) extended this analysis for IGWs by computing the leading secondary singular vectors with respect to a time-dependent simulation of the perturbed wave. (Normal-mode analysis is not suited to time-dependent basic states, while singular-vector analysis, whereby the perturbations for which energy grows by the largest factor in a given optimization time, is always possible.) They found that the wavelength of the optimal secondary perturbation can be much shorter than the wavelength of the original wave. Thus, the computational domain for a three-dimensional simulation need not necessarily have the size of the base wavelength in all three directions. They proposed the following multistep approach to set up the domain and initial conditions for a DNS of a given monochromatic gravity wave:

1) solution (in the form of normal modes or singular vectors) of the governing (Boussinesq) equations linearized about the basic-state wave, determining the primary instability structures;
2) two-dimensional (in space) numerical solution of the full nonlinear equations using the result of stage 1 as initial condition;
3) solution in the form of singular vectors (varying in the remaining spatial direction) of the governing equations linearized about the time-dependent result of stage 2; and
4) three-dimensional DNS using the linear solutions from stages 1 and 3 as initial conditions and their wavelengths for the size of the computational domain.

This procedure was applied to an unstable IGW by Remmler et al. (2013) and fully elaborated with two additional test cases by Fruman et al. (2014).

Having these properly designed DNS results available, we can now use them for the validation of computationally less expensive methods. Hence, the present study analyzes the suitability of different LES methods for the cases presented by Fruman et al. (2014): namely, an unstable IGW, a stable IGW, and an unstable HGW, all of them with a base wavelength of 3 km. The first LES method to be applied is the adaptive local deconvolution method (ALDM) of Hickel et al. (2006, 2014). It is an "implicit" LES method, since the subgrid-scale (SGS) stress parameterization is implied in the numerical discretization scheme. Based on ALDM for incompressible flows and its extension to passive scalar mixing Hickel et al. (2008), Remmler and Hickel (2012, 2013), and Rieper et al. (2013) successfully applied ALDM to stably stratified turbulent flows. For the present study, the numerical flux function for the active scalar in ALDM has been modified to prevent the method from generating spurious oscillations in partially laminar flow fields.

The second method to be applied is the well-known Smagorinsky (1963) method with the dynamic estimation of the spatially nonuniform model parameter proposed by Germano et al. (1991) and refined by Lilly (1992). The third LES method is a "naïve" approach with a simple central discretization scheme and no explicit SGS parameterization. This method is theoretically dissipation free but can lead to numerical instability if the turbulence level is high (which was the reason for the development of the first explicit SGS parameterization by Smagorinsky 1963). However, the method is computationally inexpensive and can be used in some cases without problems, as we will show.

We apply these methods to the three gravity wave test cases using grids of different refinement levels with the goal of using as few grid cells as possible while still obtaining good agreement with the DNS results. We also run small ensembles for each simulation with only slightly different initial conditions to get an estimate of the sensitivity and variability of the results. All this is done in a three-dimensional domain (with the same domain size as the DNS) and in a two-dimensional domain in which the two dimensions are chosen to be parallel to the wave vectors of the gravity wave and of the most important growing primary perturbation [without the addition of the secondary singular vector (cf. step 2 above)]. Because the velocity and vorticity fields are three-dimensional and because the turbulent cascade is direct (energy moves to smaller length scales), these simulations are sometimes called 2.5D. Fruman et al. (2014) found that 2.5D and 3D results are broadly very similar for the inertia–gravity wave test cases considered here.

The paper is organized as follows. In section 2, the governing equations used for the simulations are presented along with properties of the inertia–gravity wave solutions and the energetics of the system. Section 3 describes the numerical methods used, in particular the three LES schemes. The three test cases are reviewed in section 4, and the results of the simulations are discussed in sections 5–7.

2. Governing equations

Assuming the vertical wavelength of the inertia–gravity wave is small compared to the density scale height of the atmosphere, the dynamics are reasonably well approximated by the Boussinesq equations on an f plane. For mathematical convenience, we further assume that the molecular viscosity and diffusion, as well as the Brunt–Väisälä frequency of the background, are constants, independent of space and time.

Since there is no preferred horizontal direction on an f plane, there is no loss of generality in assuming the basic wave propagates in the y–z plane. In all three test cases, the primary perturbation is transverse [corresponding to an angle of $\alpha = 90°$ in the nomenclature of Fruman et al. (2014)]. It is thus advantageous to rotate the coordinate system with respect to the Earth coordinates (x, y, z) through an angle $90° - \Theta$ about the x axis (where Θ is the angle the wave vector makes with the y axis) such that one coordinate direction is parallel to the wave vector. We thus define the rotated Cartesian coordinates:

$$x_{\parallel} = x, \tag{1a}$$

$$y_{\perp} = z\cos\Theta + y\sin\Theta, \quad \text{and} \tag{1b}$$

$$\zeta = z\sin\Theta - y\cos\Theta, \tag{1c}$$

as well as the corresponding velocity vector $\mathbf{u} = (u_{\parallel}, v_{\perp}, w_{\zeta})$. The rotated coordinate system is sketched in Fig. 1.

The Boussinesq equations on an f plane are, in vector form,

$$\nabla \cdot \mathbf{u} = 0, \tag{2a}$$

$$\partial_t \mathbf{u} + (\mathbf{u} \cdot \nabla)\mathbf{u} = -f\hat{\mathbf{e}}_z \times \mathbf{u} + b\hat{\mathbf{e}}_z - \nabla p + \nu\nabla^2\mathbf{u} + \mathcal{F},$$

and $$\tag{2b}$$

$$\partial_t b + (\mathbf{u} \cdot \nabla)b = -N^2\hat{\mathbf{e}}_z \cdot \mathbf{u} + \mu\nabla^2 b + \mathcal{B}, \tag{2c}$$

where b is buoyancy, p is pressure normalized by a constant background density, and $\hat{\mathbf{e}}_z = (0, \sin\Theta, \cos\Theta)$ is the unit vector in the true vertical direction. The term N is the constant Brunt–Väisälä frequency; f is the Coriolis
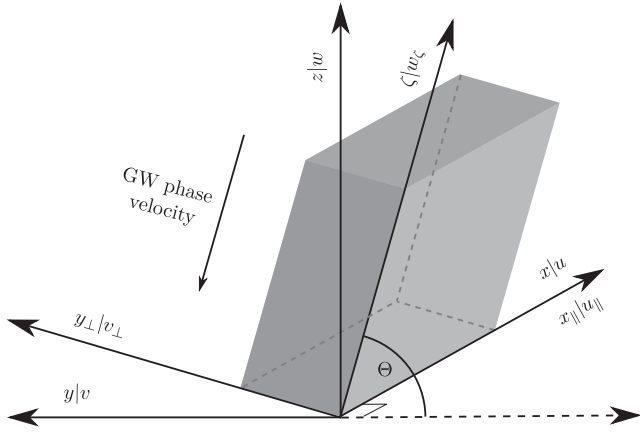
FIG. 1. Rotated coordinate system and computational domain (gray box) for the monochromatic gravity wave (after Remmler et al. 2013).

parameter; ν and μ are the kinematic viscosity and thermal diffusivity, respectively; and $\mathcal{F}$ and $\mathcal{B}$ represent the influence of an explicit turbulence SGS parameterization.

An inertia–gravity wave, propagating at an angle Θ with respect to the horizontal plane, is a solution to Eq. (2) of the form

$$
\begin{pmatrix} u_\| \\ v_\perp \\ w_\zeta \\ b \end{pmatrix} = \Re \left[a \begin{pmatrix} \dfrac{f}{k} \\ -\dfrac{iK\omega}{km} \\ 0 \\ -\dfrac{N^2}{m} \end{pmatrix} e^{i\phi} \right], \tag{3}
$$

where K is the magnitude of the wave vector; $k = K\cos\Theta$ and $m = K\sin\Theta$ are its horizontal and vertical components in the Earth frame; $\phi = K\zeta - \omega t$ is the wave phase; and

$$
\omega = -\sqrt{f^2 \sin^2\Theta + N^2 \cos^2\Theta} \tag{4}
$$

is the wave frequency (the negative sign was chosen so that the wave has an upward group velocity). The nondimensional (complex) wave amplitude a is defined such that a wave with $|a| = 1$ is neutral with respect to static instability at its least stable point. Waves with $|a| > 1$ are statically unstable, and waves with $|a| < 1$ are statically stable. The phase velocity of the wave is directed in the negative ζ direction.

The local kinetic and available potential energy densities in the flow are defined as

$$
E_k = \frac{1}{2}\mathbf{u}^\top \mathbf{u} \quad \text{and} \quad E_p = \frac{b^2}{2N^2}, \tag{5}
$$

with the total energy defined as the sum $E_t = E_k + E_p$. We obtain the transport equations of the energy components by scalar multiplying Eq. (2b) by $\mathbf{u}$ and Eq. (2c) by b/N^2 and applying the divergence constraint equation [Eq. (2a)]:

$$
\partial_t E_k + \boldsymbol{\nabla} \cdot (\mathbf{u}E_k) = -f\mathbf{u} \cdot (\hat{\mathbf{e}}_z \times \mathbf{u}) - b\mathbf{u} \cdot \hat{\mathbf{e}}_z - \mathbf{u} \cdot \boldsymbol{\nabla}p \\ + \nu[\nabla^2 E_k - (\boldsymbol{\nabla}\mathbf{u})^2] + \mathbf{u} \cdot \mathcal{F} \quad \text{and} \tag{6a}
$$

$$
\partial_t E_p + \boldsymbol{\nabla} \cdot (\mathbf{u}E_p) = b\mathbf{u} \cdot \hat{\mathbf{e}}_z + \mu \left[\nabla^2 E_p + \frac{(\boldsymbol{\nabla}b)^2}{N^2} \right] + \frac{b\mathcal{B}}{N^2}. \tag{6b}
$$

Based on these, we define the following contributions to the spatially averaged energy dissipation in an under-resolved simulation as

$$
\varepsilon_m = \varepsilon_{k,m} + \varepsilon_{p,m}
$$

$$
= \langle \nu[(\boldsymbol{\nabla}\mathbf{u})^2 - \nabla^2 E_k] \rangle_s + \left\langle \mu \left[\frac{(\boldsymbol{\nabla}b)^2}{N^2} - \nabla^2 E_p \right] \right\rangle_s, \tag{7a}
$$

$$
\varepsilon_s = \varepsilon_{k,s} + \varepsilon_{p,s} = \langle \mathbf{u} \cdot \mathcal{F} \rangle_s + \left\langle \frac{\mathbf{u} \cdot \mathcal{B}}{N^2} \right\rangle_s, \tag{7b}
$$

$$
\varepsilon_n = \varepsilon_{k,n} + \varepsilon_{p,n} = \langle \mathbf{u} \cdot (\mathbf{u} \cdot \boldsymbol{\nabla})\mathbf{u} \rangle_s + \langle \mathbf{u} \cdot (\mathbf{u} \cdot \boldsymbol{\nabla})b \rangle_s, \tag{7c}
$$

$$
= \langle \boldsymbol{\nabla} \cdot (\mathbf{u}E_k) \rangle_s + \langle \boldsymbol{\nabla} \cdot (\mathbf{u}E_p) \rangle_s, \quad \text{and} \tag{7d}
$$

$$
\varepsilon_t = -\langle \partial_t E_t \rangle_s = \varepsilon_m + \varepsilon_s + \varepsilon_n + \varepsilon_a, \tag{7e}
$$

where $\langle \cdots \rangle_s$ indicates a spatial average over the whole domain; ε_t is the total change of flow energy over time; ε_m is the resolved part of the molecular dissipation; ε_s is the dissipation of an explicit SGS parameterization scheme; ε_n is the numerical dissipation due to the discretization of the advection term in a periodic domain without fixed walls; and ε_a is the additional numerical dissipation due to the Coriolis, buoyancy, and pressure terms, as well as the temporal discretization. Note that the equality $\mathbf{u} \cdot (\mathbf{u} \cdot \boldsymbol{\nabla})\mathbf{u} = \boldsymbol{\nabla} \cdot (\mathbf{u}E_k)$ used in the derivation of the energy transport equations is valid for exact continuous operators but is only an approximation in case of discrete numerical operators.

3. Numerical methods

a. The INCA model

With our flow solver [solver for the (in)compressible Navier–Stokes equations on Cartesian adaptive grids (INCA)], the Boussinesq equations are discretized by a fractional step method on a staggered Cartesian mesh. The code offers different discretization schemes depending on

the application, two of which are described below. For time advancement, the explicit third-order Runge–Kutta scheme of Shu (1988) is used. The time step is dynamically adapted to satisfy a Courant–Friedrichs–Lewy condition.

The spatial discretization is a finite-volume method. We use a second-order central difference scheme for the discretization of the diffusive terms and for the pressure Poisson solver. The Poisson equation for the pressure is solved at every Runge–Kutta sub step. The Poisson solver employs the fast Fourier transform in the vertical (i.e., ζ) direction and a stabilized biconjugate gradient (BiCGSTAB) solver (van der Vorst 1992) in the horizontal $(x_\parallel - y_\perp)$ plane.

b. The adaptive local deconvolution method

The ALDM is based on the idea of using the discretization error as an SGS parameterization for turbulence [implicit LES (ILES)]. Given the one-dimensional generic transport equation for the quantity u:

$$\partial_t u + \partial_x F(u) = 0, \tag{8}$$

the numerical approximation of the flux $\tilde{F}$ is computed based on the available filtered numerical solution $\overline{u}$ by approximately reconstructing the unfiltered solution $\tilde{u}$ and applying a numerical regularization.

The reconstruction of the unfiltered solution on the represented scales is based on Harten-type deconvolution polynomials. Different polynomials are dynamically weighted depending on the smoothness of the filtered solution. The regularization is obtained through a tailored numerical flux function operating on the reconstructed solution. Both the solution-adaptive polynomial weighting and the numerical flux function involve free model parameters that were calibrated in such a way that the truncation error of the discretized equations optimally represents the SGS stresses of isotropic turbulence (Hickel et al. 2006). This set of parameters was not changed for any subsequent applications of ALDM. For the presented computations, we used an implementation of ALDM with improved computational efficiency (Hickel and Adams 2007).

The extension of ALDM to passive scalar transport was developed by Hickel et al. (2007). Remmler and Hickel (2012) showed that the method also performs well for the active scalar in stably stratified turbulent flows governed by the Boussinesq equations. They simplified the numerical flux function using the filtered divergence-free velocity field as the transporting velocity. The buoyancy flux in the x_j direction for an equidistant staggered grid then reads

$$\tilde{F}^s_{j\pm1/2} = \overline{v}_{j-1/2\pm1/2} \frac{\tilde{b}^-_{j\pm1/2} + \tilde{b}^+_{j\pm1/2}}{2} - \sigma_{j\pm1/2}(\tilde{b}^+_{j\pm1/2} - \tilde{b}^-_{j\pm1/2}), \tag{9}$$

where the numerical diffusion is essentially controlled by

$$\sigma_{j\pm1/2} = \sigma_b |\tilde{v}^-_{j\pm1/2} - \tilde{v}^+_{j-1\pm1/2}|, \tag{10}$$

with $\sigma_b = 0.615$ (Hickel et al. 2007). In these equations, the index $j \pm 1/2$ indicates the right and left cell faces (the velocity $\overline{v}_j$ is stored on the cell faces, and the buoyancy $\overline{b}_j$ is stored in the cell centers); $\tilde{b}^+$ and $\tilde{b}^-$ are reconstructed solution values primarily based on values of $\overline{b}$ on the right and left, respectively, of the reconstruction position.

The formulation equation [Eq. (10)] was chosen to be analogous to ALDM for the momentum equations and is consistent with turbulence theory. The SGS (hyper) diffusivity thus depends on the smoothness of the buoyancy field and scales with the velocity gradients times the square of the cell widths, which proved to work very well in fully turbulent flows (Remmler and Hickel 2012, 2013). In the present case, however, the flow is temporarily laminar, which means that $|\tilde{v}^-_{j\pm1/2} - \tilde{v}^+_{j-1\pm1/2}|$ approaches zero, and the physically motivated SGS regularization is effectively turned off. Any numerical oscillations in a passive scalar field can then grow without bound. To numerically regularize the scalar transport in case of advection by a smooth velocity field, we propose a blending of ALDM with an upwind biased flux function. A pure upwind flux function can be obtained within the given framework through

$$\sigma_{j\pm1/2}|_{\text{upwind}} = \frac{1}{2}|\overline{v}_{j-1/2\pm1/2}|. \tag{11}$$

The convex combination of standard ALDM flux and upwind flux leads to the following expression for the numerical viscosity:

$$\sigma_{j\pm1/2} = \sigma_b \left[\alpha |\tilde{v}^-_{j\pm1/2} - \tilde{v}^+_{j-1\pm1/2}| \right.$$
$$\left. + (1-\alpha)\frac{1}{2}|\tilde{v}^-_{j\pm1/2} + \tilde{v}^+_{j-1\pm1/2}| \right],$$

where we took the liberty of approximating the advection velocity by

$$\overline{v}_{j-1/2\pm1/2} \approx \frac{\tilde{v}^{-}_{j\pm1/2} + \tilde{v}^{+}_{j-1\pm1/2}}{2}. \quad (12)$$

The blending parameter α is dynamically evaluated based on the instantaneous velocity values by

$$\alpha = \frac{\mathcal{M}}{\beta\mathcal{P} + \mathcal{M}}, \quad (13)$$

where $\mathcal{M} = |\tilde{v}^{-}_{j\pm1/2} - \tilde{v}^{+}_{j-1\pm1/2}|$ denotes the velocity difference, $\mathcal{P} = |\tilde{v}^{-}_{j\pm1/2} + \tilde{v}^{+}_{j-1\pm1/2}|/2$ denotes the advection velocity as defined in Eq. (12), and $\beta < 1$ is a free parameter. The choice of β controls the ratio $\mathcal{M}/\mathcal{P}$ at which the modification will become effective. In turbulent flows, where velocity fluctuations are typically large compared to the mean advection velocity, we find $\mathcal{M}/\mathcal{P} \gg \beta$, which means that $\alpha \to 1$, and we recover the original formulation [Eq. (10)]. On the other hand, if the flow is laminar or governed by a large mean advection velocity, then $\alpha \to 0$, and we have an upwind scheme. It is important to note that this blending is proposed for purely numerical reasons (balance dispersive errors); the numerical diffusion of upwind schemes is not Galilean invariant and thus cannot replace a physical SGS turbulence model.

c. Dynamic Smagorinsky method

The Smagorinsky (1963) scheme is based on the assumption that the incompressible momentum SGS term can be parameterized as

$$\mathcal{F} = -\boldsymbol{\nabla} \cdot \boldsymbol{\tau}^{\text{mod}} = -2\boldsymbol{\nabla} \cdot (\nu_t \overline{\mathbf{S}}), \quad (14)$$

where $\overline{S}_{ij} = 0.5(\partial_{x_i}\overline{v}_j + \partial_{x_j}\overline{v}_i)$ is the filtered strain rate tensor, and $\boldsymbol{\tau}^{\text{mod}}$ is the parameterized SGS stress tensor. The unknown eddy viscosity ν_t is evaluated from the strain rate tensor via

$$\nu_t = (C_S\overline{\Delta})^2 |\overline{S}|; \quad |\overline{S}| = \sqrt{2\overline{S}_{ij}\overline{S}_{ij}}, \quad (15)$$

where $\overline{\Delta} = (\Delta_x \Delta_y \Delta_z)^{1/3}$ is either the grid size or the filter size. In this formulation, the unknown SGS fluxes can be computed directly from the resolved velocity field. The same closure can be used for scalar transport equations using an eddy diffusivity: $\mu_t = \nu_t/\text{Pr}_t$.

The value of the model constant C_S is unknown a priori but can be estimated by means of the dynamic procedure of Germano et al. (1991), given a solution available in its filtered form $\overline{v}$ with a grid filter width $\overline{\Delta}$. This filtered velocity field is explicitly filtered by a test filter with a larger filter width $\hat{\Delta}$. As a test filter, we use a

top-hat filter with $\hat{\Delta} = 2\overline{\Delta}$. The subfilter-scale stress tensor is $T_{ij} = \widehat{\overline{u_i u_j}} - \widehat{\overline{u}}_i \widehat{\overline{u}}_j$. It cannot be computed directly from the filtered velocity field, but one can compute the Leonard stress tensor $L_{ij} = \widehat{\overline{u}_i \overline{u}_j} - \widehat{\overline{u}}_i \widehat{\overline{u}}_j$. Using the Germano identity

$$T_{ij} = L_{ij} + \widehat{\tau_{ij}} \quad (16)$$

and the standard Smagorinsky method for τ_{ij} and T_{ji}, we can minimize the difference between L_{ij} and

$$\begin{aligned} L_{ij}^{\text{mod}} &= T_{ij}^{\text{mod}}(C, \hat{\Delta}, \widehat{\mathbf{u}}) - \widehat{\tau_{ij}^{\text{mod}}}(C, \overline{\Delta}, \overline{\mathbf{u}}) \\ &= -2C\hat{\Delta}^2 |\widehat{\overline{S}}|\widehat{\overline{S}}_{ij} + 2C(\widehat{\overline{\Delta}^2 |\overline{S}|\overline{S}_{ij}}) \\ &= 2CM_{ij}, \end{aligned} \quad (17)$$

where $C \equiv C_S^2$, by a least squares procedure, yielding the optimal value (Lilly 1992):

$$C = \frac{1}{2}\frac{\langle L_{ij}M_{ij}\rangle_s}{\langle M_{ij}M_{ij}\rangle_s}. \quad (18)$$

A spatial average can be applied to both the numerator and denominator of Eq. (18) in order to prevent numerical instability. In the 3D cases, we apply this spatial average in the $y_\perp$ direction, while, in the 2.5D simulations, we do not apply any average. We update the model parameter C at the beginning of every time step. For the turbulent Prandtl number, we use a constant value of $\text{Pr}_t = 0.4$ (see, e.g., Eidson 1985). We also performed numerical experiments using $\text{Pr}_t = 0.2$ and $\text{Pr}_t = 0.6$ (not shown) and found that the exact value of Pr_t is of minor importance to the overall simulation results.

d. Central discretization scheme

To evaluate the benefit of an SGS parameterization, we run under-resolved direct numerical simulations with an ordinary fourth-order accurate central interpolation: namely,

$$\tilde{u}^{-}_{j+1/2} = \frac{1}{12}(-\overline{u}_{j-2} + 7\overline{u}_{j-1} + 7\overline{u}_j - \overline{u}_{j-2}) \quad (19)$$

on an LES grid (i.e., at a resolution much too low to resolve the Kolmogorov scale).

4. Test cases

According to Prusa et al. (1996), gravity waves arriving at the upper mesosphere tend to be almost monochromatic, with horizontal wavelengths ranging from a few kilometers to more than 100 km, and with vertical wavelengths of a few kilometers. These waves break at

TABLE 1. Atmospheric parameters.

Kinematic viscosity	ν	$1\,\mathrm{m^2\,s^{-1}}$
Thermal diffusivity	μ	$1\,\mathrm{m^2\,s^{-1}}$
Latitude for Coriolis parameter	ϕ_C	70°N
Coriolis parameter	f	$1.37 \times 10^{-4}\,\mathrm{s^{-1}}$
Brunt–Väisälä frequency	N	$2 \times 10^{-2}\,\mathrm{s^{-1}}$
Gravitational acceleration	g	$9.81\,\mathrm{m\,s^{-2}}$

altitudes between 65 and 120 km. We investigate three different cases of monochromatic gravity waves in an environment representative of the upper mesosphere at an altitude of approximately 80 km. For the atmospheric parameters, see Table 1, and for the wave parameters, see Table 2. All three waves have a wavelength of 3 km and the wave phase is such that, in the rotated coordinate system, the maximum total buoyancy gradient within the wave is located at $\zeta = 750$ m, and the minimum (associated with the least stable point) is located at $\zeta = 2250$ m. The primary and secondary perturbations of the waves used to construct the initial condition for the 3D simulations were computed by Fruman et al. (2014). In Fig. 2, we show the initial perturbation energy E_{ini} (primary and secondary perturbations) as a function of ζ, integrated in the spanwise–streamwise ($x_\parallel$–$y_\perp$) plane.

Case 1 is a statically unstable inertia–gravity wave with a wave period of 8 h and a phase speed of $0.1\,\mathrm{m\,s^{-1}}$. The vertical and horizontal wave lengths are similar to those actually observed by Hoffmann et al. (2005) in

wind radar measurements at an altitude of approximately 85 km. The wavelength of the leading transverse normal mode (primary perturbation) is somewhat longer than the base wavelength ($\lambda_\parallel = 3.98$ km), while the leading secondary singular vector (with respect to an optimization time of 5 min) has a significantly shorter wavelength ($\lambda_\perp = 0.4$ km). The initial perturbation energy (Fig. 2a) is distributed rather homogeneously in the wave with a peak close to the minimum static stability and a minimum in the most stable region. The time scales of the turbulent wave breaking and of the wave propagation are similarly long, which makes this case especially interesting. Remmler et al. (2013) pointed out that a secondary breaking event is stimulated in this case when the most unstable part of the wave reaches the region where the primary breaking has earlier generated significant turbulence.

Case 2 is also an inertia–gravity wave with the same period and phase speed as case 1, but with an amplitude below the threshold of static instability. The wave is perturbed by the leading transverse primary singular vector ($\lambda_\parallel = 2.115$ km) and the leading secondary singular vector ($\lambda_\perp = 300$ m). An optimization time of 7.5 min was used for computing both the primary and secondary singular vectors. The perturbation energy in this case is concentrated exclusively in the region of lowest static stability (see Fig. 2b). This is typical for singular vectors (SVs), which maximize perturbation

TABLE 2. Parameters of the initial conditions for the investigated test cases. A_1 and A_2 are the amplitudes of the respective perturbations in terms of the maximum perturbation energy density compared to the maximum energy density in the basic state; $\hat{u}_\parallel$, $\hat{v}_\perp$, and $\hat{b}$ are the amplitudes of the original wave [Eq. (3)]; λ_y and λ_z are the horizontal and vertical wavelengths in the earth frame, corresponding to the base wavelength $\lambda = 3$ km and the propagation angle; and $\langle\varepsilon_t\rangle_{\mathrm{max}}$ is the maximum value observed in our respective highest-resolved DNS. NM indicates normal mode and SV indicates singular vector.

	Case		
	1 (unstable IGW)	2 (stable IGW)	3 (unstable HGW)
Amplitude			
a	1.2	0.86	1.2
$\hat{u}_\parallel$ $(\mathrm{m\,s^{-1}})$	8.97	6.43	0.23
$\hat{v}_\perp$ $(\mathrm{m\,s^{-1}})$	14.56	10.43	12.20
$\hat{b}$ $(\mathrm{m\,s^{-2}})$	0.229	0.164	0.244
Propagation angle Θ (°)	89.5	89.5	70
Wavelengths			
λ_y (km)	343	343	8.7
λ_z (km)	3.0	3.0	3.1
Primary perturbation			
α (°)	90 (NM)	90 (SV)	90 (NM)
$\lambda_\parallel$ (km)	3.98	2.12	2.93
A_1	0.05	0.05	0.05
Secondary perturbation			
$\lambda_\perp$ (km)	0.4	0.3	3.0
A_2	0.02	0.01	0.01
Wave period T	7.8 h (28 083 s)	7.8 h (28 083 s)	15.3 min (918 s)
Phase speed c_p $(\mathrm{m\,s^{-1}})$	0.107	0.107	3.27
Maximum dissipation during breaking $\langle\varepsilon_t\rangle_{\mathrm{max}}$ $(\mathrm{mW\,kg^{-1}})$	17	4.3	88

(a) unstable IGW (case 1)   (b) stable IGW (case 2)   (c) unstable HGW (case 3)
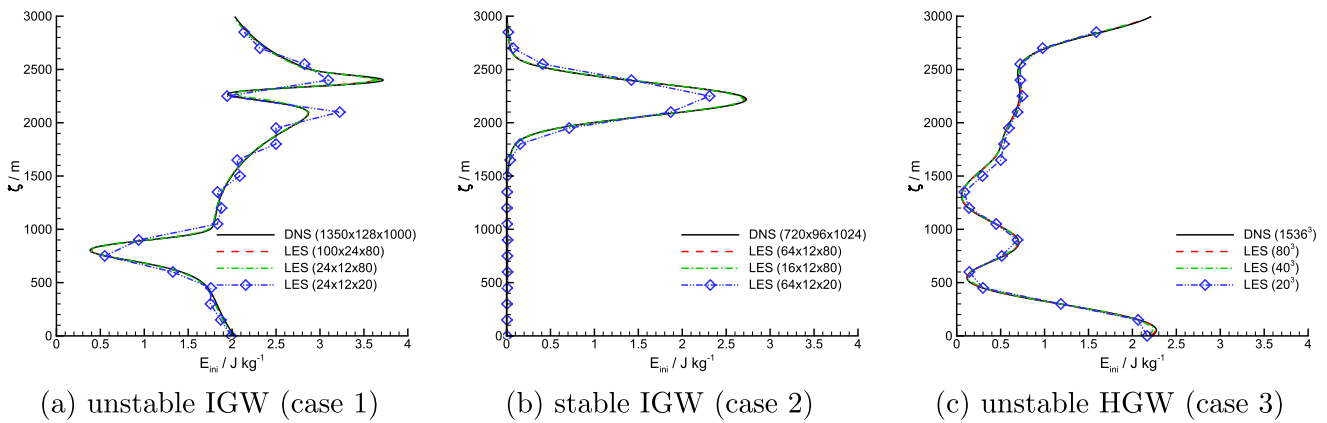
FIG. 2. Initial horizontally ($x_\parallel - y_\perp$) averaged perturbation energy at different 3D grid resolutions.

energy growth in a given time. Despite the wave being statically stable, the perturbations lead to a weak breaking and the generation of turbulence. However, the duration of the breaking event is much shorter than the wave period, and the overall energy loss in the wave is not much larger than the energy loss through viscous forces on the base wave in the same time.

Case 3 is a statically unstable high-frequency gravity wave with a period of 15 min and a phase speed of $3.3\,\mathrm{m\,s^{-1}}$ perturbed with the leading transverse primary normal mode ($\lambda_\parallel = 2.929\,\mathrm{km}$) and the leading secondary singular vector with $\lambda_\perp = 3\,\mathrm{km}$. The initial perturbation energy (Fig. 2c) has a clear maximum at $\zeta = 100\,\mathrm{m}$, which is in a region with moderately stable stratification. The breaking is much stronger than in cases 1 and 2 and lasts for slightly more than one wave period. Turbulence and energy dissipation are almost uniformly distributed in the domain during the most intense phase of the breaking.

The three different cases were chosen to represent a wide range of different configurations of breaking gravity waves. They especially differ in the duration of the breaking compared to the wave period. In case 1, the breaking duration is slightly smaller than the wave period, and the breaking involves multiple bursts of turbulence. In case 2, the breaking lasts only for a short time compared to the wave period, and, in case 3, the breaking lasts longer than one wave period.

5. Case 1: Unstable inertia–gravity wave

a. Three-dimensional DNS

Fruman et al. (2014) showed that, in 2.5D simulations, a small initial random disturbance of the flow field can lead to different global results. To investigate whether the same applies to full 3D simulations of the same case and whether the LES method has an influence on this variability, we added two new DNSs

($640 \times 64 \times 500$ cells) to the results of Remmler et al. (2013) to have a very small ensemble of four simulations from which we can compute averages and standard deviations. For these new simulations, a very small amount of white noise was added to all three velocity components at the initial time. In Fig. 3, we show the ensemble average of the amplitudes $\langle a \rangle_e$ and of the spatially averaged total dissipation rate $\langle \varepsilon_t \rangle_{s,e}$ as a solid line and the standard deviation from these ensemble averages as shaded area.

For the present case, the wave breaking consists of a series of three single breaking events. Each of those events is characterized by a peak in the energy dissipation and by an enhanced amplitude decrease. The strongest breaking event is initialized by the initial perturbations and starts directly at the beginning of the simulation. It involves overturning and generation of turbulence in the whole computational domain. The intensity of this primary breaking event is very similar in all ensemble members, independent of the resolution and initial white noise. The second breaking event around $t \approx 4\,\mathrm{h}$ is preceded by an instability of the large-scale wave and generates only a small amount of turbulence in the unstable half of the domain. The third breaking event around $t \approx 5\,\mathrm{h}$ is caused by a small amount of remaining turbulence from the first breaking event, which was generated in the stable part of the wave. At the time of the third breaking event, the wave phase has traveled approximately half a wavelength, so the unstable part of the wave has reached the region of the remaining turbulence at this time. For details of the wave breaking process, we refer to Remmler et al. (2013) and Fruman et al. (2014).

The amplitude variations in the 3D DNSs are very small. The ensemble members diverge slightly during a very weak breaking event at $t \approx 8\,\mathrm{h}$, which has very different intensity in the four simulations. The total dissipation rate varies significantly among the ensemble

(a) fine LES ($100 \times 24 \times 80$): a

(b) medium LES ($24 \times 12 \times 80$): a

(c) coarse LES ($24 \times 12 \times 20$): a

(d) medium LES ($24 \times 12 \times 80$): ε_t
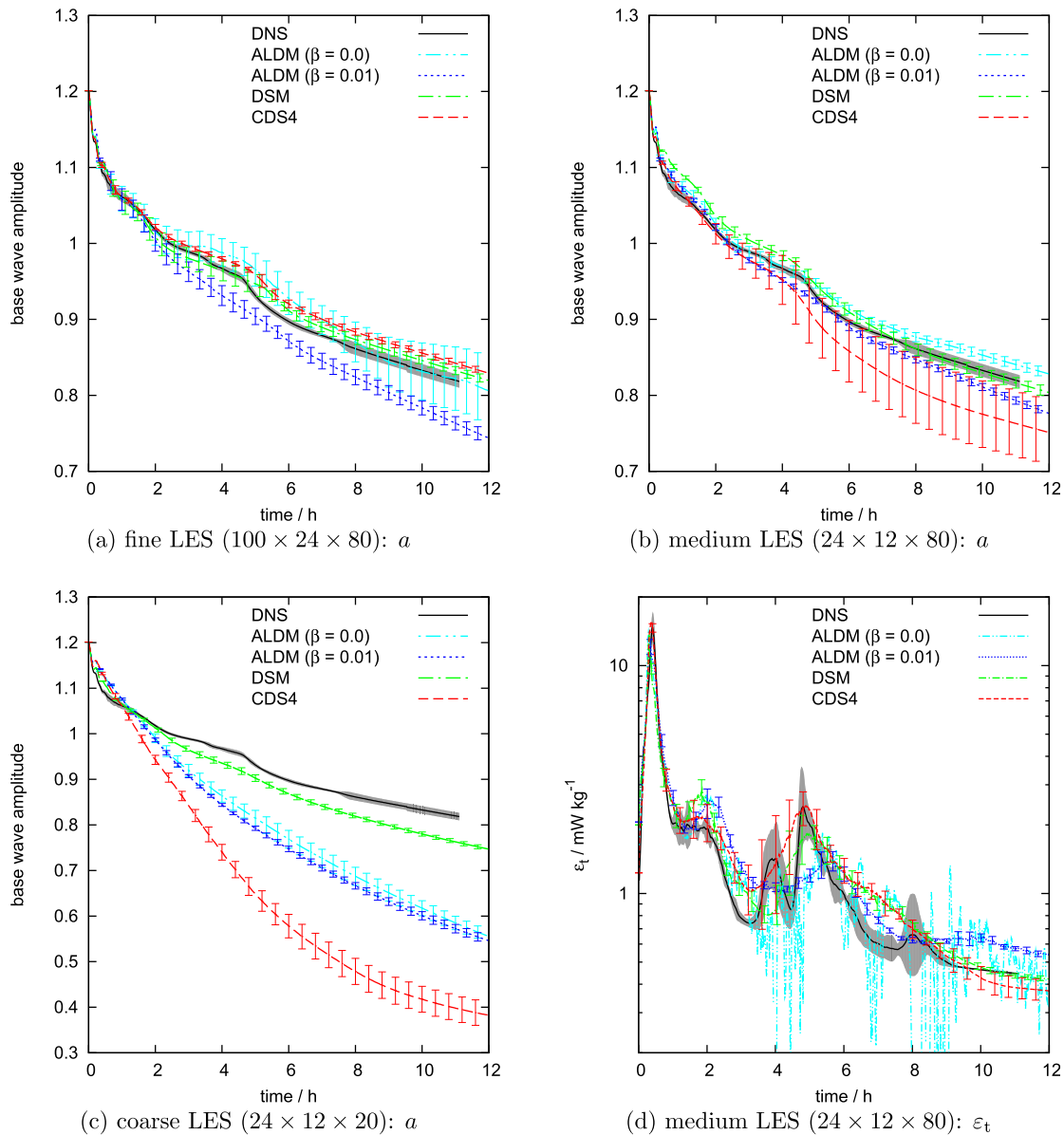
FIG. 3. Statically unstable IGW (3D). Base wave amplitudes a and total dissipation rates ε_t at coarse, medium, and fine LES resolution. The gray shaded area indicates the standard deviation of four DNSs, and the error bars indicate the standard deviation of nine LESs.

members during the weak breaking events but not during the first strong breaking event.

b. Three-dimensional LES

We simulated the 3D setup of case 1 using three different LES resolutions, which we refer to as fine ($100 \times 24 \times 80$ cells, corresponding to a cell size of $39.8\,\text{m} \times 17.7\,\text{m} \times 37.5\,\text{m}$), medium ($24 \times 12 \times 80$ cells), and coarse ($24 \times 12 \times 20$ cells). We chose these resolutions after a series of numerical experiments that showed two main results: (i) the horizontal (i.e., in the $x_\parallel - y_\perp$ plane) resolution can be reduced without much effect on the global result as long as the vertical resolution remains

comparatively high, and (ii) reducing the vertical resolution and keeping the horizontal resolution high had a strong adverse effect on the global result, independent of the LES method used. One reason for this behavior might be the insufficient resolution of the initial perturbation on the coarsest grid. From Fig. 2a, it is obvious that the initial perturbation is well resolved by 80 cells in the ζ direction but deviates in places on the coarse grid with only 20 cells in the ζ direction.

In LES, it is easily affordable to run small ensembles for many different simulations. For all presented 3D LES results, we performed the same simulation eight times with some low-level white noise superposed on the

initial condition (consisting of the base wave and its leading primary and secondary perturbations) and once with no added noise. The results of these nine realizations were then averaged. The average amplitudes of simulations with three different resolutions and four different LES methods [standard ALDM with $\beta = 0.0$, modified ALDM with $\beta = 0.01$, dynamic Smagorinsky (DSM), and plain central discretization (CDS4)] are shown in Figs. 3a–c. Figure 3d shows the total dissipation rates for the medium grid. In all figures, the error bars indicate the standard deviation of the ensemble.

Using the fine LES grid, the average wave amplitude is quite well predicted by standard ALDM, DSM, and CDS4. Modified ALDM dissipates slightly too much energy, while standard ALDM shows very large variations between ensemble members.

With the medium grid, the three SGS models (i.e., DSM and the two versions of ALDM) yield good agreement with the DNS, both in the average amplitude and in the variations among ensemble members. Only CDS4 (without an SGS model) creates a bit too much dissipation and far too much variability. The analysis of the total dissipation rates in Fig. 3d shows that the exact evolution of the dissipation is reproduced by none of the LES methods. However, the results with modified ALDM, DSM, and CDS4 are acceptably close to the DNS results. The result from standard ALDM strongly oscillates in time despite being an ensemble average. For clarity of the figure, we did not plot the error bars for this curve, but it is nevertheless obvious that the variation among the ensemble members with standard ALDM is much larger than with the other methods.

With the coarse resolution, ALDM and CDS4 dissipate far too much energy and, hence, predict a too-quick wave decay. The flow physics are not correctly reproduced. Only DSM produces an acceptable result, although the wave amplitude at the end of the breaking is considerably lower than in the DNS. The variability in the DSM results is even smaller than in the DNS, which is not necessarily an indication of a good approximation of the unresolved turbulent scales.

The strong variations of the wave amplitude (fine resolution) and total dissipation rate (medium resolution) in the simulations with standard ALDM motivated the development of the modification described in section 3b. In Fig. 4, we compare Hovmöller diagrams of resolved kinetic energy dissipation (as an indicator of velocity fluctuations) averaged in $x_\parallel$–$y_\perp$ planes from the DNS, the high-resolution LES with DSM, and with standard and modified ALDM. Standard ALDM produces a lot of velocity oscillations in the stable half of the domain ($0 < \zeta < 1500$ m) not present in the DNS and DSM results. These velocity fluctuations are generated

by numerical oscillations in the buoyancy, which are a result of the smooth velocity field that causes the numerical diffusivity to be effectively zero. These oscillations are thus only slightly smoothed but not completely eliminated by the stable stratification. If we add a passive scalar to the flow with a similar initial distribution as the buoyancy, we observe, indeed, exponentially growing fluctuations up to the limits of double-precision floating point numbers. These physically unlikely oscillations can be avoided by modifying the flux function for the scalar, as described in section 3b. The parameter β controls the intensity of the damping. In a series of numerical experiments, we found $\beta = 0.01$ to be a good compromise between excessive damping with strong wave decay (higher values of β) and no damping with strong oscillations (lower values of β). Choosing the exact value of β is, at the present time, a matter of personal judgement.

The first breaking event lasts for about 1 h and is associated with the strongest turbulence. This peak is predicted quite differently by the different SGS models. We show the energy dissipation during the first 2 h in Fig. 5. In the ALDM and DSM simulations, only a minor part of the total energy dissipation is resolved because of the coarse resolution; the remainder is provided by the implicit (ε_n) or explicit (ε_s) turbulence SGS parameterization. This is exactly how the parameterization is supposed to work. However, the total dissipation during the most intense breaking is considerably smaller than in the DNS with both SGS parameterizations.

For the CDS4 simulations, where no SGS parameterization is applied (Fig. 5e), the resolved dissipation ε_m is much higher because of the stronger small-scale fluctuations (see also the spectra in Fig. 6 described below). During the phase of highest dissipation, it is complemented by a small amount of numerical dissipation ε_n and a significant amount of dissipation ε_a because of numerical effects in terms other than the advective term. The resulting total dissipation ε_t matches surprisingly well with the DNS result.

The energy dissipation can be decomposed into mechanical energy dissipation ε_k and thermal energy dissipation ε_p. In Figs. 5b, 5d, and 5f, we show $\varepsilon_p = \varepsilon_{p,m} + \varepsilon_{p,n} + \varepsilon_{p,s}$ and the total energy dissipation. In the simulations with ALDM, the thermal energy dissipation ε_p is too strong compared to the total energy dissipation ε_t during the peak. With DSM, ε_p is smaller, but the ratio $\varepsilon_p/\varepsilon_t$ is also smaller than in the DNS. In CDS4, on the other hand, ε_p is too small during the period of peak dissipation. After the first dissipation peak, after about 1 h, the dissipation rates match the DNS results quite well with all three LES methods. In all LESs, the dissipation peaks a little bit earlier than in the
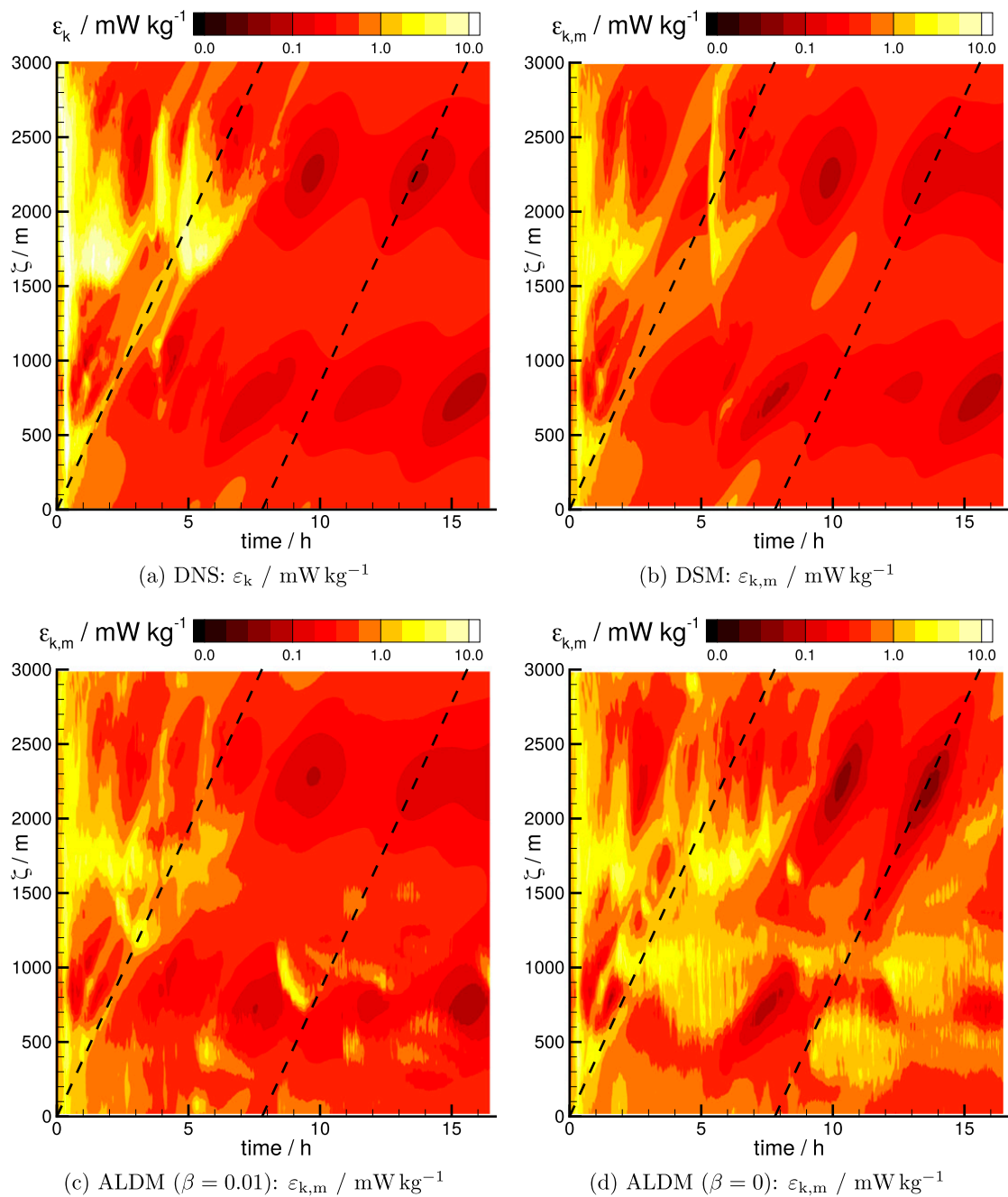
FIG. 4. Statically unstable IGW (3D). Hovmöller plots of horizontally averaged (resolved) dissipation of kinetic energy. (a) DNS ($640 \times 64 \times 500$ cells) and (b)–(d) LES ($100 \times 24 \times 80$ cells). The dashed line indicates a fixed position in space.

DNS. The time difference is surely a result of the time that flow energy needs to be transported through the spectrum from the finest LES scales to the scales of maximum dissipation in the DNS.

Instantaneous vertical energy spectra averaged in the $x_{\parallel}$ and $y_{\perp}$ directions are shown in Fig. 6. The chosen instant in time in each case is at the moment of maximum dissipation (which is a slightly different time in each simulation) and at $t = 2\,\mathrm{h}$, which is after the first

breaking event. For orientation, we added straight lines to the spectra in order to distinguish the regions of weak and strong wave interaction ($E \sim k_{\zeta}^{-3}$) and inertial turbulence ($E \sim k_{\zeta}^{-5/3}$), respectively, according to the theory of Lumley (1964) and Weinstock (1985). Especially at $t = 2\,\mathrm{h}$, when turbulence has become weaker after the first breaking, these two regions can clearly be distinguished from each other. At the time of maximum dissipation, the agreement between all of the LESs and the
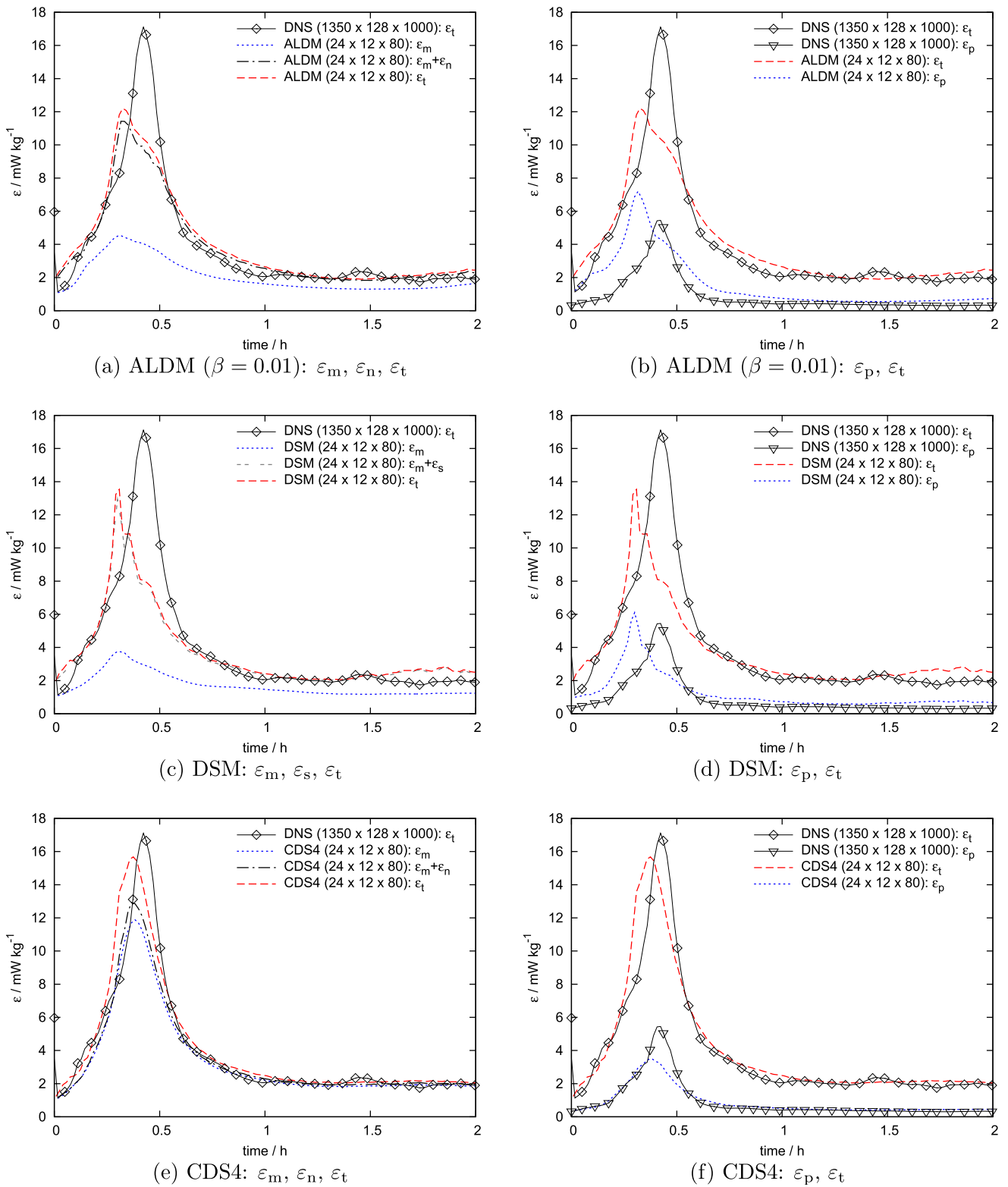
FIG. 5. Statically unstable IGW (3D). Comparison of (a),(c),(e) resolved (ε_m), numerical (ε_n), parameterized (ε_s), and total (ε_t) dissipation and (b),(d),(f) thermal (ε_p) and total dissipation during the first breaking event (DNS: single simulation; LES: ensemble averages).
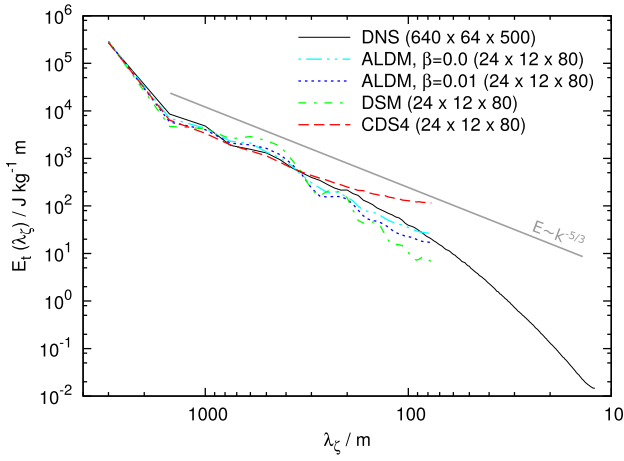
(a) E_{t} at max. dissipation
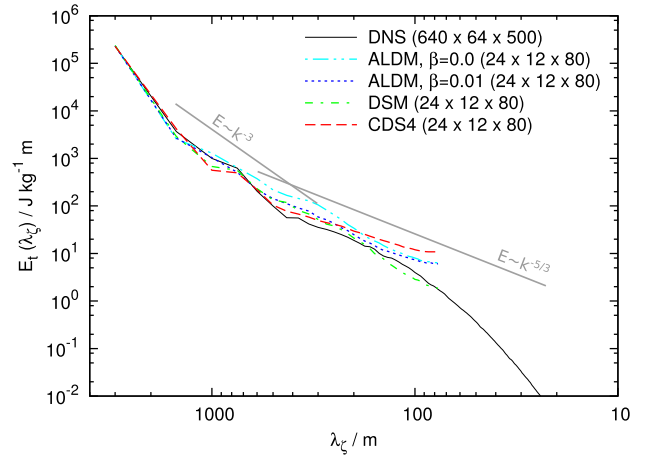
(b) E_{t} at $t = 2\,\mathrm{h}$
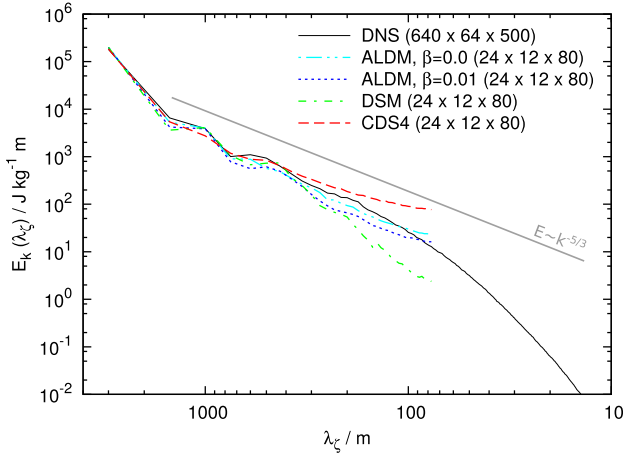
(c) E_{k} at max. dissipation
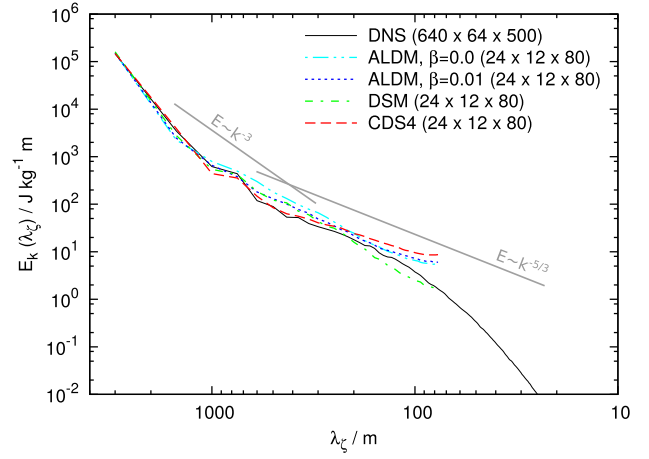
(d) E_{k} at $t = 2\,\mathrm{h}$
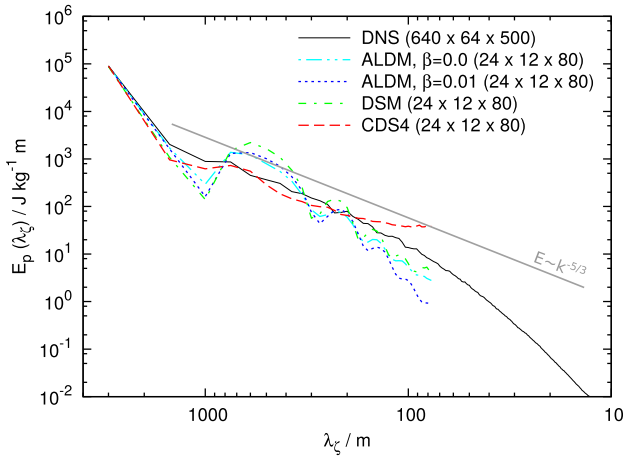
(e) E_{p} at max. dissipation
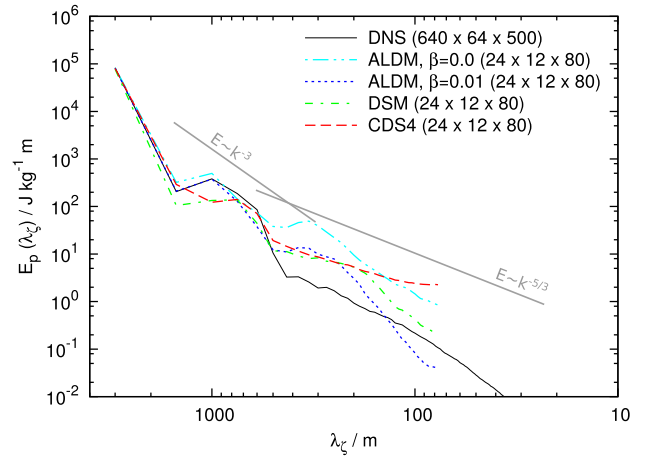
(f) E_{p} at $t = 2\,\mathrm{h}$

FIG. 6. Statically unstable IGW (3D). Distributions of total, kinetic, and potential energy over vertical wavelength λ_ζ (a),(c),(e) at the moment of maximum total energy dissipation and (b),(d),(f) at $t = 2\,\mathrm{h}$ (DNS: single simulation; LES: ensemble averages).

DNS in terms of E_t and E_k is quite good. With the DSM, the small-scale fluctuations are a bit underpredicted, and, with CDS4, they are overpredicted. With ALDM (standard and modified) the matching is also good at the smallest resolved scales. The difference between standard ALDM and the modified version is small because of the fully developed turbulence at this time. The potential energy spectrum with ALDM and DSM has the right level but does not decrease monotonically as in the DNS. The E_p spectrum with CDS4 is much closer to the DNS result than in the other LES solutions, with only the high-wavenumber fluctuations a bit overpredicted.

At $t = 2$ h, the agreement of the E_k spectra from all LES methods with the DNS is even better than at the time of maximum dissipation. The spectral slope is a bit too steep with DSM, a bit too shallow with CDS4, and somewhere in between with ALDM, with the modified version of ALDM slightly outperforming the original ALDM. The E_p spectrum is well predicted by all four LES methods in the wavelength range $\lambda_\zeta \gtrsim 500$ m. At smaller scales, the DNS spectrum suddenly falls off, which is not reproduced with any of the LES methods. The level of turbulence is already quite low at this time, so there is a clear difference in the spectra between the original and modified ALDM, the result with the modified ALDM agreeing better with the DNS than the original version.

c. 2.5D simulations

The results of the 2.5D simulations (DNS and LES) are summarized in Fig. 7. Corresponding to the 3D LESs, we chose LES grids with high (100×80 cells), medium (24×80 cells), and coarse (24×20 cells) resolution and performed the same LES eight times with some low-level white noise superposed on the initial condition (consisting of the base wave and its leading primary perturbation) and once with no added noise. The results of these nine realizations were then averaged. The reference 2.5D DNSs were run at a resolution of 660×500 cells (see Fruman et al. 2014). An ensemble of eight DNSs was used for the calculation of mean values and standard deviations. For a detailed comparison of 2.5D and 3D DNS results, see Fruman et al. (2014).

The results obtained with the highest LES resolution are very close to the DNS reference results (Figs. 7a,b), almost independent of the LES method used. The best results, both in terms of wave amplitude and total energy dissipation, were obtained with ALDM in the standard formulation. Since the spurious oscillations observed in some 3D LESs with ALDM did not occur in any of the 2.5D simulations, we do not present any results using the modified ALDM with $\beta > 0$. With DSM, the final wave amplitude is a bit too low, while the total dissipation rate

matches quite well with the DNS result throughout the whole simulated period. With pure CDS4, on the other hand, the final wave amplitude is a little bit too high. The total dissipation rate has some deviations from the 2.5D DNSs in some regions. Specifically, there is a peak (in mean value and variability) after approximately 5.5 h, which is not present in the 2.5D DNSs but which did occur in the 3D DNSs.

With a grid coarsened in the $x_\parallel$ direction (Figs. 7c,d), the CDS4 method becomes less reliable. The amplitude decay is strongly overpredicted, and the variability among ensemble members is much larger than in the DNS. With ALDM and DSM, the results are very similar: during the first hour, the dissipation is a bit too high, but this is compensated for later on, and the final wave amplitude is predicted quite well.

The grid further coarsened in the ζ direction causes the CDS4 simulations to quickly break down. The ALDM and DSM simulations are stable, but the quality of the result is poor, showing too much total energy dissipation and wave amplitude decay.

d. Summary of case 1

The unstable IGW is the most complex test case presented here. It involves multiple breaking events, and the total time of the breaking is similar to the wave period. It is thus a challenging test for the LES methods in 3D and 2.5D. In 3D LESs, we obtained good agreement with the reference DNS using the DSM and ALDM (with $\beta = 0.01$). With the original ALDM ($\beta = 0.0$), there are spurious oscillations in the stable half of the domain that reduce the overall result quality. The LESs using the CDS4 method, although utilizing neither explicit nor implicit numerical viscosity, remain stable throughout all simulations. A certain pileup of energy close to the grid cutoff wavenumber is visible in the spectra, but because of the low overall turbulence level, it is not strong enough to cause the simulations to diverge.

The 3D and 2.5D LES results depend strongly on the numerical resolution in the ζ direction (of the wave phase), while the resolution in the $x_\parallel$ direction has only minor influence on the results. With a resolution of 80 cells in the ζ direction, the results are generally in good agreement with the DNS, while basically all simulations with a ζ resolution of only 20 cells deviate strongly from the reference DNS.

## 6. Case 2: Stable inertia–gravity wave

a. Three-dimensional DNS

The reference DNS results are taken from Fruman et al. (2014). They presented simulations
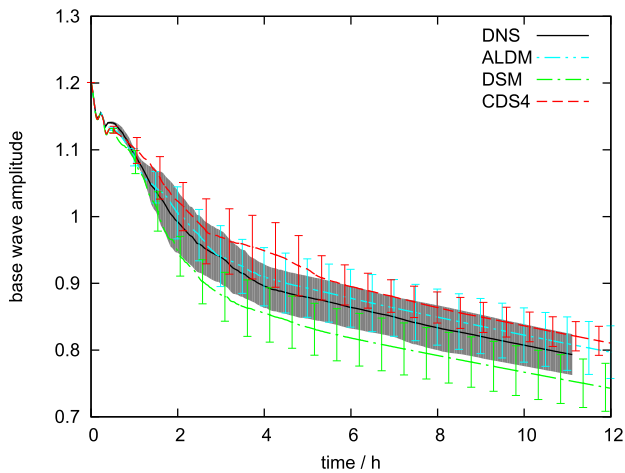
(a) fine LES (100×80): a
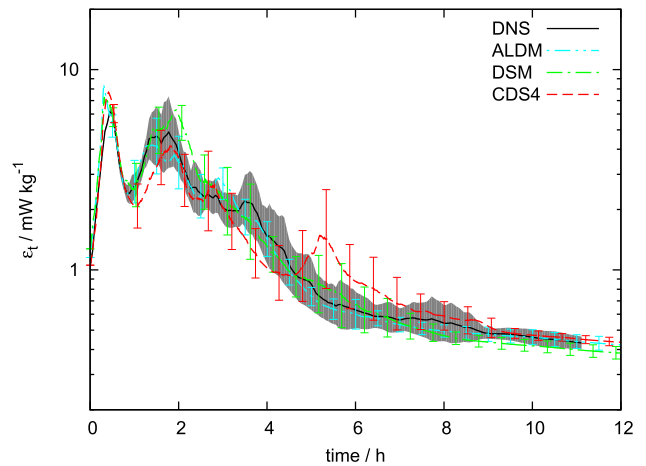
(b) fine LES (100×80): ε_t
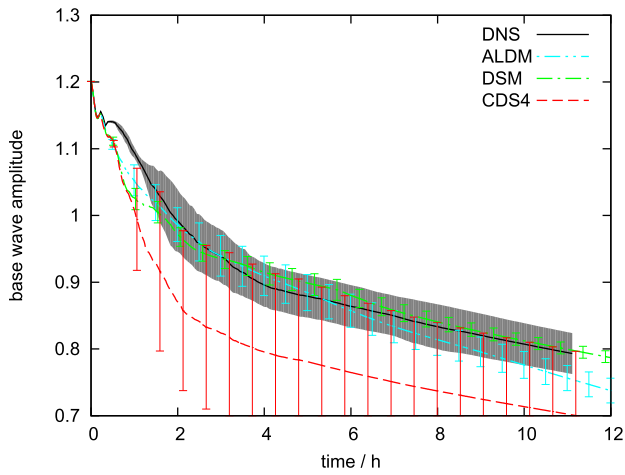
(c) medium LES (24×80): a
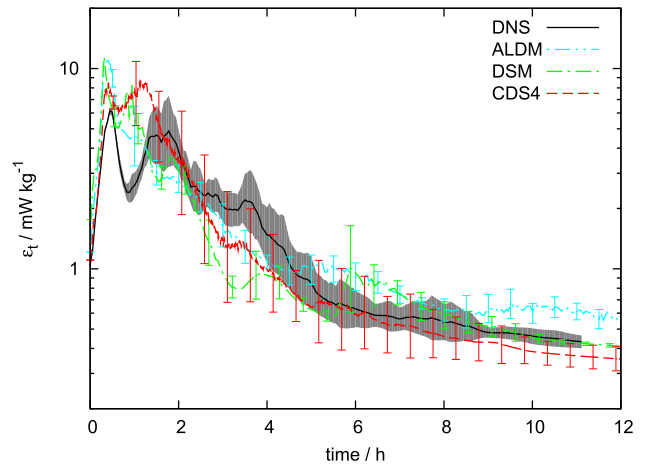
(d) medium LES (24×80): ε_t
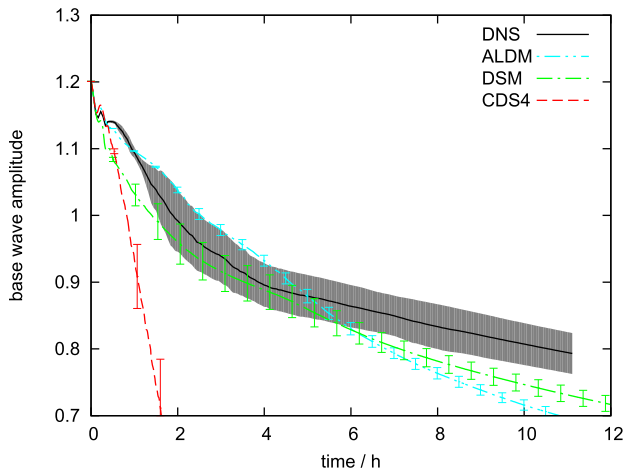
(e) coarse LES (24×20): a
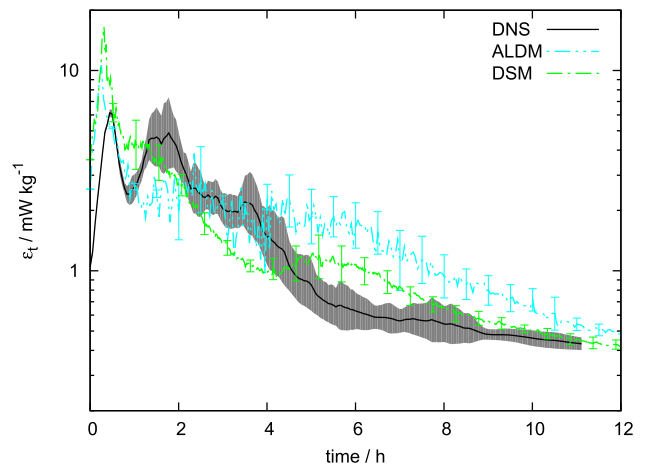
(f) coarse LES (24×20): ε_t

FIG. 7. Statically unstable IGW (2.5D). Base wave amplitude a and total dissipation rate ε_t at coarse, medium, and fine LES resolution compared with a and resolved dissipation rate ε_m from DNS. The gray shaded area indicates the standard deviation of eight DNSs, and the error bars indicate the standard deviation of nine LESs.

with $720 \times 96 \times 1024$ cells and with $512 \times 64 \times 768$ cells. To have at least a small ensemble of four members for comparison, we repeated these simulations (adding low-level white noise to the velocity components of the initial condition) running until $t = 1\,h$. The ensemble average and standard deviation of these four simulations is shown in Fig. 8.

The breaking of the wave is weaker than in the unstable IGW case, and it lasts only for a short period in time. The initial perturbations grow during the first minutes and generate some turbulence, which remains confined to the least stable part of the domain and is dissipated quickly. The dissipation peak occurs at $t = 11\,min$, and, 30 min later, the turbulence has vanished completely.

b. Three-dimensional LES

The computational domain for the stable inertia–gravity wave is smaller in the $x_\parallel$ and $y_\perp$ directions than for the unstable wave in case 1. To have approximately the same cell size for the LESs as for case 1, we chose an LES grid with $64 \times 12 \times 80$ cells (corresponding to a cell size of $33.0\,m \times 25.0\,m \times 37.5\,m$) for the highest LES resolution. After experimenting with different coarsening levels in the $x_\parallel$ and ζ directions, we found the most interesting results with one grid coarsened in the $x_\parallel$ direction with $16 \times 12 \times 80$ cells and another coarsened in the ζ direction with $64 \times 12 \times 20$ cells. With a fully coarsened grid of $16 \times 12 \times 20$ cells, the model performance was as poor as for case 1. The initial perturbation energy (Fig. 2b) is well resolved by the fine LES grid and the grid coarsened in the $x_\parallel$ direction but probably insufficiently resolved on the grid coarsened in the ζ direction.

We performed LESs using ALDM ($\beta = 0$, $\beta = 10^{-2}$, and $\beta = 10^{-5}$), DSM, and CDS4. With the fine LES grid, the DSM and CDS4 results agree well with the DNS in terms of base wave amplitude (Fig. 8a) and total dissipation rate (Fig. 8b). The original ALDM introduces spurious oscillations in the buoyancy and, consequently, also in the velocity field, as in case 1. These oscillations manifest themselves in strong fluctuations of the total dissipation rate, and the wave amplitude decays a little bit too strongly. The modified ALDM with additional damping ($\beta = 10^{-2}$) avoids these spurious oscillations at the cost of a too-high energy dissipation rate after the breaking event when the flow has become almost laminar. The results do not strongly depend on the exact value of β. For $\beta = 10^{-5}$, we obtain a very similar result as for $\beta = 10^{-2}$; only the dissipation rate of the laminar wave is slightly smaller. If the value of β is further decreased, a similar solution as with the unmodified ALDM is obtained. We could not find a value that yields

low dissipation and suppresses oscillations at the same time.

With the grid coarsened in the $x_\parallel$ direction (Figs. 8c,d), the DSM and CDS4 results do not differ very much from those with the fine grid. In both cases, the single dissipation peak has become multiple peaks, but the total dissipation during the breaking event remains approximately the same. With the original ALDM, the spurious oscillations are weaker than with the fine grid but still apparent. As with the fine grid, ALDM with additional damping eliminates these oscillations. With $\beta = 10^{-2}$, the dissipation rate is again slightly too high, resulting in a too-rapid amplitude decay, but, with $\beta = 10^{-5}$, the result agrees very well with the DNS and with the LESs using DSM and CDS4.

If the grid is not coarsened in the $x_\parallel$ direction but in the direction of the base wave ζ (Figs. 8e,f), all LES methods fail to predict the wave amplitude and dissipation rate correctly. This is consistent with the findings for case 1 (unstable IGW). Especially with ALDM, the dissipation rates are far too high. With DSM and CDS4, the shape of the dissipation peak is not predicted correctly, and the partial recovery of the base wave amplitude in the last phase of the breaking is too weak, so the predicted final wave amplitude after the breaking is too low, although the dissipation rate in the relaminarized wave is overpredicted only slightly.

c. 2.5D simulations

The results of the 2.5D simulations (DNS and LES) are summarized in Fig. 9. As for the 3D LESs, we chose LES grids with high resolution (64×80 cells) and grids coarsened in the $x_\parallel$ direction (16×80 cells) and in the ζ direction (64×20 cells), and we performed the same LES eight times with some low-level white noise superposed on the initial condition (consisting of the base wave and its leading primary perturbation) and once with no added noise. The results of these nine realizations were then averaged. The reference 2.5D DNSs were run at a resolution of 350×55 cells. An ensemble of six DNSs was used for the calculation of mean values and standard deviations. For a detailed comparison of 2.5D and 3D DNS results, see Fruman et al. (2014).

The matching of the simulation results is very similar to the 3D cases. With the highest resolution (64×80 cells), the agreement is almost perfect, independent of the LES method used. With the grid coarsened in the $x_\parallel$ direction (16×80 cells) there are some small deviations from the DNS, but the overall agreement is still good, except that, with ALDM, the dissipation and amplitude decay at the end of the simulation are a bit too high. With the grid coarsened in the ζ direction (64×20 cells), the results are equally wrong with all three LES
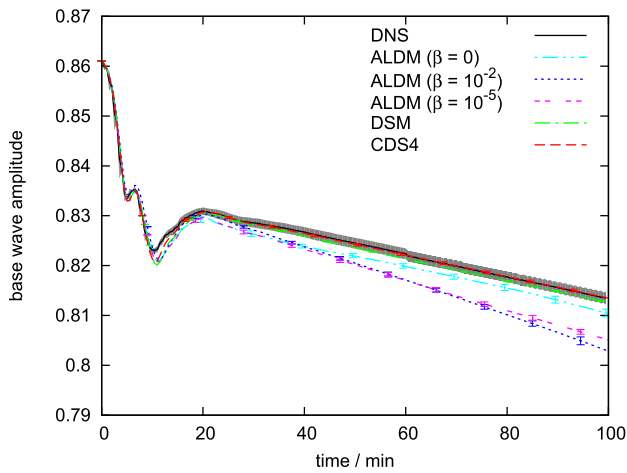
(a) fine LES ($64 \times 12 \times 80$): a
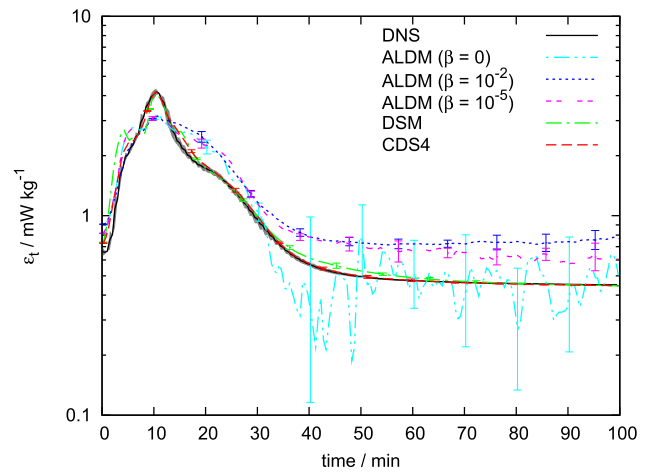
(b) fine LES ($64 \times 12 \times 80$): ε_{t}
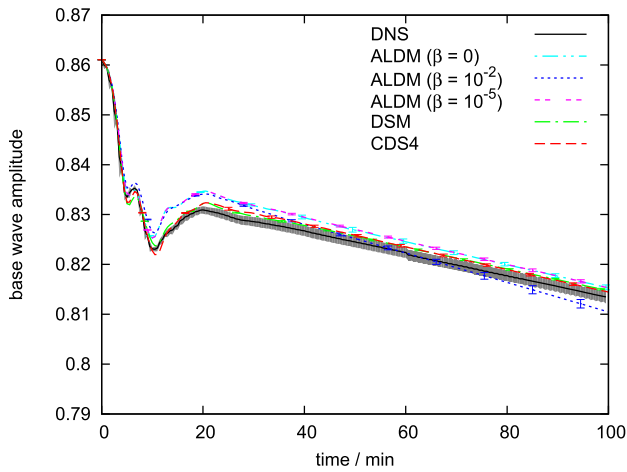
(c) LES, coarse in $x_{\parallel}$ ($16 \times 12 \times 80$): a
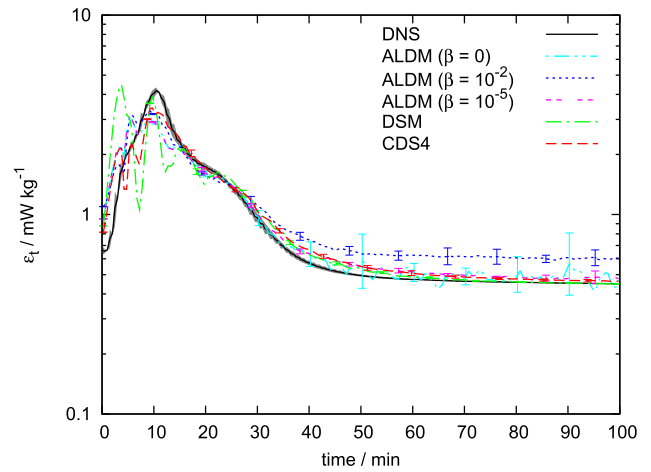
(d) LES, coarse in $x_{\parallel}$ ($16 \times 12 \times 80$): ε_{t}
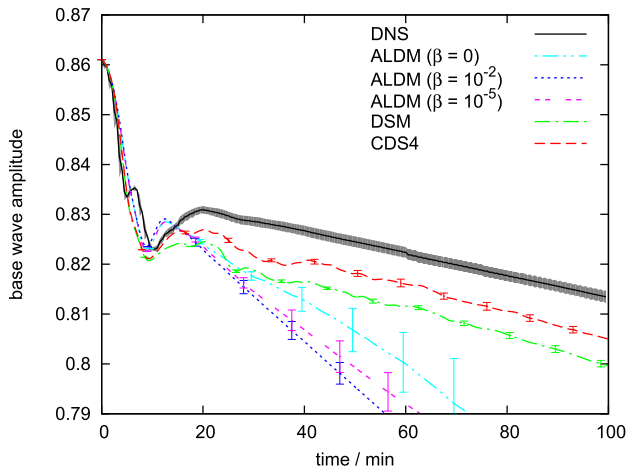
(e) LES, coarse in ζ ($64 \times 12 \times 20$): a
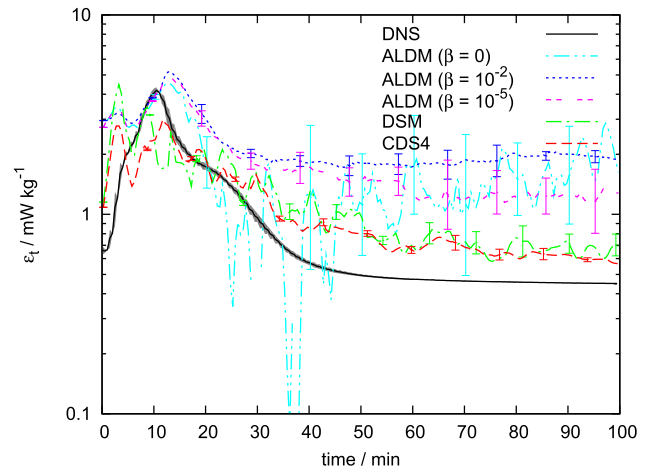
(f) LES, coarse in ζ ($64 \times 12 \times 20$): ε_{t}

FIG. 8. Statically stable IGW (3D). Base wave amplitude a and total dissipation rate ε_t at three different LES resolutions. The gray shaded area indicates the standard deviation of five DNSs, and the error bars indicate the standard deviation of nine LESs.
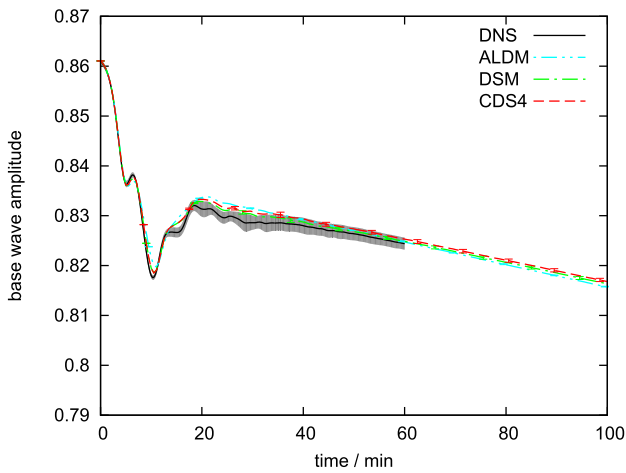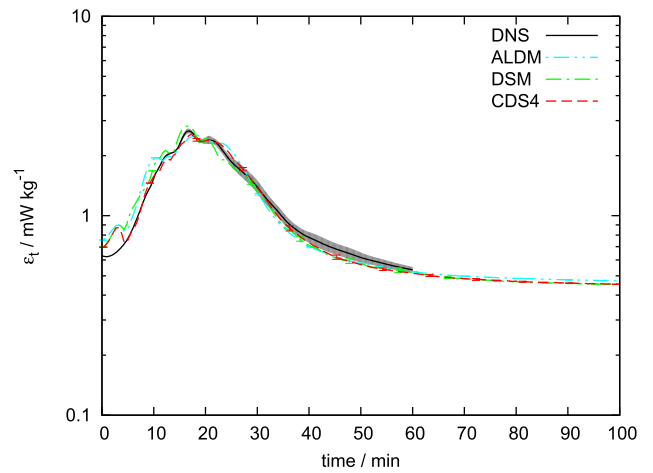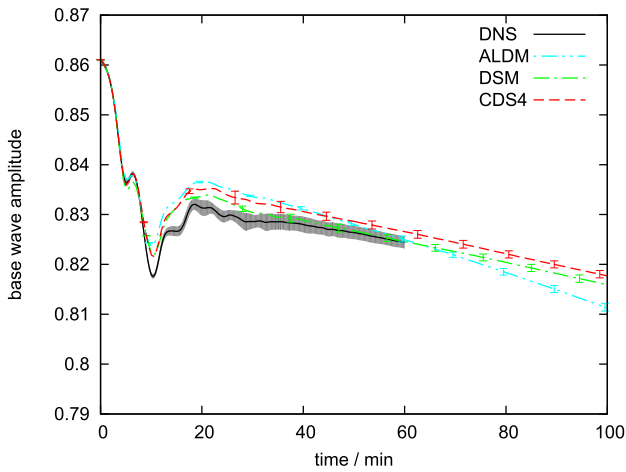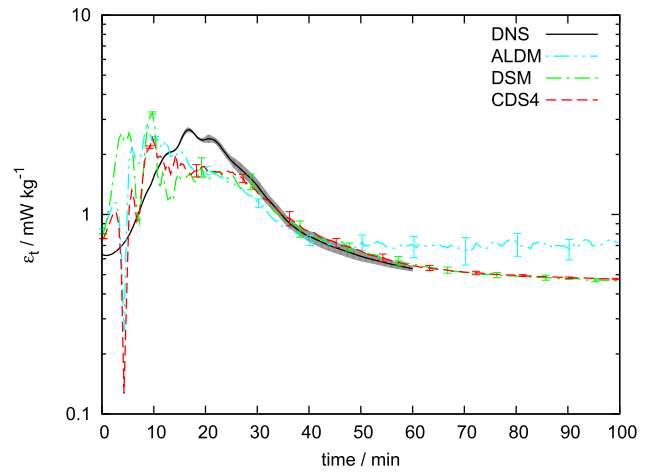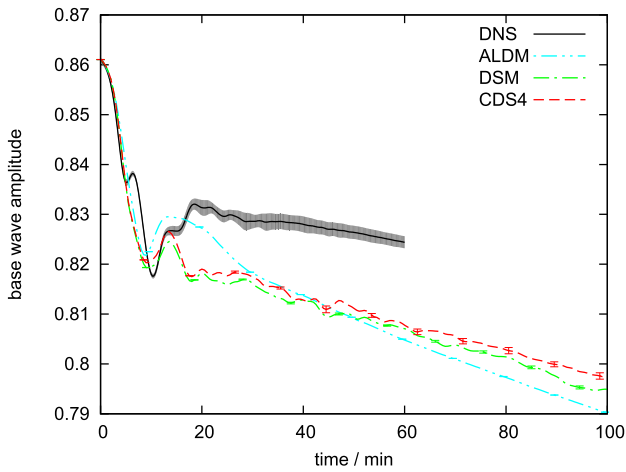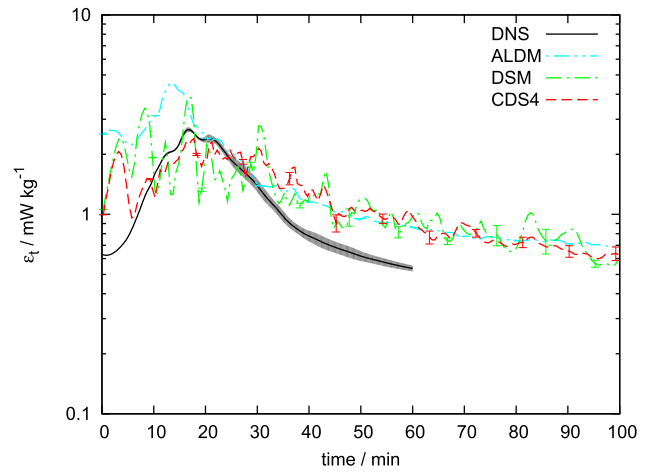
FIG. 9. Statically stable IGW (2.5D). Base wave amplitude a and total dissipation rate ε_t at three different LES resolutions compared with a and resolved dissipation rate ε_m from DNS. The gray shaded area indicates the standard deviation of six DNSs, and the error bars indicate the standard deviation of nine LESs.

methods. The dissipation and amplitude decay are strongly overpredicted during the whole simulation.

d. Summary of case 2

The breaking of the stable IGW is weak and lasts only for a fraction of the wave period. Both in 3D and in 2.5D LESs, we obtained good agreement with the reference DNSs as long as we chose a comparatively high resolution in the ζ direction, while the results were not much affected by choosing a low resolution in the $x_\parallel$ direction. Since the 2.5D DNSs were sufficient for estimating the breaking duration and intensity (see Fruman et al. 2014), LESs with only $16 \times 80 = 1280$ cells are thus sufficient for computing the basic characteristics of the wave breaking. Good LES results were obtained without any SGS parameterization and with DSM.

7. Case 3: Unstable high-frequency gravity wave

a. Three-dimensional DNS

Fruman et al. (2014) simulated the case of a breaking unstable HGW on grids with 1536^3 cells, 768^3 cells, and 384^3 cells. They found no notable differences between the two highest resolutions. We added another two simulations with 768^3 cells and 384^3 cells and averaged the results of these five DNSs. The results are presented in Fig. 10.

The wave breaking is much more intense than in both IGW cases. The generation of turbulence starts immediately after the initialization in the unstable part of the wave and is quickly advected also into the stable part because of the high phase velocity of the wave. At the time of maximum energy dissipation (around $t = 15$ min) turbulence is distributed almost homogeneously in the whole domain. The nondimensional wave amplitude rapidly decreases from an initial value of $a = 1.2$ to $a \approx 0.3$ after 30 min and does not change significantly any more after that time. The breaking process is analyzed in more detail by Fruman et al. (2014).

b. Three-dimensional LES

The domain for the unstable high-frequency gravity wave case is almost cubic. In a number of LESs with different resolutions in the horizontal and the vertical directions, we could not find any indication that different resolutions in the different directions make a great deal of difference. Hence, we present here the results of three LES grids with coarse (20^3), medium (40^3), and fine (80^3) resolution (with the fine resolution corresponding to a cell size of $36.6\,\text{m} \times 37.5\,\text{m} \times 37.5\,\text{m}$). On the medium and fine grid, the initial perturbation is resolved almost perfectly (see Fig. 2c), while, on the coarse

grid, there are some slight deviations in the initial perturbation energy distribution. We performed LESs on these grids using ALDM ($\beta = 0$ and $\beta = 0.01$), DSM, and CDS4. For all of these cases, we averaged the results of nine simulations to get an estimate of the ensemble average and the standard deviations.

With the high LES resolution of 80^3 cells, the results are very similar to the DNS (Figs. 10a,b). The base wave amplitude decay is slightly overpredicted with ALDM and CDS4, but the amplitude remains almost within the variations among the DNS ensemble members. The peak dissipation rate matches well with the DNS in all cases. With CDS4, the dissipation falls off a bit too rapidly after the peak. With modified ALDM ($\beta = 0.01$), the dissipation rate is overpredicted during the phases of weak turbulence (i.e., before and after the peak). Actually, using the modified version is not necessary for this simulation, since no physically unlikely oscillations develop at any time because of the high level of turbulence during most of the simulation.

When the resolution is reduced to 40^3 cells (Figs. 10c,d), the main difference is in the CDS4 simulations. The turbulence during the peak of breaking is too strong, and the molecular dissipation is not sufficient on the coarse grid to keep the energy balance. Energy piles up at the smallest resolved wavenumbers (see the energy spectra in Fig. 12), and numerical errors lead to an increase of flow total energy, which eventually also affects the largest resolved scales and therefore the amplitude of the base wave. The time of simulation breakdown is almost the same in all ensemble members. By using the turbulence parameterization schemes, this instability can be avoided. The best matching with the DNS results is obtained with the original ALDM. Only about 10% of the peak energy dissipation is resolved (see Fig. 11a), but the sum of resolved molecular and numerical dissipation matches quite well with the DNS result. Also, the ratio between ε_k and ε_p is well reproduced (see Fig. 11b). The modified ALDM dissipates too much energy. The DSM predicts a slightly too-high base wave amplitude after the breaking, and the total dissipation rate starts oscillating moderately after approximately 60 min. The total dissipation rate presented in Fig. 11c is overpredicted a bit at the peak but matches well with the DNS before $t = 10$ min and after $t = 15$ min.

In Fig. 12, we present the energy spectra of all LESs with 40^3 cells compared to the DNS spectra. The CDS4 spectra are wrong, as mentioned above, and the method fails for this case. The ALDM and DSM spectra are very close to the DNS reference for wavelengths $\lambda_\zeta > 400$ m. For smaller wavelengths, the spectral energy is slightly underpredicted, with only very small differences between ALDM ($\beta = 0.0$) and DSM. With ALDM
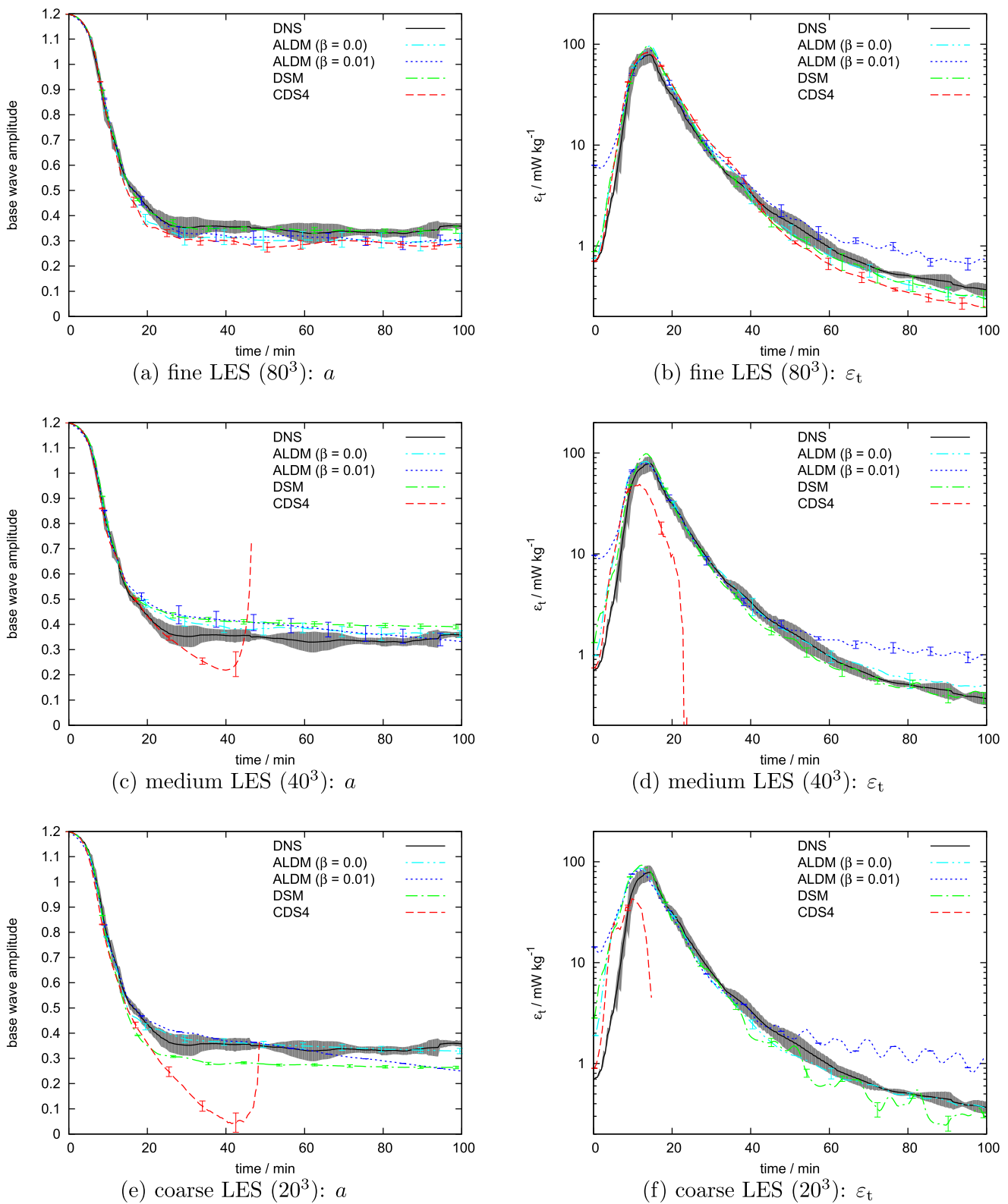
FIG. 10. Statically unstable HGW (3D). Base wave amplitude a and total dissipation rate ε_t at coarse, medium, and fine LES resolution. The gray shaded area indicates the standard deviation of five DNSs, and the error bars indicate the standard deviation of nine LESs.
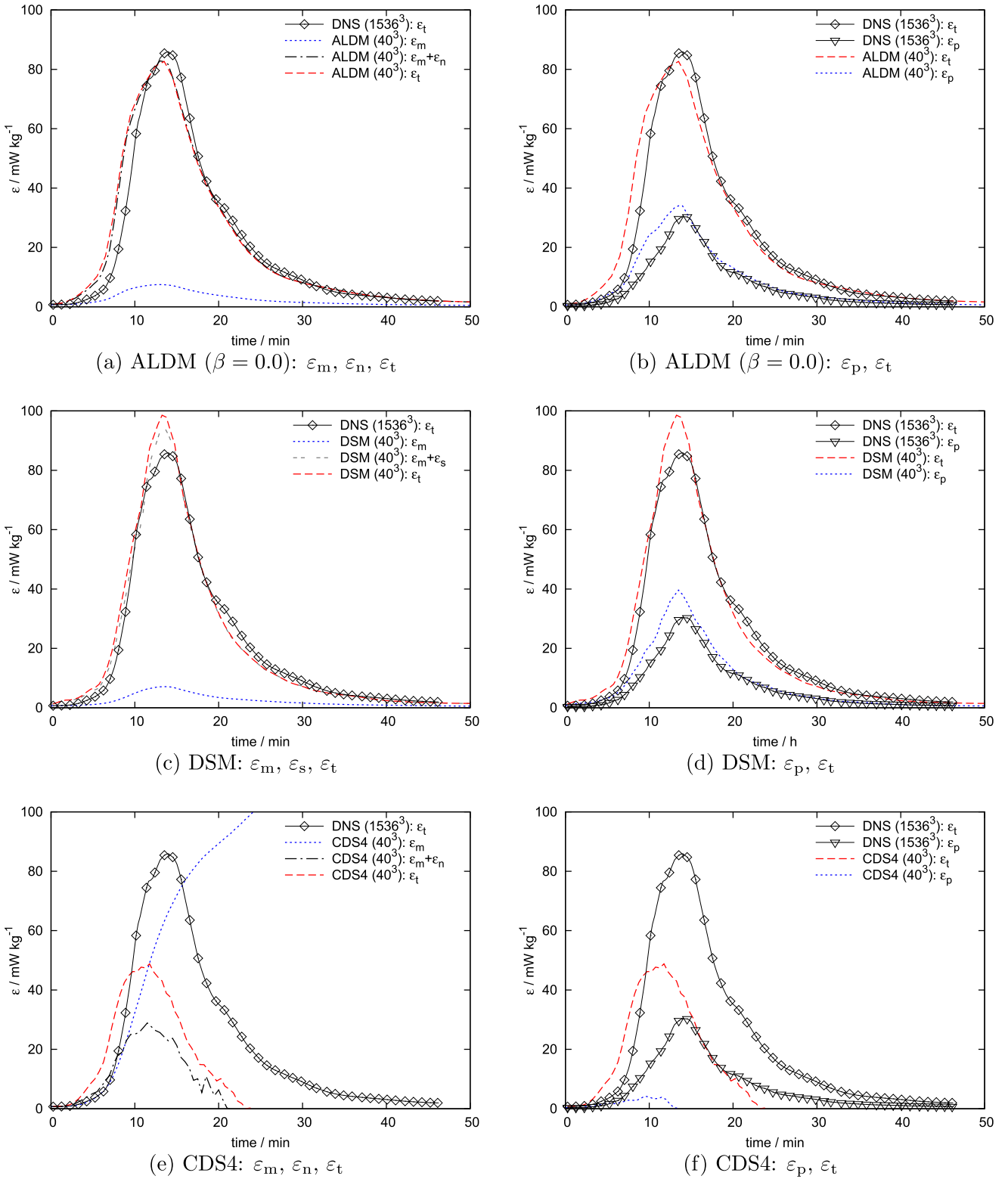
FIG. 11. Statically unstable HGW (3D). Comparison of (a),(c),(e) resolved (ε_m), numerical (ε_n), parameterized (ε_s), and total (ε_t) dissipation and (b),(d),(f) thermal (ε_p) and total dissipation during the first breaking event (DNS: single simulation; LES: ensemble averages).
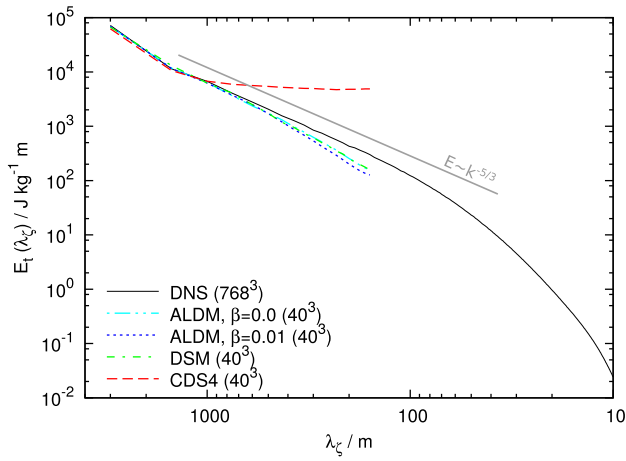
(a) E_t at max. dissipation ($t = 15\,\mathrm{min}$)
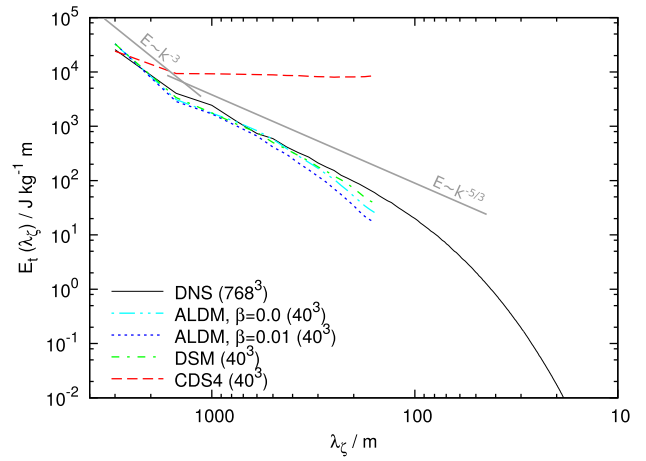
(b) E_t at $t = 30\,\mathrm{min}$
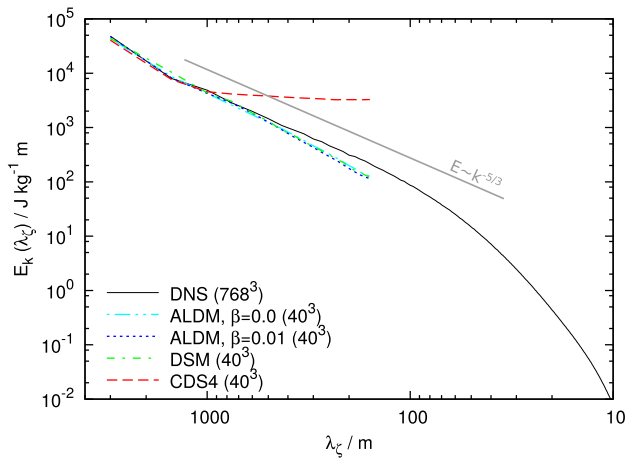
(c) E_k at max. dissipation ($t = 15\,\mathrm{min}$)
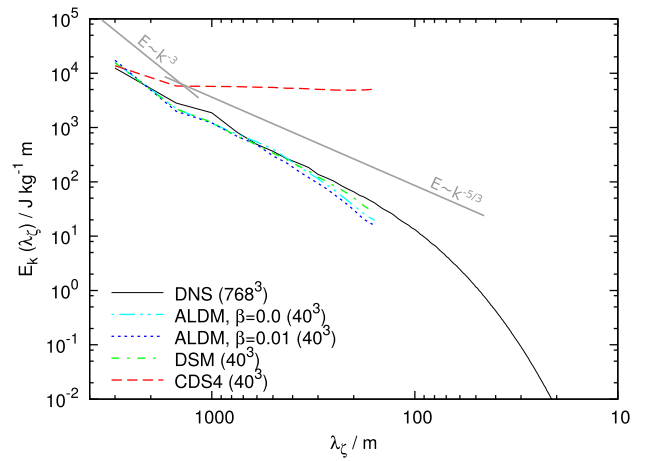
(d) E_k at $t = 30\,\mathrm{min}$
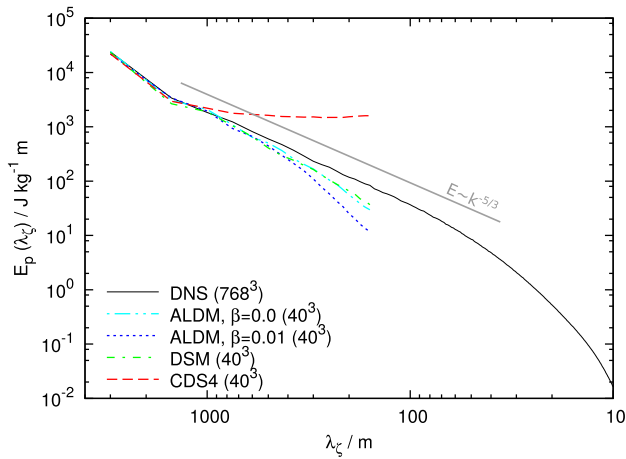
(e) E_p at max. dissipation ($t = 15\,\mathrm{min}$)
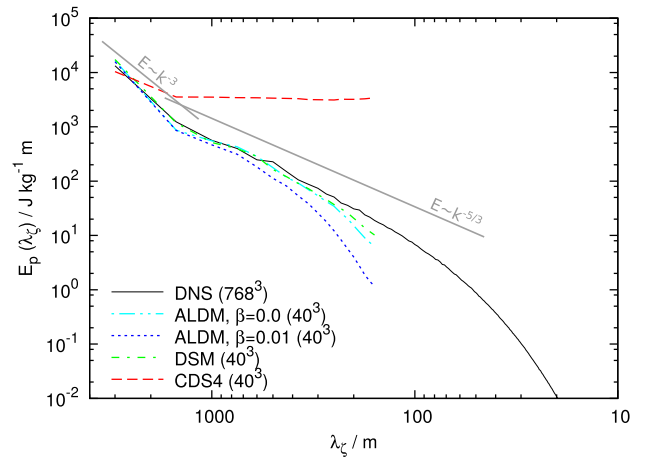
(f) E_p at $t = 30\,\mathrm{min}$

FIG. 12. Statically unstable HGW (3D). Distributions of total, kinetic, and potential energy over vertical wavelength λ_ζ (a),(c),(e) at the moment of maximum total energy dissipation and (b),(d),(f) at $t = 30\,\mathrm{min}$ (DNS: single simulation; LES: ensemble averages).

($\beta = 0.01$), the thermal energy dissipation is over-predicted; hence, the spectra of potential and total energy fall off rapidly close to the grid cutoff wavelength.

The results obtained with the coarsest grid, with 20^3 cells (Figs. 10e,f), are similar to those with the medium resolution. The simulations with CDS4 break down as a result of the unbounded growth of numerical errors. ALDM with $\beta = 0.01$ is far too dissipative before and after the peak of dissipation. The DSM now under-predicts the final wave amplitude and generates oscillations of total dissipation after the breaking. The closest match with the DNS is obtained with the original ALDM, both in terms of base wave amplitude and total dissipation rate. Also, the variations among ensemble members are similar to the DNSs. The onset of dissipation is, in all LESs, a little bit earlier than in the DNSs. This is consistent with our observations in case 1.

c. 2.5D simulations

The results of the 2.5D simulations (DNS and LES) are summarized in Fig. 13. LES grids with high (80^2 cells), medium (40^2 cells), and coarse resolution (20^2 cells) were used. The same LESs were performed eight times with some low-level white noise superposed on the initial condition (consisting of the base wave and its leading primary perturbation) and once with no added noise. The results of these nine realizations were then averaged. The reference 2.5D DNSs were run at a resolution of 500×500 cells. An ensemble of six DNSs was used for the calculation of mean values and standard deviations.

With the highest resolution (80^2 cells), the results in terms of wave amplitude and total dissipation rate are in very close agreement with the reference DNSs. Only for CDS4 is the dissipation rate a bit too low during the period of decreasing dissipation.

At the medium resolution (40^2 cells), the DSM and ALDM results are very similar and still in good agreement with the DNSs. The dissipation peak is slightly shifted to earlier times according to the dissipation acting at larger wavenumbers and the hence reduced time required for flow energy to reach this range. CDS4, however, predicts the wrong evolution of the wave amplitude and dissipation rate and cannot be recommended for this resolution.

At the coarsest resolution (20^2 cells), ALDM and DSM still do a very good job in predicting the amplitude decay and the dissipation maximum. The dissipation peak is further shifted forward in time because of the reduced time the flow energy needs to move through the spectrum. In the CDS4 simulation, however, the dissipation rate becomes negative after approximately 20 min, and, hence, the predicted flow field is completely wrong, although the simulations remain stable in a numerical sense during the whole simulated period.

d. Summary of case 3

The unstable HGW involves much stronger turbulence than the IGW cases, and thus the buoyancy forces are weaker compared to the acceleration associated with turbulent motions. The original ALDM and the DSM thus do an excellent job in predicting the dissipation rates and the wave amplitude decay over time, even at a very coarse resolution with a cell size of about $\Delta = 150$ m, both in 3D and 2.5D simulations. According to Fruman et al. (2014), the 3D and the 2.5D solutions are similar in this case. We conclude that for a proper estimation of the key parameters of breaking time, maximum dissipation, and amplitude decay, only a 2.5D simulation with $20^2 = 400$ cells is necessary if ALDM or DSM is applied.

8. Conclusions

We scrutinized different methods of large-eddy simulation for three cases of breaking monochromatic gravity waves. The methods tested included the following: the adaptive local deconvolution method (ALDM), an implicit turbulence parameterization; the dynamic Smagorinsky method (DSM); and a plain fourth-order central discretization without any turbulence parameterization (CDS4). The test cases have been carefully designed and set up by Remmler et al. (2013) and Fruman et al. (2014) based on the primary and secondary instability modes of the base waves and included an unstable and a stable inertia–gravity wave, as well as an unstable high-frequency gravity wave. All simulations presented were run in 2.5D and 3D domains, and, for all simulations, a small ensemble of simulations starting from slightly different initial conditions was performed in order to assess the sensitivity and robustness of the results.

The original ALDM leads to spurious oscillations of the buoyancy field in some 3D simulations, where the velocity field is very smooth for a long time. We thus developed a modified version of the ALDM flux function. The modification led to a significant reduction of the oscillations but also increased the overall energy dissipation.

For all three test cases, we started at an LES resolution of 80 cells per wavelength of the original wave and gradually reduced the resolution in all three directions. The inertia–gravity wave cases, in which the wave vector almost coincides with the vertical direction, were very sensitive to the resolution in the direction of the wave vector, while the resolution in the other directions could be strongly reduced without a massive negative effect on the overall results.
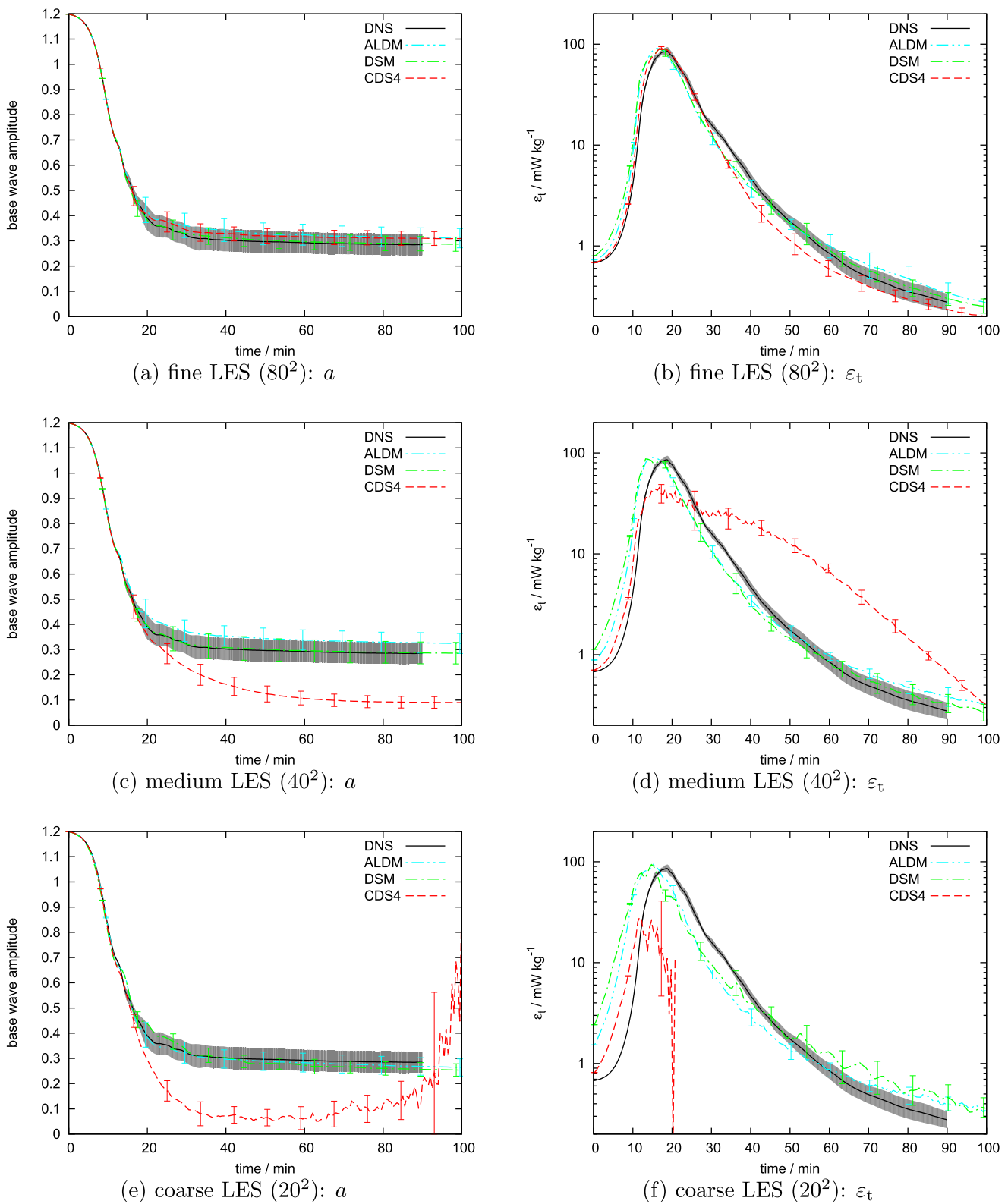
FIG. 13. Statically unstable HGW (2.5D). Base wave amplitude a and total dissipation rate ε_t at coarse, medium, and fine LES resolution compared with a and resolved dissipation rate ε_m from DNS. The gray shaded area indicates the standard deviation of six DNSs, and the error bars indicate the standard deviation of nine LESs.

We found that results obtained with ALDM and DSM are generally in good agreement with the reference direct numerical simulations as long as the resolution in the direction of the wave vector is sufficiently high. The CDS4 simulations, without turbulence parameterization, are only successful if the resolution is high and the level of turbulence comparatively low. In cases with low turbulence intensity and a smooth velocity field for long time periods (unstable and stable IGW) ALDM generated spurious oscillations in the buoyancy field, which we could avoid by using the modified numerical flux function. However, this was not necessary in the case with a high turbulence level (unstable HGW) and in all 2.5D simulations.

Our results back the findings of Remmler and Hickel (2012, 2013, 2014), who showed that both DSM and ALDM are suitable tools for the simulation of homogeneous stratified turbulence. Applying the same methods to gravity wave breaking, where turbulence is spatially inhomogeneous and intermittent in time, reveals that DSM is, in some cases, more robust than ALDM, although ALDM provides a better approximation of the spectral eddy viscosity and diffusivity in homogeneous stratified turbulence (Remmler and Hickel 2014).

In all simulations, we observed that the peak of dissipation occurs earlier in simulations with coarser computational grids. This is more pronounced in 2.5D LESs but also apparent in 3D LESs. We explain this time difference by the time required for flow energy to move from the smallest resolved wavenumbers in an LES to the dissipative scales in a DNS. Among the tested LES methods, there is no method that can account for this time lag. However, the large-scale flow and the maximum dissipation can still be predicted correctly.

Fruman et al. (2014) have shown that, in some cases, 2.5D simulations can be sufficient to get a good estimate of the energy dissipation during a breaking event. We showed that, with ALDM and DSM, reliable results can be obtained in 2.5D simulations with fewer than 2000 computational cells. Such inexpensive simulations will allow for the running of large numbers of simulations in order to study the influence of various parameters on wave breaking, such as stratification, wavelength, amplitude, propagation angle, and viscosity. A possible automated approach would involve computing the growth rates of perturbations of the original waves, setting up an ensemble of 2.5D LESs initialized by the base wave and its leading primary perturbation, and extracting key data from the LES results, such as the maximum energy dissipation, the amplitude decay, and the duration of the breaking event. Another potential application of our findings is the (2.5D or 3D) simulation of wave packets in the atmosphere, which is computationally feasible only if small-scale turbulence remains unresolved and is treated by a reliable subgrid-scale parameterization, such as ALDM or DSM.

REFERENCES

Achatz, U., 2005: On the role of optimal perturbations in the instability of monochromatic gravity waves. *Phys. Fluids,* **17,** 094107, doi:10.1063/1.2046709.

——, and G. Schmitz, 2006a: Optimal growth in inertia–gravity wave packets: Energetics, long-term development, and three-dimensional structure. *J. Atmos. Sci.,* **63,** 414–434, doi:10.1175/JAS3637.1.

——, and ——, 2006b: Shear and static instability of inertia–gravity wave packets: Short-term modal and nonmodal growth. *J. Atmos. Sci.,* **63,** 397–413, doi:10.1175/JAS3636.1.

Afanasyev, Y. D., and W. R. Peltier, 2001: Numerical simulations of internal gravity wave breaking in the middle atmosphere: The influence of dispersion and three-dimensionalization. *J. Atmos. Sci.,* **58,** 132–153, doi:10.1175/1520-0469(2001)058<0132:NSOIGW>2.0.CO;2.

Andreassen, Ø., P. Øyvind Hvidsten, D. C. Fritts, and S. Arendt, 1998: Vorticity dynamics in a breaking internal gravity wave. Part 1. Initial instability evolution. *J. Fluid Mech.,* **367,** 27–46, doi:10.1017/S0022112098001645.

Baldwin, M. P., and Coauthors, 2001: The quasi-biennial oscillation. *Rev. Geophys.,* **39,** 179–229, doi:10.1029/1999RG000073.

Chun, H.-Y., M.-D. Song, J.-W. Kim, and J.-J. Baik, 2001: Effects of gravity wave drag induced by cumulus convection on the atmospheric general circulation. *J. Atmos. Sci.,* **58,** 302–319, doi:10.1175/1520-0469(2001)058<0302:EOGWDI>2.0.CO;2.

Dörnbrack, A., 1998: Turbulent mixing by breaking gravity waves. *J. Fluid Mech.,* **375,** 113–141, doi:10.1017/S0022112098002833.

Dunkerton, T. J., 1997: Shear instability of internal inertia–gravity waves. *J. Atmos. Sci.,* **54,** 1628–1641, doi:10.1175/1520-0469(1997)054<1628:SIOIIG>2.0.CO;2.

Eidson, T. M., 1985: Numerical simulation of the turbulent Rayleigh–Bénard problem using subgrid modelling. *J. Fluid Mech.,* **158,** 245–268, doi:10.1017/S0022112085002634.

Fritts, D. C., and M. J. Alexander, 2003: Gravity wave dynamics and effects in the middle atmosphere. *Rev. Geophys.,* **41,** 1003, doi:10.1029/2001RG000106.

——, and L. Wang, 2013: Gravity wave–fine structure interactions. Part II: Energy dissipation evolutions, statistics, and implications. *J. Atmos. Sci.,* **70,** 3735–3755, doi:10.1175/JAS-D-13-059.1.

——, ——, J. Werne, T. Lund, and K. Wan, 2009a: Gravity wave instability dynamics at high Reynolds numbers. Part I: Wave field evolution at large amplitudes and high frequencies. *J. Atmos. Sci.,* **66,** 1126–1148, doi:10.1175/2008JAS2726.1.

——, ——, ——, and ——, 2009b: Gravity wave instability dynamics at high Reynolds numbers. Part II: Turbulence evolution, structure, and anisotropy. *J. Atmos. Sci.,* **66,** 1149–1171, doi:10.1175/2008JAS2727.1.

——, ——, and J. A. Werne, 2013: Gravity wave–fine structure interactions. Part I: Influences of fine structure form and orientation on flow evolution and instability. *J. Atmos. Sci.,* **70,** 3710–3734, doi:10.1175/JAS-D-13-055.1.

Fruman, M. D., and U. Achatz, 2012: Secondary instabilities in breaking inertia–gravity waves. *J. Atmos. Sci.,* **69,** 303–322, doi:10.1175/JAS-D-10-05027.1.

——, S. Remmler, U. Achatz, and S. Hickel, 2014: On the construction of a direct numerical simulation of a breaking inertia–gravity wave in the upper mesosphere. *J. Geophys. Res. Atmos.,* **119,** 11 613–11 640, doi:10.1002/2014JD022046.

Germano, M., U. Piomelli, P. Moin, and W. H. Cabot, 1991: A dynamic subgrid-scale eddy viscosity model. *Phys. Fluids,* **A3,** 1760–1765, doi:10.1063/1.857955.

Grimsdell, A. W., M. J. Alexander, P. T. May, and L. Hoffmann, 2010: Model study of waves generated by convection with direct validation via satellite. *J. Atmos. Sci.,* **67,** 1617–1631, doi:10.1175/2009JAS3197.1.

Hickel, S., and N. A. Adams, 2007: A proposed simplification of the adaptive local deconvolution method. *ESAIM: Proc.,* **16,** 66–76, doi:10.1051/proc:2007008.

——, ——, and J. A. Domaradzki, 2006: An adaptive local deconvolution method for implicit LES. *J. Comput. Phys.,* **213,** 413–436, doi:10.1016/j.jcp.2005.08.017.

——, ——, and N. N. Mansour, 2007: Implicit subgrid-scale modeling for large-eddy simulation of passive-scalar mixing. *Phys. Fluids,* **19,** 095102, doi:10.1063/1.2770522.

——, T. Kempe, and N. A. Adams, 2008: Implicit large-eddy simulation applied to turbulent channel flow with periodic constrictions. *Theor. Comput. Fluid Dyn.,* **22,** 227–242, doi:10.1007/s00162-007-0069-7.

——, C. Egerer, and J. Larsson, 2014: Subgrid-scale modeling for implicit large eddy simulation of compressible flows and shock-turbulence interaction. *Phys. Fluids,* **26,** 106101, doi:10.1063/1.4898641.

Hines, C. O., 1965: Dynamical heating of the upper atmosphere. *J. Geophys. Res.,* **70,** 177–183, doi:10.1029/JZ070i001p00177.

——, 1997: Doppler-spread parameterization of gravity-wave momentum deposition in the middle atmosphere. Part 1: Basic formulation. *J. Atmos. Sol.-Terr. Phys.,* **59,** 371–386, doi:10.1016/S1364-6826(96)00079-X.

Hoffmann, P., M. Rapp, A. Serafimovich, and R. Latteck, 2005: On the occurrence and formation of multiple layers of polar mesosphere summer echoes. *Geophys. Res. Lett.,* **32,** L05812, doi:10.1029/2004GL021409.

Kim, Y.-J., S. D. Eckermann, and H.-Y. Chun, 2003: An overview of the past, present and future of gravity–wave drag parametrization for numerical climate and weather prediction models. *Atmos.-Ocean,* **41,** 65–98, doi:10.3137/ao.410105.

Lelong, M.-P., and T. J. Dunkerton, 1998a: Inertia–gravity wave breaking in three dimensions. Part I: Convectively stable waves. *J. Atmos. Sci.,* **55,** 2473–2488, doi:10.1175/1520-0469(1998)055<2473:IGWBIT>2.0.CO;2.

——, and ——, 1998b: Inertia–gravity wave breaking in three dimensions. Part II: Convectively unstable waves. *J. Atmos. Sci.,* **55,** 2489–2501, doi:10.1175/1520-0469(1998)055<2489:IGWBIT>2.0.CO;2.

Lilly, D. K., 1992: A proposed modification of the Germano subgrid-scale closure method. *Phys. Fluids,* **A4,** 633–635, doi:10.1063/1.858280.

Lindzen, R. S., 1981: Turbulence and stress owing to gravity wave and tidal breakdown. *J. Geophys. Res.,* **86,** 9707–9714, doi:10.1029/JC086iC10p09707.

Lumley, J. L., 1964: The spectrum of nearly inertial turbulence in a stably stratified fluid. *J. Atmos. Sci.,* 21, 99–102.

Lund, T. S., and D. C. Fritts, 2012: Numerical simulation of gravity wave breaking in the lower thermosphere. *J. Geophys. Res.,* **117,** D21105, doi:10.1029/2012JD017536.

McFarlane, N. A., 1987: The effect of orographically excited gravity wave drag on the general circulation of the lower stratosphere and troposphere. *J. Atmos. Sci.,* **44,** 1775–1800, doi:10.1175/1520-0469(1987)044<1775:TEOOEG>2.0.CO;2.

McLandress, C., 1998: On the importance of gravity waves in the middle atmosphere and their parameterization in general circulation models. *J. Atmos. Sol.-Terr. Phy.,* **60,** 1357–1383, doi:10.1016/S1364-6826(98)00061-3.

Muraschko, J., M. D. Fruman, U. Achatz, S. Hickel, and Y. Toledo, 2014: On the application of Wentzel–Kramer–Brillouin theory for the simulation of the weakly nonlinear dynamics of gravity waves. *Quart. J. Roy. Meteor. Soc.,* **141,** 676–697, doi:10.1002/qj.2381.

O'Sullivan, D., and T. J. Dunkerton, 1995: Generation of inertia–gravity waves in a simulated life cycle of baroclinic instability. *J. Atmos. Sci.,* **52,** 3695–3716, doi:10.1175/1520-0469(1995)052<3695:GOIWIA>2.0.CO;2.

Plougonven, R., and C. Snyder, 2007: Inertia–gravity waves spontaneously generated by jets and fronts. Part I: Different baroclinic life cycles. *J. Atmos. Sci.,* **64,** 2502–2520, doi:10.1175/JAS3953.1.

Prusa, J. M., P. K. Smolarkiewicz, and R. R. Garcia, 1996: Propagation and breaking at high altitudes of gravity waves excited by tropospheric forcing. *J. Atmos. Sci.,* **53,** 2186–2216, doi:10.1175/1520-0469(1996)053<2186:PABAHA>2.0.CO;2.

Remmler, S., and S. Hickel, 2012: Direct and large eddy simulation of stratified turbulence. *Int. J. Heat Fluid Flow,* **35,** 13–24, doi:10.1016/j.ijheatfluidflow.2012.03.009.

——, and ——, 2013: Spectral structure of stratified turbulence: Direct numerical simulations and predictions by large eddy simulation. *Theor. Comput. Fluid Dyn.,* **27,** 319–336, doi:10.1007/s00162-012-0259-9.

——, and ——, 2014: Spectral eddy viscosity of stratified turbulence. *J. Fluid Mech.,* **755,** R5, doi:10.1017/jfm.2014.423.

——, M. D. Fruman, and S. Hickel, 2013: Direct numerical simulation of a breaking inertia–gravity wave. *J. Fluid Mech.,* **722,** 424–436, doi:10.1017/jfm.2013.108.

Rieper, F., S. Hickel, and U. Achatz, 2013: A conservative integration of the pseudo-incompressible equations with implicit turbulence parameterization. *Mon. Wea. Rev.,* **141,** 861–886, doi:10.1175/MWR-D-12-00026.1.

Shu, C.-W., 1988: Total-variation-diminishing time discretizations. *SIAM J. Sci. Stat. Comput.,* **9,** 1073–1084, doi:10.1137/0909073.

Smagorinsky, J., 1963: General circulation experiments with the primitive equations. I: The basic experiment. *Mon. Wea. Rev.,* **91,** 99–164, doi:10.1175/1520-0493(1963)091<0099:GCEWTP>2.3.CO;2.

Smith, R. B., 1979: The influence of mountains on the atmosphere. *Advances in Geophysics,* Vol. 21, Academic Press, 87–230, doi:10.1016/S0065-2687(08)60262-9.

Vallis, G. K., 2006: *Atmospheric and Oceanic Fluid Dynamics.* Cambridge University Press, 745 pp.

van der Vorst, H. A., 1992: Bi-CGSTAB: A fast and smoothly converging variant of Bi-CG for the solution of nonsymmetric linear systems. *SIAM J. Sci. Stat. Comput.,* **13,** 631–644, doi:10.1137/0913035.

Weinstock, J., 1985: Theroretical gravity wave spectrum in the atmosphere: Strong and weak wave interactions. *Radio Sci.,* **20,** 1295–1300, doi:10.1029/RS020i006p01295.

Winters, K. B., and E. A. D'Asaro, 1994: Three-dimensional wave instability near a critical level. *J. Fluid Mech.,* **272,** 255–284, doi:10.1017/S0022112094004465.